ISBN 978-82-326-4748-4 (printed version)
ISBN 978-82-326-4749-1 (electronic version)
ISSN 1503-8181

Doctoral Thesis

Richard Hann

Doctoral theses at NTNU, 2020:200

NTNU
Norwegian University of
Science and Technology

Doctoral theses at NTNU, 2020:200

Richard Hann

Atmospheric Ice Accretions, Aerodynamic Icing Penalties, and Ice Protection Systems on Unmanned Aerial Vehicles

NTNU
Norwegian University of
Science and Technology
Faculty of Information Technology
and Electrical Engineering
Department of Engineering Cybernetics

NTNU
Norwegian University of
Science and Technology

Richard Hann

Atmospheric Ice Accretions, Aerodynamic Icing Penalties, and Ice Protection Systems on Unmanned Aerial Vehicles

Thesis for the degree of Philosophiae Doctor

Trondheim, July 2020

Norwegian University of Science and Technology
Faculty of Information Technology
and Electrical Engineering
Department of Engineering Cybernetics

NTNU
Norwegian University of
Science and Technology

NTNU
Norwegian University of Science and Technology

Thesis for the degree of Philosophiae Doctor

Faculty of Information Technology
and Electrical Engineering
Department of Engineering Cybernetics

ISBN 978-82-326-4748-4 (printed version)
ISBN 978-82-326-4749-1 (electronic version)
ISSN 1503-8181

Doctoral theses at NTNU, 2020:200

Printed by Skipnes Kommunikasjon as

I was born not knowing and have had only
a little time to change that here and there.

– Richard P. Feynman

Summary

This thesis focused on atmospheric ice accretions, aerodynamic icing penalties, and ice protection systems (IPS) on fixed-wing unmanned aerial vehicles (UAVs). The motivation for this work was to increase the knowledge about the mechanisms and effects of atmospheric in-flight icing on UAVs. These insights were directed to aid in the development of systems to mitigate the adverse effects of icing on UAVs. Therefore, this thesis aimed to answer the following questions: Why is icing on UAVs a problem? What are the specific issues of icing on UAVs? How can we predict ice accretions on UAVs? What impacts does icing have on UAVs? How can we protect UAVs from icing? And, how much energy is required for an active UAV IPS?

The methods of this thesis included experimental tests and numerical simulations. Four experimental campaigns were conducted in the scope of this work. Icing wind tunnel tests were performed at Cranfield University in fall 2018 and at the facilities of the Technical Research Centre of Finland (VTT) in spring and fall 2019. Conventional wind tunnel tests with artificial ice shapes were conducted in summer 2019 in the fluid mechanics laboratory at the Norwegian University of Science and Technology (NTNU). Numerical simulations were conducted with LEWICE (2D) and FENSAP-ICE.

The first objective of this thesis was to investigate the special issues related to icing on UAVs and to identify differences to icing on manned aircraft. This included technical aspects originating from disparities in airframe size, airspeed, propulsion, mission objectives, etc. Operational challenges included differences in icing environments, difficulties in icing forecasting, and path-planning. Furthermore, an overview was given over general topics related to icing detection, IPS, icing wind tunnels, and simulation methods of icing for UAVs. Also, wind turbine icing was highlighted as a research field with significant similarities and potential synergies with UAV icing.

The second objective of the thesis was to collect experimental ice shapes from icing wind tunnel tests and compare them to numerical icing simulations. This work was relevant because the numerical methods used in this thesis have originally been developed for manned aircraft applications and were not validated for UAVs. One of the main concerns was the difference in the Reynolds number regime, which for UAVs is about an order of

magnitude lower than for manned aircraft. The comparison between numerical and experimental ice shapes revealed significant limitations of the codes. In general, both numerical simulation tools seemed to predict lower ice masses, smaller icing limits, and smoother ice shapes. The smallest deviations occurred for rime ice, the largest for glaze, especially for LEWICE. In general, FENSAP-ICE offered better results with a sufficient level of similarity to the experimental ice shapes. LEWICE showed more limitations, especially with regards to the shape and complexity of the ice shapes.

The third objective of the thesis was to investigate the effects of icing on the aerodynamic performance of UAVs. This work included a comparison of FENSAP-ICE to experiments with artificial ice shapes at low Reynolds numbers. This validation showcased the accuracy and the limitations of the numerical method, the latter which existed especially for flow conditions with large separations. Following this validation, two numerical studies were performed. One to identify the most hazardous meteorological icing conditions for UAVs, and the other to investigate the influence of airspeed and airfoil size on performance penalties. These studies showed that UAVs are more sensitive to icing conditions than manned aircraft and that the most hazardous conditions occur near the freezing point and in conditions with high water content.

The fourth and final part of this thesis focused on an electrothermal IPS for UAVs and the required heat loads for anti-icing and de-icing. A numerical study using LEWICE and FENSAP-ICE was conducted to investigate the differences between running-wet and fully-evaporative anti-icing systems, showing that running-wet was more efficient. Furthermore, an experimental campaign was conducted to test anti-icing, ice detection, and autonomous operation on a UAV IPS. Another experimental study was performed focusing on determining the heat loads for anti-icing and de-icing. A variety of icing and IPS parameters were tested on two different IPS systems (conventional and parting strip). The results showed that the least energy-efficient operation of the IPS was anti-icing. De-icing was substantially more efficient, especially at low temperatures. De-icing with a parting strip was shown to be the most efficient IPS mode.

Keywords: icing; in-flight icing; atmospheric icing; unmanned aerial vehicle (UAV); unmanned aerial system (UAS); remotely piloted aircraft system (RPAS); urban air mobility (UAM); advanced air mobility (AAM); drone; wind energy; wind turbine; ice accretion; icing penalties; ice protection system; ice detection; computational fluid dynamics (CFD); icing wind tunnel; low Reynolds.

Preface

This thesis is submitted in partial fulfilment of the requirements for the degree of Philosophiae Doctor (PhD) at the Norwegian University of Science and Technology (NTNU). The work has been conducted between the summers of 2016 and 2020 at the Centre for Autonomous Marine Operations and Systems (AMOS), the Centre for Integrated Remote Sensing and Forecasting for Arctic Operations (CIRFA), and the Department of Engineering Cybernetics (ITK). The main supervisor for this work was Professor Tor Arne Johansen and the co-supervisor was Adjunct Associate Professor Rune Storvold.

Acknowledgements

This work has received funding from the Research Council of Norway under grant numbers 237906-CIRFA and 223254-NTNU AMOS. The numerical simulations were performed on resources provided by the National Infrastructure for High-Performance Computing and Data Storage in Norway (UNINETT Sigma2) on the Vilje supercomputer, under project code NN9613K-Notur/NorStore.

First and foremost, I thank my main supervisor Tor Arne Johansen, whose support and guidance were critical for finishing this thesis. I also want to thank my co-supervisor Rune Storvold who always had good input on my work and aided me to build my research networks. I also thank the Department of Engineering Cybernetics, the Faculty of Information Technology and Electrical Engineering, and the Norwegian University of Science and Technology for allowing me to work in a world-class research environment.

I thank my colleagues from UBIQ Aerospace, who have collaborated with me on a wide scale of activities. Specifically, all of the icing wind tunnel testing was conducted together with UBIQ Aerospace on their D•ICE IPS technology and they were part of the discussions for the strategic orientation of this thesis. In particular, my gratitude goes to Kasper T. Borup, Kim L. Sorensen, Artur P. Zolich, Mikkel C. Nielsen, and Bård N. Stovner. I am looking forward to not being the only person on the team without a doctorate degree.

Much of the experimental work in this thesis would not have happened without the help of several people. I want to thank the team from VTT Technical Research Centre of Finland in Helsinki for their support of our icing wind tunnel experiments. I thank especially Tuomas Jokela, Mikko Tiihonen, Timo Karlsson, and Raul Prieto – I hope we are going to have many more opportunities for collaboration in the future.

I also thank Tania Bracchi, R. Jason Hearst, and Lars Sætran from the NTNU Department of Energy and Process Engineering for our collaboration in their wind tunnel facilities.

My gratitude also goes to all the co-authors and reviewers of the papers included in this thesis. I especially thank Adriana Enache from the Von Karman Institute for all the scientific discussions we had. I hope we are going to have many more research opportunities coming our way.

Svalbard is a very special place for me, so I want to express my appreciation towards the University Centre in Svalbard for the many study, research, and teaching opportunities it provided for me. In particular, my gratitude goes to Marius O. Jonassen and Andy Hodson for the collaboration and our ongoing research in the fields of meteorology and glaciology in the Arctic. I also thank Mark H. Hermanson for introducing me to the topic of atmospheric pollution and offering me opportunities to work together.

Last, but certainly not least, I want to thank my family and friends for supporting me on a sometimes-rocky road during this thesis. My very special thanks go to Annakaisa who is the light of my days and my companion in adventures, small and big.

– Richard Hann

Contents

Abbreviations and Definitions

α	Angle of attack
AOA	Angle of attack
BVLOS	Beyond visual line of sight
c	Chord
c_d	Drag coefficient
CFD	Computational fluid dynamics
c_l	Lift coefficient
c_m	Moment coefficient
D•ICE	An electrothermal ice protection system
FENSAP-ICE	An icing simulation code
HALE	High-altitude long-endurance
IPS	Ice protection system
IWT	Icing wind tunnel
k-ω SST	Menter shear stress transport turbulence model
LEWICE	An icing simulation code
LWC	Liquid water content
MVD	Mean volume diameter
q	Heat flux
RANS	Reynolds-averaged Navier–Stokes equations
Re	Reynolds number
RMSE	Root mean square error
SA	Spalart-Allmaras turbulence model
SLD	Supercooled large droplets
SWT	Small wind turbine
T	Temperature
t	Duration
UAM	Urban air mobility
UAS	Unmanned aerial system
UAV	Unmanned aerial vehicle
UBIQ Aerospace	A start-up company
v	Airspeed
VLOS	Visual line of sight
VTT	Technical Research Centre of Finland

1 Introduction

1.1 Motivation

Unmanned aerial vehicles (UAVs) – sometimes also called unmanned aerial systems (UAS), or colloquially called drones – are an emerging technology that are on their way to becoming an integral part of our everyday lives. Until recently, UAVs were mostly used only by selected defence forces around the world and hobbyists using model aircraft for sport. As UAV technology became widely available, new applications were developed for military but also for commercial purposes. The Federal Aviation Administration estimated in a recent report that the commercial use of UAVs, in the USA alone, will increase threefold between 2019 and 2023 [1].

This steep growth is fuelled by new business ideas and commercial applications of UAVs [2]. Examples include the use of UAVs in agriculture, construction, film industry, infrastructure inspections, shipping, meteorology, remote sensing, urban air mobility, and research. One commercial concept that has recently gained a lot of momentum and media coverage is package deliveries with UAVs. This last example is likely to be the first application that will lead to the widespread commercial utilization of UAVs.

There are many key challenges and risks related to the increased utilization of UAVs, for example, their integration into non-segregated airspace [3]. One particular risk is related to icing [4]. Atmospheric icing occurs mostly in clouds and leads to ice accretions of the airframe (Figure 1.1) which can severely decrease the aerodynamic performance and controllability of the vehicle. In-flight icing is a severe risk for all aircraft and has in the past led to several catastrophic incidents on manned aircraft [5]. Consequently, a large body of research exists on the topic for icing in manned aviation [6], whereas this issue is only an emerging question for UAVs.

Atmospheric icing can occur all year round and almost anywhere in the world [7, 8], not limited to cold climate regions (Figure 1.2). This implies that in practice, all missions that require beyond visual line of sight (BVLOS) operation are at risk of encountering icing conditions if the pilot cannot ensure that cloud environments are avoided. Consequently, icing imposes a severe limitation on the operational envelope of most

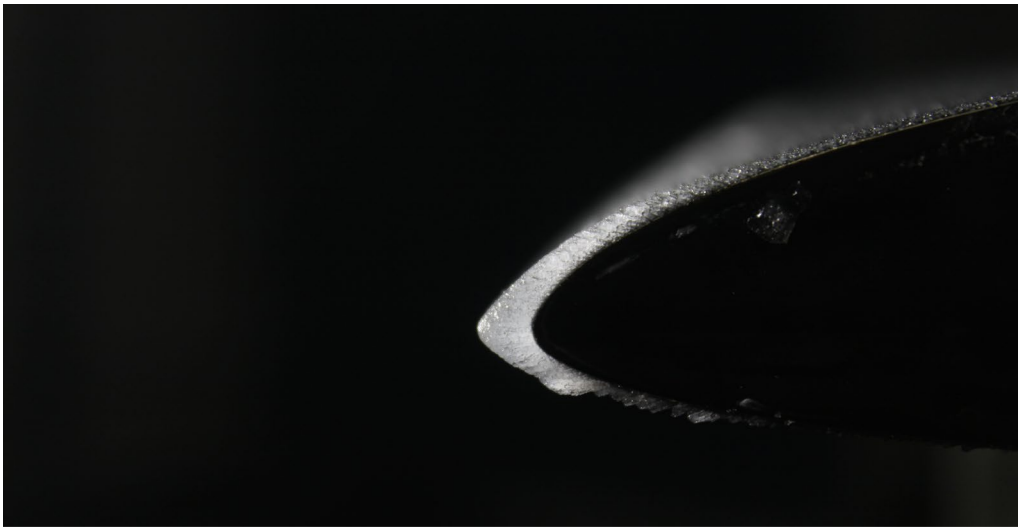

Figure 1.1: Ice accretion on the leading-edge of a UAV airfoil from icing wind tunnel tests.

Figure 1.2: A UAV flying in cold climate conditions in the Arctic. Photo: UBIQ Aerospace.

UAVs. A wide range of UAV applications, both military and commercial, are affected by this risk, as without suitable measures, UAVs cannot fly through clouds without taking substantial risks.

The main motivation of this thesis is to provide a better understanding of the effects of icing on UAVs and to support the development of all-weather capable UAVs that overcome the current icing limitations.

1.2 Literature Overview

The first mentioning of icing on UAVs in the literature dates back to 1990 in a study by the US Naval Air Development Center describing the hazards of icing for military UAV operations [9]. Because UAVs were mostly used by defence forces, information about operational issues are rare in the open literature. For more than ten years, no further information was published on the topic. In the 2000s, two reports described icing issues during UAVs operations in Hungary, Afghanistan, Serbia, and Kosovo in the 1990s [10, 11]. In 2017, the crash of a British Army Watchkeeper UAV became known and was attributed to pitot tube icing [12].

Since UAV technology became more widely available, also for commercial applications, icing started to shift into the focus of research. The existing UAV-specific research can be grouped by the following categories: icing on fixed-wing aircraft, icing on rotors, ice protection systems (IPS), ice detection, and path-planning in icing conditions.

An early paper on fixed-wing icing was published by Koenig et al. who performed UAV icing flight simulations with LEWICE2D to predict ice accretion rates and ice shapes on an unspecified airfoil [13]. Another study with LEWICE was conducted by Bottyán, simulating ice accretion for a short-range and a high-altitude long-endurance UAV [14]. The impact of icing on the aerodynamic performance degradation was investigated by Williams et al., who tested an RG-15 airfoil at low Reynolds numbers in the altitude icing wind tunnel at the Canadian National Research Council [15]. In the same study, they also tested 3D-printed ice shapes from the icing wind tunnel experiments in the conventional wind tunnel at the University of Auckland. Also in Auckland, Oo et al. conducted two numerical studies on airfoils at low Reynolds numbers [16, 17]. Szilder and Yuan used a morphogenetic icing simulation tool for three airfoils (HQ309, SD7032, and SD7037) and a 3D swept wing to calculate performance penalties [18]. The same

numerical model was also used by Szilder and McIlwan to investigate the effect of Reynolds number on ice accretion to show the differences in ice accretion on UAVs compared to manned aircraft [19]. Avery produced a thesis on the ice accretion of small UAVs with focus on cylinder accretion models with numerical and experimental methods [20]. Numerical simulations of ice accretions and electrothermal IPS have been performed by Tran et al. on a fixed-wing and rotary-wing UAV with FENSAP-ICE [21]. Last but not least, a study by Li et al. investigated the role of thermal conductivity of the airframe on ice accretions, showing that icing accretion processes are affected by the type of substrate (metal or composite) [22].

Another research direction focuses on icing on rotors and propellers. Most of the experimental work in this field has been conducted at Iowa State University. The transient ice accretion process on a UAV propeller has been studied by Liu et al. showing that ice introduced significant aerodynamic penalties (70% thrust reduction, 250% power consumption increase after 90s of glaze) [23]. An experimental study by Liu et al. tested a UAV propeller in two different icing conditions (rime and glaze) with particle imaging velocimetry technique to study the wake of iced propellers, finding complex vortices [24]. One study by Liu et al. investigated the effect of surface wettability on ice accretion and performance degradation on a UAV propeller [25]. They tested hydrophilic and super-hydrophobic coatings and showed that the latter mitigated performance penalties. Yan et al. conducted experimental work on coaxial-rotor UAVs, demonstrating that icing leads to a rapid loss of control and the ability to hover, after only 40s of icing duration [26, 27]. A noteworthy report has been produced by the Swiss company Meteomatics AG, who performed an experimental campaign showing the hazards of atmospheric icing on a rotary-wing mini-UAV developed for meteorological observations [28].

The mitigation of the adverse effects of icing on UAVs with IPS has also been covered in the literature. In his thesis, Sørensen proposes an autonomous IPS for small UAVs based on nano-carbon coatings, which was the precursor for the IPS system studied in this thesis [29]. Buschhorn et al. developed an IPS for UAVs based on aligned carbon nanotube arrays capable of de-icing and anti-icing [30]. An overview of general IPS requirements for a medium-altitude long-endurance UAV with special emphasis on electrically powered IPS is given by Lawson [31].

Ice detection is another important aspect of icing and UAVs have special requirements for ice sensors. Rashid et al. discussed the significance of ice sensors for UAVs and methods to incorporate them into the autopilot design [32]. An icing detection method based on the diagnosis of lift and drag changes on a UAV wing was proposed by Sørensen [33]. Botura and Fahrner developed a lightweight ice detection system based on using impedance measurements to detect ice on the surface of UAV wings [34]. A method for fault diagnosis and recovery from icing on UAVs was proposed by Tousi and Khorasa [35]. Rotondo et al. proposed an icing diagnosis method for UAVs using linear parameter varying observers [36]. An icing detection method for UAVs with adaptive nested multiple models was suggested by Cristofaro et al. [37]. Armanini discussed methods for decision-making for UAVs in icing environments [38]. A more in-depth review of in-flight detection and identification on manned aircraft is given by Caliskan and Hajiyev [39].

Path-planning in icing conditions is another special challenge for UAVs. Hovenburg et al. and Narum et al. both use the same method to calculate optimized flight paths for UAVs equipped with IPS in icing conditions [40, 41]. A weather information gap analysis for UAV operations that identifies icing as a key challenge has been generated by Campbell et al. [4].

For manned aviation, a substantially larger body of literature is available, which will be briefly addressed below in section 2.4.

1.3 Contribution

The main contributions of this thesis were experimental (Figure 1.3) and numerical (Figure 1.4) investigations of icing on UAVs. While a considerable amount of research exists for icing on manned aircraft at high Reynolds numbers, this thesis produced novel results for the low-Reynolds number regime that most UAVs operate in. Results are related to the topics of ice accretion on airfoils, effects of icing on UAV performance, and required heat loads of UAV ice protection systems. A key aspect of this work was also the comparison of experimental and simulation results with the aim to validate the numerical methods for UAV applications. In addition, a review was conducted to identify special issues of icing on UAVs and key differences to icing on manned aircraft.

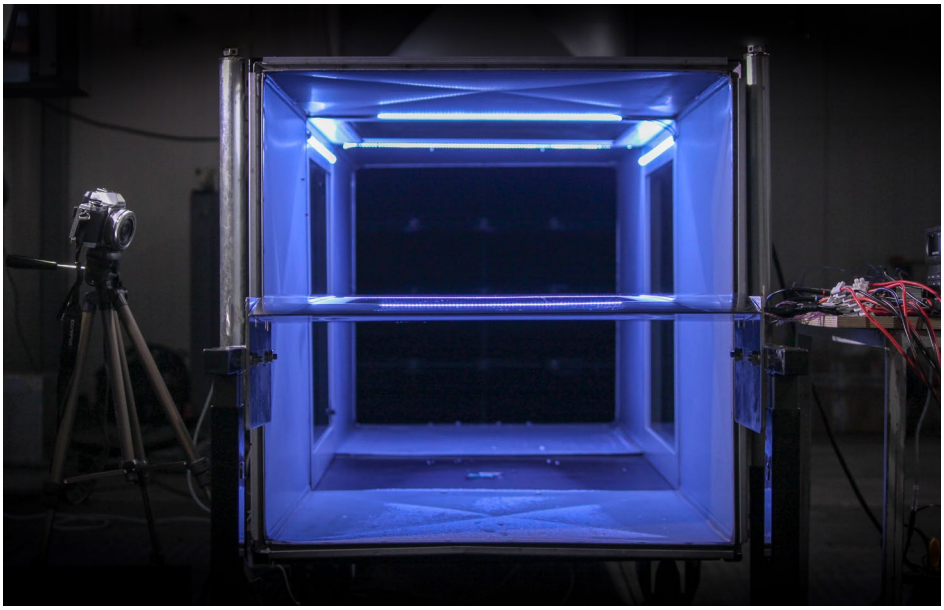

Figure 1.3: Experimental setup during an icing wind tunnel test.

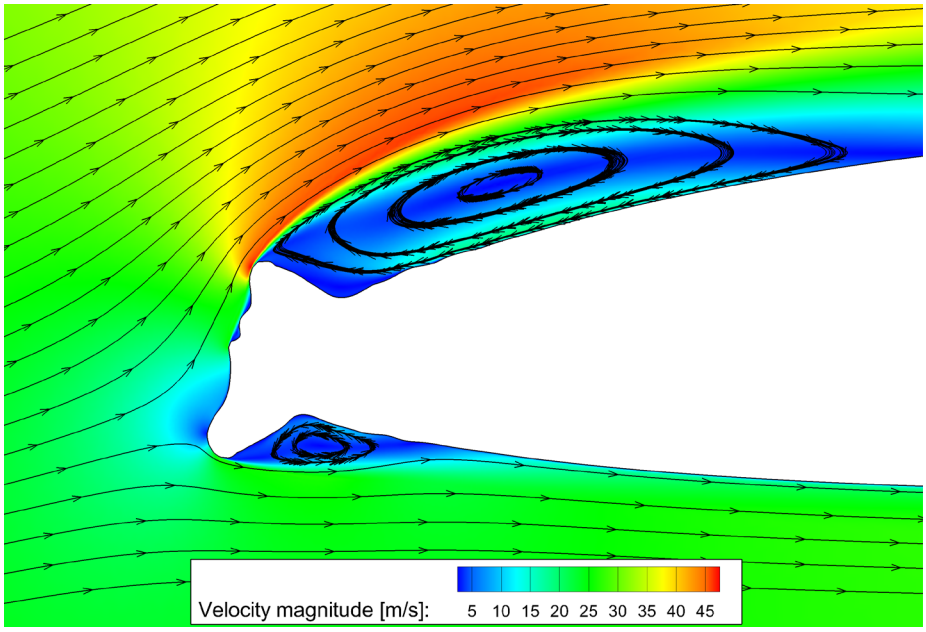

Figure 1.4: Numerical simulation of the airflow around an iced UAV airfoil.

1.4 Publications

This thesis is based on publications in international journals and conference proceedings.

Journal Publications

- [42] Hann, R., Johansen, T.A.: Unsettled Topics in Unmanned Aerial Vehicle Icing. SAE International, SAE EDGE Research Report, EPR2020008, 2020.
- [43] Hann, R., Hearst, R.J., Sætran, L., Bracchi, T.: Experimental and Numerical Icing Penalties of an S826 Airfoil at Low Reynolds Numbers. Aerospace, 7(4), 46, 2020.
- [44] Hann, R., Johansen, T.A.: UAV Icing: The Influence of Airspeed and Chord Length on Performance Degradation, Aircraft Engineering and Aerospace Technology, submitted 2020.

Conference Publications

- [45] Hann, R.: UAV Icing: Ice Accretion Experiments and Validation. SAE Technical Paper. No. 2019-01-2037, 2019.
- [46] Fajt, N., Hann, R., Lutz, T.: The Influence of Meteorological Conditions on the Icing Performance Penalties on a UAV Airfoil. 8th European Conference for Aeronautics and Aerospace Sciences (EUCASS), 2019.
- [47] Hann, R.: UAV Icing: Comparison of LEWICE and FENSAP-ICE for Anti-Icing Loads. AIAA SciTech Forum, 2019.
- [48] Hann, R., Borup, K., Zolich, A., Sorensen, K., Vestad, H., Steinert, M., & Johansen, T.A.: Experimental Investigations of an Icing Protection System for UAVs. SAE Technical Paper. No. 2019-01-2038, 2019.
- [49] Hann, R., Enache, A., Nielsen, M.C., Stovner, B.N., van Beeck, J., Johansen, T.A., Borup, K.T.: UAV Icing: Experimental Heat Loads for Electrothermal Anti-Icing and De-Icing, AIAA Atmospheric and Space Environments Conference, 2020.

Publications included as appendices

- [50] Hann, R., Wenz, A., Gryte, K., & Johansen, T. A.: Impact of atmospheric icing on UAV aerodynamic performance. Workshop on Research, Education and Development of Unmanned Aerial Systems (RED-UAS), IEEE, 2017.

- [51] Winter, A., Hann, R., Wenz, A., Gryte, K., Johansen, T. A.: Stability of a Flying Wing UAV in Icing Conditions. 8th European Conference for Aeronautics and Aerospace Sciences (EUCASS), 2019.

Other related publications not included in this thesis

- [52] Krøgenes, J., Brandrud, L., Hann, R., Bartl, J., Bracchi, T., Sætran, L.: Aerodynamic performance of the NREL S826 airfoil in icing conditions. Wind Energy Science Discussions, 2017.
- [53] Hann, R.: UAV Icing: Comparison of LEWICE and FENSAP-ICE for Ice Accretion and Performance Degradation. AIAA Atmospheric and Space Environments Conference, 2018.
- [54] Gryte, K., Hann, R., Alam, M., Roháč, J., Johansen, T. A., Fossen, T. I.: Aerodynamic modeling of the skywalker X8 fixed-wing unmanned aerial vehicle. International Conference on Unmanned Aircraft Systems (ICUAS). IEEE, 2018.
- [40] Hovenburg, A. R., Andrade, F. A. A., Hann, R., Rodin, C. D., Johansen, T. A., Storvold, R.: Long range path planning using an aircraft performance model for battery powered sUAS equipped with icing protection system. IEEE Journal on Miniaturization for Air and Space Systems, 2020.
- [41] Narum, E.F.L., Hann, R., Johansen, T.A.: Optimal Mission Planning for Fixed-Wing UAVs with Electro-Thermal Icing Protection and Hybrid-Electric Power Systems. International Conference on Unmanned Aircraft Systems (ICUAS), 2020.

1.5 Thesis Structure

The thesis is divided into four parts: The first part gives a general overview of issues related to icing on UAVs. The second part concerns ice accretion on fixed-wing lifting-surfaces. The third part explores various effects of icing conditions on the aerodynamic performance of UAVs. The fourth part investigates IPS and their required heat loads for icing mitigation.

Part I: Icing on UAVs

- **Chapter 2:** This chapter introduces the main challenges related to icing on UAVs. It expands on the motivation and background of this research field and discusses UAV applications that are at risk of UAV icing. The basic physical mechanisms of ice accretion on aircraft are introduced, together with a description of potential icing effects. Furthermore, this chapter outlines the differences of icing on manned and unmanned aircraft with regard to technical and operational aspects. In addition, the main operational principles of IPS will be introduced, with a focus on electrothermal systems. Last, a brief overview of numerical simulation tools and experimental facilities is given which are used throughout the rest of the thesis. This chapter is adapted from [42].

Part II: Ice Accretion

- **Chapter 3:** This chapter contains the results from the first experimental campaign in the icing wind tunnel at Cranfield University. The main focus of this chapter is on the generation and documentation of ice shapes on a UAV airfoil at low Reynolds numbers. The ice geometries are compared to two simulation tools, LEWICE and FENSAP-ICE, that have been developed for predicting ice shapes in manned aviation. The results show that the simpler tool shows significant discrepancies to the ice shapes that occur at temperatures close to freezing. Three methods of documenting the ice shapes were tested: manual tracing with pen and paper, photogrammetry, and a handheld 3D scanning device. The two latter methods had problems with the translucency of the ice. Last, a calibration error was identified during the tests and the means to rectify the results are presented. Based on [45].

Part III: Icing Performance Penalties

- **Chapter 4:** This chapter investigates the aerodynamic icing penalties on an airfoil at low Reynolds numbers with wind tunnel experiments and numerical simulations. The goal is to generate experimental data on the degradation of lift and drag of an airfoil, which can be used for the validation of numerical methods. The experiments are conducted in a (regular, non-icing) wind tunnel at NTNU with artificial 3D printed ice shapes. The experimental results are then

compared to a numerical simulation tool to assess its capabilities at low Reynolds numbers, which are typical for UAVs. The results show that the accuracy of the tool is inversely correlated to the complexity of the ice shape geometries. Based on [43].

- **Chapter 5:** This chapter is a parameter study on the influence of meteorological parameters on ice accretion and consequent performance degradation on a UAV airfoil. A total of 16 simulation cases are chosen based on the typical icing envelopes that are used for the certification of manned aircraft. For each case, the ice shapes are simulated, and then the resulting performance penalties calculated. The simulation methods are validated against experimental results and include a grid dependency study. The results show that the most hazardous icing conditions occur at temperatures close to the freezing point and in conditions with high water content. Based on [46].

- **Chapter 6:** This chapter is a parameter study on the influence of flight velocity and chord length of a UAV airfoil on icing penalties, using numerical simulations. The simulation results showed that the effect of airspeed variation on aerodynamic penalties was depending on the temperature and icing regime. The variation of chord length had a substantial impact on relative ice thicknesses, ice area, ice limits, and performance degradation, independent from the icing regime. This study showed that UAVs are more sensitive to icing compared to manned aircraft, primarily due to smaller chord lengths resulting in larger ice accretion in relation to the airfoil size. Furthermore, lower airspeeds led to lower aerodynamic heating which increased the risk of icing at temperatures close to freezing. These insights can help to improve flight planning in icing conditions and are essential for the identification of critical design cases for de-icing systems. Based on [44].

Part IV: Ice Protection Systems

- **Chapter 7:** This chapter compares two numerical simulation tools, LEWIE and FENSAP-ICE, to predict the minimum required energy for anti-icing for UAVs. Simulations are conducted for two different operational modes (fully-evaporative and running-wet) in 2D and 3D. The results demonstrate that

running-wet systems require typically less energy than fully-evaporative systems, except for cases with very low ambient temperatures. Furthermore, the simulations indicate that no significant 3D effects affect the anti-icing loads on the 3D wing. Based on [47].

- **Chapter 8:** This chapter presents the results from the experimental campaign with a prototype of the D•ICE IPS at the Cranfield icing wind tunnel. A full description of the electrothermal system and the ice detection algorithm is given. The experiments show the capability of the ice detection system to identify ice accretion on the surface and to distinguish between clean, wet, and iced conditions. Furthermore, the anti-icing loads for two temperatures are determined. The tests are finished with a full-system test that autonomously detected and mitigated icing. Based on [48].

- **Chapter 9:** This chapter presents the results from two experimental campaigns in the icing facilities of the Technical Research Centre of Finland. The work investigated the energy efficiency of three different IPS modes: anti-icing, de-icing, and de-icing with a parting strip. Two electro-thermal ice protection systems for fixed-wing UAVs were tested. One system that was operated in anti-icing and de-icing mode, and one variant with a parting strip de-icing system. Experiments were conducted in an icing wind tunnel facility for varying icing conditions at low Reynolds numbers. A parametric study over the ice shedding time was used to identify the most energy-efficient operation mode. The results showed that longer intercycle duration led to higher efficiencies and that de-icing with parting strip was superior compared to anti-icing and de-icing without parting strip. Based on [49].

Appendix

- **Appendix 1:** This appendix combines the simulation results on the aerodynamic performance degradation of a UAV airfoil with a flight simulator. Three different icing scenarios are chosen based on typical meteorological conditions. For each of these cases, the impact of icing on lift, drag, and moment is simulated. This data is then used for the input into a simple flight simulator to demonstrate the impact of icing on flight performance and the ability of the

autopilot to compensate. The results show that the autopilot is able to control the aircraft in case of the two less severe icing cases, but fails to keep control in case of the most severe icing case. Based on [50].

- **Appendix 2:** This appendix aims to use computational fluid dynamics (CFD) methods to determine the dynamic stability derivatives for an iced UAV. An established reduced-frequency approach using time-dependent 3D CFD and a arbitrary Lagrangian-Eulerian (ALE) method is used to calculate the static, quasi-static and dynamic stability derivatives of a clean and severely iced flying wing UAV at two angles of attack. Together with stationary 3D simulations, a quantitative assessment of changes to flight behaviour can be made. The method can be used for any aircraft in any icing condition with minor limitations. The results show a severe degradation to some stability derivatives, especially in static longitudinal performance, whereas others are less affected and some even improved. Based on [51].

Part I

Icing on UAVs

2 An Overview of UAV Icing Issues

2.1 UAV Applications

Unmanned aerial vehicles (UAVs) were originally developed at the beginning of the 1900s for the use by armed forces. The technology has resumed advancing since then and today UAVs are an essential part of most defence forces in the world. Military UAVs exist in a wide range of types and sizes, from micro-UAVs to large, high-altitude UAVs comparable in size to passenger transport airplanes. Military mission objectives typically involve intelligence, surveillance, reconnaissance, security, attack, combat support, sustainment, as well as command, control, and communication support. It is clear that many of these activities are of high importance and that mission success can be critical. Therefore, UAVs need to be able to operate without weather limitations, including atmospheric icing.

Besides military functions, UAVs have been developed for recreational purposes. For years, radio-controlled model aircraft have been flown for sport by a small community. In recent years, quadcopters have become a commonly available consumer product. Commercial use has increased as UAV technologies have become cheaper, and more accessible. Nowadays, UAVs are applied by many civil operators [2]. Frequent users of UAVs are the construction and agriculture sectors, where UAV applications are used for surveying, stockpile volume measurements, and crop monitoring. Common UAV applications today include also photography, film, inspection, mapping, remote operations, research, as well as search and rescue.

One key distinction of UAV operations is between missions flown within visual line of sight (VLOS) and beyond visual line of sight (BVLOS). Today, most commercial UAV operations are conducted in VLOS using rotary-wing UAVs with low degree of automation and autonomy. UAVs used for these applications are easy to operate and provide birds-eye view imagery.

There is a large potential for new applications that rely on BVLOS operations. These novel ideas are either based on remotely piloted aircraft systems, or on fully autonomous aircraft. Such UAVs are typically fixed-winged and with automated and/or vertical take-

Table 2.1: Visual line of sight (VLOS) and beyond visual line of sight (BVLOS) operation of commercial UAVs by application.

Civil UAV Applications	VLOS	BVLOS
Photography & filming	×	×
Inspection & monitoring	×	×
Mapping & surveying	×	×
Research	×	×
Search & rescue	×	×
Emergency response	×	×
Meteorology	×	×
Communications	×	×
Remote operations		×
Deliveries		×
Arctic operations		×

off and landing abilities. A popular example of this are UAV package delivery services. One more developing area is the energy industry, where UAVs may be deployed for monitoring power lines, pipelines, solar panels, and storage tanks and for detecting oil spills. Table 2.1 gives an overview of existing and future civil applications for UAVs and the flight environment (VLOS or BVLOS) associated with them.

Weather limitations need to be considered for any UAV that is supposed to operate BVLOS. Atmospheric icing is a severe risk for UAVs that can have hazardous outcomes. Consequently, UAVs require an icing risk mitigation strategy. Depending on the application, the strategies may consist of using nowcasting and forecasting data to avoid icing conditions, or of using dedicated ice protection systems (IPS) that mitigate the adverse effects of icing. VLOS operations are usually less vulnerable to in-cloud icing as the pilot can avoid clouds, but freezing precipitation can still be a risk.

The Arctic is a highly relevant area for UAVs. Polar regions are a very important domain for research on climate change, as temperatures are rising at significantly higher rates in the Arctic compared to the rest of the globe [55]. Furthermore, geopolitics, security, and the exploration of resources are important topics in the Arctic. Also, the reduction of sea ice extent leads to the opening of the Northwest Passage between Europe and Asia, which facilitates large economic opportunities in the shipping sector. Satellite coverage in the Arctic is typically very limited. Consequently, UAVs may be a key element for

many future operations in remote locations, both commercial, scientific, and military. Ship-launched UAVs with the ability to identify and track the movement of icebergs and sea ice, for instance, can increase navigation safety for shipping in the polar oceans. Due to the cold climate, icing is a frequent and relevant risk for UAVs operating in the Arctic [56].

2.2 In-Flight Icing

Atmospheric icing is a term for a meteorological condition where supercooled (water temperature below the freezing point) liquid water exists in the atmosphere. The supercooled liquid water occurs mostly in clouds (in-cloud icing) or less often in precipitation. When an aircraft flies into such conditions, the droplets will collide with the aircraft and freeze onto its surface. This is called atmospheric in-flight icing and is a global phenomenon that can occur all-year-round [7, 8].

The rate at which ice is accumulating on the airframe depends on meteorological parameters: air temperature, liquid water content (LWC), and droplet size. The latter is mostly described by the median volume diameter (MVD). In addition, properties of the aircraft affect the icing rate via the size of the airframe and the airspeed. Ice shapes are defined by the ice accretion regime which is mainly driven by the ambient temperature and airspeed. Several ice types can be defined, which will be briefly introduced below (Figure 2.1). It should be noted that the opposite of in-flight icing is ground icing. Ground icing refers to the accumulation of ice before take-off, related to supercooled fog, frost, or precipitation and will not be covered in this thesis.

2.2.1 Rime Ice

Rime is formed when the temperature of the droplets is so low, that they freeze instantly when they collide with a surface. During this process, small air pockets are trapped between the freezing droplets, which gives rime ice its characteristic white appearance (Figure 2.1 & Figure 2.3). The surface of rime is rough and often exhibits ice feathers. Rime ice builds into streamlined geometries with a usually low potential for disrupting the airfoil [57].

2.2.2 Glaze Ice

Glaze, also called clear ice, forms at temperatures near the freezing point (Figure 2.1 & Figure 2.2). In this temperature regime, the incoming droplets do not freeze instantly but remain in the liquid phase. The ensuing liquid water layer will then run back on the surface (runback water) and freeze in that process (Figure 2.4). The resulting ice will be translucent (no trapped air) with a smooth surface. Glaze usually grows into irregular ice geometries, sometimes with protruding ice horns. Consequently, glaze is typically associated with high aerodynamic performance degradation [57].

2.2.3 Mixed Ice

The ice that forms in between the icing regimes of rime and glaze is called mixed ice. This form of ice occurs when only part of the incoming water freezes while the rest builds a liquid layer (Figure 2.1 & Figure 2.3). This process is also supported by the latent heat release of the freezing water and aerodynamic heating. Mixed ice can come in many different geometries, and can sometimes grow into large ice horns which can be responsible for substantial aerodynamic penalties [58].

2.2.4 Supercooled Large Droplets (SLDs)

Icing related to freezing precipitation is less common than in-cloud icing but can be much more severe. The main reason for this is that cloud droplets are significantly smaller (40–50μm) compared to precipitation droplets (up to several millimeters). For this reason, icing in freezing rain or freezing drizzle is named supercooled large droplet (SLD) icing [59]. SLD icing can result in severe ice accretion, covering large surface areas, with substantial icing penalties [57].

2.2.5 Snow and Ice Crystals

Usually, snow and ice crystals are a lesser hazard for aircraft. The main reason for this is that snow normally does not stick to the airframe because of the high airspeeds. Snow is a larger hazard for static objects such as power lines, towers, masts, or wind turbines. In particular, wet snow can stick to these structures and add substantial weight loads that can lead to mechanical failure [60]. Ice crystals, often found in clouds, can become an issue when ingested in large numbers by aircraft engines [61].

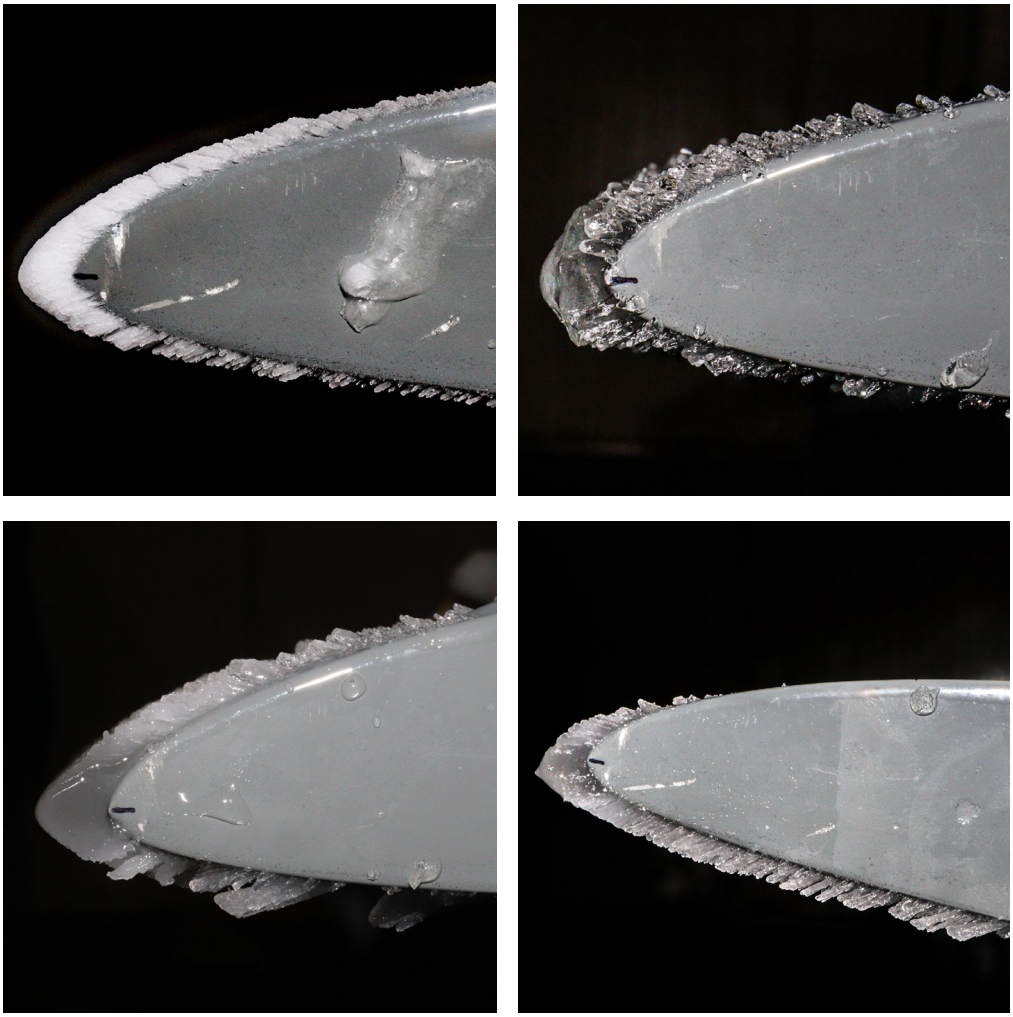

Figure 2.1: Rime ice (top, left), glaze ice (top, right), mixed ice (bottom, left), and mixed ice at high angle of attack (bottom, right).

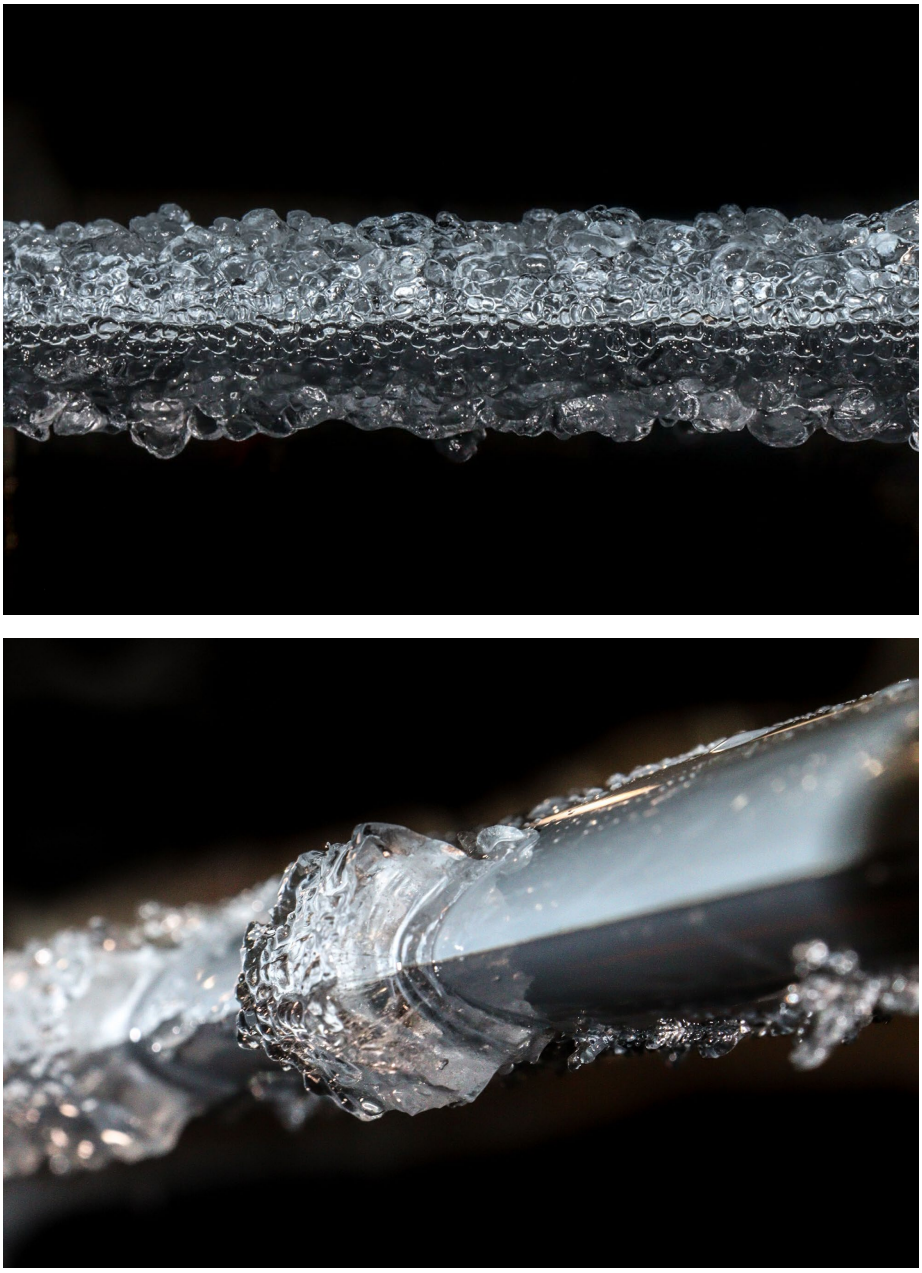

Figure 2.2: Glaze ice on the leading-edge of a UAV airfoil. Front-view (top) and side-view on a wing section that has been cut free (bottom).

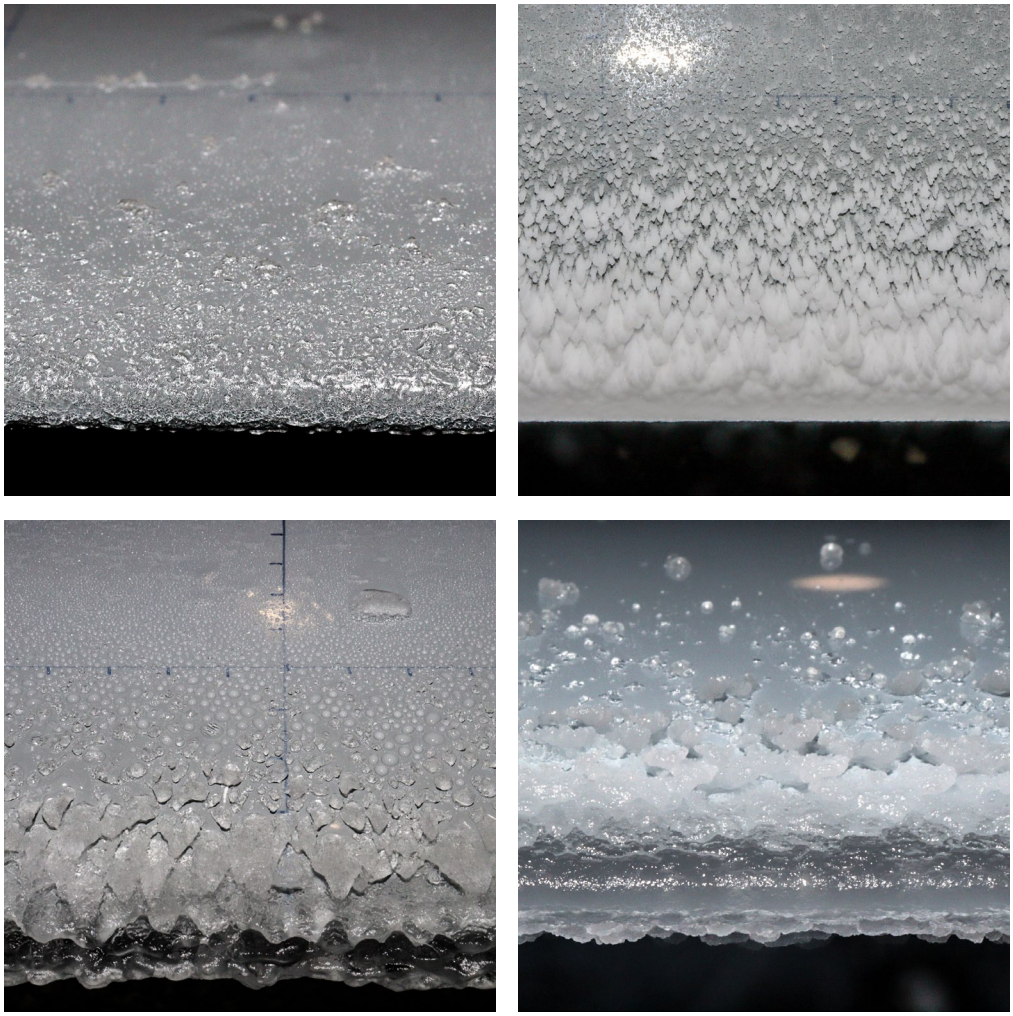

Figure 2.3: Ice roughness after 2min of ice accretion (top, left), rime ice feathers (top, right), mixed ice at low velocities (bottom, left), and mixed ice at cruise speed (bottom, right).

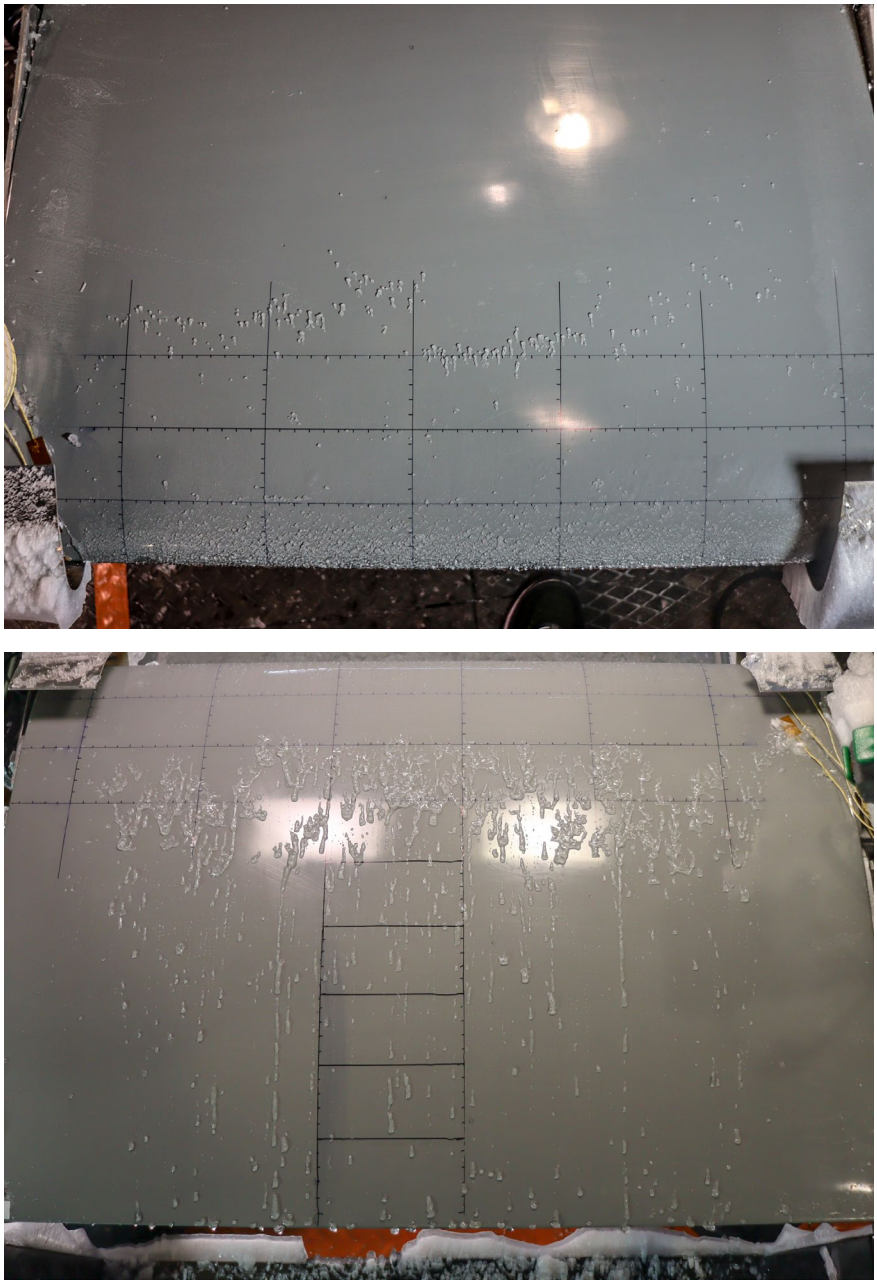

Figure 2.4: Runback ice during glaze icing conditions without IPS operation (top), and runback icing from an IPS after several cycles of de-icing (bottom).

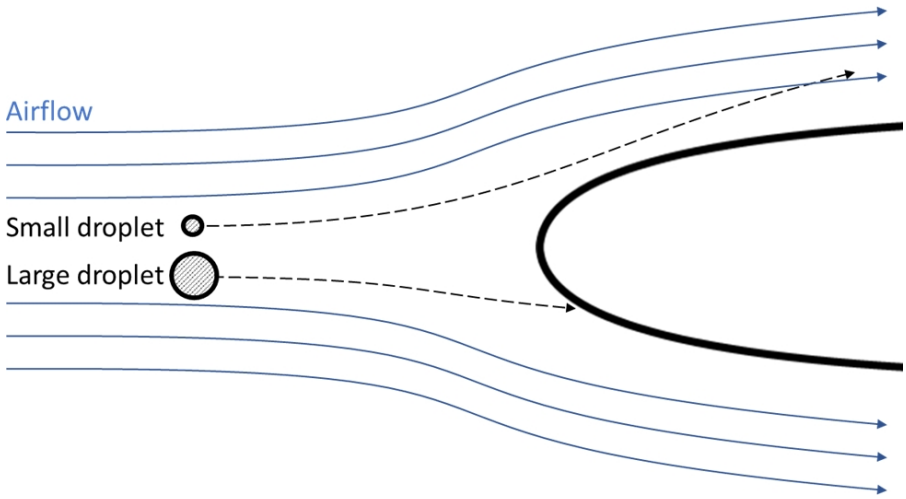

Figure 2.5: Trajectories of small and large droplets. The ratio of droplet size to cross-sectional area is influencing the collision efficiency.

2.2.6 Icing rate

The icing rate $\dot{m}_{\text{icing}}$ can be described with the Makkonen icing model [62]:

$$\dot{m}_{\text{icing}} = \eta_1 \cdot \eta_2 \cdot \eta_3 \cdot v \cdot LWC \cdot A \quad \left[\frac{\text{kg}}{\text{s}}\right]$$

with the collision efficiency η_1, sticking efficiency η_2, accretion efficiency η_3, airspeed v, liquid water content LWC, and cross-sectional area A of the object. The collision efficiency mostly depends on the droplet size, airspeed, and dimension of the object. A droplet is likely to hit the object when its inertia is large compared to the aerodynamic forces that deflect the droplet from the object, see Figure 2.5. Consequently, high collision efficiencies are obtained for when droplets are relatively large compared to airframe size (e.g. SLDs on airliners or cloud droplets on small UAVs). The sticking efficiency describes the ratio of how many of the incoming droplets remain on the surface after impact. This value mainly depends on the droplet size and is typically close to unity, except for SLDs, where splashing and droplet breakup can occur. The ice accretion efficiency describes the ratio of freezing water to incoming water and depends on the ambient temperature and the subsequent icing regime. For rime, the ice accretion efficiency is typically unity, as all incoming droplets freeze. The freezing

fraction can be substantially lower in cases where liquid water layers exist on the surface, e.g. for glaze ice conditions.

2.3 Icing Effects

Ice accumulations on the leading-edge of an airfoil will lead to a degradation of its aerodynamic performance, see example in Figure 2.6. This has been shown in numerous wind-tunnel experiments, in-flight tests, and numerical simulations [63]. The ice shapes change the geometry of the airfoil, which consequently leads to the introduction of flow disturbances and an increase in turbulence. This usually negatively affects the aerodynamic performance in lift, drag, and pitch moments, as well as stall [57, 64]. Moreover, icing deteriorates aircraft stability and control [65]. The degree of performance loss is linked to the form of the ice shapes and the level of aerodynamic disruption. A numerical simulation study on the performance degradation of a UAV airfoil in different meteorological icing conditions estimates lift reduction by 35%, stall angle reduction by 33%, and drag increase by up to 400% for the worst case [46].

Four icing types can be defined [57]: ice roughness, horn ice, streamwise ice, and spanwise-ridge ice, see Figure 2.7. The icing process begins with ice forming a rough surface layer (Figure 2.3). The surface roughness enhances skin friction and can set off early laminar-turbulent transitioning of the boundary layer. This leads to added drag and earlier stall. Horn ice is commonly formed during glaze and mixed ice conditions. Horn ice is a complex ice shape and typically exhibits large horns that induce flow separation at the leading-edge. This recirculation zone at the leading-edge sets off early laminar-turbulent transition and leads to a substantial increase of drag and reduction of lift. Streamwise ice is usually building in connection with rime ice conditions. It results in streamlined ice geometries, which have a much smaller effect on the flow field compared to horn ice, because leading-edge flow separations are small or non-occurring. The fourth type, spanwise-ridge ice, is a special case that occurs only in combination with IPS that cover only a part of the leading-edge. Spanwise ice-ridges can also form in SLD conditions, when droplets hit the airfoil behind the protected area. This may also occur in cases when the IPS is generating substantial amounts of meltwater during operation and the resulting runback liquid water film refreezes downstream on the unprotected surface of the airfoil. This is called runback icing, see Figure 2.4. Runback ice shapes can act as spanwise flow barriers. This is typically associated with very high-

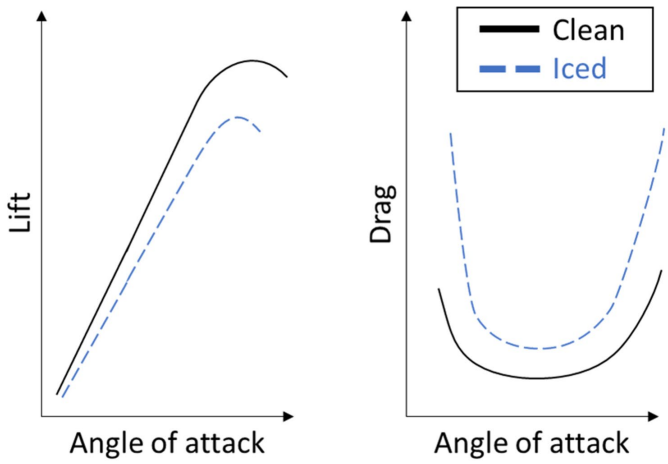

Figure 2.6: Example of the aerodynamic performance degradation due to icing on an airfoil or wing.

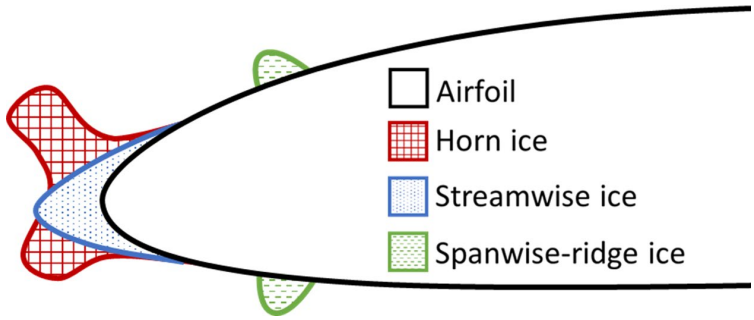

Figure 2.7: Typical ice morphologies on an airfoil.

performance penalties, as laminar-turbulent transition is forced, and separation bubbles can occur behind the ice ridge. SLD and runback icing could also affect control surfaces, degrading their performance or obstructing their movement.

The overall effect of the four different morphologies on the aerodynamic performance can be ranked from highest to lowest impact as: spanwise-ridge ice, horn ice, streamwise ice, and ice roughness [57].

2.4 Icing in Manned Aviation

Icing in manned aviation has been studied since the 1940s and 1950s, when the groundwork for modern icing research was laid [64]. Numerous experiments and flight tests were conducted to understand icing physics and to develop the first IPS [6]. In the 1970s and 1980s, computer technology made it possible to develop advanced numerical icing simulation models. The first generation of icing simulation tools was developed during that timeframe and some of those tools are still in use.

Nowadays, the icing risk on manned aircraft is generally a well-understood topic [66]. A large number of studies on the consequences of icing on aircraft systems exist in the literature, covering topics such as lifting surfaces [57, 64, 65], propellers [67], rotors [68, 69], pitot tubes [70], carburetors [71], engines [61], and inlets [72]. Aircraft certification and pilot education are also covering the risk of in-flight icing [73, 74]. Even though, there are still questions to be addressed within icing research. For example, the aftermath of the crash of American Eagle Flight 4184 in 1994, led to an increased recognition of the hazards of freezing precipitation icing with research starting to focus on SLD icing [75]. Other current topics include the advancement of simulation methods, the improvement of real-time nowcasting and forecasting, the hazard of ice crystal icing to jet engines, and the development of novel concepts for ice detection and IPS.

2.5 Manned vs Unmanned

Icing on UAVs must be addressed with the same vigour as icing on manned aircraft. This is required to achieve the possibility of reliable UAV operations in icing on BVLOS conditions on an everyday basis. There are key distinctions between icing on manned aircraft and UAVs. The comparison is challenging since manned and unmanned aircraft come in a large range of designs and application areas. For example, a significant amount of research has been focused on airliners. While airliners are normally quite similar to each other and vary mostly in size and capacity, UAVs are much more dissimilar to each other. UAVs can range from hand-launched micro UAVs to large high-altitude military aircraft, see Figure 2.8. Table 2.2 displays some key parameters of a selection of UAVs and contrasts them to a small and large airliner.

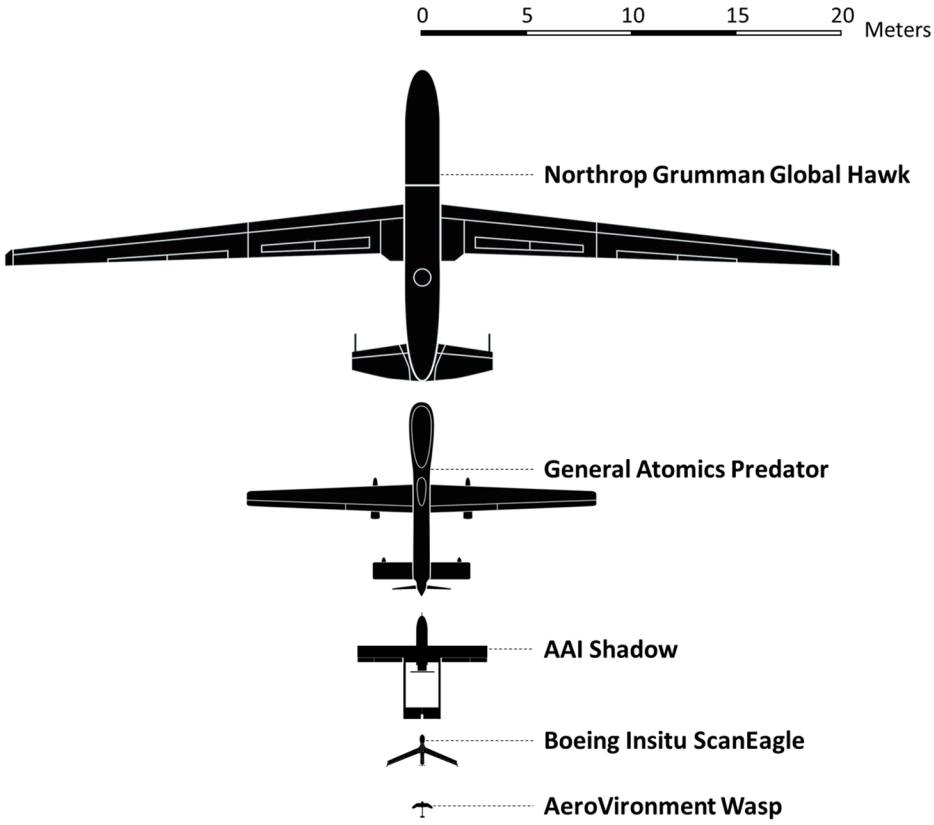

Figure 2.8: Comparison of different military UAV dimensions.

Table 2.2: Comparison of UAV and large transport aircraft characteristics.

	Span	MTOW	Cruise	Ceiling
Northrop Grumman Global Hawk RQ-4B	39.9 m	11,600 kg	160 m/s	60,000 ft
General Atomics Predator MQ-1B	14.8 m	1,000 kg	41 m/s	25,000 ft
AAI Shadow RQ-7B V2	6.2 m	212kg	38 m/s	18,000 ft
Boeing Insitu ScanEagle	3.1 m	22 kg	31 m/s	19,500 ft
AeroVironment Wasp	1.0 m	1.3 kg	10 m/s	500 ft AGL
Boeing 737 MAX 8	35.9 m	82,200 kg	233 m/s	41,000 ft
Airbus A380-800	79.8 m	575,000 kg	250 m/s	43,000 ft

The most obvious difference between UAVs and manned aircraft is that UAVs do not have a pilot on board who can identify icing conditions. Instead, UAVs must rely completely on onboard instruments. Furthermore, UAVs tend to fly at lower airspeed than manned aircraft. The reason for this is that UAVs are often used for endurance-driven missions with the objective to loiter for a long time above a target area. Because of the lower speed requirements, a great number of UAVs rely on propulsion by propellers using electrical, piston, or turbo engines. Only few UAVs use jet engines.

Most UAVs tend to be considerably lighter and have a significantly smaller payload capacity than manned aircraft. The majority of UAVs are smaller than manned aircraft, even though the largest UAVs have wingspans comparable to small manned passenger transport aircraft. There is also a large variation in the altitude that UAVs operate in. There are large UAVs operating at altitudes higher than most manned aircraft, mostly for surveillance (e.g. HALE UAVs). But there are also smaller UAVs that maneuver in localized areas, flying close to the ground.

Last but not least, it should be noted that UAVs share similarities with other aircraft types too. Icing on manned rotorcraft shares many aspects with UAVs. Rotorcrafts are more comparable in size to UAVs and operate at lower altitudes. Also, UAVs have many connections with general aviation, in terms of airframe dimensions and airspeeds. IPS systems developed for general aviation might be particularly interesting for UAVs, since they share comparable requirements (weight, energy-efficiency, etc.).

2.6 Technical Aspects

UAVs face several special technical challenges that are different from manned aircraft. The following is a broad overview of the most relevant topics:

- **Vehicle type:** Icing effects and severity depends very much on the type of UAV. Icing on rotary-wing UAV is dissimilar than icing on fixed-wings. Different types of propulsion system (propeller, rotor, or jet) have their individual vulnerabilities to icing.
- **Size:** Smaller airframes experience higher impingement rates than larger ones. This is because the generate lower aerodynamic deflection forces, while the droplet inertias are unchanged. In practice, this means that smaller airfoils collect more ice relative to their size. Since icing penalties are related to the relative ice size [64], smaller aircrafts experience icing more severe than a larger aircraft in the same conditions [57].

- **Flight velocity:** High airspeeds cause aerodynamic heating of the leading-edges of lifting surfaces (wings or rotors). This heating effect can lead to a decrease of icing at temperatures near the freezing point [76]. At the same time, lower airspeeds also generate reduced surface friction, which can decrease ice shedding efficiency for de-icing [77].
- **Reynolds number**: The Reynolds number is a dimensionless number describing the ratio of viscosity to inertia (momentum) in the fluid:

$$Re = \frac{\rho \cdot L \cdot v}{\mu}$$

with the air density ρ, characteristic length L, airspeed v, and dynamic viscosity μ. The Reynolds number is, therefore, be used to characterize the flow with regards to laminar and turbulent effects. The difference in the Reynolds number regime between manned and unmanned aircraft means that many simulation tools and empirical methods developed for manned aviation may not be applicable for smaller UAVs.

- **Weight:** The additional weight on the airframe due to ice can be an issue since it needs to be compensated with additional lift. Also, the weight can affect the location of the centre of gravity, stability, and manoeuvrability of the aircraft.
- **Materials:** UAVs are often built from composite materials with low heat conductivity. In contrast, manned aircraft wings are mostly built of metal which has substantially higher heat conductivities. This difference can affect the ice accretion process, especially in glaze and mixed ice cases [22].
- **Rotor and propellers:** Most fixed-wing UAVs rely on propellers for propulsion, with a few exceptions of military UAVs that use jet engines. Rotors are used on many smaller UAVs for lift and thrust generation. Icing on rotating surfaces can occur at high ice accretion rates see Figure 2.9. One study showed that a UAV propeller in glaze ice conditions lost 75% of thrust and required 250% more power after only 100s of icing time [24]. Icing on a rotor can also occur very quickly and can cause imbalances and stability issues [26].
- **Sensors:** The most critical sensor with respect to icing is the pitot tube which indicates the airspeed to the aircraft. Erroneous airspeed indications due to iced pitot tubes have led to documented UAV crashes before [12]. Camera lenses, antennas, radomes, and other sensors can also be affected by icing which may limit their functionality and add weight to the aircraft.
- **Autopilot and controls:** The autopilot is a key system in UAVs, responsible for flight controls, navigation, path planning, landing, etc. [78]. In-flight icing is changing aircraft flight behaviour [51]. Autopilots of UAVs need to be able to identify [36] and adapt (e.g. by increasing speed, reducing altitude, changing path) to icing, to ensure safe operation in all-weather conditions [39].

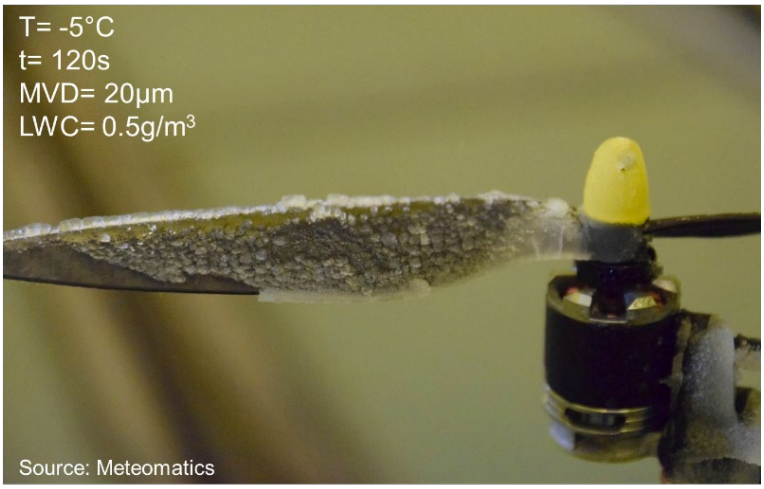

Figure 2.9: Icing on the rotor of a quadcopter.

2.7 Icing Environments

Icing envelopes characterize the meteorological icing conditions (LWC, MVD, temperature, cloud extent) that an aircraft can encounter during flight. Consequently, icing envelopes are a crucial input for the design of aircraft and IPS. For the certification of large passenger transport aircraft in icing conditions, four different icing envelopes are used: continuous maximum, intermittent maximum, take-off, and SLD icing [73].

The icing envelopes most used in manned aviation are found in 14 CFR Part 25 Appendix C, see Figure 2.10. The continuous maximum icing envelope describes icing in stratiform clouds between sea-level and altitudes of up to 22,000ft and a horizontal extent of 17.4nmi. The intermittent maximum icing envelope describes icing in cumuliform clouds at altitudes of 4,000 to 22,000ft with a horizontal extent of 2.6nm. A third envelope, applicable near ground levels up to 1,500ft exhibits lower LWC values and is relevant for take-off scenarios. Recently, a fourth envelope that covers SLD icing in freezing drizzle and freezing rain conditions was added as Appendix O states. Special envelopes exist for helicopters, applicable for operations below 10,000ft. These envelopes contain lower LWC values that were found during two experimental flight campaigns [79, 80].

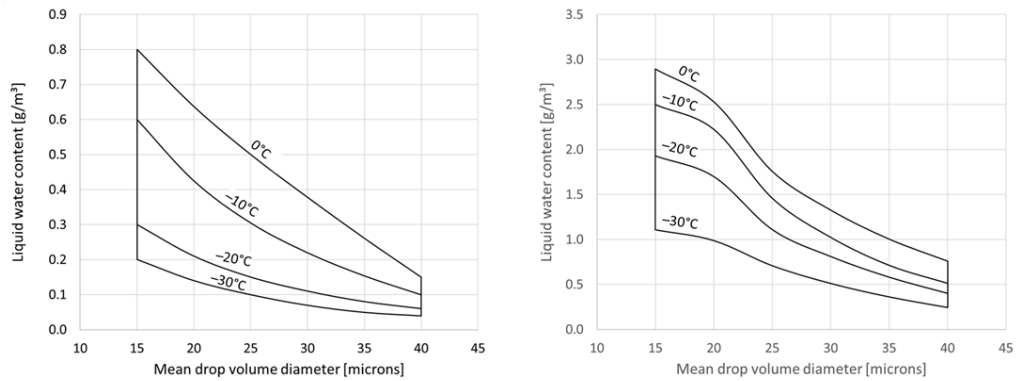

Figure 2.10: Appendix C icing environments: continuous maximum (left) and intermittent maximum (right). Lines indicate a combination of MVD and LWC for a given air temperature. Adapted from [73]**.**

Due to the large variation of UAV designs and applications, the icing environments encountered by UAVs can vary significantly. Large, HALE UAVs can operate at higher altitudes than airliners, whereas small UAVs typically operate close to the ground. UAVs may also be exposed to icing conditions for significantly longer times than manned aircraft (e.g. during surveillance missions). At present, it is still unclear how these special icing environments for UAVs are different from the established icing envelopes in manned aviation. Icing near ground levels is of particular interest, since small UAVs are expected to primarily operate at low altitudes. At low altitudes, the topography can have a substantial influence on icing environments [81]. For example, near mountain slopes or near open bodies of water. This makes the prediction of low-altitude icing risks particularly difficult.

2.8 Icing Nowcasting and Forecasting

Nowcasting is a term for short-term weather predictions based on observations, whereas forecasting refers to long-term weather predictions based on numerical weather models. Knowledge about the weather and icing risks are important for all aircraft operations, to ensure that hazardous weather scenarios are identified and avoided. This information can also be used for path-planning of UAVs [40].

Most of the existing nowcasting and forecasting products have been developed for manned aviation and cover the typical altitudes at which airliners travel. Consequently, the resolution of the models is typically very coarse. For example, the Current Icing Product and Forecast Icing Product provided by the United States National Weather Service predicts icing risk with a horizontal grid point spacing of 13km and a vertical spacing of 500ft/150m [82]. These resolutions would be too coarse for use of small UAVs that operate at low altitudes and in limited areas [9]. Another issue that the icing severity which is predicted by these numeric weather models. The levels of ice severity (trace, light, moderate, severe) are calibrated to large manned aircraft but may be much more severe for smaller UAVs [83]. For example, light icing conditions for a large passenger transport aircraft may be severe for a small UAV.

2.9 Icing Detection

The ability to detect that the aircraft is experiencing icing is essential for all UAVs. Aircraft without IPS need to be warned that they are flying in hazardous conditions to give them sufficient time to exit the icing conditions before significant negative icing effects occur (typically less than a minute). UAVs with IPS need to know when to turn on and when to turn off their system.

When flying VLOS, the pilot can usually make the assessment about the icing risk by observing the local cloud situation. Naturally, this assessment is subjective and depending on the individual experience and knowledge of the pilot. As soon a UAV is flying BVLOS it will require onboard sensors to identify the presence of atmospheric icing conditions.

UAVs have specific requirements for ice sensors. First and foremost, they must be cheap, small-sized, and light. In addition, they must be very reliable and accurate since – due to the lack of a pilot – ice detection is only instrument-based. This also means that ice detection has to be autonomous [32], functioning as a primary automatic ice detection system. Since ice accretion rates and consequent performance degradation can occur in a short timeframe, ice sensors need to have a quick response time, a high sensitivity (also to low LWCs), and high accuracy. Without these attributes, an ice sensor may result in reporting false positives (incorrect icing warning) or false negatives (ice risk ignored). The first case will lead to unnecessary operation of the IPS, while the second can cause significant undetected ice accretions and consequent performance penalties. Another

desirable feature for ice detectors is the ability to give information about the current icing rate. This can be used to assess the icing severity which in turn can be used in risk assessment. Additionally, such information can be useful for choosing the lowest required energy for an IPS in a specific icing scenario.

There are many different physical concepts that can be used for ice detection. In practice, the most common approach is to detect ice accretion on a surface (known icing). Other approaches aim to identify the presence of supercooled droplets in the atmosphere or use performance degradation as an indicator. An overview of different ice detection sensor concepts is given in [84].

2.10 Ice Protection Systems

Ice protection systems are designed to prevent or reduce the negative effects of icing. In general, two types of IPS strategies exist: anti-icing and de-icing. Anti-icing systems provide continuous protection to the aircraft that does not allow any ice to build up on protected surfaces such as wings or rotors. De-icing systems operate cyclically, allowing for uncritical amounts of ice (intercycle ice) to build up on a surface which are subsequently removed. Typically, anti-icing systems require more energy to operate but generate no or less performance penalties. In contrast, de-icing systems usually need less energy to operate but generate performance penalties (added drag, reduced lift, earlier stall) due to the intercycle ice [85]. Three main IPS technologies have evolved in manned aviation: thermal systems, chemical systems, and mechanical systems [86]. Thermal systems supply heat to critical aircraft surfaces that need to be protected from icing. Chemical systems usually distribute a freezing point depressing fluid (FDP) on the protected surface to remove existing ice and prevent further ice formation. These systems are commonly used in general aviation on wings and propellers and disperse the FDP via small holes on the surface (weeping-wings). Mechanical systems break the adhesion between the surface with mechanical energy. One of the most common systems in general aviation are pneumatic (rubber) boots that can be inflated to remove ice from the surface. Newer technologies rely on electro-mechanical concepts to dislodge the ice from aircraft surfaces [31].

In the scope of this thesis, an electrothermal system is considered that generates heat by running an electrical current through carbon fibre material. Such a system can run in both, anti-icing and de-icing mode, see Figure 2.11. There are two different methods of

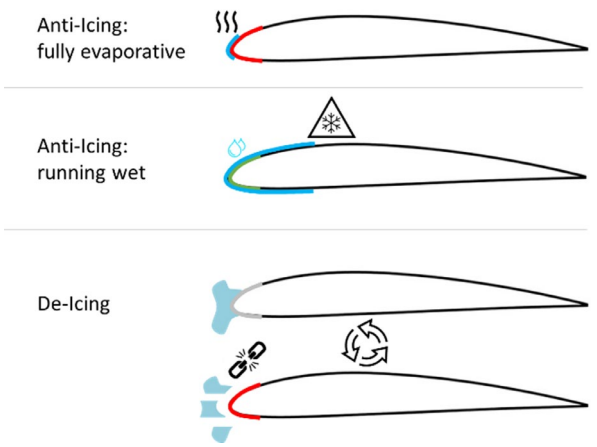

Figure 2.11: Operation modes of thermal ice protection systems. Anti-icing provides continuous heat to the surfaces and prevents any ice formation, whereas de-icing systems run periodically and allow for ice accretions in-between cycles.

anti-icing. Systems that supply enough heat to evaporate all impinging droplets are called fully-evaporative anti-icing systems. The opposite of this are anti-icing systems, which are running-wet, meaning they supply just enough heat to the surface to prevent water from freezing. Instead, the incoming water stays on the surface and forms a liquid water layer. This water layer is flowing downstream of the surface as runback water and may refreeze in unprotected areas of the airframe as runback icing.

Electrothermal de-icing is accomplished by two mechanisms: melting and shedding [86]. First, de-icing systems melt the interface between the aircraft surface and the ice. As a result, a liquid water layer starts to develop at the interface, reducing the adhesion of the ice to the surface.Second, the ice on top of this layer is shed in the presence of sufficient aerodynamic forces. Designing a de-icing system is a complex task since it involves many interlinked parameters (intercycle time, heating period, heat flux). In addition, the effect of the intercycle ice on performance penalty and the risk of ice shedding into downstream aircraft components (e.g. propellers) needs to be taken into account.

2.11 Numerical Icing Simulation

Large parts of this thesis rely on numerical simulation of in-flight icing. Numerical methods are generally an important element in the design of aircraft, since their

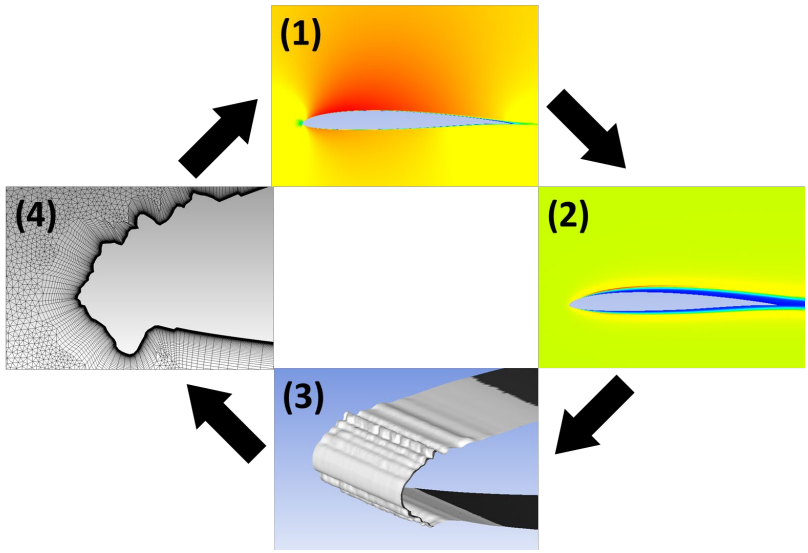

Figure 2.12: Simulation of ice accretion in four steps.

development in the 1970s and 1980 [63]. Simulation tools can help to identify relevant design cases, predict potential icing penalties, and optimize IPS. Also, numerical simulations are typically much faster and cheaper compared to experimental tests. For this reason, a multitude of numerical icing methods have been developed for manned aircraft. Typically, icing simulation is conducted via four iterative steps, see Figure 2.12

1. **Calculation of the flow field**. Most modern codes achieve this by solving the Reynolds-Averaged Navier-Stokes (RANS) equations with computational fluid dynamics (CFD) methods [87]. Older codes use panel-methods for this step, often enhanced with empirical functions [88].
2. **Droplet impingement on surfaces**. The information how much water impinges on a surface can be calculated with either a Lagrangian or a Eulerian method.
3. **Solution of the energy and mass balance**. This step calculates how much of the impinging water turns into ice and is affected by a large number of terms such as aerodynamic heat transfer coefficients, evaporation, latent heat release, aerodynamic heating, IPS loads, etc. [87].
4. **Calculation of the new ice shape**. The new, iced surface is calculated based on the amount of water turning into ice and the ice density at each calculation point. For CFD tools this step includes the re-meshing of the new geometry.

All simulation tools need to be validated with experimental data. In manned aviation, a significant amount of data is available for this task on airfoils (e.g. [89]). Less data is available for rotors on propellers. There is an acute lack of validation data specifically for UAVs with regards to UAV-specific geometries or Reynolds numbers.

2.12 Icing Wind Tunnels

Experimental testing of icing conditions under laboratory conditions is a critical step of the design of any all-weather capable aircraft. Usually, two types of tests are typically conducted in icing wind tunnels (IWTs) [63]. Ice accretion experiments to identify worst-case icing conditions and functionality tests for IPS systems. One experimental process is to generate iced geometries in the IWT and to replicate them (e.g. 3D printing) for testing in conventional wind tunnels or flight tests.

The design of IWTs is very similar to conventional wind tunnels and comes in many different designs (Figure 2.13 & Figure 2.14). Typically, two additional elements have to be added. First, the possibility to control the temperature and to maintain subzero conditions for prolonged periods of time. Second, the possibility to inject water with controlled flowrates and specified droplet distributions. A large variety of IWT facilities exist, most of which have been designed for manned aircraft applications. One challenge when it comes to testing on UAVs is that the minimum airspeed these tunnels can achieve are above the flight speeds to UAVs. Another challenge is related to the typically high costs for renting facilities that are regularly used for the certification of large passenger aircraft. One advantage, however, is related to the fact that UAVs are smaller and testing can be conducted at original scales without the need for scaling – the latter which is a highly complex challenge for icing [90]. Some smaller wind tunnels that have been developed for research or icing on wind turbines fit the low-speed requirement of UAVs well and can be accessed at lower costs. An overview of international IWT facilities, many of which are suited for UAVs, is given in [91].

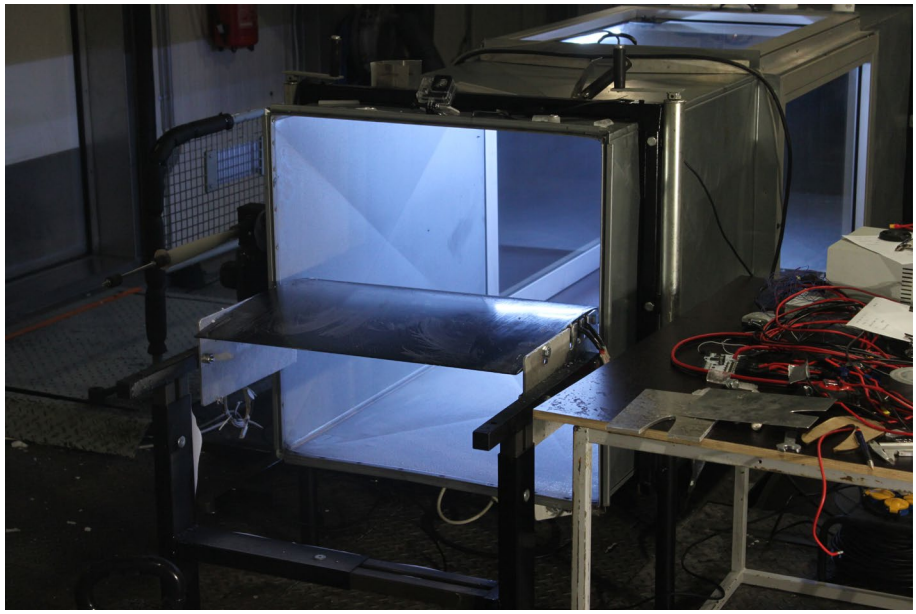

Figure 2.13: Open-loop icing wind tunnel at the Technical Research Centre of Finland (VTT).

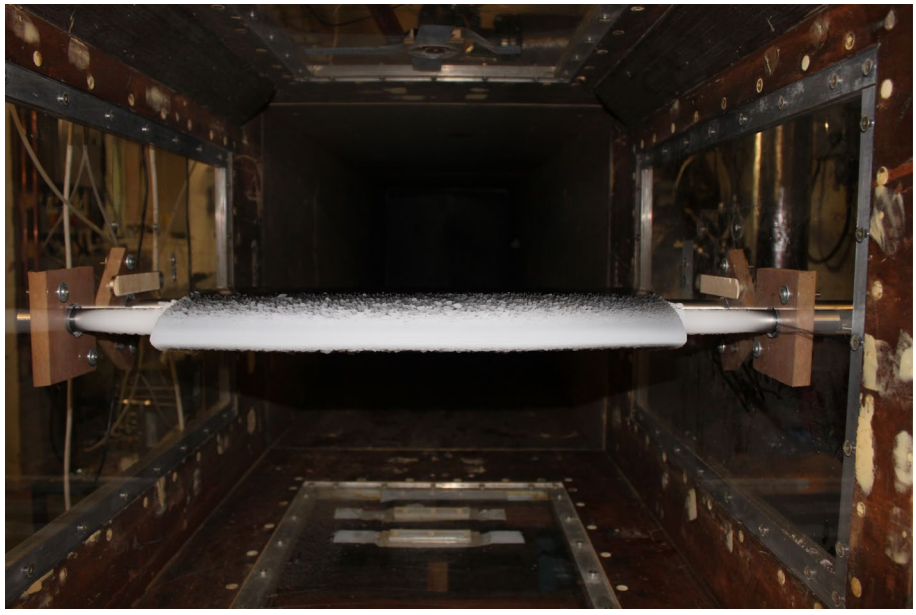

Figure 2.14: Closed-loop icing wind tunnel at Cranfield University.

Figure 2.15: Iced wind turbine.

2.13 Wind Energy

Wind energy is another field that is experiencing in-cloud icing (Figure 2.15). Icing on wind turbines may lead to production losses over days, structural damages to the turbine blades, higher noise generation, and the risk of falling ice fragments from the turbine [81]. Wind turbine icing was in the focus of the industry and research since the 1990s, when wind energy became more prominent in northern countries like Sweden, Finland, or Canada. Today, many technological solutions exist for protection, detection, and forecasting of wind turbine icing [91]. UAVs and wind turbines share several aspects of icing, such as:

- Autonomous ice detection and IPS operation without human intervention.
- Icing occurs at similar airspeeds/Reynolds numbers, especially for small wind turbines.
- Atmospheric icing occurs at low altitudes close to the ground.
- Low barrier to test new technologies due to less certification constraints compared to manned aircraft.

This makes wind turbines an interesting field that offers many potential synergies to icing on UAVs.

Part II

Ice Accretion

3 Ice Accretions from Experiments and Numerical Simulations

3.1 Introduction

Atmospheric in-cloud icing is a severe hazard for all types of aircraft. In particular, medium-sized fixed-wing unmanned aerial vehicles (UAVs) with wings spans of few meters are limited in their operational envelope by icing [9]. These types of UAVs are usually designed for long-range and long-endurance missions that often require all-weather capabilities. Example applications for such UAVs are remote sensing in cold climates, ship-based iceberg detection, oil spill response, or search & rescue [92]. Today, there is no mature IPS available for this category of UAVs. Effectively, UAVs have to stay grounded when icing conditions are expected during a mission, or else they are exposed to severe hazards and the risk of losing the vehicle [10].

Icing in manned aviation is a well-studied process [57], whereas little research has been conducted for UAVs to date. One of the main differences is that most UAVs, except for the largest, operate at significantly lower flight velocities and altitudes compared to the manned aviation, and are smaller in size. The Reynolds numbers occurring during UAV icing are therefore an order of magnitude lower compared to icing on commercial or military aircraft. This difference in flow physics is likely to play an important role in the icing process [19], which justifies the need for dedicated research.

At this point, very limited work has been performed on UAV icing. Most existing studies are using different numerical methods to investigate icing on fixed-wing UAVs, e.g. [13, 18, 21, 53]. Numerical icing simulation tools are a good approach for studying the effects of icing on aerodynamic performance. Numerical models also play an important role in the design of efficient IPSs [47]. Several icing simulation tools have been developed for the use in manned aviation but have so far not been validated for the application on UAVs. This is partly due to the lack of experimental data, as very sparse information on UAV icing exists in the open literature. Up to recently, only a single study

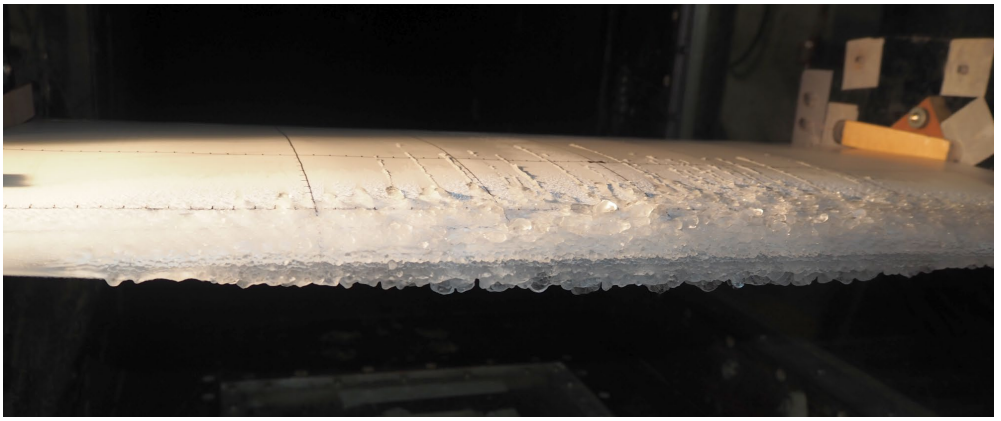

Figure 3.1: RG-15 airfoil test section mounted in the wind tunnel with mixed ice accretions and some runback ice rivulets visible.

on the ice accretion on a UAV airfoil [15] was available, whereas a few more exist for icing on UAV propellers [93].

This paper describes a test campaign that was conducted in the icing wind tunnel at Cranfield University with the aim to generate ice shape validation data for icing on fixed-wing UAV airfoils at low Reynolds numbers (Re=0.8…1.6×10^6). A key characteristic of such data is the requirement of a high level of accuracy and confidence. Since previous work has found that ice shapes may show high degrees of variability [94], another objective was to investigate the consistency of the experimental ice shapes with regards to spanwise distribution and repeatability of tests. In addition, different methods to measure the ice shapes were tested with the aim to obtain higher fidelity ice shapes for the validation process.

It should be noted that icing at low Reynolds numbers is also occurring on small to mid-sized wind turbines [81]. There are several similarities between wind turbine icing and UAV icing, especially the lack of experimental data for validation. For this reason, tests were also conducted on a wind turbine airfoil. This also yields insights into how different airfoil parameters may influence ice accretion.

3.2 Method

Ice accretion tests were performed in the Cranfield icing wind tunnel [95] on rectangular airfoil models, as shown in Figure 3.1. The facilities at Cranfield offer a test section of

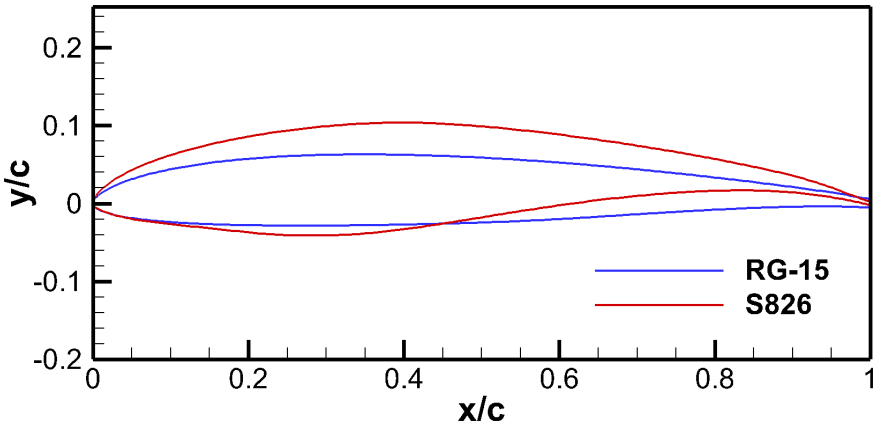

Figure 3.2: Comparison of the RG-15 and S826 airfoil geometries.

0.76×0.76m and the capability to provide total temperatures from T=−30…+30°C, liquid water concentrations from LWC=0.05…3g/m³ and droplet sizes from MVD=15…80µm. The tunnel can generate wind speeds in the Mach number range of Ma=0.1…0.5, enabling the tunnel to be used for aerospace, automotive, and wind energy applications. A particle size distribution record was provided for the nominal droplet diameter setting of 20µm, stating median droplet volume distributions of $DV(10)$=7.93µm, $DV(50)$=19.06µm, $DV(90)$=32.70µm, and a relative span of RS=1.30.

Two airfoil models were investigated, both with a chord length of c=0.45m: an NREL S826 wind turbine airfoil with a span of b=0.50m, and an RG-15 UAV airfoil with a span of b=0.76m. Figure 3.2 shows the two airfoil geometries. A total of 25 ice accretion runs were performed with 9 runs on the S826 and 16 runs on the RG-15. The objective for choosing the icing test conditions was to generate ice shapes representing the three main ice morphologies: rime, glaze, and mixed ice. In order to build confidence in the data, the repeatability of the experiments was tested by running identical conditions multiple times. An overview of the icing conditions that were tested is given in Table 3.1.

For each test, three manual ice shape tracings were taken in order to assess the spanwise variability. One measurement was taken at the centerline of the test section, one at −10cm to the left (looking downstream) of it, and +10cm to its right. In addition, for each tracing, the maximum leading-edge thickness of the ice was measured with a

caliper. Post-processing of the manual tracings included the digitalization of the ice contours with software WebPlotDigitizer [96]. The resulting data were further processed with Matlab to calculate the total ice area, the ice thickness, and the icing limits. The latter two values are given in relation to the distance *s* from the upper trailing-edge.

Supporting numerical icing simulations were conducted with LEWICE (2D, version 3.2.2) and FENSAP-ICE (version 19.2). LEWICE is a 1st generation icing code developed by NASA based on a panel method for manned aviation applications. LEWICE is technically not validated for low Reynolds numbers (Re_{min}=2.26×10^6) but has been applied for UAV applications before [13, 47]. ANSYS FENSAP-ICE is a 2nd generation icing simulation code that is based on modern computational fluid dynamic (CFD) methods [87]. The code is suitable for a wide range of applications, but with limited reported validation data. The FENSAP-ICE simulations were performed with hybrid 2D meshes, consisting of a structured boundary layer and an unstructured far field. The Spalart-Allmaras turbulence model was used for all cases. In the scope of this work, all simulations were conducted with monodisperse droplet distributions and 10 multi-shot icing simulations.

3.3 LWC Calibration

The calibration of the LWC in the tunnel was performed according to the icing blade method described in ARP5905 [97]. With this method, a blade was inserted into the icing tunnel at very low temperatures (T>−18°C) for a short period of time (1–2min). The

Table 3.1: Overview of different icing condition configurations and liquid water contents before and after the correction.

Case	*v* [m/s]	*T* [°C]	*Re* [×10^6]	MVD [µm]	Target LWC [g/m³]	Initial LWC [g/m³]	Corrected LWC [g/m³]	e_{blade} [-]
Glaze 1	25	-2	0.8	30	0.34	0.38	0.46	0.90
Glaze 2	25	-2	0.8	20	0.34	0.38	0.51	0.82
Glaze 3	25	-2	0.8	20	0.59	0.60	0.80	0.82
Rime 1	25	-10	0.9	20	0.43	0.42	0.56	0.82
Rime 2	25	-15	1.0	20	0.32	0.38	0.51	0.82
Mixed 1	25	-5	0.9	20	0.53	0.54	0.72	0.82
Mixed 2	40	-4	1.6	20	0.55	0.58	0.75	0.85
Mixed 3	40	-5	1.6	20	0.2	0.33	0.43	0.85

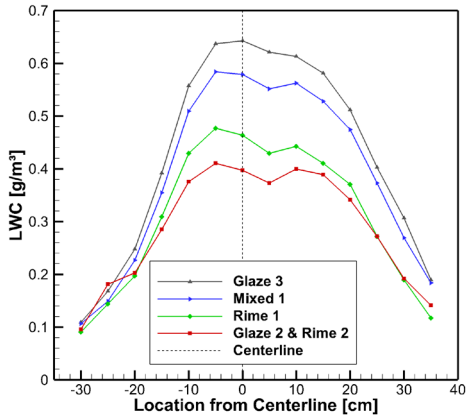

Figure 3.3: Spanwise liquid water content distribution in the wind tunnel test section for the test cases at *v*=25m/s and *MVD*=20µm.

LWC in the airstream can be estimated by measuring the thickness of the accumulated ice along the blade and the following equation:

$$LWC_{\text{blade}} = \frac{\rho_{\text{ice}} \cdot \tau_{\text{ice}}}{e_{\text{blade}} \cdot v \cdot t}$$

with the density of ice ρ_{ice}, the ice thickness accumulated on the blade τ_{ice}, the blade collection coefficient e_{blade}, the test section velocity v, and the blade exposure time t. During the initial calibrations, the collection coefficient was assumed as e_{blade}=1 and ice density as ρ_{ice}=800kg/m³. For flow velocities of *v*=25m/s, the exposure time was selected as *t*=120s. For the higher velocities of *v*=40m/s the time was reduced to *t*=60s. An example of the resulting initial LWC distribution on the blade is shown in Figure 3.3 for the nozzle configuration of *v*=25m/s and *MVD*=20µm. The distribution shows significant variability across the wind tunnel test section. Relatively constant values were reached near the centerline location where the ice shapes were measured.

After the first few icing runs substantially larger ice accretions were observed, compared to what was expected from previous simulation results. The resulting ice thicknesses were more than double as high as anticipated based on prior LEWICE and FENSAP-ICE simulations. While differences between simulation and experiment were expected, the magnitude of these differences exceeded what could be accounted for model errors. This has led to the investigation of the LWC calibration procedure.

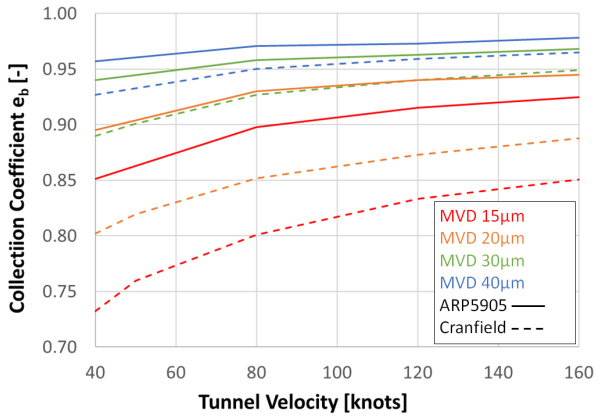

Figure 3.4: Comparison of the collision coefficient of the original ARP5905 blade to the Cranfield blade for different MVDs and flow velocities.

A key discovery was that the cross-section of the blade used for calibration at Cranfield had different dimensions (6.3×15.8mm) compared to the blade specified in ARP5905 (3.2×50.8mm). A different blade geometry, especially the almost doubled thickness, is likely to affect the blade collection coefficient. In order to investigate this effect, we followed the same procedure as in ARP5905 to determine the collection coefficients. LEWICE calculations on the Cranfield and the ARP5905 blade geometry were conducted for different values of MVD and airspeeds. Figure 3.4 compares the results for both blade shapes. The simulations show that the thicker Cranfield blade is leading to a significantly reduced droplet collection efficiency. This effect is largest for small droplets with reduced inertia, that are more easily deflected by the flow field around the airfoil. For the MVD=20µm and v=25m/s case the simulation results yield blade collection coefficients of $e_{\text{blade,Cranfield}}$=0.82 compared to $e_{\text{blade,ARP5905}}$=0.91. This shows that the actual blade collection coefficient of the Cranfield blade can result in a more than 20% LWC increase compared to the initial (e_{blade}=1) calibration. Confidence in the simulation data is added by the good match of the ARP5905 results with the literature values [97]. In addition, FENSAP-ICE simulations were run for selected cases, and fully supported the LEWICE results in Figure 3.4.

Another discussion point in the calibration was the choice of ice density. The recommended value from ARP5905 is ρ_{ice}=880kg/m³ which is 10% higher than the value used in the initial calibration. The literature suggests that ice densities can vary significantly [98, 99], especially for rime ice. A more recent study by Vargas et al. [100]

using an x-ray contact micro-radiography method to determine ice densities of rime, glaze, and mixed suggest that a density of ρ_{ice}=880kg/m³ can be assumed for all ice types. Without explicit data from the Cranfield tunnel on ice densities on the calibration blade, we believe that it is justified to use the higher density for the LWC calibration.

Table 3.1 shows an overview of all the tunnel configurations used in this study. The target LWC is the nominal value that has been specified before the tests, the initial LWC is what was achieved after the initial calibration, and the corrected LWC includes the aforementioned adjustments to the blade collection coefficient and ice density. Depending on airspeed and droplet size, the actually achieved LWC values are between 31–114% higher than the originally targeted LWC.

3.4 Icing Simulation

Numerical icing simulations were conducted and compared to the experimental ice shapes. This preliminary validation was performed on a run with a "Rime 2" and a "Glaze 1" configuration.

The first case (run #11) was chosen because it was conducted at very low temperatures (T=−15°C), which ensures instantaneous freezing of all droplets upon impact on the airfoil surface. This type of icing was shown to be the easiest to simulate numerically due to its simple ice accretion mechanism [101]. Simulations were carried out with LEWICE and FENSAP-ICE for different LWC values: the initial value prior to correction (LWC=0.31g/m³) and the corrected value considering the blade collection coefficient and adjusted ice density (LWC=0.51g/m³). Further, an LWC value was determined based on the simulation results that would match the experimental ice shape thickness best. The outcome for LEWICE is shown in Figure 3.5 and for FENSAP-ICE in Figure 3.6.

The results for run #11 showed clearly how large the difference between the expected ice shapes and the actual ice was. Using the initial LWC, LEWICE predicted a maximum ice thickness of 8.4mm and FENSAP-ICE of 7.6mm, whereas the experimental measurements indicated ice thicknesses between 12–14mm. With the adjusted LWC values, LEWICE predicted a thickness of about 11.1mm whereas FENSAP-ICE matched the experiments well with 13.2mm. To match the experiments with LEWICE, the LWC had to be increased to 0.61g/m³. Both codes are significantly underpreded the total ice

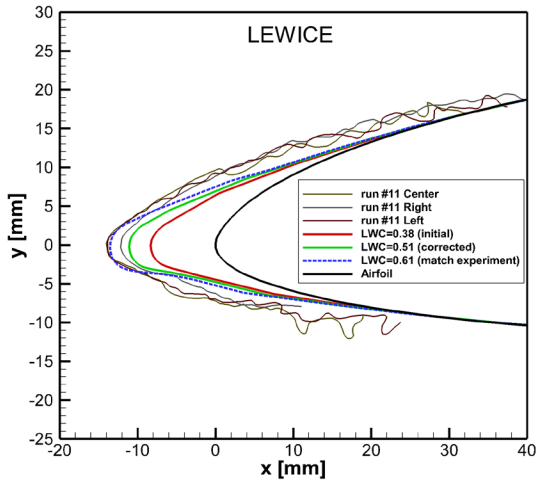

Figure 3.5: Comparison of experimental ice shapes to the numerical simulation results from LEWICE for the rime ice case.

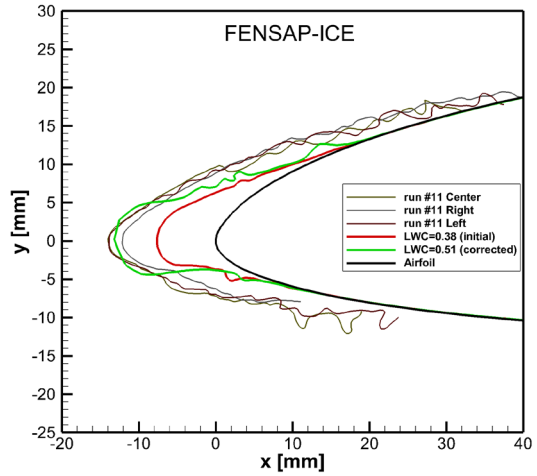

Figure 3.6: Comparison of experimental ice shapes to the numerical simulation results from FENSAP-ICE for the rime ice case.

area and the upper and lower icing limits. The experimental ice shapes also exhibited a more irregular and more rugged surface compared to the relatively smooth FENSAP-ICE and very smooth LEWICE simulation.

A second comparison was conducted for a glaze case (run #14) with the corrected LWC value, see Figure 3.7. The LEWICE result exhibited a significantly smoother surface

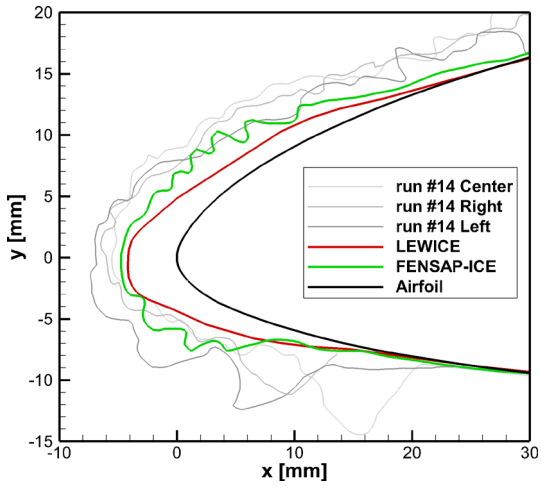

Figure 3.7: Comparison of experimental ice shapes to the numerical simulation results from LEWICE and FENSAP-ICE for the glaze ice case.

with a substantially lower ice area. FENSAP-ICE captured the convoluted surface geometry well but also showed a lower ice area. Both codes were underpredicting the icing limits, although FENSAP-ICE performed betters, especially on the upper surface. Notably, the ice thickness was substantially higher in the experiments compared to the numerical simulations. Neither of the codes showed the large horn/nodule structure on the lower side of the experimental ice shapes between x=4–16mm.

3.5 Ice Shape Variability

Ice accretion on airfoils is an inherently stochastic process. Previous studies indicate that ice shapes in icing wind tunnels can vary significantly between facilities, but also between runs [94]. As such it is of interested to investigate the variability and repeatability of the ice shape tracings. In this study, the temporal variability (between runs) and the spatial variability (along the span of the test section) were investigated.

Table 3.2 shows an overview of all experimental runs that were considered to study the ice shape variability. The table shows the measured ice thicknesses as well as calculated results for thickness, area, and icing limits. For each set of identical runs, the mean $\bar{x}$ is given along with the standard deviation σ.

Table 3.2: Overview of ice accretion runs with measured ice thicknesses, as well as calculated ice thickness, area, and limits.

Run ID	Airfoil	Config	Time [min]	Max. thick. measured [mm]			Max. thick. calculated [mm]			Ice area [mm²]			Lower ice limit [s/c]			Upper ice limit [s/c]		
				Center	Right	Left	Center	Right	Left	Center	Right	Left	Center	Right	Left	Center	Right	Left
run #1	S826	Rime 1	40	23.5	17.6	28.3	25.0	18.4	26.8	450	515	599	-0.11	-0.12	-0.08	0.13	0.11	0.17
run #2	S826	Rime 1	40	25.7	27.0	23.5	24.1	27.1	22.8	451	543	458	-0.10	-0.11	-0.10	0.17	0.18	0.19
					$\bar{x}$= 24.3	σ= ±3.8		$\bar{x}$= 24.1	σ= ±3.2		$\bar{x}$= 503	σ= ±61		$\bar{x}$= -0.10	σ= ±0.01		$\bar{x}$= 0.16	σ= ±0.03
run #4	S826	Glaze 1	40	12.6	11.7	13.5	11.8	12.8	12.5	699	740	879	-0.11	-0.13	-0.14	0.05	0.17	0.18
run #5	S826	Glaze 1	40	12.8	10.3	13.0	11.8	11.7	13.1	853	543	718	-0.20	-0.20	-0.10	0.05	0.19	0.05
					$\bar{x}$= 12.3	σ= ±1.2		$\bar{x}$= 12.3	σ= ±0.6		$\bar{x}$= 739	σ= ±121		$\bar{x}$= -0.15	σ= ±0.04		$\bar{x}$= 0.12	σ= ±0.07
run #10	RG-15	Rime 1	20	15.1	14.4	14.4	13.9	12.8	13.3	230	246	255	-0.10	-0.13	-0.13	0.03	0.05	0.06
run #16	RG-15	Rime 1	20	14.5	13.1	13.8	12.5	12.0	13.3	238	226	235	-0.13	-0.12	-0.11	0.03	0.05	0.04
run #20	RG-15	Rime 1	20	16.2	14.5	15.0	14.4	12.7	13.3	278	260	249	-0.14	-0.14	-0.12	0.05	0.04	0.04
					$\bar{x}$= 14.6	σ= ±0.9		$\bar{x}$= 13.1	σ= ±0.7		$\bar{x}$= 246	σ= ±16		$\bar{x}$= -0.12	σ= ±0.01		$\bar{x}$= 0.04	σ= ±0.01
run #12	RG-15	Mixed 1	20	14.7	13.1	14.0	13.2	11.7	13.2	321	279	332	-0.12	-0.14	-0.11	0.04	0.06	0.07
run #17	RG-15	Mixed 1	20	13.5	13.5	14.4	11.1	11.2	12.8	257	287	242	-0.11	-0.15	-0.11	0.05	0.05	0.03
run #21	RG-15	Mixed 1	20	14.4	12.8	13.4	13.7	13.5	13.7	268	309	264	-0.12	-0.15	-0.11	0.05	0.04	0.05
					$\bar{x}$= 13.8	σ= ±0.7		$\bar{x}$= 12.7	σ= ±1		$\bar{x}$= 284	σ= ±30		$\bar{x}$= -0.12	σ= ±0.02		$\bar{x}$= 0.05	σ= ±0.01
run #14	RG-15	Glaze 1	20	6.5	6.0	6.2	5.8	6.5	7.8	379	307	309	-0.16	-0.18	-0.17	0.09	0.04	0.06
run #18	RG-15	Glaze 1	20	7.1	6.3	6.9	7.0	7.5	7.8	338	287	413	-0.16	-0.19	-0.16	0.06	0.06	0.09
run #22	RG-15	Glaze 1	20	7.0	6.2	6.8	7.3	6.2	5.3	476	427	362	-0.18	-0.19	-0.16	0.08	0.05	0.06
					$\bar{x}$= 6.6	σ= ±0.4		$\bar{x}$= 6.8	σ= ±0.9		$\bar{x}$= 366	σ= ±63		$\bar{x}$= -0.17	σ= ±0.01		$\bar{x}$= 0.07	σ= ±0.02

The comparison between the measured and calculated maximum thickness reveals that the post-processing of the ice tracings was not without fault. Differences ranging from −1.6…+2.5mm occurred between the two methods. The reason why the calculated values diverged from the caliper measurements can be attributed to the manual tracing errors and the digitalization process. One challenge we found was to correctly capture the exact location of the airfoil in relation to the ice shape on the tracing papers.

Generally, the data showed the largest variations for the S826 airfoil, for the cases with an icing duration of 40min. The resulting ice shapes were very large and exhibited significantly higher variability in all characteristic parameters. The choice for the initial icing times of 40min was based on numeric simulations that were carried out before the experiments. When the large deviations between simulation and experiment – related to the LWC calibration issue – were detected, the icing times were consequently reduced to 20min for all tests on the RG-15 airfoil.

Figure 3.8 to Figure 3.10 show the spanwise distribution of the ice area on the RG-15 airfoil for a rime, mixed, and glaze case with three identical runs each. The ice area is a good overall indicator of the accretion process. The results display that there was a considerable degree of temporal and spatial variability for all three cases. No consistent trends of more/less ice accretion on any side of the test section could be observed. However, it seemed that the icing conditions had an impact on the degree of variability. The rime case exhibited a significantly lower amount of variation, compared to mixed and glaze, the latter showing the largest spread.

Icing limits were identified on the upper and lower side of the airfoil. The variation of the limits appeared to be consistent, with values varying within the range of 1–2cm. The only exception was the glaze case for the 40min test run, where the variation of the upper and the lower limit were significantly elevated. The RG-15 airfoil showed a clear trend for more ice accretion on the lower side, whereas the S826 exhibited a more symmetric ice distribution between the lower and upper sides.

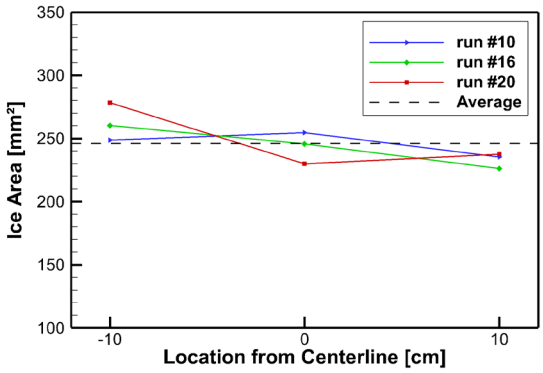

Figure 3.8: Calculated ice area for three identical rime ice runs.

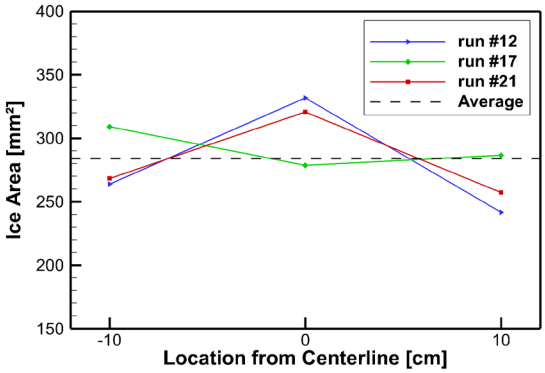

Figure 3.9: Calculated ice area for three identical mixed ice runs.

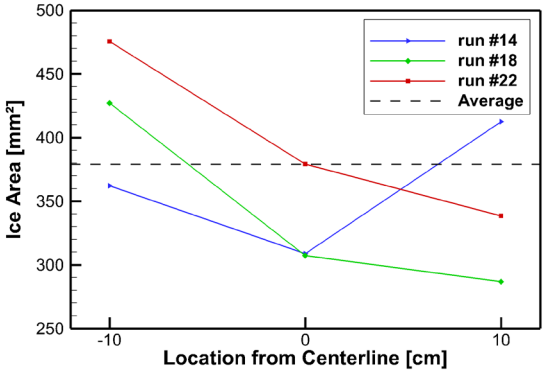

Figure 3.10: Calculated ice area for three identical glaze ice runs.

3.6 Ice Shape Acquisition

The main results in this study were based on manual tracings of ice shapes. The data suggests that there was a considerable amount of variation of the ice shapes in the spanwise direction. This information was only partially captured, as only three locations were used for ice tracings. Furthermore, the manual tracing method was subjective and susceptible to variations, depending on the skill and experience of the person taking the measurements. This was the motivation to investigate other – more objective – methods to obtain ice shapes. Two methods were tested. First, we used the Structure Sensor [102], which is a handheld 3D scanning device. The sensor was an accessory for iPads and captured its surroundings by infrared structured light technology. The scanner was used on the iced airfoil inside the wind tunnel. Figure 3.11 to Figure 3.13 show different examples of the resulting ice geometries. In general, the ice shapes were captured better than expected. It was anticipated that the ice shapes would be problematic to scan due to their optical properties (translucency and reflectivity). This, however, turned out not to be a major issue, which was likely related to the infrared technology of the scanner. However, we found that the resolution of the ice shapes was inconsistent. The scanned mesh consisted of cells with lengths between 3–9mm length, which was widespread and relatively coarse. The resulting ice shapes were missing key features, such as feathers, clear icing limits, and surface roughness. However, the 3D scans allowed for a good assessment of the spanwise distribution of ice, as best seen in Figure 3.11. This example was a scan from a rime ice run (run #2) on the S826 airfoil. The scan was performed after the manual tracings were taken, which can be seen from the three cuts in the ice. From the scan, it is obvious that less ice had accumulated on the left side – which was also confirmed by the measurements in Table 3.2. Generally, the ice thickness measurements from the scanned data were matching well with the caliper measurements.

Figure 3.12 shows a mixed ice case (run #8). The results clearly showed the horn formation and how the horn occurred only in the middle and right sections of the model. A feature that was consistent with all scanned results was that the upper surface was much better resolved than the lower. This may be related to the handling of the device because it was easier for the person sitting inside the tunnel to scan the upper surface. For runs with less ice accretion, for example on the RG-15 airfoil in Figure 3.13 (run #16), the ice shapes became less clear and less distinct.

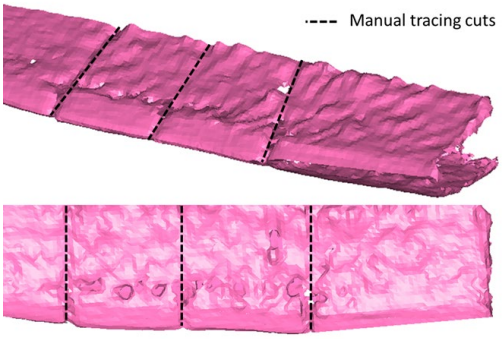

Figure 3.11: 3D scan result of a rime ice case with 40min duration.

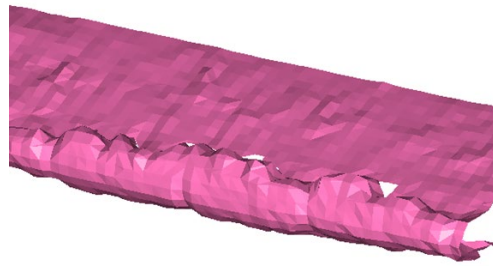

Figure 3.12: 3D scan result of a mixed ice case with 20min duration.

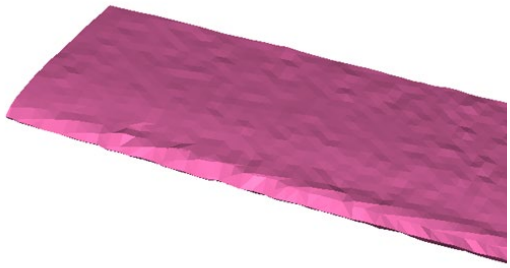

Figure 3.13: 3D scan result of a rime ice case with 20min duration.

Figure 3.14: Photogrammetry result of a painted (dry) mixed ice segment that was carefully removed from the airfoil.

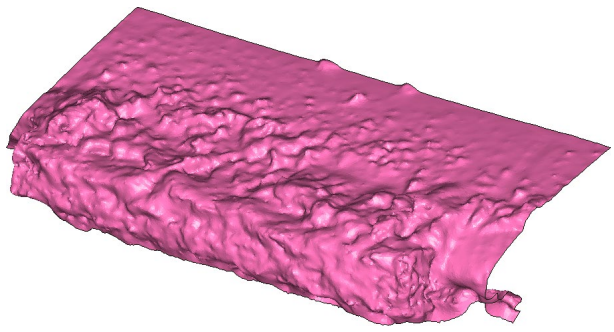

Figure 3.15: Photogrammetry result of an unpainted rime ice segment still attached to the airfoil.

The second method to acquire ice shapes was to use photogrammetry. The structure-from-motion method allowed creating 3D models based on multiple images of an object, taken from various locations and angles [103]. For the model generation, the software Agisoft Photoscan [104] was used. The first tests revealed that the optical properties of ice made it difficult to generate an accurate model. For this reason, the ice was painted black with a fine brush, which significantly improved the results. Two approaches were selected. First, ice segments were carefully removed from the airfoil and placed in a freezer until further processing. The segments were then painted and returned to the freezer until the paint was dried. Then, the ice segments were placed in front of a white background and a series of pictures were taken in all directions. An example of the results is shown in Figure 3.14 for a mixed ice shape. The resulting 3D model showed a good resolution of the ice geometry and were able to capture details well. Removal of intact ice shapes was successful for most glaze and mixed cases, whereas the adhesion forces for rime ice were too high so that it was often not possible to remove a segment without damaging it. For this reason, the second approach was to take images of the ice while still attached to the airfoil, inside the wind tunnel. Figure 3.15 shows an unpainted rime ice shape that was captured with this method. It was found that the method works reasonably well, although the surface features are less detailed compared to the previous photogrammetry result. The reason for this was the optical properties of ice. Painting the ice segment inside the tunnel proved to be difficult and time-consuming. Especially the drying process took very long, and the test was aborted. Pictures taken of a painted wet ice shape were not processable with the photogrammetry software due to excessive reflections of the surface.

3.7 Discussion

Obtaining high-fidelity ice shapes, that are representable for certain icing conditions and are suitable for the validation of numerical icing models, comes with many intricate challenges. On the experimental side, there are several factors that can have a large impact on the resulting ice geometries. As shown in this study, the calibration of the LWC is a key issue, that may introduce a significant (systematic) error. The LWC problem in this campaign arose partly because of the lack of experience of testing at low Reynolds numbers and because testing was conducted at the lower limits of the wind tunnel capabilities. The effect of the blade collection coefficient and the off-specification icing blade were magnified by low tunnel speeds. The effects would have had

significantly smaller at wind speeds which are typical for aviation, due to higher droplet inertia. It is important to highlight, that the LWC calibration problem was detected early in the testing phase due to the availability of simulation data. This underlines the benefits of conducting experimental work in close collaboration with numerical methods.

There were several other parameters that add to the uncertainty of the ice shape data. The droplet size distribution had not been verified in the scope of this work and remained a significant unknown. The droplet sizes play an important role for the droplet impingement limits on the airfoil and may be responsible for the large observed deviations between the numerical and experimental data. This was an issue that should be investigated in further detail in the future. Furthermore, the density of the ice was a variable that had not been investigated and may affect ice shapes (and LWC calibration) to a large degree. It is highly recommended that future experiments focus on these uncertainties in order to build more confidence in the experimental data.

Investigations of the repeatability of the tests showed a dependency on the icing type. For rime and mixed ice, the results exhibited a significantly lower variability compared to glaze. Since the numerical simulation of glaze ice was more challenging than for rime (due to the complex icing processes on the surface), the validation data for these cases were particularly interesting and require good confidence. The preliminary numerical results showed large deviations compared to the experimental glaze geometries, which indicated that special attention must be given to the accuracy of the experimental glaze data. One aspect was that the spanwise distribution of ice was showing the largest variability for glaze. Therefore, it seemed a good practice to take several spanwise ice tracings, which should not take too much additional time.

Last but not least, manual tracing of the ice comes with an inherent stochastic error that was related to the skill and experience of the experimenter. The post-processing of the tracings, especially the digitalization, also introduces errors. Using caliper measurements and comparing them to the calculated thicknesses prived as a good method to identify large deviations and flag cases for re-processing to increase accuracy. In general, the manual process was very time-consuming and requires special attention to detail. For this reason, the exploration of alternative methods of ice shape capturing seemed highly beneficial.

The 3D handheld scanner was able to capture the ice shapes well, however with a very low degree of detail. Further investigations are required on how to improve accuracy and

how to reduce the large spread in the resolution. Otherwise, the method was very fast and may be very well suited for measuring the spanwise distribution of ice, ice area, and icing limits. The second approach was to use photogrammetry on the ice shapes. This approach has shown to be very sensitive to the optical properties of ice. Clean ice, as well as painted ice that was still wet, was very difficult to process and yielded low-quality results. However, the specimens that were painted and dried, have shown a very high level of detail and are well suited for further investigations. Such high-fidelity ice shapes are required for aerodynamic performance degradation studies, e.g. with CFD or experimental methods with 3D printed artificial ice shapes. One problem that was related to painting the ice was that the painting procedure might alter the ice shape. Powders might therefore be better suited for this purpose. An improvement that should be considered for both approaches is to add optical markers with known distances between each other. This information will help to set the correct scaling and to get the overall dimensions in the correct magnitude.

The icing simulation results can be considered as preliminary results for the validation of LEWICE and FENSAP-ICE for UAV applications. The rime case showed a good match with the experimental data in terms of general thickness and shape. However, icing limits and the ruggedness of the surface were not well represented. For glaze, the consistency with the experimental data was less, especially for LEWICE. This may be related to the more complex icing processes inherent to the glaze ice formation, due to the presence of a freezing water film on the surface. At this stage, more detailed investigations are required to improve the predictive qualities of the numerical codes. There are a multitude of parameters that can be adjusted in order to obtain better predictions, in particular within FENSAP-ICE. Future work will focus on a more in-depth comparison of FENSAP-ICE and LEWICE to these experimental data.

3.8 Conclusion

The main goal of this study was to generate reliable experimental ice shape data for UAV icing applications at low Reynold numbers. Such data is required for the validation of numerical icing methods, which have typically been developed and verified for manned aviation purposes. This study generated a large dataset containing the three main characteristic icing types: rime, mixed, and glaze. Special focus was paid to investigate the variability of ice shapes. Cases were repeated at identical icing conditions and

manual ice tracings were taken at three spanwise locations. The results showed that the degree of variability is depending on the ice type and is highest for glaze and lowest for rime. However, even for the glaze case, the variability was within moderate limits, and may therefore still be used for validation purposes.

Several sources of errors were identified and addressed. A significant systematic error was discovered, that was related to the calibration of the LWC. The icing wind tunnel facility is following the ARP5905 icing blade method, however with a blade that had different dimensions than required by the document. It was shown that the thicker blade has a detrimental effect on the droplet collection coefficient at low flow velocities. Furthermore, the icing density used for the calibration was not verified for these tests and was assumed with a potentially low value. These systematic errors were accounted for and indicate that the actual LWC during the tests was much higher than initially planned.

A secondary goal of this study was to investigate novel methods to capture ice shapes. Two methods were tested. A low-cost 3D scanner was able to capture the overall ice shape on the airfoils using infrared technology. The resolutions of the resulting meshes were varying and generally found to be too coarse to capture fine details. However, bulk measurements such as spanwise distribution, ice area, and icing limits could potentially be performed with the device if the resolution was more consistent. The second approach was performed with structure-from-motion photogrammetry on ice segments. The optical properties of ice made it difficult to generate 3D point clouds. By painting the ice shapes, the outcome could be significantly improved, and very detailed ice shapes were generated. This required the paint to dry first. In the future, powders may be instead of paints.

Icing simulations with FENSAP-ICE and LEWICE were performed and compared to experimental rime and glaze shapes. These preliminary validation results showed that LEWICE predicted in both cases lower ice thicknesses, smaller ice areas, lower icing limits, and generally lacked to capture the uneven, rugged surface of the ice. FENSAP-ICE generally was able to capture the ice thicknesses and surface ruggedness better. However, FENSAP-ICE also showed limited fidelity when it came to ice area and icing limits. More work is planned to investigate the best parameter setting within the icing codes that will give the best predictions for UAV icing conditions. Further research

questions are also related to the aerodynamic performance effects (lift, drag, stall) that are induced by these ice geometries.

3.9 Addendum

This paper was based on experimental tests in the icing wind tunnel facilities of Cranfield University, conducted in fall 2018. Since then, two more test campaigns were performed at the icing facilities of the VTT Technical Research Centre of Finland in spring 2019 and fall 2019. In the scope of these tests, a large database with ice shapes on the RG-15 and S826 airfoil was generated and is aimed to be published in the future. Two selected cases from this database were used in other publications for validation of FENSAP-ICE and are included in this thesis in section 5.4.2 and section 6.3.

Part III

Icing Performance Penalties

4 Experimental and Numerical Icing Penalties of a S826 Airfoil at Low Reynolds Numbers

4.1 Introduction

Atmospheric icing occurs when supercooled liquid droplets collide with a structure – for example, an aircraft or a wind turbine – and freeze. Such meteorological conditions can be found in icing clouds or during freezing precipitation events. The resulting ice accretions are responsible for significant aerodynamic performance penalties and added weight [57].

The topic of atmospheric in-flight icing has been primarily studied on manned aircraft since the 1940s and 1950s [64]. Since then, large efforts have been conducted to understand the physics of icing, to develop computational tools to simulate icing, and to generate experimental datasets for validation (e.g. [57, 89, 105]). Most of this research has been performed at high Reynolds numbers which in aviation are typically the order of Re=10^7–10^8.

More recently, applications have emerged where in-flight icing occurs at significantly lower Reynolds numbers compared to manned aircraft, for example in wind energy and unmanned aerial vehicles (UAVs). This creates a need for more detailed information on low Reynolds icing flows, or at a minimum, a demonstration that the tools used for high Reynolds number flows are adequate.

Icing became an issue for wind turbines around the 1990s, driven by increased demand for renewable energy especially in cold climate areas of Northern America and Northern Europe [81]. Icing on wind turbines is a source for many problems such as reduced power generation, risk of ice throw, increased fatigue, and increased noise [106]. Wind turbine blades experience a wide range of Reynolds numbers, with low values near the hub, that increase towards the tip. Commercial large wind turbines typically operate in the Reynolds number regime of Re=10^6–10^7 [107].

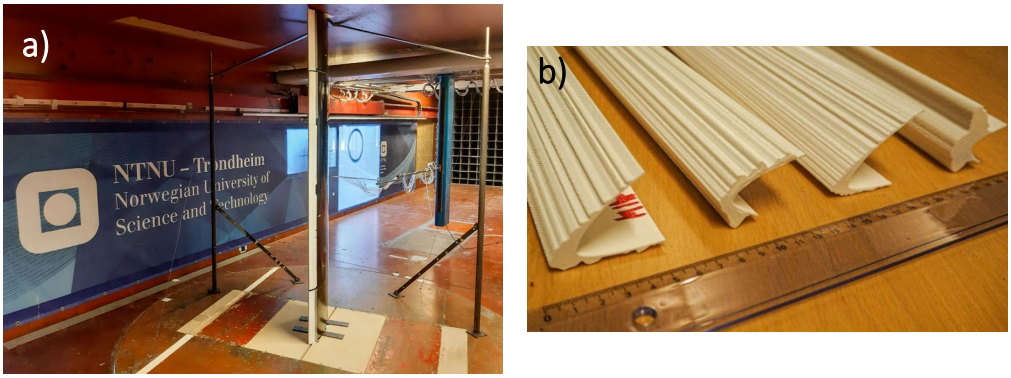

Figure 4.1: The wind tunnel set-up of the S826 consisting of dummy sections and the main part mounted vertically, with attached artificial ice shapes (a). The 3D printed ice shapes, from left to right: mixed, glaze, rime, and horn* (b).

Small wind turbines (SWTs) with power ratings typically below 50kW are a renewable energy source that can be used in locations where conventional large wind turbines are not feasible [108]. Typical applications of SWTs are in the electrification of rural or remote areas [109], as hybrid systems in combination with other energy sources like photovoltaic or hydrogen [110], or in microgeneration to reduce carbon emissions [111]. Icing on SWTs has similar effects as icing on larger wind turbines, although due to their smaller size and different designs the sensitivity to icing can be increased [112, 113]. Typically, SWTs operate at comparatively low Reynolds numbers in the order of Re=10^4–10^5 [108].

UAVs are an emerging technology that are also affected by icing. Icing was identified in the 1990s as a major hazard to UAVs and as a severe limitation to their operational envelope [9]. Since then, icing has shifted into the focus of research. This development is related to the increasing availability of the technology and proposals for wide-spread use of UAVs (e.g. for package deliveries, urban air mobility).

Studies on UAVs have shown that the Reynolds number has a significant influence on the physics of ice accretion and also on the subsequent aerodynamic performance penalties [15, 18, 46]. Icing on UAVs is similar to icing on manned aircraft with some key differences related to airframe size, mission profiles, and icing sensitivity [42]. Most UAVs (except for the largest) operate at Reynolds numbers in between large and small wind turbines, typically in the order of Re=10^5–10^6.

The difference in the Reynolds number regime between the majority of the existing research data and the low-Reynolds applications of wind turbines, SWT, and UAVs is important because the flow physics are closely linked to the Reynolds number. At low Reynolds numbers (here defined as $Re<10^6$), laminar flow characteristics and laminar separation bubbles become more dominant [114]. The boundary layer thickness is also larger. This may have an effect on both the ice accretion and the consequent aerodynamic performance degradation. A numerical study by Szilder and McIlwan [19] on the influence of the Reynolds number on UAV ice accretion suggests that there are significant Reynolds number influences on ice mass, area, and location between $Re=5\times10^4$–5×10^6. These parameters govern the geometry of the ice accretions which in turn are strongly linked to performance penalties [57].

One aspect of this question is that there is a lack of data that can be used to validate numerical simulation tools for icing at low Reynolds numbers. This includes typical validation data such as ice shapes from experimental icing wind tunnel (IWT) tests as well as aerodynamic performance experiments of iced airfoils. In the open literature, few experimental studies exist that are suitable for the validation of numerical tools. Table 4.1 gives an overview of available data in the fields of wind energy and UAVs. The table reveals that there is a gap when it comes to datasets that can be used for the validation of predicting aerodynamic icing penalties at low Reynolds numbers. The existing data in the literature either lacks well-defined experimental ice geometries [115–117], has no or limited performance data [118, 119], offers only one data point for lift and drag for each icing case [120, 121], or is performed at low or high Reynolds numbers [15, 122–124]. Also, none of these datasets share the coordinates of the ice geometries or the tabularized data of lift and drag.

This study serves three objectives. The first objective is to investigate the aerodynamic performance of an iced airfoil at low Reynolds numbers. The second objective is to make the experimental data available to be used for validation of other numerical methods in the future. The last objective is to exemplify the use of the validation dataset by comparing it to FENSAP, a computational fluid dynamics (CFD) tool commonly used for icing.

Table 4.1: Overview of existing data in the literature on airfoil performance degradation on iced airfoils at low Reynolds numbers.

Source		$Re \times 10^6$	Airfoil	Chord	Icing Cases	Comments
Seifert & Richert, 1997	[111]	0.6	NACA4415	0.225 m	4	Unknown icing conditions. Ice shapes from fragments found near wind turbine.
Jasinski et al., 1998	[112]	1.0–2.0	S809	0.457 m	4	Ice accretion from LEWICE.
Hochart et al., 2008	[116]	0.3–0.7	NACA63-415	0.200 m	6	Performance data only at a single AOA.
Han et al., 2012	[114]	1.0–1.4	S809	0.267 m	17	No performance data included in the study.
Etemaddar et al., 2012	[113]	2.0	NACA64-618	1.000 m	2	Ice accretion from LEWICE.
Hudecz et al., 2013	[117]	1.0	NACA64-618	0.900 m	3	Performance data only at a single AOA.
Gao et al., 2017	[115]	0.5	DU96-W-180	0.152 m	6	No performance data included in study.
Williams et al., 2017	[14]	0.2	RG-15	0.210 m	4	Low Reynolds number. Performance data from water and wind tunnel experiments.
Knobbe-Eschen et al., 2019	[118]	2.3	AH94W-145	0.750 m	2	High Reynolds number.
Jin & Virk, 2019	[119]	3.0	DU96	0.500 m	2	High Reynolds number.
Jin & Virk, 2020	[120]	3.0	S826, S832	0.500 m	4	High Reynolds number.
This study		0.2–0.6	S826	0.450 m	6	Ice shapes from IWT and LEWICE. Geometries and performance data shared.

4.2 Experimental Setup

The experimental part of this work was performed in the closed-loop low-speed wind tunnel at the Norwegian University of Science and Technology (NTNU). An NREL S826 airfoil with a chord of c=0.45m was used in this study. This work follows the experimental methods described by Bartl et al. and their extensive study on the clean S826 airfoil, previously conducted at NTNU [125]. The dimensions of the wind tunnel test section are 1.8×2.7×12m (height×width×length), with the height increasing to 1.85m at the end of the test section to compensate for the boundary-layer growth of the wind tunnel walls. Measurements were conducted for angle of attacks (AOAs) ranging from α=−7.5…17.5 at three Reynolds numbers: Re=2×10^5, 4×10^5, and 6×10^5. The corresponding inflow turbulence intensities for each Reynolds number are I=0.44%, 0.30%, and 0.26% [125].

Figure 4.1a shows the experimental setup, watching at the leading edge of the wing, which spans the whole wind tunnel height. The wing consists of two "dummy" parts near the tunnel walls and the main section. The total height is h=1.78m. Only the middle section was connected to a force balance. All wing elements were CNC-milled from Ebazell foam and coated with black paint. Surface roughness measurements confirmed that the surface was hydraulically smooth. The trailing edge thickness was 2mm.

A six-axis force balances recorded the aerodynamic forces acting on the main wing section during a period of 30s with a sampling rate of 2000Hz. Two load cells were aligned with the flow direction of the wind tunnel and one was perpendicular to it. The results from Bartl et al. [125] showed that lift measurements could be accurately obtained with the force balance, but the accuracy was insufficient for drag estimations due to excessive signal-to-noise ratios. Instead, drag was measured with a wake rake using an integrated momentum deficit method. The rake was constructed with 21 uniformly distributed tubes of 1mm diameter, with 10mm spacing between the centerline of each tube. It was located in a distance of 0.7c downstream of the trailing edge, mounted on a traverse. All pressure ports were connected to a pressure scanner and were sampled for a duration of 20s with a sampling rate of 200Hz.

In addition, 32 pressure taps were located in the middle of the main section and connected to a piezoresistive pressure scanner inside the wing. The reference pressure was taken from the static pitot tube upstream of the wing. Surface pressure data were collected at a sampling rate of 800Hz for 30s. The artificial ice shapes covered the

pressure taps near the leading edge up to x/c=0.09–0.15 (depending on the size of the ice shapes), Therefore, the pressure readings were not used for any force calculation, but only to calculate the local pressure coefficients. The flow velocity and the reference pressures for the wake rake and surface pressures were measured with a pitot-static tube at a distance of 5c upstream of the wing.

In order to change the angle of attack, the entire set-up, including the force balance, was mounted on a turntable with a rotational accuracy of ±0.25°. The largest blockage ratio occurring between the model and the flow cross-section is calculated to σ_{max}=5.1% at the highest angle of attack α=18°C. This was below the limit of σ=10% above which blockage correction needs to be considered [126]. Earlier investigations showed that small losses in static pressure between the upstream pitot probe and the downstream rake occurred. Measurements also showed that the static pressure at the location of the rake is not fully stabilized. Both these effects contributed to a reduction of the drag coefficients, which has been approximated to be in the order of up to 20% [125]. In addition, the wake rake measurements were only reliable as long as no strong separation effects occur. This was because the rake cannot capture the resulting 3D velocity field. This means that for high angles of attack α>12° for clean and α>6–12° (depending on the ice shape) drag measurements from the wake rake were increasingly erroneous. More details on the general wind tunnel configuration and measurement method can be found with Bartl et al. [125].

Artificial ice shapes were 3D-printed via fused deposition modeling at NTNU in polylactide plastic, on an Ultimaker S5 and S2+ printer with a layer height of 100µm, see Figure 4.1b. The artificial ice shapes cover the entire height of the wing, including the dummy sections, and were attached with tape.

In order to assess the influence of the laminar-turbulent transition, a series of runs were performed with a tripped boundary-layer. For this purpose, self-adhesive zig-zag tape, acting as a turbulator was applied to the upper and lower side of the leading edge at the location x/c=0.05. The tape thickness was 0.4mm with a width of 8mm and a pattern angle of 60°.

4.3 Numerical Methods

Two numerical tools were used for this study. FENSAP is a CFD tool to study the aerodynamic performance penalties due to icing and LEWICE is a tool to generate simulated ice shapes.

4.3.1 Aerodynamic Performance Prediction

The aerodynamic performance degradation due to icing was simulated with FENSAP, a state-of-the-art Navier-Stokes CFD solver [127]. The solver is part of the software package ANSYS FENSAP-ICE (version 19.2) which is a 2nd generation icing simulation tool suitable for a wide range of applications but with limited published validation data - in particular for low Reynolds numbers [128]. One objective of this study was to use FENSAP as an example to compare it to the experimental dataset and assess its capability to capture icing performance penalties at low Reynolds numbers. All FENSAP calculations were run as steady-state 2D simulations with a streamline upwind artificial viscosity model. The airfoil geometries were discretized in Pointwise (version 18.2R2) as a hybrid O-grid with a far-field diameter of 60*c*. The boundary-layer was resolved with a structured 3D anisotropic tetrahedral extrusion (T-Rex) with a growth factor of 1.1 [129], see Figure 4.2.

The comparison consisted of three steps. First, the clean airfoil aerodynamics were simulated and compared to the experiments (see section 4.4). One of the main challenges for the clean airfoil simulation was the laminar-turbulent transition. Two turbulence models are implemented in FENSAP [130]. The Spalart-Allmaras (SA) turbulence model is a classical one-equation model (eddy-viscosity) whereas the Menter's k-ω SST model is a two-equation model (turbulence kinetic energy and eddy dissipation rate) [131]. For both these turbulence formulations, a transition model are available. For the SA model, free transition was captured based on adverse pressure gradients whereas the Menter's k-ω SST model used a one-equation local correlation-based intermittency transition mode [130].

The second step was to ensure that the chosen numerical discretization (grid) of the iced airfoils did not significantly affect the results. For this, a 2D grid convergence study was performed in order to find a grid resolution that was sufficiently accurate while optimizing computational power and time. The grid dependency study was performed on four grid resolutions, at three different angles of attack α=[0°, 5°, 10°] on one of the

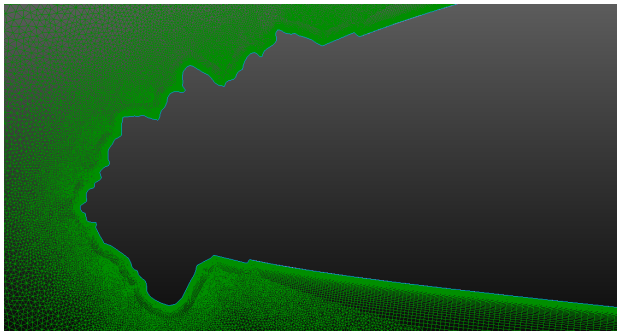

Figure 4.2: Numerical T-Rex grid for the glaze ice shape generated in Pointwise with a structured resolution of the boundary-layer and unstructured far field.

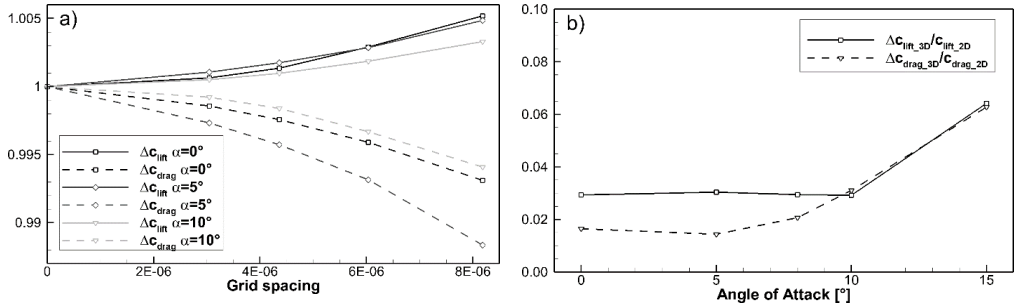

Figure 4.3: Grid dependency study on the 2D airfoil (a) and the fully resolved 3D wind tunnel (b).

ice shapes (glaze ice, see section 4.4). The results are shown in Figure 4.3a with the drag and lift coefficients normalized by a Richardson extrapolation $\Delta c_{lift}=c_{lift}/c_{lift,Richardson}$ and $c_{drag}=c_{drag}/c_{drag,Richardson}$ [132]. The results showed good convergence for lift and drag for all angles of attack. In order to limit the computational requirements for this study, the second-coarsest grid (ca. 170,000 points) was used for all subsequent simulations.

The third comparison step consisted of a study to compare the differences between the 3D constrained flow in the wind tunnel to the 2D simulations. For this purpose, the entire wind tunnel and test section were modeled in 3D with no-slip walls. Lift and drag forces were calculated on the main wing section, excluding the dummy parts. Figure 4.3b compares the simulated 3D flow field inside the entire wind tunnel to the 2D solution lift and drag with $\Delta c_{lift,3D/2D}=[c_{lift,3D} / c_{lift,2D}-1]$ and $\Delta c_{drag,3D/2D}=[c_{drag,3D} / c_{drag,2D}-1]$ for five angles of attack. The results show that for angles of attack up till $\alpha=10°$ the difference between the 2D and the 3D solution is about 3% and increases to about 7% for the highest angle of attack. These deviations are assumed to be comparatively minor and justify the use of 2D simulations (e.g. [133]).

4.3.2 Ice Shape Generation

LEWICE (2D, version 3.2.2) was used to simulate ice shapes that were then 3D printed and tested in the NTNU wind tunnel. LEWICE has been developed by NASA and is a widely used 1st generation 2D panel-method icing simulation tool [88]. The code has been validated over a wide range of parameters with extensive experimental IWT data [89]. However, the validation focus was on aviation and therefore the investigated Reynolds numbers Re_{min}=2.26 ×10^6 are significantly higher than those for example of UAVs or SWTs. The numerical methods implemented in the LEWICE are not explicitly excluding low Reynolds numbers, but previous work suggests that there is limited fidelity of the LEWICE ice shapes at low Reynolds number [45, 53].

4.4 Icing Cases

Icing cases are generally defined by the following parameters: free-stream velocity v_∞, duration of icing t_{icing}, airfoil chord length c, angle of attack α, liquid water content LWC, median volume diameter MVD, and ambient temperature T_∞. Typically, three icing typologies can be identified, that are characterized by the temperature during which the icing process occurs [64, 134]. At very low temperatures, all droplets freeze on impact and form rime ice. Due to entrapped air between the frozen droplets, rime appears white in color and displays a rugged, rough surface. Glaze is an ice typology that forms at temperatures close to freezing conditions. It is dominated by a low mass fraction of particles that freeze on impact. Most droplets form a liquid water film on the surface of the airfoil. This film will flow downstream (called runback) where it gradually freezes or evaporates. Glaze typically appears as transparent ice with a smooth surface. Mixed icing is an ice type that is formed in the temperature regime between rime and glaze. It is characterized by a balanced ratio between instantaneous freezing and surface freezing. Glaze and mixed ice shapes can exhibit complex ice horn features, whereas rime typically has more streamwise ice characteristics [57].

4.4.1 Baseline Airfoil

The NREL S826 airfoil is the baseline geometry for this study. The original design of the airfoil is intended to be used at the blade tip of a 20–40m diameter horizontal axis wind turbine for Reynolds numbers Re=1–3×10^6 [135]. A key characteristic is a constant drag value for lift coefficients c_l=0.4–1.2. The airfoil has a good lift-to-drag ratio, low

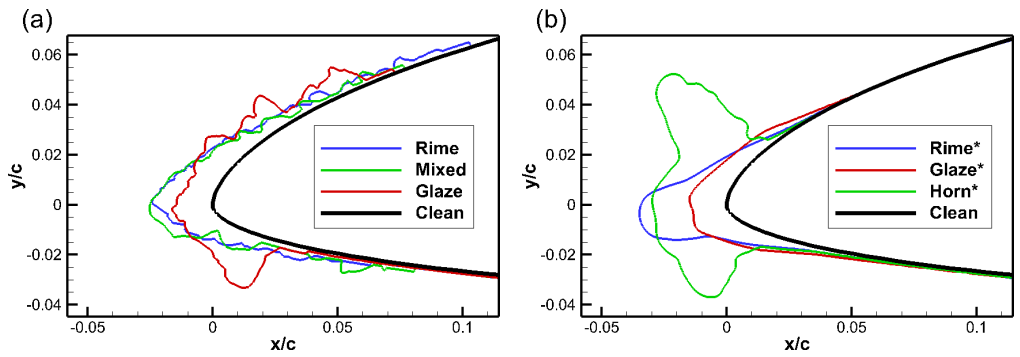

Figure 4.4: Experimental ice shapes (a) and LEWICE ice shapes (b).

sensitivity to transition point changes and docile stall behavior. This airfoil was selected for this study as it has been extensively investigated in the NTNU wind tunnel before as part of a series of blind test experiments on performance and wake development of an S826-based wind turbine – Bartl et al. give a comprehensive overview of the previous experimental work [125].

4.4.2 IWT Ice Shapes

Experimental ice shapes were collected by manually tracing them during a test campaign at the IWT facilities of the Technical Research Centre of Finland (VTT) [136]. The icing tests were conducted on the main section of the NTNU airfoil model at Re=0.9×10^6. Three different meteorological icing conditions have been selected to represent the three main icing morphologies and are presented in Table 4.2 and Figure 4.4a.

Surface roughness is a key element for the aerodynamic performance degradation of airfoils [57]. In order to compensate for the missing surface roughness of the ice shapes, additional surface roughness was superimposed onto the 3D printed ice geometries. Using an empirical correlation suggested by Shin and Bond [137], an equivalent sand-grain roughness k_s was calculated for all three icing cases, see Table 4.2. A staggered pattern of spheres with the diameter of k_s was added to all three shapes as can be seen on the leftmost ice shape in Figure 4.1b. In order to investigate the significance of this effect, a set of smooth experimental ice shapes, without the superimposed surface roughness, was printed.

4.4.3 LEWICE Ice Shapes

Three additional ice shapes were generated with the numerical simulation code LEWICE with the icing parameters presented in Table 4.2. The resulting ice geometries are depicted in Figure 4.4b. In the following, these simulated ice shapes are marked with an asterisk (e.g. glaze*) to distinguish them from the experimental shapes. The LEWICE ice shapes have been used in previous studies [138] and have been included to represent extreme cases of smooth, streamlined, and horn ice shapes. The glaze* and rime* case have been selected from the continuous maximum icing envelope in CFR 14, Part 25, Appendix C [73] at Re=0.9×10^6. A third case named horn* was specifically chosen to result in large horns on the upper and lower surface and thus represents a worst-case scenario. All LEWICE ice shapes were printed with additional surface roughness. Note that this study does not intend to compare the aerodynamic effects or the ice shape fidelity of real ice shapes to simulated ones.

4.5 Experimental Results

This section presents the experimental measurements of lift and drag from the NTNU wind tunnel for the two types of ice shapes. In addition, the influence of the small-scale surface roughness is investigated by comparing the (rough) IWT ice shapes to smooth ice shapes.

Table 4.2: Overview of icing conditions used to the generation of the experimental and LEWICE ice shapes.

	Icing Wind Tunnel (IWT)			LEWICE		
	Glaze	**Mixed**	**Rime**	**Glaze***	**Horn***	**Rime***
Source	Experiment			Simulation		
v_∞	25m/s			25m/s	40m/s	25m/s
Re	0.9×10^6			0.9×10^6	1.4×10^6	0.9×10^6
T_∞	−2°C	−5°C	−10°C	−2°C	−4°C	−10°C
MVD	26µm			30µm	20µm	20µm
LWC	0.44g/m³			0.34g/m³	0.55g/m³	0.43g/m³
t_{icing}	20min			40min		
α_{icing}	0°					
c	0.45m					
k_s	1.0mm	0.9mm	0.7mm	1.0mm	1.0mm	1.0mm

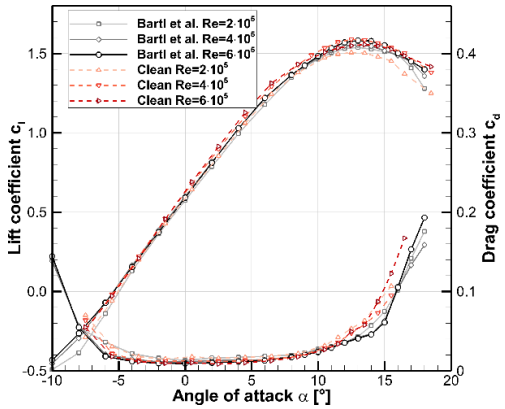

Figure 4.5: Comparison of experimental results to Bartl et al. for Re=2×10^5, 4×10^5, and 6×10^5. Data adapted from [125].

4.5.1 Comparison to Existing Data

Figure 4.5 compares the experimental lift and drag results for the clean airfoil from this study to the results from Bartl et al. [125]. In general, the datasets are in good agreement, which is not surprising because identical facilities and methods were used. The largest deviations occurred in the stall area, in particular for drag, which is most likely related to the high measurement uncertainty of the wake rake in that area. The small level of Reynolds-dependency for Re=2–6×10^5 that was observed by Bartl et al., was also reproduced in this work. The decision to investigate three Reynolds numbers in this work was based on the possibility that iced airfoils may show a higher degree of Reynolds dependency. In conclusion, the good match between the clean curves gives confidence that the experimental setup is accurate, and that data is repeatable.

4.5.2 IWT Ice Shapes

The lift and drag results for the three experimental IWT ice shapes are compared to the clean airfoil in Figure 4.6a–c. The first observation was that all ice shapes introduced significant penalties on lift and drag. Lift was decreased and drag increased over the entire span of angles of attack. The degree of degradation was depending on the ice shape type. The low Reynolds number results generally showed higher drag levels and lower lift for both clean and iced airfoils.

The **glaze ice** shapes gave the largest penalties. For zero angle of attack, the lift was decreased between Δc_l=−26–31% and drag was increased by Δc_d=+220–290%, as a

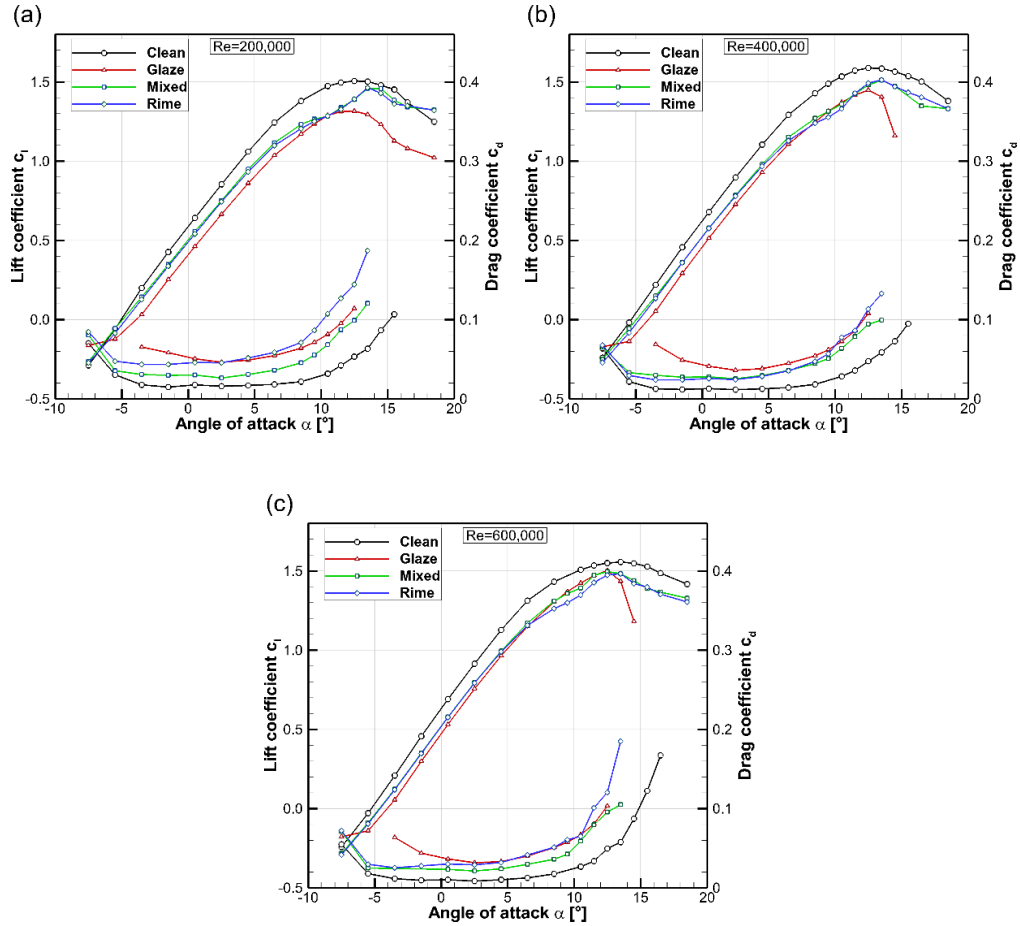

Figure 4.6: Experimental results for lift and drag of the IWT ice shapes for *Re*=2×10^5 (a), 4×10^5 (b), and 6×10^5 (c).

function of the Reynolds number. The stall angle seemed unaffected, but the maximum achievable lift was reduced, and the drag increased. Furthermore, the stall behavior was more aggressive, with a rapid loss of lift, especially for the higher Reynolds numbers.

For **rime ice** the degree of performance degradation was smaller with Δc_l=−17–19% and Δc_d=+100–190% at zero angle of attack. The drag curve at the lowest Reynolds number showed a significant increase compared to the other drag curves. In addition, the stall region showed an irregular behavior. The linear lift region ends at around α≈7° with an apparent onset of stall. However, at about α≈11° lift was suddenly increased, reaching a maximum at α≈13–14 before showing a docile lift decrease. This uncharacteristic

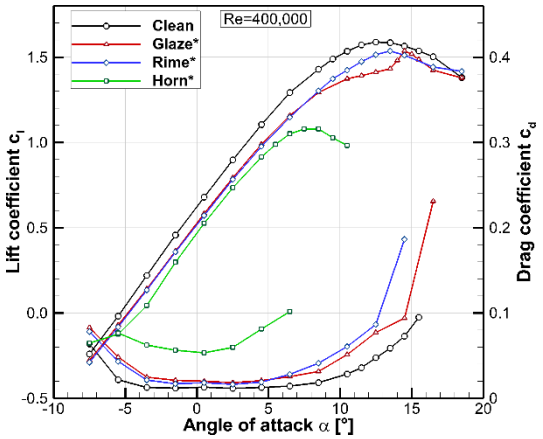

Figure 4.7: Experimental results for lift and drag of the LEWICE ice shapes for Re=4×10^5.

behavior occurred at all Reynolds numbers but was most distinct at the lowest Reynolds number. Potential explanations for this will be addressed in the discussion section.

Last, **mixed ice** exhibited the lowest performance penalties with Δc_l=−15–18% and Δc_d =+80–130% at zero angle of attack. In the stall region, the same unexpected behavior with a sudden lift increase was observed, similarly to the rime case. This lift behavior showed a dependency on the Reynold number and decreased in distinction at higher Reynolds numbers.

4.5.3 LEWICE Ice Shapes

The experimental results for the ice shapes obtained from LEWICE simulations are shown in Figure 4.7. Due to time limitations and because the IWT ice shapes did not show a major Reynolds number dependency, the LEWICE ice shapes were conducted only at Re=4×10^5. The largest penalties occurred for the **horn*** ice shape. At zero angle of attack, lift was decreased by Δc_l=−26% and drag substantially increased with Δc_d=+330%. The maximum lift angle occurred significantly earlier compared to the clean airfoil, at α≈7°.

The **rime* and glaze*** ice shapes showed similar degrees of degradation in both lift and drag with Δc_l=−16–17% and Δc_d=+40–60% at zero angle of attack. Differences showed in the stall region, where the glaze ice shape displayed a similar lift behavior as the IWT rime and mixed ice shapes. However, in this case, the lift increase arose significantly

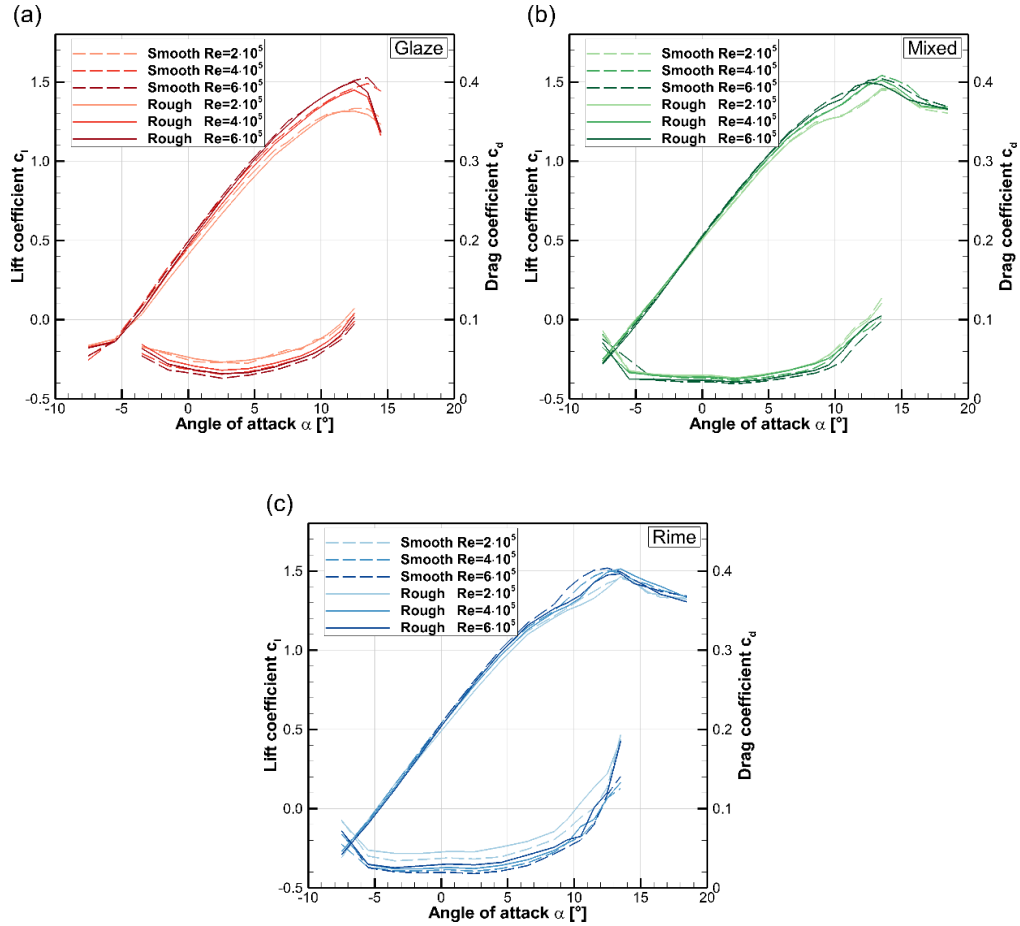

Figure 4.8: Comparison of experimental results for lift and drag between the smooth and rough IWT ice shapes for Glaze (a), Mixed (b), and Rime (c).

later, at α≈14° and the maximum lift was reached at α≈15°. The rime ice shape exhibited a normal stall behavior.

4.5.4 Influence of Roughness

Figure 4.8 shows the comparison of smooth and rough IWT ice shapes to highlight the influence of the small-scale roughness. The general trend that was observed for all lines is that the additional surface roughness led to a decrease in lift and an increase in drag.

For the glaze ice shapes, the smooth surfaces seemed to delay the maximum stall angles by Δα≈1° while increasing the maximum lift slightly. The sudden lift increase in the stall

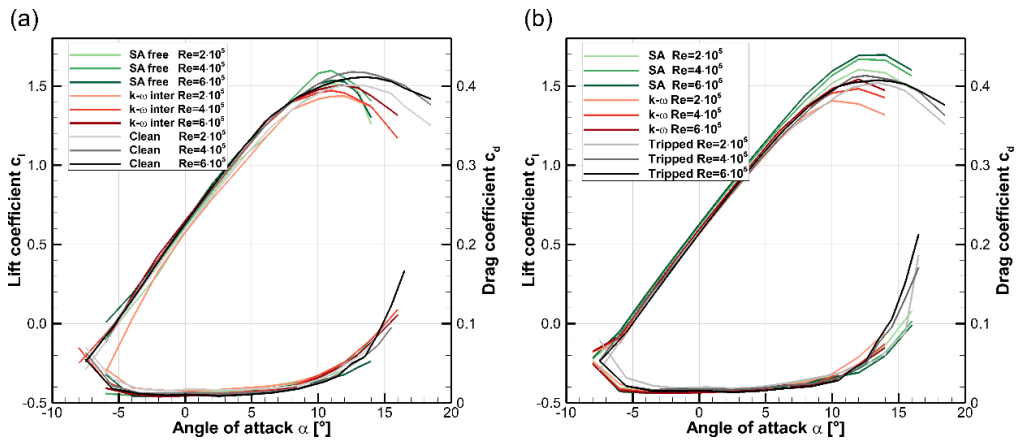

Figure 4.9: Comparison between numerical and experimental results of lift and drag for the clean (a) and the tripped (b) airfoil.

region of the rime and mixed ice shapes prevailed in the absence of the surface roughness. The results indicated that the effect may be slightly more pronounced for the rough airfoils, especially for rime ice. These results are in line with findings for higher Reynolds numbers [57].

4.6 Simulation Results

4.6.1 Clean and Tripped

The first simulations aimed to establish that the clean airfoil aerodynamics could be captured accurately. Figure 4.9a shows the results for the clean airfoil with free transition and numerical results with transition modeling. Both turbulence models seemed to capture the experimental results with a good degree of accuracy. Lift and drag values in the linear region showed a good overlap at all Reynolds numbers. Notable differences occurred in the stall region, where both turbulence models failed to reproduce the experimental stall behavior. Generally, the numerical results predicted the maximum lift angle about $\Delta\alpha \approx 2°$ earlier than the experiments and a more aggressive stall behavior. The k-ω SST model tended to predict lower maximum lift levels, whereas the SA model resulted in a maximum lift comparable to the experiments. Drag was captured in all cases with good accuracy, although deviations occurred in the stall region due to earlier predicted stall from the numerical models.

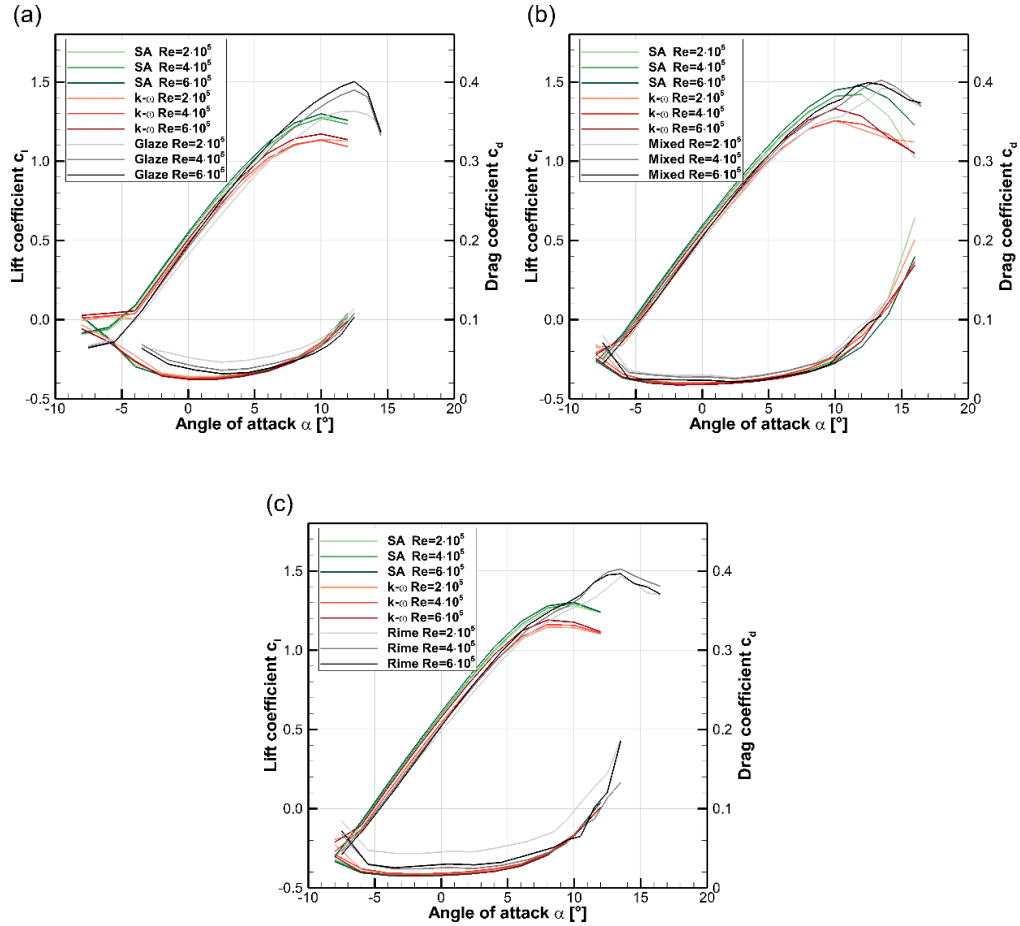

Figure 4.10: Comparison between numerical and experimental results of lift and drag for the IWT shapes of glaze (a), mixed (b), and rime (c).

In addition, an experimental run with a forcibly tripped boundary at x/c=0.05 was conducted to be able to compare it to fully-turbulent numerical simulations, see Figure 4.9b. Compared to the experiments with free transition, the tripped runs exhibited slightly lowered levels of lift and increased levels of drag. Stall and the maximum lift angle were marginally delayed. The fully-turbulent numerical results showed that both turbulence models slightly overpredicted the lift in the linear region, whereas drag seemed to be captured. well. The fully-turbulent SA model estimated significantly higher maximum lift values in the stall region with a slightly earlier stall. In contrast, the fully turbulent k-ω SST model predicted the maximum lift value well but showed stall at earlier angles of attack and also with a more aggressive stall behavior.

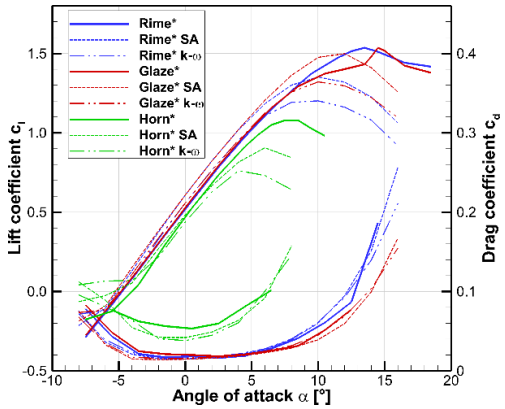

Figure 4.11: Comparison between numerical and experimental results of lift and drag for the LEWICE ice shapes for Re=4×10^5.

4.6.2 IWT Ice Shapes

Figure 4.10a–c show the comparison between the experimental and the computational results. For glaze ice the simulation results of lift and drag exhibited a constant offset. The lift simulations in the linear area were shifted to lower angles of attack with an offset of Δα≈0.3/0.8° for the k-ω SST/SA models. Maximum stall angles were captured better with the SA model than k-ω SST, but both predicted the maximum stall angle Δα≈2° earlier compared to the experiments. The numerical drag predictions gave significantly lower results compared to the experiments, in particular for α<4°. The numerical results also indicated a substantially lower effect of the Reynolds number, compared to the experiments.

The mixed ice experimental results had a better overlap between the simulations and the experiments. In the linear lift section, both turbulence models tended to predict higher lift and lower drag compared to the experiments. In the stall region, the k-ω SST model showed the maximum lift with a significantly lower lift value and at lower angles of attack. The SA model seemed to capture the stall behavior better, with maximum lift and stall angle closer to the experiments. However, none of the simulation results reproduced the sudden lift increase in the experimental results starting at α≈11°.

The simulation results for rime ice showed a similar trend as for mixed ice, however with larger levels of deviations. In the linear region, the simulations predicted higher lift values and significantly lower drag. None of the turbulence models captured neither the

stall angle nor the maximum lift value correctly. Again, the unusual behavior of the sudden lift increase in the stall region was not reproducible with the numeric methods.

4.6.3 LEWICE Ice Shapes

The simulation results for the LEWICE ice shapes are shown in Figure 4.11. For rime* ice the SA model predicted higher lift in the linear region and an earlier stall angle – however, the maximum lift was matched well. The k-ω SST model matched lift in the linear region but predicts earlier stall at lower maximum lift. For drag, both turbulence models matched the experiments well. The glaze* ice resulted show similar trends. The main difference, however, was that the sudden lift increase at $\alpha \approx 14°$ was not captured by the numerical simulations. The simulations of the horn* ice shapes predicted lower lift, particularly in the stall region. Furthermore, the drag results from the numerical models were substantially lower compared to the experiments. Both these effects may be related to the significant separation zones induced by the ice horns.

4.7 Discussion

4.7.1 Experiments

In general, the experiments showed that the performance degradation is linked to the geometry of the ice shape. The largest differences between the results can be observed for the drag curves. The most streamlined ice shapes (glaze* and rime*) resulted in the smallest increases in drag, compared to the more complex IWT ice shapes. The largest drag penalties occurred for the glaze and horn* ice shapes, which can be explained by the large horn geometry that resulted in large separation bubbles. The correlation between performance degradation and ice shape geometry can also be detected for lift. In the linear lift region, this effect is less obvious, but it can be observed for the stall behavior – especially for glaze and horn* which exhibited earlier stall, lower maximum lift, and rapid lift decrease.

The variation of the Reynolds numbers seemed to play a lesser effect on the results. The general trends are that higher Reynolds numbers lead to increased lift and a decrease in drag levels. One notable occurrence was found for the rime ice shape at $Re=2 \times 10^5$, where the drag was increased substantially compared to the higher Reynolds numbers.

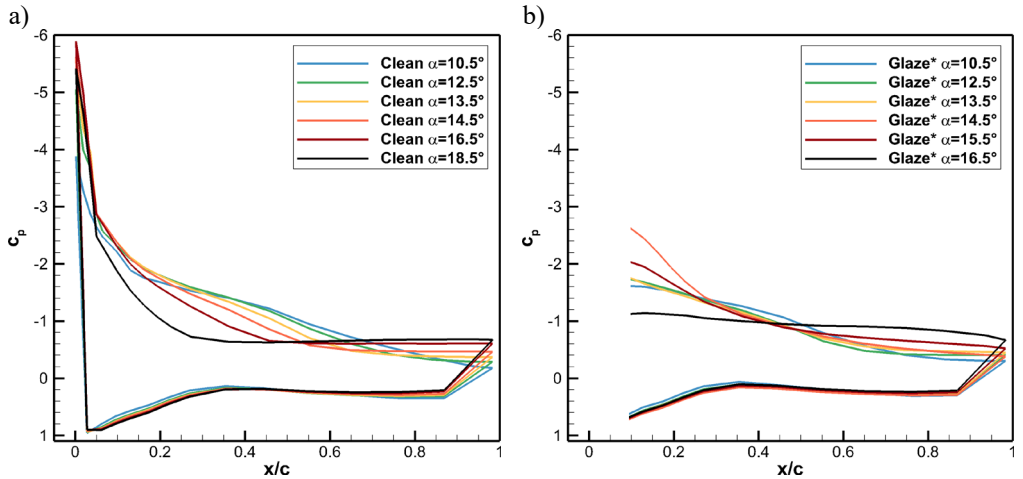

Figure 4.12: Pressure coefficient distribution for the clean airfoil (a), and the glaze* ice shape (b).

This can most likely be linked to the relatively high measurement uncertainties related to the small forces acting on the measurement balance.

A surprise from the experimental data was the stall behavior occurring for the IWT mixed, IWT rime, and the LEWICE glaze* ice shapes. In all these cases, a sudden lift increase occurred in the stall region. A measurement error was very unlikely as this effect was reliably reproduced for the ice shapes in question. No unsteady behavior was found, neither in the force balance measurements nor the pressure tap data. The effect showed a slight tendency to decrease for higher Reynolds numbers, Figure 4.8b–c.

To investigate the stall behavior, the pressure distributions over the clean and an iced airfoil were examined. Figure 4.12a displays the distribution of the pressure coefficient c_p over the clean airfoil and shows how the stall was starting from the trailing-edge. For the iced airfoil, the LEWICE glaze* case was investigated since it showed the clearest lift increase behavior, see Figure 4.7. The glaze* pressure distribution in Figure 4.12b showed that the additional lift seemed to originate from the leading-edge, where increased suction pressure occurred at $x/c<0.3$ for $\alpha=13.5–15.5°$.

One hypothesis for the origin of this increase in leading-edge suction is an increase of the airfoil camber. According to this idea, the initial break in the lift curve ($\alpha\approx9°$) occurs due to the onset of trailing-edge separation. The lift increase ($\alpha\approx14°$) would originate either from the ice shape acting as a nose droop [139], or possibly, from a localized

separation bubble [140]. This effect would decrease at higher Reynolds numbers because the onset of the trailing-edge separation moves to higher angles of attack due to the higher boundary-layer inertia. This would explain why this effect has not been observed on a wider scale for high-Reynolds applications. Comparable effects have indeed been documented before at low Reynolds numbers by Jasinski et al. who suggest a "leading-edge flap" like behavior as an explanation, ([116] pp. 61–62). Also, a lift increase occurs in Seifert and Richert's experiments, however to a lesser degree and without them addressing it explicitly ([115] pp. 459–460).

The exact mechanism of the unexpected stall behavior could not be fully proven within the scope of this work. To test the hypothesis, flow visualization techniques, wider Reynolds number range, moment measurements, and pressure measurements on the ice shapes should be conducted in follow-up studies.

4.7.2 Simulations

The experimental results were qualitatively compared to FENSAP, using the SA and k-ω SST turbulence models. For the clean airfoil with free transition and tripped boundary-layer, both turbulence models showed a good match in lift and drag with the experiments and were able to reproduce the linear drag behavior of the airfoil. Larger differences occur in the stall regions, where both models do not capture the experimental stall behavior. The SA model tends to predict higher lift values, whereas the k-ω SST tends to predict lower maximum lift angles and earlier stall.

The quality of the lift and drag prediction of iced airfoils appears to depend on the ice shape. For the most streamlined cases (LEWICE rime* and glaze*) both turbulence models capture the drag well. In the linear lift region, the k-ω SST model seemed to match the experiments better, whereas the SA model tended to overpredict the lift. The stall behavior was not captured well by either of the turbulence models, resulting in an earlier stall and lower maximum lift values. This is likely to be related to the shortcomings of the turbulence models in the presence of large separation zones [131]. For the more rugged shapes of the IWT rime and mixed ice shapes, the codes behave similarly, with exception to the drag results, which are significantly lower compared to the experiments. This is likely to be related to the ruggedness of the surface and the inability of the turbulence models to capture the associated drag increase. This trend

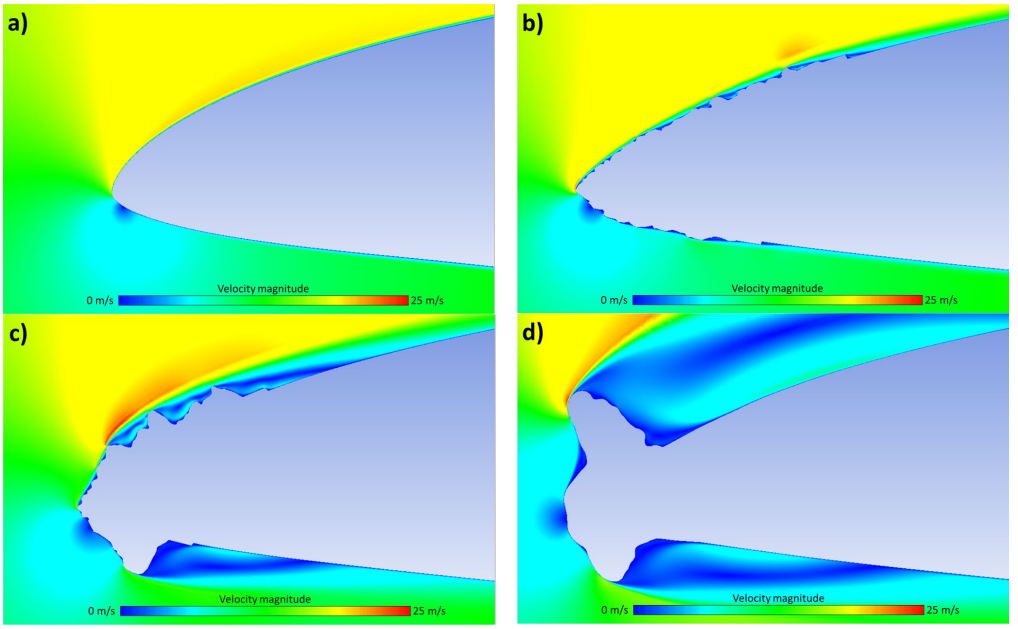

Figure 4.13: FENSAP results for the velocity field of the clean (a), rime (b), glaze (c), and horn* (d) cases.

amplifies for the more complex ice shapes of glaze and horn* where the large separation areas also occur in the linear lift region, see Figure 4.13a–d.

The unexpected stall behavior of some of the ice shapes was not captured by the simulation with any of the turbulence models. This is not entirely surprising and is most likely related to the limitations of the SA and k-ω SST turbulence models. Further work should investigate the possibility of 3D flow effects, transient flow behavior, and the use of higher-order models.

In summary, the comparison between FENSAP and the experimental data showed that even CFD-RANS can be used to get reasonable lift and drag predictions at low Reynolds numbers. Limitations exist in the stall area and for complex ice shapes with large leading-edge separation zones. Consequently, FESNAP may be suited for example to predict intercycle ice penalties for the design of de-icing systems at low Reynolds numbers [85]. Similarly, effects on wind turbine power production or UAV flight behavior may be simulated with sufficient accuracy with FENSAP.

4.8 Conclusion

This study conducted experimental and numerical investigations on the performance degradation of an S826 airfoil with 3D printed ice shapes at low Reynolds numbers. The experimental data of this work is shared as supplemental material and is suitable to be used for the validation of other numerical tools for the prediction of icing penalties at low Reynolds numbers. The experimental results show that the overall degree of performance penalties due to icing are correlated with the geometry of the ice shapes. Rough, rugged, and complex geometries result in higher aerodynamic performance degradation in the form of increased drag, decreased lift, and earlier stall. The experiments were compared to simulations with the CFD flow solver FENSAP with two turbulence models. The fidelity of the results was linked to the geometry of the ice shapes. The ice shapes that result in higher penalties had the largest discrepancies between the experiments and the simulations. This was most likely related to the limitations of the turbulence models. For some ice shapes, an unexpected lift behavior was observed in the stall region. This was hypothesized to be related to a local increase in camber. This effect may be related to similar behaviors observed in the literature before and is likely to be an aerodynamic effect related to low Reynolds numbers.

5 Parameter Study on the Influence of Meteorological Conditions on Icing Penalties

5.1 Introduction

Recent development has shown that atmospheric icing is one of the main operational limitations of small and medium-size fixed-wing unmanned aerial vehicles (UAVs) with a wingspan of approximately 2–4 m in their growing field of applications [9]. Ice accretion on airfoils changes the aerodynamic performance (e.g. lift, drag, stability, stall behavior) [57] and thereby limits flight capabilities such as range and duration. To ensure safe operation of UAVs, without ice protection systems (IPS), a common approach is to ground the aircraft when icing conditions are expected [10].

The main challenge of UAV icing is that the well-understood icing process of manned civil and military aircraft does not apply to most UAVs. Due to the typically lower airspeed and smaller sizes, most UAVs operate at a lower Reynolds number regime of $Re = 1–10\times10^5$, whereas manned aviation is characterized by a Reynolds number regime of roughly $Re = 1–10\times10^6$ [57]. This difference implies the necessity to gain a better understanding of the icing process at low Reynolds numbers.

The work by Szilder and McIlwain [19] with their morphogenetic icing model has shown that the ice shapes are strongly dependent on the Reynolds number. One major finding is that higher Reynolds numbers lead to a reduction of rime and increase of glaze ice in a parametric space defined by air temperature and liquid water content. Further, a comparison of an airfoil traveling the same distance through icing conditions at various Reynolds numbers revealed that higher Reynolds numbers lead to significantly smaller ice extents. This implies the importance to separate studies on the ice accretion process of small-sized fixed-wing UAVs from general aircraft icing. Other commonly utilized tools for the ice accretion simulation on UAV airfoils are the NASA code LEWICE [13] and FENSAP-ICE [21]. A purely numerical comparison between LEWICE and

FENSAP-ICE for 2D UAV airfoils has been covered by Hann [53]. It showed that both codes predict a significant decrease in maximum lift, stall angle, and increase of drag for all three investigated icing cases (rime, glaze and mixed ice). However, the comparison also revealed limitations of the panel-method used within LEWICE. Whereas the ice shapes of both codes were congruent for the rime ice case, they deviate significantly for the mixed and glaze ice case. This, in consequence, led to similar performance results for the rime ice case but discrepancies for the mixed and glaze ice case.

This study aims to investigate the influence of various meteorological conditions on the aerodynamic performance of the RG-15, a typical UAV airfoil, using FENSAP-ICE. The above mentioned earlier work on UAV icing has shown that ice accretion affects the aerodynamic performance negatively, but no study has been conducted that investigates the relation of meteorological conditions to the degradation of performance. For the successful development of an effective and efficient IPS for UAVs it is crucial to identify worst-case icing conditions. Additionally, the knowledge about the influence of different icing conditions on the performance of the airfoil is essential for the adaption of flight controllers, to enable safe flight in varying weather conditions and thereby extending the UAV's operational capabilities.

5.2 Methods

5.2.1 Numerical Methods

Two different simulation models are set up to capture the ice accretion and the performance of the iced airfoil. The first model, FENSAP-ICE, generates an iced geometry which is the input geometry for the second model, FENSAP (Figure 5.1). This will, subsequently, be used to determine the aerodynamic performance of the iced airfoil. All simulations are performed with ANSYS FENSAP-ICE (version 2019 R1). The software package consists of several linked modules to obtain the ice accretion process. Within this work, the three modules FENSAP, DROP3D, and ICE3D are used. Figure 5.2 shows how the three modules interact with each other.

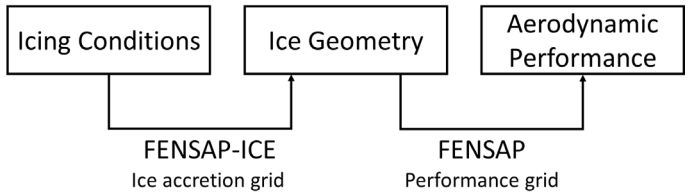

Figure 5.1: Overview of the simulation process.

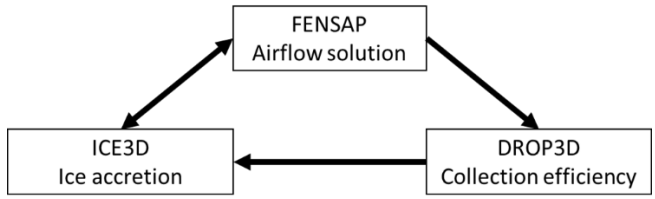

Figure 5.2: Linked modules of FENSAP-ICE from (adapted from [141]**).**

FENSAP is a state-of-the-art CFD solver that obtains the airflow solution by solving compressible Reynolds Averaged Navier-Stokes (RANS), also called Favre-averaged equations [127]. The FENSAP CFD solver is used in both simulation models (to provide the flow solution). For the ice accretion FENSAP is utilized as a part of the loop presented in Figure 5.2, whereas for the simulation of aerodynamic performance, FENSAP is used as a stand-alone system. Ultimately, all FENSAP simulations are set up with a streamline upwind artificial viscosity, to increase numerical stability.

DROP3D is a Eulerian droplet impingement module. Based on the airflow solution, it solves partial differential equations to calculate the droplet velocity, collection efficiency, and impingement limits [142].

ICE3D is solving partial differential equations, similar to the impingement module DROP3D [141]. ICE3D requires the shear-stresses and the heat flux distribution across the wing, obtained by FENSAP, as well as the mass of water, caught by DROP3D, to calculate the ice accretion. The ice shape acquired by the ICE3D module provides the new geometry, to be used by FENSAP for the next airflow calculation.

Table 5.1: Grid features of ice accretion and performance grid.

Feature	Ice accretion grid	Performance grid
Grid dimension	3D	2D
Chord length *c*	0.45 m	0.45 m
Farfield diameter	9 m (20 c)	30 m (66.7 c)
Boundary layer resolution	Constant number of structured layers – 50 layers	Variable number of structured layers – ensures ideal isotropic cell height at the boundary from structured to unstructured grid
Spanwise discretization	Triangular elements – fine resolution of the leading-edge to capture the ice accretion	None – extrusion by one cell
Trailing edge resolution	Blunt – 1 mm height	Blunt – 1 mm height
Number of cells	~5 400 000	~80 000
Reference wing area	0.02025 m²	0.45 m²

Following the efforts of Hann et al. [43] Spalart Allmaras (SA) one-equation turbulence model with fixed transition is applied for the performance simulations of the clean/un-iced airfoil. This includes the clean airfoil simulation for the validation of the performance model. Additionally, a simulation with Menter's two-equation k-ω-SST turbulence model is set up for the validation.

Clean airfoil simulations using the SA model with fixed transition obtain the transition location from XFOIL [143]. In cases, where surface ice is present, an immediate transition from laminar to turbulent boundary layer is expected at the leading-edge, due to the increased surface roughness in comparison to an un-iced airfoil. Therefore, simulations including ice, such as ice accretion and iced airfoil performance, are set up fully turbulent with the SA model.

Multishot ice accretion. The concept of FENSAP-ICE as interactive loop enables a segmentation of the overall icing duration into smaller time frames. This way, the influence of ice on the airflow, catch efficiency, and further ice accretion is considered. ICE3D offers two different automatic remeshing processes to generate a displaced grid around the new ice shape: OptiGrid and Fluent remeshing. For this study Fluent remeshing was used since it offers more control and stability on the remeshing process. OptiGrid is part of the FENSAP-ICE package and a fully automatic process that deforms

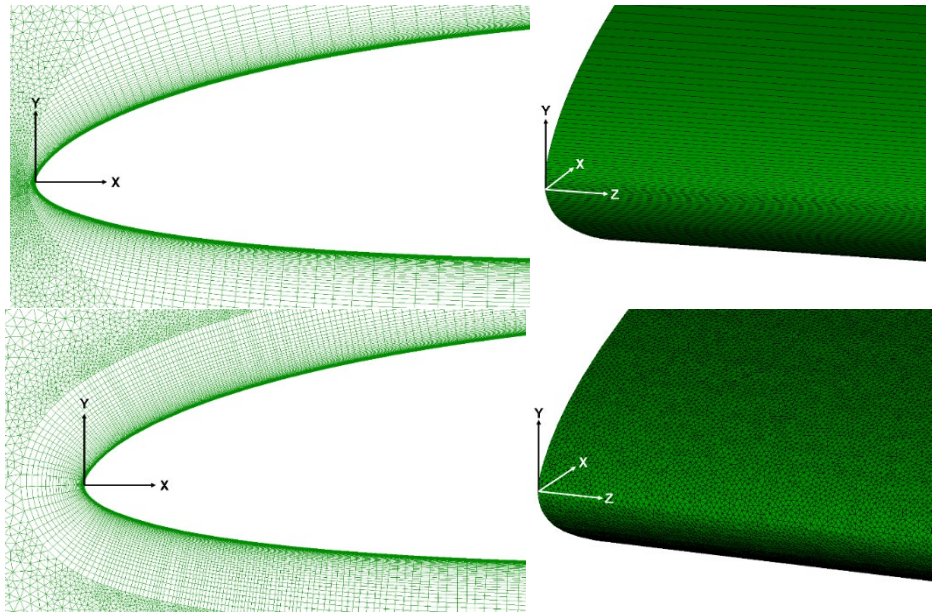

Figure 5.3: Grid differences of performance (top) and ice accretion grid (bottom).

the existing grid by moving nodes and coarsening and refining edges. Fluent remeshing on the other hand uses ANSYS FLUENT for a complete re-meshing of the new geometry after each step. Grid creation, grid control parameters and the interaction between FENSAP and FLUENT are covered by additional files in the simulation setup.

5.2.2 Grid Setup

For the discretization of all airfoils in this study, Pointwise (version 18.2) has been used. The grids are set up as hybrid O-grid with a structured resolution of the boundary layer and an unstructured resolution of the farfield. The simulation of ice accretion requires a different grid setup than the simulation of aerodynamic performance. The different features of both types of grids are listed in Table 5.1 and shown in Figure 5.3. Grid dependency studies have been conducted for both grid types to ensure independence of the results from the grids. The detailed description and the results of the grid dependency studies are documented in [144].

Since the focus for the ice accretion grid is not on precise calculation of aerodynamic coefficients, a smaller farfield, a constant number of structured layers and a smaller spanwise extrusion is initialized, to keep the number of cells within reasonable range.

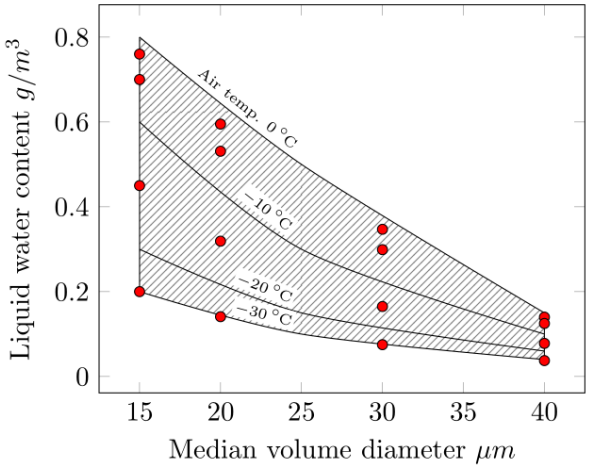

Figure 5.4: Icing case overview, modified from [73].

5.3 Icing Conditions

The CFR 14, Part 25, Appendix C [73], used for the certification of manned aircraft, offers two different envelopes that define the icing conditions for continuous maximum and intermittent maximum icing. The envelope for maximum continuous icing applies for cloud ceiling heights from 22000 ft (6700 m) down to sea level and therefore includes flight altitudes of small UAVs. For this reason, all icing cases investigated in this work are within the envelope of maximum continuous icing conditions of the Federal Aviation Administration (FAA) requirements. Figure 5.4 and Table 5.2 give an overview over the icing cases and the corresponding parameters.

The parameters cover a temperature range of −30 °C to −2 °C, a median volume diameter range of 15 µm to 40 µm and the corresponding liquid water content of 0.038 g/m³ to 0.760 g/m³. All ice accretion simulations are set up with a monodisperse droplet distribution. The constant parameters for the ice accretion simulations are summarized in Table 5.3. The icing time is determined by the cruising speed of 25 m/s and the maximum horizontal cloud extent of 17.4 nmi, resulting to 21.5 min.

Table 5.2: LWC in g/m³ as function of MVD and temperature for continuous maximum icing.

MVD [µm]	T_{icing} [°C] −2	−5	−15	−30
15	0.760	0.700	0.450	0.200
20	0.595	0.531	0.319	0.141
30	0.347	0.299	0.165	0.070
40	0.140	0.125	0.078	0.038

Table 5.3: Constant parameters for the ice accretion simulations.

Parameter	Value
Free stream velocity u_∞	25 m/s
Reynolds number *Re*	ca. 1×10^6
Icing time t_{icing}	1290 s
Angle of attack α	0°
Chord length *c*	0.45 m
Ice density ρ_{ice}	917 kg/m³
Air static pressure *p* at 500m flight altitude	95500 Pa

5.4 Model Validation

5.4.1 Clean / Iced Airfoil Performance Validation

The validation of clean airfoil performance is based on experimental data of two wind tunnel tests at a Reynolds number of *Re* = 200 000, published in [145, 146]. Two simulations were performed using the k-ω-SST and the Spalart Allmaras (SA) turbulence model. For the k-ω-SST model transition is predicted by a one-equation local correlation-based intermittency model, whereas the SA turbulence model is set up with fixed transition locations, previously determined with XFOIL. The comparison of experimental and simulation results is presented in Figure 5.5.

Both simulation results show good general agreement with the experimental results. At angles of attack (AOA) from −3° to −1° both simulations show a minor deviation of predicted lift coefficients to the experimental data. A possible explanation could be that the simulations both predict slightly earlier transition from a laminar to turbulent boundary layer.

The stall is captured within reasonable range to the experimental results with both turbulence models. The simulation model using the k-ω-SST model predicts a lower maximum lift coefficient and lower maximum lift angle, compared to the SA model. The tendency of estimating lower maximum lift coefficients and respective AOA with the k-ω-SST model, has already been observed in previous work, by Hann et al. [43]. The drag prediction of both simulations shows good agreement to the experimental results

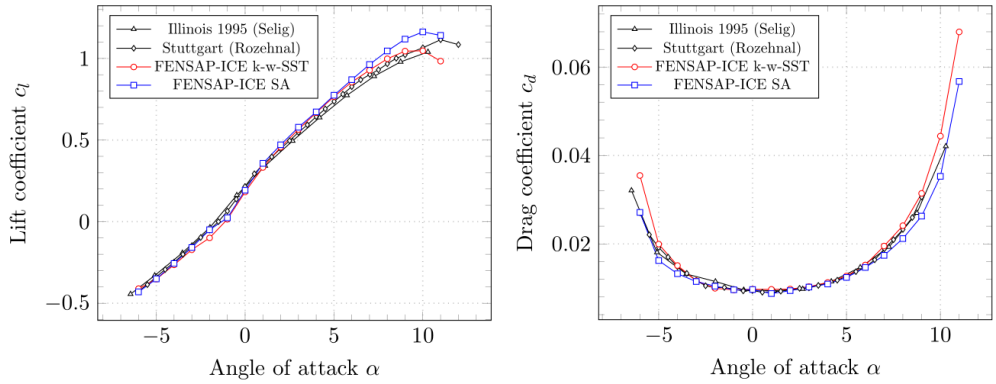

Figure 5.5: Validation of clean airfoil performance on a clean RG-15 airfoil at *Re* = 200 000.

for the whole AOA range. For α>7°, with the onset of a stall, the k-ω-SST predicts higher drag compared to the SA model.

Since no suitable literature data of an iced RG-15 airfoil was found, wind tunnel test results of an iced S826 airfoil at a Reynolds number of *Re* = 400 000, published in [138], were used for the validation of the performance simulation of an iced airfoil. The data for the iced S826 are gathered by 3D-printing the ice geometry and attaching it to the clean airfoil for the wind tunnel tests. The simulation results are presented in Figure 5.6.

For the AOA range of −8° to 0° the simulation results for the lift show good agreement with the experimental data. Regarding the stall, the simulation predicts an earlier stall at a lower maximum lift coefficient and maximum lift angle. Further, the simulation shows a smaller lift gradient. Regarding the drag, the simulation captures a similar trend of drag over AOA but under-predicts the drag at all points. The reason for the diverging results is suspected to be in the use of the turbulence model (Spalart-Allmaras) in combination with a high level of turbulence, caused by the horns. The surface roughness and the horn shape results in a high level of turbulence and flow separation already at very low AOAs. For the degree of turbulence and separated flow from the leading-edge, like in this case, different numerical methods like Large-eddy simulations (LES) and direct numerical simulations (DNS) or higher-level turbulence models like nonlinear eddy viscosity models and Reynolds stress models might be more suitable.

The icing conditions, in this case, were specifically chosen to create severe icing with a horn-shaped structure. To achieve that, several icing parameters were modified. In

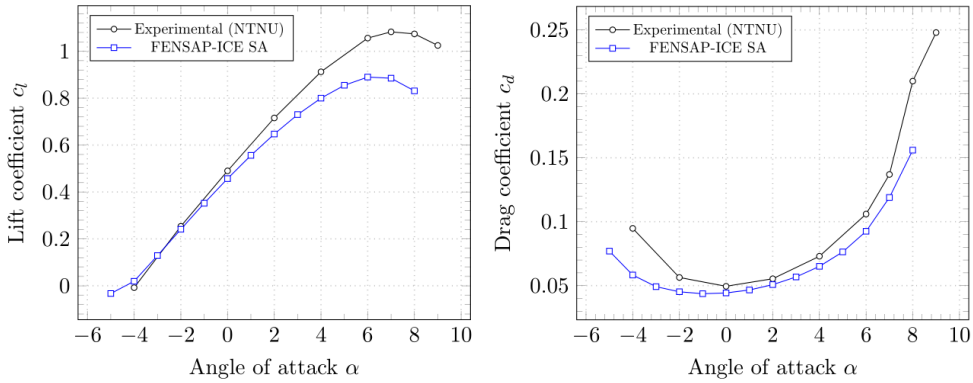

Figure 5.6: Validation of aerodynamic performance on an iced S826 airfoil at *Re* = 400 000.

particular, the icing time was set to 40 min, twice of what is used in this work. Details on the ice shapes are given in [138]. Therefore, a much smaller extent of ice and turbulence is expected for the icing cases in this work.

5.4.2 Ice Accretion Validation

For the validation of the ice accretion simulation, experimental data from an icing wind tunnel was available [45]. From those experiments, two different conditions, presented in Table 5.4 were selected for validation.

These conditions represent a rime and a glaze ice case with their typical shapes. Rime ice has a more streamlined shape and icing limits further upstream compared to glaze ice, due to instant freezing of all impinging water. The experiments were conducted on a 2D wing section [45]. Ice shapes were traced on three spanwise locations, of which only the middle one is shown in Figure 5.7 for reasons of clarity.

The simulation captures the lower icing limit and the expansion of ice accretion in x-direction correctly in both cases. However, the simulation predicts less ice and further upstream icing limits compared to the experimental results. Further findings, that the simulation predicts a more regular and smooth ice shape could not be confirmed. The general ice shapes of the simulation results within this work, match the experimental results [45]. The under-prediction of upper icing limits could be caused by the wide variety of ice shapes for the experimental results, which is not untypical for icing wind tunnel results, e.g. [105, 147].

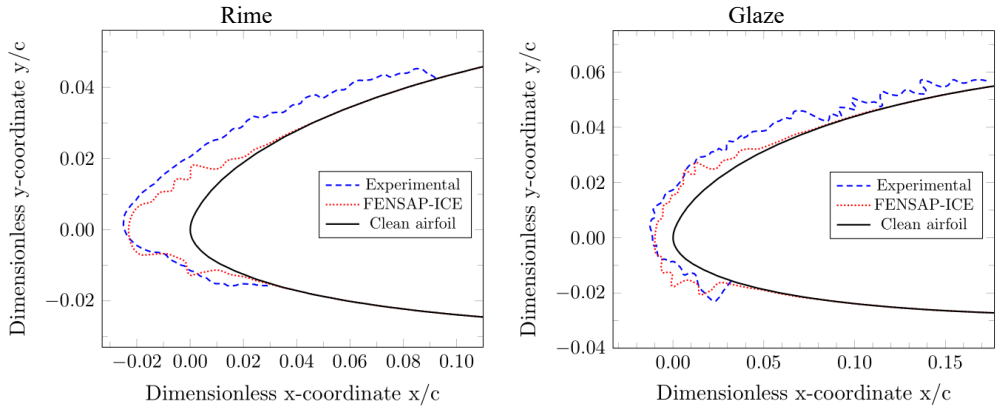

Figure 5.7: Ice shape results vs. experimental results for the a) rime ice and b) glaze ice case for *Re* = 800 000.

Table 5.4: Icing conditions for the validation of ice accretion.

Parameter	**Icing case**	
	Rime	Glaze
Free stream velocity u_∞	25 m/s	25 m/s
Reynolds number *Re*	9.0×10^5	8.5×10^5
Chord length *c*	0.45 m	0.45 m
Icing time t_{icing}	1200 s	1200 s
Angle of attack α	0°	0°
Icing temperature T_{icing}	−15 °C	−2 °C
Median volume diameter MVD	20 µm	30 µm
Liquid water content LWC	0.51 g/m³	0.51 g/m³

Considering the generally good agreement and the wide variation of experimental results, the prediction of ice shapes is within a reasonable range of the experimental results.

5.5 Results

5.5.1 Ice Accretion Results

Figure 5.8 shows the simulated ice shape results for all icing cases, specified in Table 5.2 and Table 5.3. For reasons of readability, the MVD will be mentioned without unit at some points.

The results show that both liquid water content and droplet diameter have a significant influence on the ice shape. As previously shown in Fig. 5, droplets with small MVDs around 15 µm can contain a higher range of liquid water content, compared to large MVDs. Therefore, the results at a temperature of −2 °C and droplet diameters 15, 20 and 30 show a distinct glaze ice shape with a rough surface. At a droplet diameter of 40 µm, the maximum liquid water content has decreased to a point, where all results show a streamline shaped ice geometry, independently from the prevailing temperatures. All results at the diameter of 40 µm are close to the un-iced airfoil geometry. The extent only differs slightly, following the liquid water content at different temperatures.

MVD 15, 20 and 30 share the same behavior with decreasing extent of the ice shape for decreasing temperatures from −5 °C to −30 °C. The change from −2 °C to −5 °C however, shows a different result for these three MVDs. The extent in the x-direction is significantly increasing, while the extent in y-direction shrinks. Regarding the general geometry, this behavior marks the transition from a glaze ice to a more streamlined rime ice structure.

In terms of accumulated ice, Figure 5.9 shows that the highest ice masses occur at an MVD of 20 µm and the lowest at an MVD of 40 µm. Since all simulations are 2D airfoil simulations, the resulting ice masses are considered as mass per wingspan extent. The results show a differentiated influence of droplet MVD and liquid water content on the overall ice mass. Increasing the droplet size from 15 to 20 results in a higher ice mass, whereas the increase from MVD 20 to 40 results in lower ice mass, although the liquid water content decreases consistently. Comparing MVD 15 with 30, the results of MVD 30 µm show higher ice masses for temperatures −2 °C and −5 °C and lower ice masses

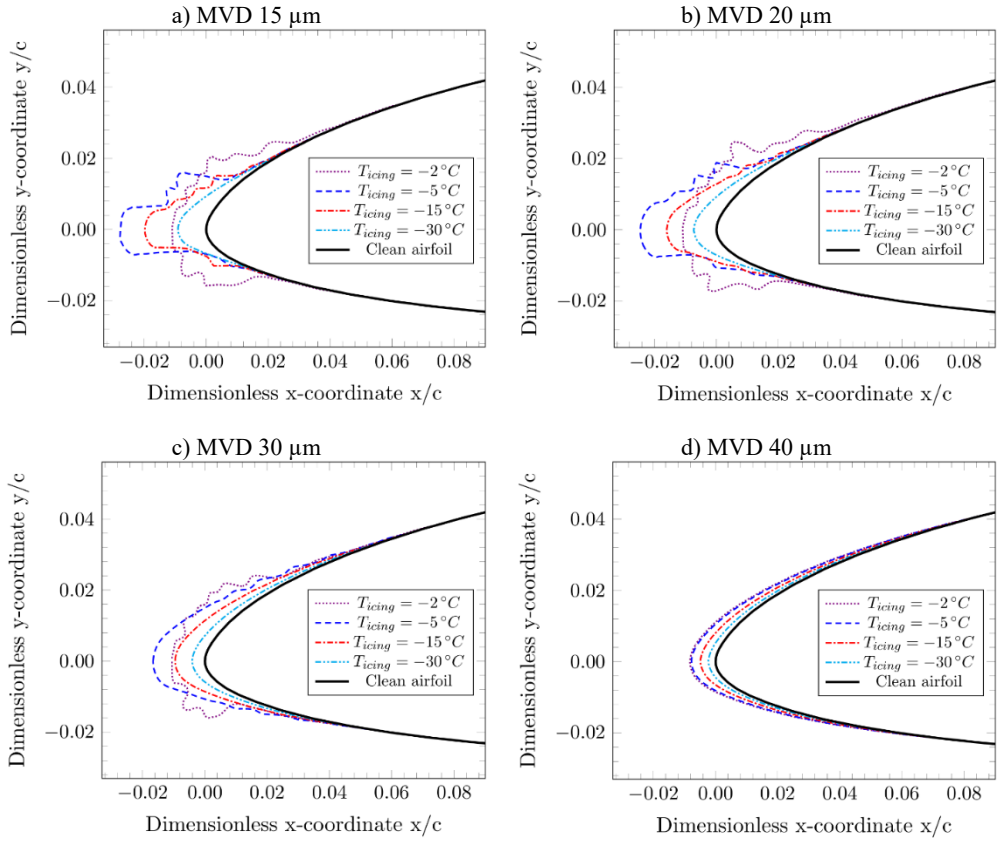

Figure 5.8: Ice shape results for droplet sizes a) 15 µm, b) 20 µm, c) 30 µm and d) 40 µm at *Re* = 800 000.

for the temperatures −15 °C and −30 °C. This indicates that the shift from increasing droplet size to decreasing liquid water content being the dominating factor on the ice mass occurs at different droplet sizes, depending on the temperature.

All ice shapes, with one exception, show a shift of icing limits towards the leading-edge with decreasing temperatures. While all impinging water freezes instantly at low temperatures, the impinging water at temperatures close to 0 °C only freezes partially, leaving a liquid water film that runs downstream on the surface before freezing completely. This extends the icing limits to positions further away from the leading-edge. Solely the icing limit on the lower surface of the airfoil at an MVD of 30 µm and a temperature change from −2 °C to −5 °C shows a shift of the limit toward the trailing-

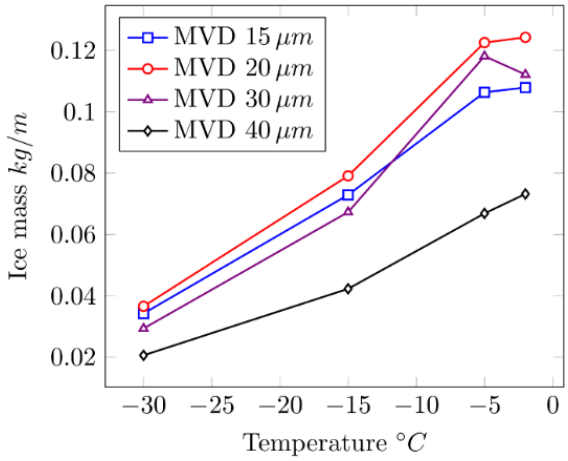

Figure 5.9: Accumulated ice mass per wingspan extent.

edge. Finally, in all cases, except for one, larger droplets lead to further downstream icing limits.

5.5.2 Performance Degradation Results

Based on the acquired ice shapes that were presented in the previous section, FENSAP simulations were run to determine the performance of the iced airfoils. Figure 5.10 and Figure 5.11 present the lift and drag coefficient of the iced airfoils in comparison to the clean airfoil. In general, the simulation predicts decreased lift and increased drag for all icing cases and the entire range of AOAs. The curves show a strong correlation between the aerodynamic performance and the iced airfoil shape. For streamline shaped ice (e.g. ice shapes at an MVD of 40 µm), the simulation predicts a smaller decrease of lift and increase of drag, compared to icing cases with rough surfaces and a larger ice shape extension in the y-direction (e.g. MVD 15 µm and −2 °C icing temperature). Additionally, rime ice cases with more streamline shaped ice seem to have less effect on the maximum lift angle.

The maximum deterioration of lift, corresponding AOA, and increase of drag occurs at −2 °C/MVD 20. In this icing case, the lift coefficient decreases by 35 % and the AOA by 33 %, compared to the clean airfoil. Drag increases by 160 %. At the AOAs of 0° and 6° the lift coefficient decreases by 6.5 % and 12.5 % and the drag increases by 80.0 % and 90.5 % respectively.

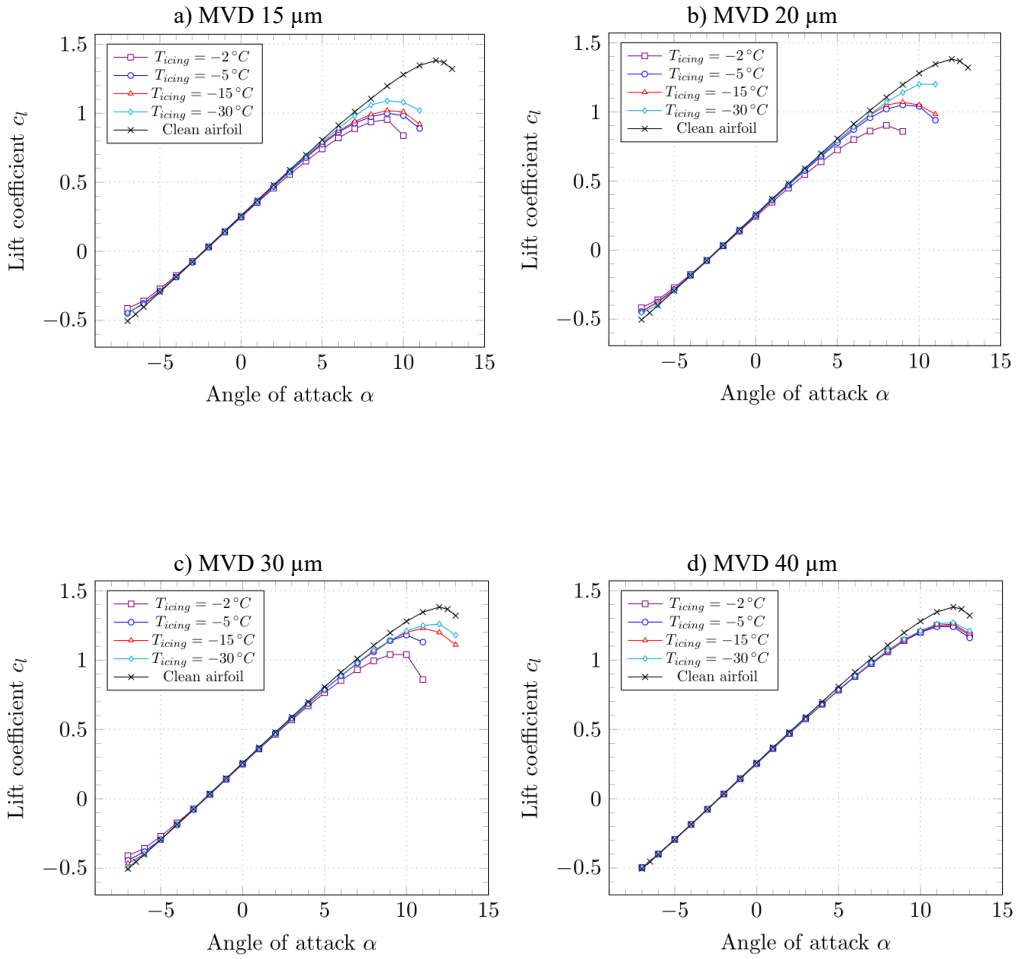

Figure 5.10: Lift of the iced airfoils for MVDs a) 15 µm, b) 20 µm, c) 30 µm and d) 40 µm at *Re* = 800 000.

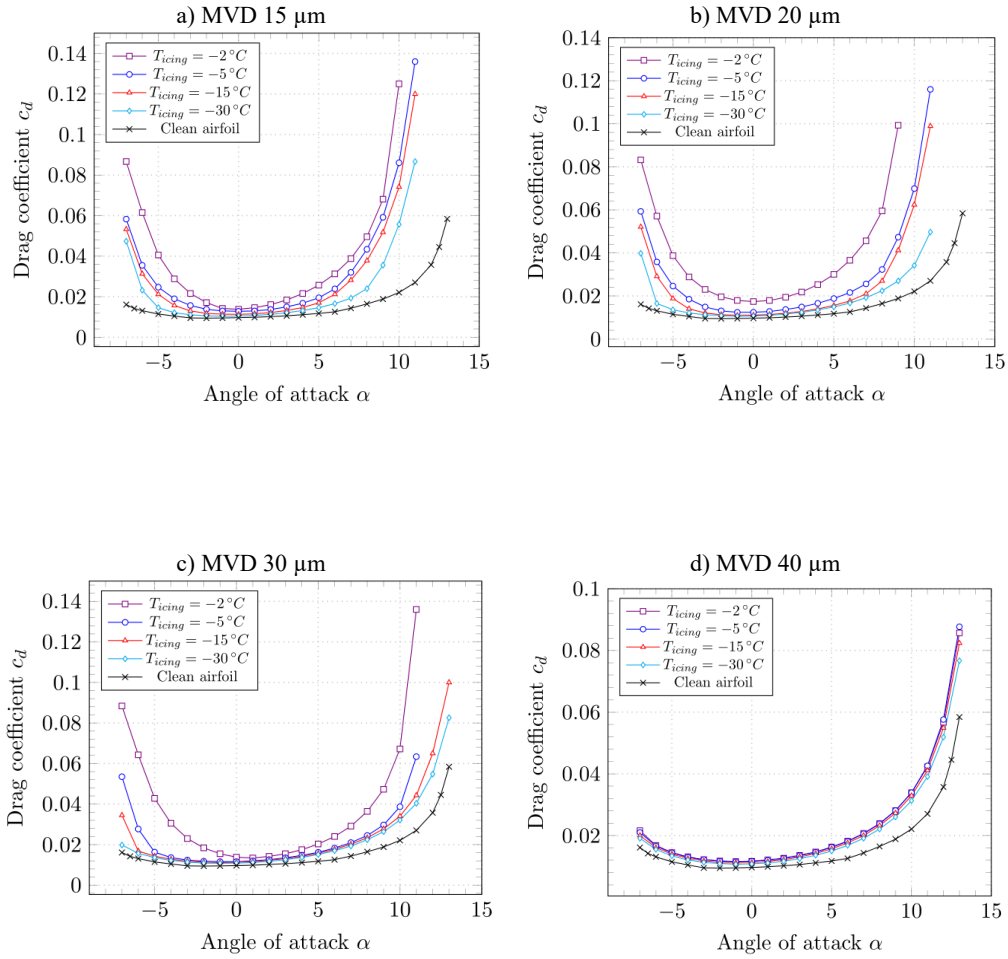

Figure 5.11: Drag of the iced airfoils for MVDs a) 15 µm, b) 20 µm, c) 30 µm and d) 40 µm at *Re* = 800 000.

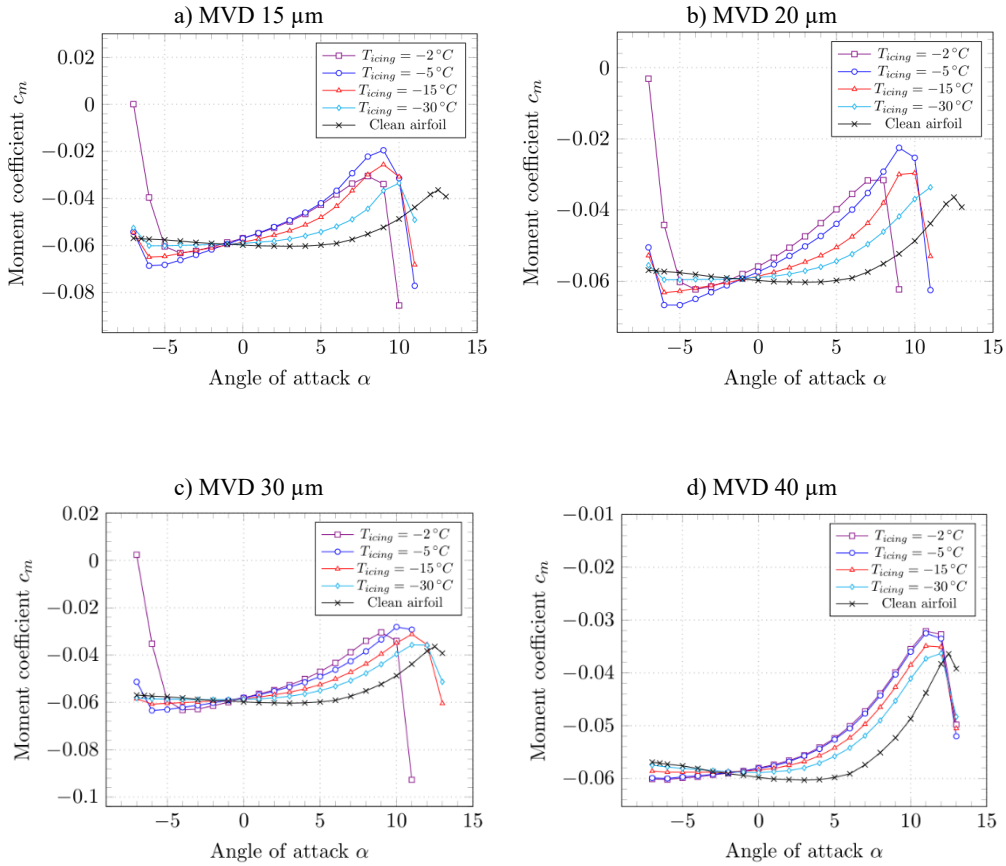

Figure 5.12: Moment of the iced airfoils for MVDs a) 15 µm, b) 20 µm, c) 30 µm and d) 40 µm at *Re* = 800 000.

The airfoil moment curves in Figure 5.12 show increased moment gradients for all icing cases. As for lift and drag, higher temperatures in combination with high LWC values show greater influence on the moment, compared to lower temperatures and low LWC values.

To visualize the different influences on the aerodynamic performance for all icing cases, an index for the lift, drag, stall AOA, and the moment shall be introduced at this point. Three discrete points are representing the iced airfoil performance for lift and drag in comparison to the clean airfoil:

- **AOA 0°:** Smallest changes in drag compared to the clean airfoil and minor changes in lift.
- **AOA 6°:** Limit of the quasi-static range of moment.
- **Stall angle:** Maximum spread between iced and clean airfoil.

For the moment index, two different discrete points are chosen:

- **AOA 0°:** Small changes in moment compared to the clean airfoil.
- **AOA 4°:** Limit of the linear AOA range of the clean airfoil – maximum spread to the clean airfoil.

The severity index I is calculated with the following equations:

$$I_{\text{lift}} = \frac{1}{3}\left[\frac{\Delta c_{\text{l,stall}}}{\Delta c_{\text{l,stall,max}}} + \frac{\Delta c_{\text{l},\alpha 0}}{\Delta c_{\text{l},\alpha 0,\text{max}}} + \frac{\Delta c_{\text{l},\alpha 6}}{\Delta c_{\text{l},\alpha 6,\text{max}}}\right]$$

$$I_{\text{drag}} = \frac{1}{3}\left[\frac{\Delta c_{\text{d,stall}}}{\Delta c_{d,\text{stall,max}}} + \frac{\Delta c_{\text{d},\alpha 0}}{\Delta c_{d,\alpha 0,\text{max}}} + \frac{\Delta c_{\text{d},\alpha 6}}{\Delta c_{d,\alpha 6,\text{max}}}\right]$$

$$I_{\text{moment}} = \frac{1}{2}\left[\frac{\Delta c_{\text{m},\alpha 0}}{c_{\text{m},\alpha 0,\text{max}}} + \frac{\Delta c_{m,\alpha 4}}{c_{\text{m},\alpha 4,\text{max}}}\right]$$

$$I_{\text{stall}} = \frac{\Delta \alpha_{\text{stall}}}{\Delta \alpha_{\text{stall,max}}}$$

All maximum values (denominators) represent the difference between the clean airfoil value and the worst-case performance within all icing cases for certain AOAs. The numerator values are the difference between the clean airfoil performance and the respective value of the current icing case. As a result, the fractions and the overall index can result in values $0 \leq I \leq 1$. An index value of 1 represents the maximum deterioration of lift whereas a value of 0 would indicate no difference to the clean airfoil performance.

The drag, stall AOA, and moment index values are calculated the same way, as described for the lift. The only difference for the stall AOA index is that the calculation consists of one instead of three fractions that describes the ratio between current stall angle reduction and worst-case stall angle reduction.

Figure 5.13 shows the index for each icing case as a color value. The areas between the discrete points that were investigated by simulation are determined by linear interpolation. The results for the lift and drag coefficient clearly show that the worst

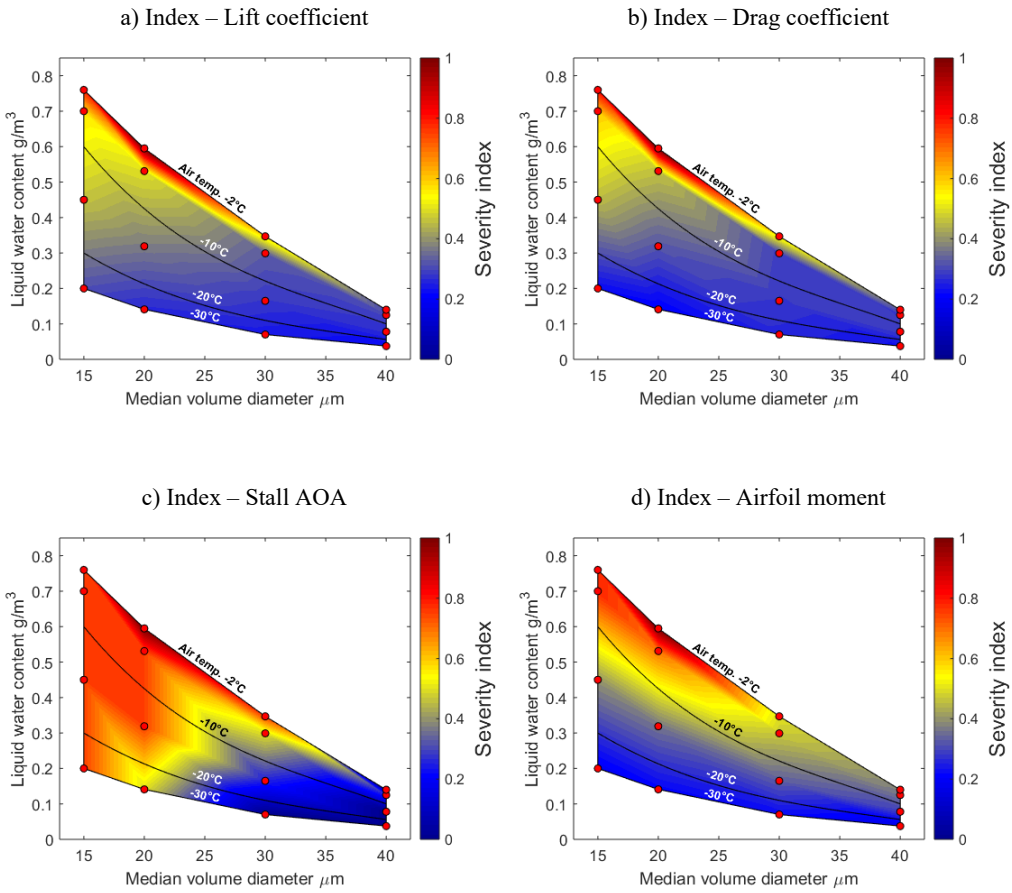

Figure 5.13: Lift (a), drag (b), stall AOA (c), and moment change (d) with index visualization.

performance degradations can be found at temperatures close to 0 °C and high liquid water contents. Further, the influence of liquid water content at different droplet sizes can be noticed. At small droplet MVDs the LWC has a larger impact on performance degradation. At larger droplet sizes, different LWCs show less impact on the performance. This can be explained with the decreasing LWC for bigger droplet MVDs. For example, at −30 °C/MVD 15 the LWC only differs slightly to the one at −2 °C/MVD 40. Also, the performance loss at both these points is almost similar. This behavior arises the impression that the droplet size has almost no impact on performance degradation at low LWCs. For high temperatures, however, different droplet sizes show a more significant influence.

The index visualization for the moment shows a distribution closely related to the one for lift and drag. The most severe icing conditions that result in the highest lift reduction and highest drag increase also show the largest increase of the moment.

Besides changes in lift and drag and moment, Figure 5.13c visualizes the change of maximum lift angles. Small droplet MVDs in combination with high LWCs lead to the smallest maximum lift angles, whereas large MVDs and low LWCs show no to minimal influence on the stall AOA. This gives a good insight on the general influence of different weather conditions on the maximum lift angle.

5.6 Discussion

Regarding the influence of the different weather parameters, larger LWC values generally showed a greater impact on the lift, drag, and moment, whereas, for droplet sizes, the greatest impact on performance were identified at an MVD of 20 µm. However, the influence of only droplet size could not be determined, since the comparison of different droplet sizes at identical icing temperatures always includes different amounts of LWC (for the icing conditions identified by CFR 14, Part 25, Appendix C). For the investigation of droplet size influence only, further simulations, with constant LWC and constant icing temperature at different MVDs would be necessary.

In terms of maximum lift angle, the results clearly show that glaze ice horns have a greater effect on the stall angle compared to more streamline shaped rime ice cases. However, the setup of simulations with 1° AOA steps and a maximum stall angle of 12° for the clean airfoil, restricts the resolution of stall angle degradation to a minimum of 8.5 %. and therefore, limits the validity of the results. Additional simulations with smaller AOA steps, would increase the accuracy of the maximum lift angle prediction and give more detailed information on the influence of the different icing conditions on the stall angle. Depending on the flight envelope of the aircraft, further investigation, including the stall at negative AOAs could be of interest.

The results on the moment have revealed that all icing cases reduce the nose down moment of the airfoil. Since the overall aircraft's moment gradient must be $dc_m/d\alpha < 0$ for longitudinal static stability, all icing cases reduce this stability at first sight. However, further aircraft parameters such as the general aircraft configuration and icing of the horizontal stabilizer or even the elevator must be considered, to identify possible dangers

on the aircraft's overall longitudinal stability. Therefore, apart from a reduced airfoil nose-down moment compared to the clean airfoil, no statement about absolute aircraft stability can be made.

In terms of numerical methods, the validation of the iced airfoil performance in Fig. 6 showed that for severe ice shapes, the simulation setup with the SA model predicts earlier onset of stall and therefore a higher performance degradation, compared to the experimental results. Different numerical methods, e.g. higher-level turbulence models might be more suitable in such cases. Additionally, the assumption that the airflow around iced airfoils is fully turbulent has not been verified and could be false. A partial laminar flow around iced airfoils, would not only affect the aerodynamic performance. As mentioned by Hann in [47], the turbulent flow may also increase the evaporation rate and lead to earlier disappearance of water layers compared to laminar conditions. This points out the importance to investigate flow transition at iced airfoils further, not only to gain a better understanding of the impact on aerodynamic performance but also to successfully define energy requirements for an IPS. Therefore, more wind tunnel tests would be required to validate the simulation results of the iced airfoils at the specific Reynolds number and to investigate flow transition on iced airfoils.

Also, the monodisperse distribution of droplet sizes for the ice accretion simulations is not likely to be found in reality. The Advisory Circular No 20-73A from the FAA suggests using a Langmuir-D distribution for droplet sizes up to 50 µm, for the icing certification of manned aircraft [66]. Since FENSAP-ICE already provides the Langmuir-D distribution within DROP3D, further simulations, using the FAA's suggested distribution, could give insight on the effect of differently distributed droplet sizes.

The general results are also limited by the number of simulations and the choice of meteorological conditions. This study gives a good overview of which temperature and droplet regimes the worst-case conditions are to be expected. However, a more detailed investigation is required to identify the absolute worst cases. Future work should, therefore, focus on the areas where large gradients occur, i.e. for T=[−2…−5°C] and MVD<30µm.

Overall, investigating the influence of different meteorological conditions on the aerodynamic performance including the identification of a worst-case condition at −2 °C/MVD 20 provides essential information for the development of an efficient IPS.

The prevailing meteorological conditions that lead to the greatest performance degradation can be used for further simulations and wind tunnel tests to determine the maximum required heat flux of the IPS. The knowledge about the influence of different icing conditions on the aerodynamic performance can be used for the adaptation of flight controllers and control systems of IPSs. Based on the results for lift, drag, moment, and AOA, flight controllers could adapt the flight envelope according to the present icing conditions to maximize the aircraft's aerodynamic efficiency.

In terms of adapting IPS control systems, the results provide useful information to maximize energy efficiency for example of a promising concept for an electrothermal IPS with fully autonomous icing detection for UAVs, presented in [29] and [48]. The icing detection system operates intermittently to detect possible ice accretion. With the additional information on the influence of different icing conditions, the ice detection frequency could be reduced in less critical conditions to save electrical energy.

Finally, the identification of the worst-case icing condition is an essential finding, as earlier studies showed that the ambient temperature is a major factor for the power requirements of evaporative or running wet anti-icing systems [47]. With the worst-case icing condition at −2 °C/MVD 20 this study offers new information on the problem of how to operate an IPS.

5.7 Summary

In this study 16 different meteorological icing conditions were investigated, using FENSAP-ICE simulation tool. Two different simulation models for the accretion of ice and the evaluation of aerodynamic performance were set up. The ice accretion model was validated with experimental data on a RG-15 airfoil from an icing wind tunnel. The ice accretion model showed good capability of capturing the shape and extent of ice, depending on the prevailing weather conditions. The results showed that the greatest ice masses occur at an MVD of 20 µm, compared by temperature.

Clean airfoil performance was validated with literature data on the RG-15. Iced airfoil performance was validated with literature data on an iced NREL S826 airfoil. The performance simulations showed that all icing conditions affect aerodynamic performance negatively. Generally, high liquid water contents and temperatures close to 0 °C showed the greatest influence on the performance. Additionally, within all 16

different icing conditions, the worst-case condition for lift, drag, and stall angle was identified at an icing temperature of −2 °C and a droplet MVD of 20 µm.

In summary, the results were well suitable for comparison with each other, gave a good insight on the influence of different meteorological icing conditions on the aerodynamic performance penalties and provide essential design information for the development of an IPS for UAVs.

Future work should aim to perform more simulations in the Appendix C icing envelopes (continuous maximum and intermittent maximum) and Appendix O (supercooled large droplets) to get a more detailed overview of the worst-case scenarios. The investigation of the performance degradation with higher order CFD models (e.g. LES, DNS) may offer better results than RANS simulations. Last but not least, more validation with experimental results is required.

6 Influence of Airspeed and Chord Length on Performance Penalties

6.1 Introduction

Unmanned aerial vehicles (UAVs) face several special challenges when it comes to atmospheric icing [42]. The operations of fixed-wing UAVs can be substantially limited by in-flight icing [9]. Such atmospheric icing can occur in many regions around the world and is a severe risk for all types of airborne vehicles [64]. While the icing topic is well researched for manned aviation, few results are available for UAVs.

In general, icing leads to significant aerodynamic penalties [57]. Ice accretions on airfoils reduce lift, increase drag, and worsen stall behavior. This can have severe consequences on the overall aerodynamic performance of a UAV, which can even lead to the loss of the aircraft [42]. It is therefore important to have a good understanding of the most hazardous meteorological and flight scenarios for UAVs and how these may differ from manned aircraft.

A previous numerical study by Szilder and McIlwan [19] studied the effect of the Reynolds number on the ice accretion process [19]. The study used a morphogenetic icing approach to simulate ice accretion over a range of Reynolds numbers from Re=5×10^4…5×10^6 on a NACA0012 airfoil in 2D. Szilder and McIlwan coupled chord length c and velocity v with a proportionality factor to investigate the Reynolds number as a single parameter in their study. They simulated ice accretion over a range of meteorological icing conditions of air temperature, LWC, and droplet sizes. Szilder and McIlwans results show that the Reynolds number has an impact on the type of ice (rime or glaze), on the total ice mass, and on the relative ice thickness. Lower Reynolds numbers lead to more rime-like ice shapes, less total ice mass, and increased relative ice thickness. Szilder and McIlwan suggested that the latter could lead to increased aerodynamic penalties, which has been shown for icing on manned aircraft at higher Reynolds numbers before [57].

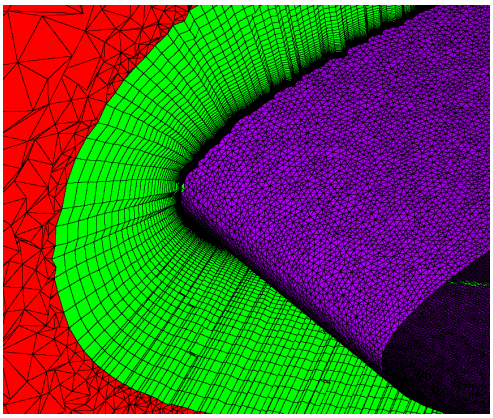

Figure 6.1: Hybrid ice accretion mesh.

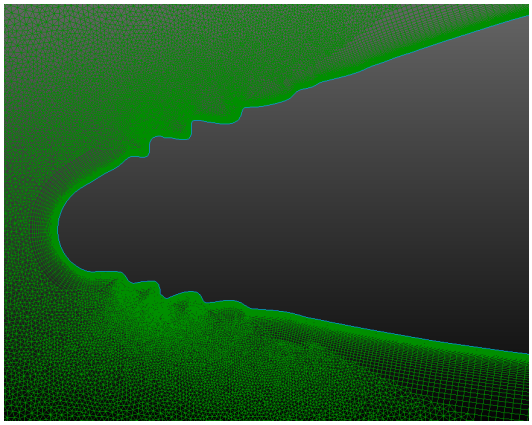

Figure 6.2: Performance calculation mesh with T-Rex.

The objective of this paper is to extend the existing research on the effect of Reynolds number on ice accretion on UAVs to its effect on aerodynamic performance penalties. In contrast to Szilder and McIlwan, we decided to investigate the effects of airspeed and chord length independently from each other. We believe that this offered more differentiated insights into the icing mechanisms. We considered three different meteorological icing conditions for each variation of airspeed and chord length.

This study was closely related to previous work conducted at NTNU on similar topics, such as the comparison of two numerical codes for icing penalties [53], the effect of meteorological conditions on performance [46], experimental ice accretion results [45], and experimental icing performance degradation studies [43]. Further relevant work on icing performance degradation on UAV airfoils has been conducted by Williams et al. [15] and Szilder and Yuan [18] – none of which take the effect of varying airspeeds or chord lengths into closer account.

The main objective of this work is to increase the overall understanding of which icing conditions are most hazardous for UAVs. This knowledge is an important input for example for UAV path-planning applications [41] or for the design of ice protection systems [48].

6.2 Methods

This study used the numerical icing code ANSYS FENSAP-ICE (version 2020 R1) to simulate ice accretion and aerodynamic performance penalties on lift, drag, and stall. FENSAP-ICE is a state-of-the-art computational fluid dynamic (CFD) icing tool [130]. The tool has been mainly developed for icing on manned aircraft but is applied to a wide field of applications, including UAVs [21, 87]. In this study, FENSAP-ICE was used to generate ice shapes on an airfoil and to simulate the aerodynamic icing penalties on lift and drag over a range of angles of attack. All simulations were conducted as fully-turbulent, steady-state, 2D simulations with streamline upwind artificial viscosity. Turbulence is modeled with the one-equation Spalart-Allmaras model [148], which is recommended for icing simulations [149].

The computational meshes for the icing simulation were generated with Fluent whereas the meshes for the lift and drag simulations were generated in Pointwise (version 18.2R2). Both types of meshes were a hybrid O-grid with a far-field diameter of 40·c. The boundary-layer was resolved with a regular structured grid for icing and a structured anisotropic tetrahedral extrusion (T-Rex) for the performance grid [129]. Both meshes use a growth factor of 1.1. An example of the icing grid is given in Figure 6.1 and an example for the performance grid in Figure 6.2.

Icing simulations were carried out as FENSAP-ICE multi-shot runs with automatic Fluent remeshing [150]. Each ice accretion run was simulated with 10 shots, monodisperse droplet distribution, and a constant ice density of ρ_{ice}=917kg/m³. The first shot was set to a shorter duration in order to capture the initial roughness build-up on the airfoil. Table 6.1 shows the duration of the shots for each simulation case.

Table 6.1: Flight conditions for the variation of chord length and airspeed and icing durations.

Velocity [m/s]	Chord [m]	Reynolds number	Icing duration [min]	1st shot duration [s]	2nd–10th shot duration [s]
12.5	0.45	0.5×10^6	43.0	60.0	280.0
25.0	0.45	0.9×10^6	21.5	30.0	140.0
50.0	0.45	1.8×10^6	10.8	15.0	70.0
100.0	0.45	3.6×10^6	5.4	7.5	35.0
25.0	0.11	0.2×10^6	21.5	30.0	140.0
25.0	0.23	0.5×10^6	21.5	30.0	140.0
25.0	0.90	1.8×10^6	21.5	30.0	140.0

The base geometry in this study was the RG-15 airfoil, which is a widely used design for UAVs and model airplanes. The airfoil has been used for numerical and experimental studies on UAV icing before [45, 46]. To investigate the effect of the chord length on ice accretion and performance penalties, the simulations were carried out on four chord lengths c=[0.11, 0.23, 0.45, 0.90 m], each at a velocity of v=25m/s. In order to assess the influence of the airspeed, four velocities v=[12.5, 25.0, 50.0, 100.0 m/s] were simulated on a chord of c=0.45m. Table 6.1 gives an overview of all the cases.

Three meteorological icing conditions were investigated for each of the flight configurations in Table 6.2. The basis for choosing meteorological icing conditions is the continuous maximum icing envelope in CFR 14, Part 25, Appendix C [73]. Icing conditions are chosen to represent the three main icing morphologies: rime, mixed, and glaze ice [65], and are shown in Table 6.2. Icing durations are calculated based on a horizontal extent of the stratiform icing cloud of 17.4nmi/32.2km [73]. The performance calculations of lift and drag were all conducted at the same Reynolds number Re=1×10^6 for easier comparison of the results.

6.3 Validation

The accuracy and validity of simulation results is a key challenge for all studies that are based on numerical methods. Substantial validation work has been performed in previous work at NTNU. In particular, work has been conducted on investigating the grid dependency, the number of required shots for ice accretion, and the capability of FENSAP-ICE to predict aerodynamic penalties [43, 45, 144]. This study followed the findings and experiences from these results and added a comparison of ice accretion simulations with FENSAP-ICE. For this, experimental ice shapes were obtained during icing wind tunnel tests at the Technical Research Centre of Finland (VTT) during fall 2019 [136]. Two icing conditions were chosen to represent different ice accretion

Table 6.2: Overview of the meteorological icing conditions.

Variable	Glaze	Mixed	Rime
Temperature	−2 °C	−4 °C	−15 °C
MVD	20 µm	20 µm	20 µm
LWC	0.59 g/m³	0.55 g/m³	0.32 g/m³
AOA	0°	0°	0°

regimes. For each case, manual ice tracings were taken from each icing run at three different spanwise locations [45]. The numerical simulations were conducted with the same parameters as stated in the method section. The results are shown in Figure 6.3. For mixed ice, the overall geometry of the ice seemed well-captured. However, the simulated ice shapes exhibited lower ice limits, lower ice thickness, and lower ice area. The same differences also occurred for glaze ice, but in addition, there were horn features on the experimental ice shapes that were missing on the simulated ice accretion.

A detailed investigation of the potential reasons for the differences went beyond the scope and objective of this study. The most likely error sources included the assumption of constant ice density and a monodisperse droplet distribution for the simulations, as well as measurement uncertainties in the icing wind tunnel.

Although there were differences between the simulated and the experimental ice shapes, the differences were in line with the general capability of numerical icing codes, both on manned and unmanned aircraft (e.g. [19, 89, 151]). Therefore, the validation results gave confidence that the ice accretion physics were captured with sufficient accuracy to serve the purpose of this paper – which was to show general trends for variations of airspeed and chord length on ice accretion and icing performance.

6.4 Results

6.4.1 Ice Accretion

The resulting ice shapes for all the cases are shown in Figure 6.4. The airspeed had the lowest impact on the **rime ice** shapes. An increase in airspeed led to slightly increased relative ice thickness (i.e. maximum ice extent in relation to the chord length) and to a larger droplet impingement area. The ice geometry was a typical streamlined rime ice shape and the geometries were similar to each other at all airspeeds. The reason for these small differences was related to the low air temperatures – the ice accretion mechanism was governed by instant freezing of the incoming droplets. The increase in ice limits was directly related to the increase in impingement limits, which resulted from higher droplet inertias and thus higher collection efficiencies. This also led to an increase in relative ice thickness.

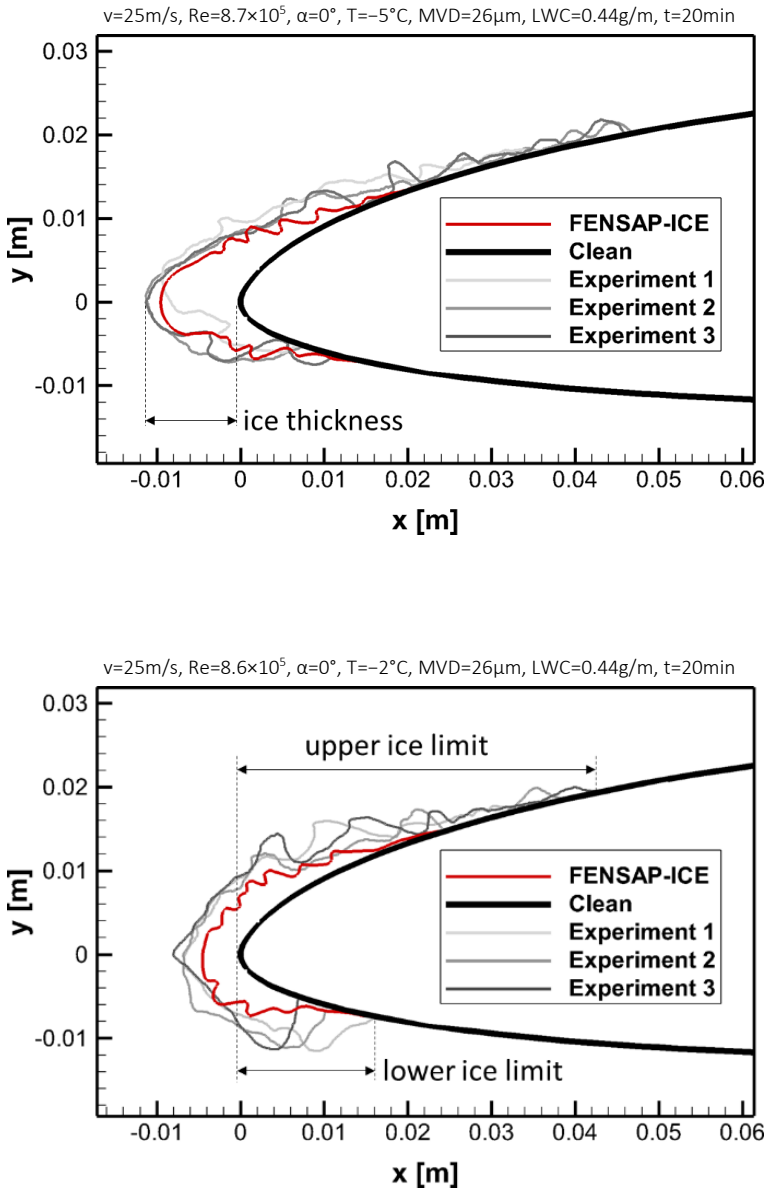

Figure 6.3: Comparison of FENSAP-ICE simulations with icing wind tunnel tests for ice accretions of mixed (top) and glaze (bottom).

The airspeed had a larger impact on the **mixed ice** shapes. The ice geometry at the lowest airspeed was almost identical in shape to rime ice. This was related to the lower aerodynamic heating term, leading to a substantial increase in the freezing fraction. For higher airspeeds the aerodynamic heating increased, thereby decreasing the freezing fraction. Consequently, the mixed ice shapes became more convoluted and glaze-like. For v=25m/s the ice horn exhibited a distinct V-shape and large ice thickness. For higher airspeeds, the ice thickness decreased, and ice limits increased significantly. This was related to the higher aerodynamic heating, lower freezing fractions, and consequently higher runback water amounts. This led to higher ice limits and a reduction in ice thickness. For all airspeeds, except the lowest, the mixed ice shapes developed distinct horn structures. The size of these increased with higher airspeeds.

The airspeed had a significant influence on the **glaze ice** cases. At the lowest velocity, relatively high levels of instantaneous freezing occurred, which resulted in a streamlined ice shape. The similarity to rime was less compared to the low-speed mixed ice case. At higher velocities, the freezing fraction decreased substantially due to an increase in aerodynamic heating. This resulted in more complex ice shapes and significantly increased icing limits. For the highest velocity, the aerodynamic heating became so dominant, that the surface temperatures rose above the freezing point and no icing occurred on the airfoil. Instead, the surface was covered with a water layer over its entire length.

The absolute ice mass for each simulation case is shown in Figure 6.5. For the airspeed variation, it shows that an increase in airspeed led to higher total ice accumulation. This was related to the higher droplet inertias and higher collection efficiencies. When aerodynamic heating exceeded a threshold value, the heating became so high that no ice formation would be possible. This only occurred for the glaze ice at the highest velocity. The reason why the rime ice masses are lower compared to the other cases, is related to the substantially lower LWC at lower temperatures, see Table 6.2.

The influence of the **chord length** of the airfoil was much more consistent between the three meteorological cases in Figure 6.4. The following effects were observed in all cases consistently. First, the relative ice thickness increased significantly for the smaller airfoils. Second, the relative ice limits increased significantly as well. Third, the ice shape geometry was not significantly affected by changes in chord length. This indicated that the ice accretion regime was not affected by the chord length.

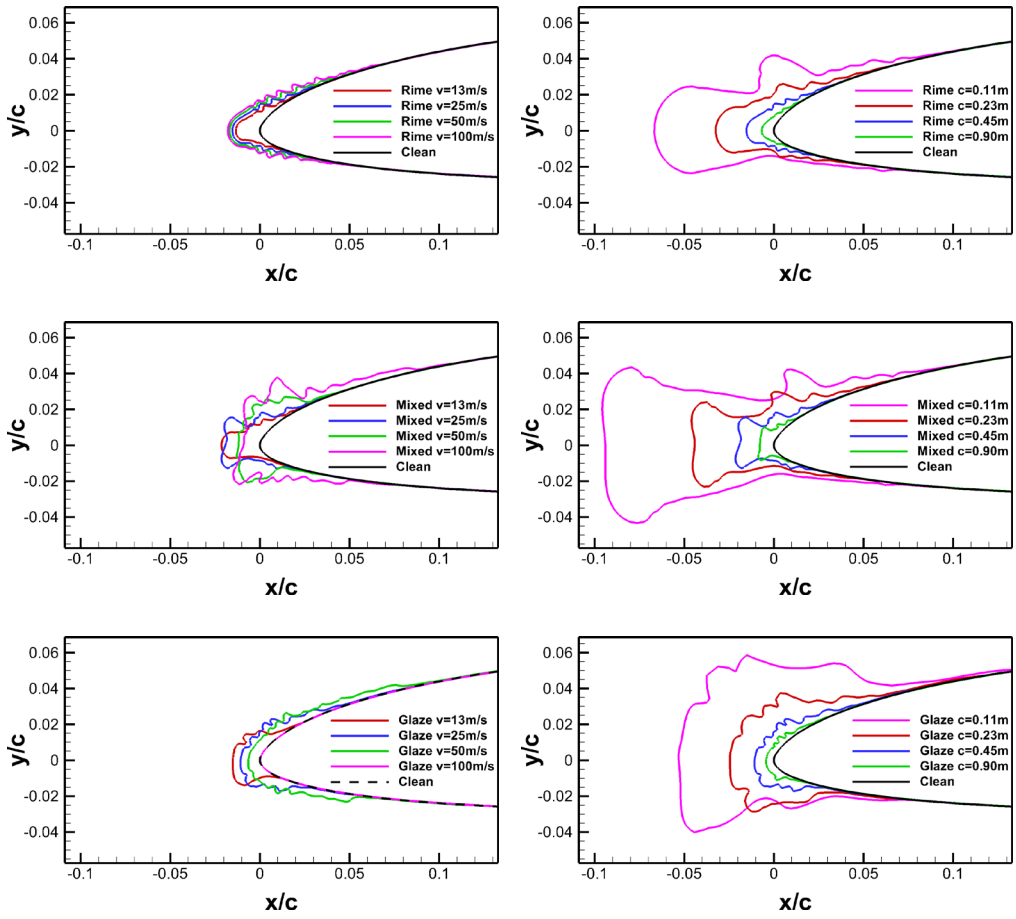

Figure 6.4: Ice shapes for the three meteorological icing conditions rime (top), glaze (middle), and mixed (bottom) for the variation of airspeed (left) and chord length (right).

This qualitative assessment was confirmed in Figure 6.5, showing that the absolute mass of ice was decreasing with smaller chord lengths. This means that while the relative ice thicknesses and the relative ice coverages on the smaller airfoils increased, the absolute ice masses decreased. Due to the lower size of the airfoil, the aerodynamic deflection forces are reduced, which results in a higher droplet collision efficiency. Thus, the relative ice thickness, droplet impingement area, and ice limits increased. Since the surface area for droplet impingement was smaller (due to the smaller airfoil geometry) a lower absolute number of droplets collide with the airfoil. This resulted in the lower absolute ice masses.

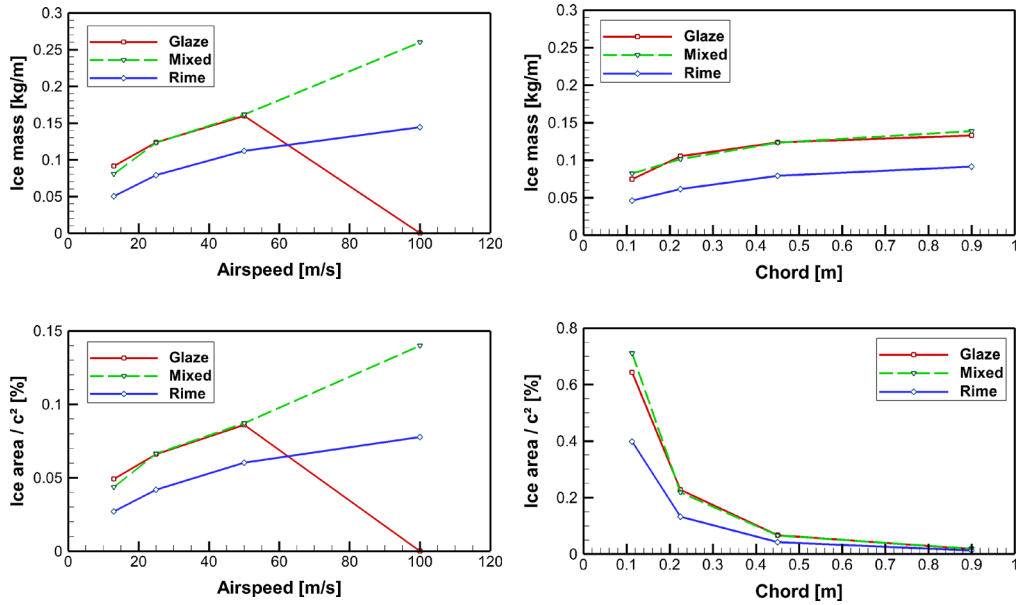

Figure 6.5: Total ice mass (top) and relative ice area with regards to the chord *c* (bottom) for the variation of airspeed (left) and chord length (right).

6.4.2 Performance Penalties

First, the comparison was made between the **clean airfoil** with free transition and the three basic icing cases (rime, mixed, and glaze), see Figure 6.6. The results clearly showed the negative impact of the ice accretions. The stall angles were reduced by $\Delta\alpha = -2°$ from clean to iced cases. The maximum lift was reduced by $\Delta c_{l,stall} = -12\ldots30\%$, zero angle lift decreased by $\Delta c_{l,\alpha=0°} = -5\ldots8\%$, and zero angle drag increased by $\Delta c_{d,\alpha=0°} = +110\ldots170\%$ depending on the ice type. Mixed ice showed the highest penalties and rime the lowest. A large part of this drag increase was related to the absence of laminar flow on the iced airfoils.

The impact of airspeed and chord length variation is shown in Figure 6.7. The **airspeed variation** on the rime ice geometries showed two separate effects. In the linear area ($\alpha < 7°$) an increase in airspeed led to higher performance penalties, i.e. lower lift and higher drag. This was related to the increase in ice area and ice thickness. Consequently, the rough and uneven ice surface increased turbulence, leading to higher drag and lower lift. In the stall region, higher airspeeds led to a delay of stall and higher

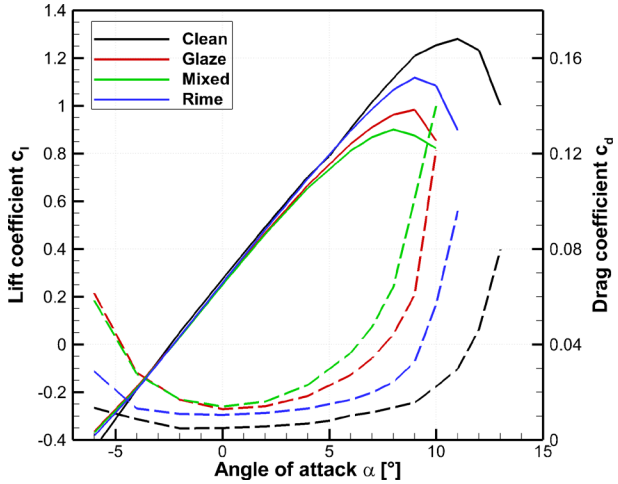

Figure 6.6: Comparison of the clean case with the three meteorological conditions rime, glaze, and mixed at airspeed v=25m/s and chord c=0.45m. Solid lines represent lift and dashed lines drag.

maximum lift values. This was related to the relatively streamlined form of the ice shape. The larger ice thicknesses acted extended the effect chord length and acted the same way as a leading-edge slat (high-lift device). This effect was only possible because the rime ice shapes were relatively streamlined and did not trigger larger flow separation areas.

For mixed ice, the airspeed variation had a different effect. The lowest performance penalties occurred for the lowest airspeed. In this case, that ice geometry was identical to a rime ice shape with streamlined from, resulting in low penalties. As airspeeds increased, the aerodynamic penalties increased as well. The ice shapes at the higher airspeeds all exhibited ice horns that led to large aerodynamic separations at the leading-edge, resulting in substantial performance losses. As the size of the ice horns increased at higher airspeeds, the aerodynamic performance degradation increased as well.

The variation of the airspeed resulted in a significant variation of the glaze ice geometries. These cases were dissimilar to each other with regards to ice mass, ice limits, and relative ice thickness. However, the performance penalties on the glaze ice shapes were very similar to each other. This can likely be explained by the inverse correlation between relative ice thickness and relative ice area. At low airspeeds the relative ice thickness was large, resulting in large separation zones. At higher airspeeds the ice

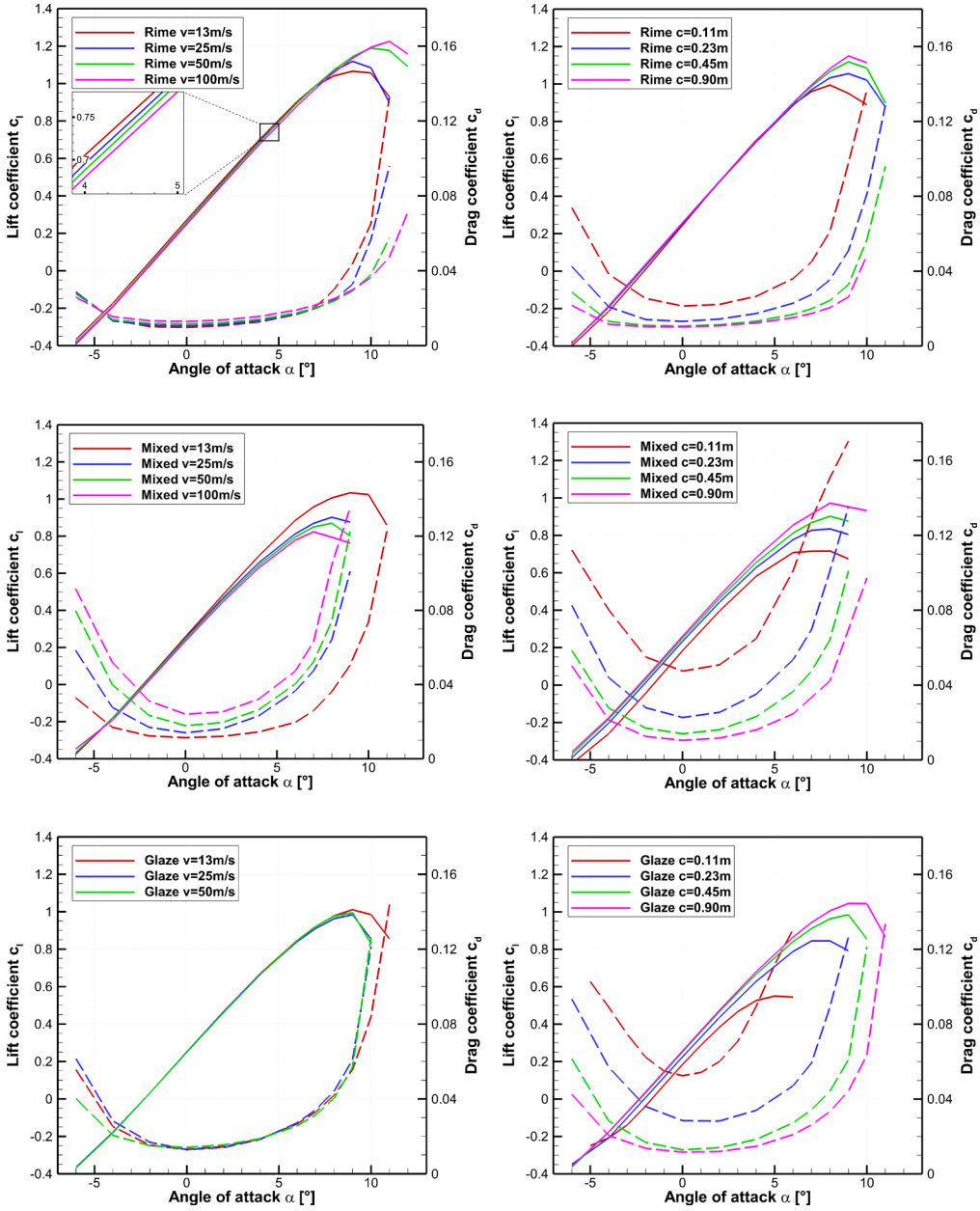

Figure 6.7: Aerodynamic performance for the three meteorological icing conditions rime (top), glaze (middle), and mixed (bottom) for the variation of airspeed (left) and chord length (right). Solid lines represent lift and dashed lines drag.

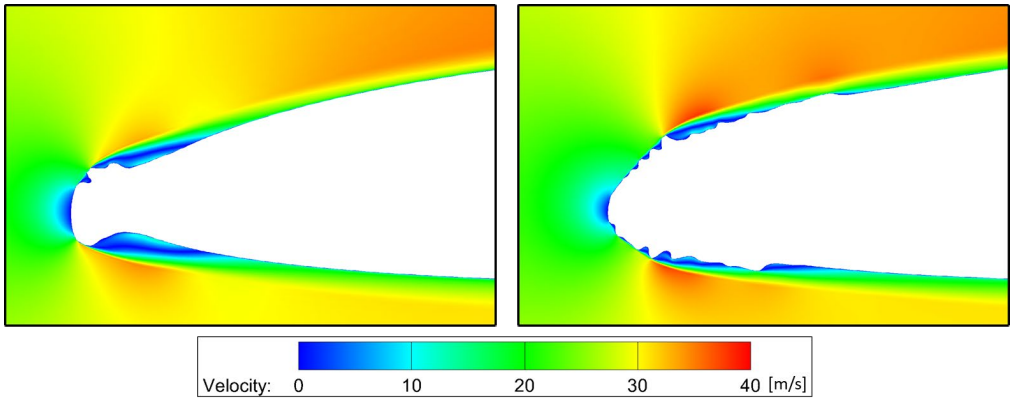

Figure 6.8: Flow separation on the leading-edge on the glaze ice shape at v=25m/s (left) and v=100m/s (right).

thickness was smaller but the ice area was larger. No large ice horns built at larger airspeeds, in contrast to mixed ice. At high airspeeds, the size of the leading-edge separations decreased, while due to the large surface coverage by ice, the roughness effects increased. This can be seen in Figure 6.8, where the ice shape at lower speeds results in a large separation area, whereas in the higher speed case the ice area is larger but results in weaker flow separation. These two effects seemed to be in balance with each other, which resulted in very similar performance penalties in all cases.

The effect of the **chord length variation** on the performance penalties of the rime ice shapes showed a clear trend in Figure 6.7. A decrease in chord length led to larger relative ice thicknesses and larger relative ice area, which resulted in larger aerodynamic performance penalties.

For mixed ice, the same trends occurred. For lower chord lengths, the relative ice thicknesses, ice area, and icing limits increased and led to higher degrees of aerodynamic penalties. The effect was non-linear, and substantially larger penalties occurred for the lowest airfoil size compared to the largest, especially on drag.

The glaze ice cases followed this trend as well. Lower chord lengths led to higher penalties. In particular, the largest overall penalties occurred for the glaze ice on the smallest airfoil. This was related to the large flow separations that occurred on the upper and lower side of the airfoil.

6.5 Discussion

The objective of this of study was to investigate the effect of airspeed and chord size on the ice accretion and aerodynamic performance of a UAV airfoil with numerical simulations. The results revealed several mechanisms. The variation of the airspeed showed two opposite effects, depending on the icing regime. In low-temperature cases (rime ice), an increase in velocity primarily resulted in higher droplet inertias and thus increased droplet collection efficiencies. Consequently, the ice shapes had larger relative ice thicknesses, larger ice areas, and larger ice mass. This led to higher aerodynamic penalties. At the same time, the larger rime ice horns acted as leading-edge slates which delayed stall to slightly higher angles of attack – but still below the values of the clean case.

At temperatures closer to the freezing point – where a substantial part of the incoming droplets would not freeze instantly (mixed & glaze ice) – an increase in airspeed led primarily to an increase in aerodynamic heating. As a result, the instant freezing fraction decreased, generating an increased amount of runback water. Generally, this led to lower ice thicknesses and higher ice limits. For the mixed ice cases, this shift resulted in the formation of very large ice horns and in substantial performance losses. For glaze ice, the ice shapes did not form horns and thus the performance losses did not increase significantly. For glaze, at the highest airspeed, the freezing fraction would decrease to zero as the surface temperature would rise to positive degree values. This prevented any ice formation.

The difference between the two aforementioned mechanisms was clearly showcased with the mixed ice cases. For the lowest airspeed, the ice type was streamlined rime with low performance penalties. For higher airspeeds, horn formation occurred due to the availability of runback water, which consequently led to high performance losses. This indicates that the transition zone between rime and glaze conditions may result in significant icing penalties and should be investigated further.

The variation of the chord length showed the same trend for all icing conditions. For smaller airfoil dimensions, the relative ice thicknesses and the specific ice area increased, whereas the absolute ice mass decreased. In all cases, the lower chord lengths generated larger aerodynamic penalties. However, there were differences in the degree of the changes. For rime ice, the increase in penalties was the smallest and for glaze ice the

largest. This was most likely related to the more complex glaze ice shapes compared to the streamlined rime ice shapes.

These findings were in good agreement with the work of Szilder and McIlwan on the effect of the Reynolds number (with coupled airspeed and chord) on ice accretion physics [19]. Their finding, that the total ice mass decreases at lower Reynolds numbers, has been shown in this study to occur independently for airspeeds and chord length variations. Their finding that the relative ice area increases with lower Reynolds numbers was shown in this study to be primarily driven by the decrease in chord length. Decreasing airspeed also led to lower relative ice areas, but at a much lower rate compared to the effect of the decreasing chord lengths.

The understanding of these mechanisms is highly relevant as they showcase the differences between icing on UAVs and manned aircraft. Most UAVs are typically smaller and fly slower than large passenger aircraft (airliners) and even most aircraft found in general aviation. The results indicate that icing on UAVs can occur at temperatures at which insignificant icing would occur on manned aircraft. Also, changes in airspeed can lead to shifts in the ice accretion regime which can drastically change the ice shape geometries consequently leading to much higher penalties (e.g. going from rime to mixed).

This work also demonstrated that the smaller size of UAVs leads to larger relative ice thicknesses and larger performance penalties. This effectively means that UAVs are significantly more sensitive to icing conditions compared to manned aircraft. Indirectly, this also means that low LWC conditions, which result in low ice accretion rates that may be less significant for manned aircraft, can be more severe for UAVs.

This does have a very important implication for icing nowcasting and forecasting methods. These numerical weather models typically predict an icing severity index that is calibrated for manned aircraft. Icing conditions which are evaluated as “trace” or “light” for manned aircraft [83] may be severe for smaller UAVs. This highlights the need to develop suitable icing forecasting tools specifically for UAV applications.

The limitations of this study are mostly related to the quality of the numerical simulations of ice accretions and aerodynamic performance. Previous work and this validation have shown that FENSAP-ICE generally is able to capture the main icing features but is limited in predictive power when it comes to details. Hence, it is important to highlight that the simulated performance penalties in this study may differ from real icing

conditions and that more validation work is needed. However, the general trends and mechanisms that have been revealed by this study are in line with previous work and are expected to be valid qualitatively, if not quantitatively.

6.6 Summary

Numerical simulations were carried out to investigate the effects of variation of airspeed and chord size on the aerodynamic icing penalties on a UAV airfoil. Three different meteorological icing conditions, based on the continuous maximum icing envelope for manned aircraft, were used to generate rime, mixed, and glaze icing regimes.

The results showed that the ice accretion regime had a significant influence on the resulting ice geometries, which were linked to the degree of aerodynamic performance penalties. The ice accretion regime was driven by temperature and airspeed (aerodynamic heating). For rime ice conditions an increase in velocity led to higher total ice mass and relative ice thicknesses, resulting in an increase in performance penalties. It was shown that the streamlined rime ice shapes can also delay stall. For glaze ice conditions an increase in velocity led to an increase in ice mass and area, but with thinner relative ice thicknesses and a larger coverage of the airfoil. The aerodynamic penalties did not change significantly with airspeed variations for glaze. At high velocities, the aerodynamic heating effect became so high that the surface temperatures on the airfoil rose above freezing and no ice accretion occurred. For mixed ice conditions, a shift from the rime-like behavior to the glaze-like behavior occurred for increasing velocities. The transition phase generated large ice horn features associated with very high aerodynamic performance degradation.

The variation of chord length had similar effects at all icing conditions. A decrease in chord length led to a decrease in total ice mass but an increase in relative ice area, relative ice thickness, and extended icing limits. This led in all cases to substantially higher aerodynamic performance penalties.

UAVs are smaller in size than manned aircraft and operate at lower flight velocities. This study showed that both these characteristics likely lead to UAVs being more sensitive to icing than larger manned aircraft. The lack of aerodynamic heating makes UAVs more susceptible to icing at near-freezing-point temperatures where icing would not occur on faster manned aircraft. The lower chord lengths led to larger ice horns relative to the

airfoil size, which was connected to substantial performance penalties. The worst icing penalties occurred for small chord lengths and temperatures close to freezing – which may be commonly encountered by UAVs. This underlines the continued need for further research of icing effects on UAVs, especially at low Reynolds numbers.

6.7 Addendum

In the scope of this study, three meteorological conditions were selected to represent rime, glaze, and mixed ice. The motivation for this was that each of these ice shapes has a characteristic geometry that leads to a significant difference in the aerodynamic performance penalties. To help identify suitable conditions, a small investigation was conducted on the temperature dependency of the ice shapes for the base case of v=25m/s, c=0.45m, and MVD=20µm for T=[−2.0, −3.0, −3.5, −4.0, −4.5, −5.0, −15°C]. Note that LWCs were chosen according to 14 CFR Part 25 Appendix C continuous maximum icing conditions [73].

A selection of the resulting ice shapes is shown in Figure 6.9. The ice geometries could be grouped into three categories. At T=[−4.5 … −15°C] the ice shapes had a streamlined shape that is typically characteristic of rime ice. This was confirmed by the freezing fractions for these cases, which were close to unity. The second category were ice shapes for T=[−2.0 … −4.5°C] which all exhibited a highly convoluted surface geometry and low freezing fraction. This could be associated with glaze ice. The ice shape at T=−4°C was different from both rime and glaze. The geometry exhibited a V-shaped or lobster-tail type horn and an intermediate level of freezing fraction.

These differences were also represented in the aerodynamic performance of each of these ice shapes in Figure 6.10. The rime ice shapes had – due to their streamlined form – the lowest aerodynamic penalties. For glaze, the performance degradation was temperature-dependant and increased for lower temperatures. The highest aerodynamic penalties occurred at T=−4°C.

Due to the singularity of the ice geometry associated with the highest performance penalties, the T=−4°C case was chosen as mixed ice. In summary, this investigation revealed the sensitivity of the degree of icing penalties to the temperature. Small temperature changes can change the ice accretion regime e.g. from rime to mixed and lead to substantially higher performance losses.

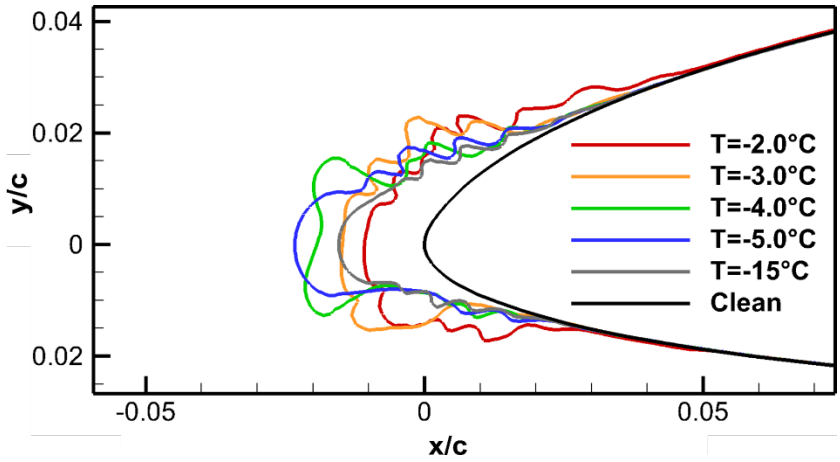

Figure 6.9: Ice shapes for temperature variation cases.

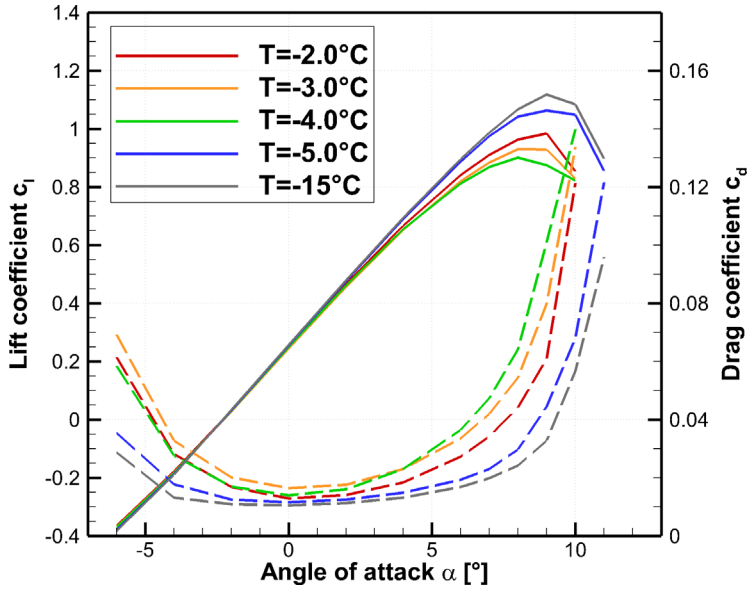

Figure 6.10: Aerodynamic performance for the temperature variation cases.

Part IV

Ice Protection Systems

7 Numerical Simulation of Anti-Icing Loads

7.1 Introduction

Atmospheric icing imposes a significant limitation on the operational envelope of unmanned aerial vehicles (UAVs) [9, 42]. While there is a good understanding of icing for manned aviation [57], few studies discuss icing on UAVs. The existing studies indicate that icing on a UAV degrades its aerodynamic performance by reducing lift, increasing drag, and negatively affecting the stall behaviour [15, 18, 21, 43]. All these factors constrain the flight envelope and significantly increase the risk of losing the aircraft. In order to mitigate the adverse effects of icing, ice protection systems (IPS) are required. Whereas for commercial and military aviation a wide range of mature IPS exists [152], such solutions are very limited for UAVs.

This study focuses on fixed-wing UAVs with wing-spans of several meters. These UAVs are suited for many autonomous applications, for example for remote sensing, search and rescue, oil spill detection, ship-based iceberg tracking, etc. [92]. Typical mission profiles require the capability to operate autonomously, beyond line of sight, for extended periods, in all-weather conditions. Atmospheric in-cloud icing imposes a significant barrier to the ability of a UAV to execute the aforementioned tasks [9]. Essentially, UAVs today are grounded during icing conditions or face a substantial risk of losing control and crashing. Therefore, developing a suitable IPS for UAVs is one of the key challenges for the successful use of autonomous fixed-wing UAVs in the future.

A multitude of IPS solutions exists for manned aviation [152], but they are only partly transferable to UAVs. There are several key differences between manned and unmanned aircraft [42]. UAVs are typically smaller in size. This implies that there are more strict weight and dimensional constraints to an IPS. Consequently, power is a limited resource on UAVs which means that an IPS needs to be particularly energy-efficient. The most common energy form for small and medium-sized UAVs is often electric. Icing detection on a UAV needs to be fully autonomous, without any visual information from a human

pilot [29]. The instrumentation for detection should be minimal and energy-efficient. Last but not least, UAVs are less cost-intensive compared to manned aircraft, which means that smaller budgets are available for IPS development. On a side note, many of these characteristics can be found in cold climate wind energy [81].

For the development of manned aircraft, much more resources in design, engineering, and testing are available than for UAVs. Normally, experiments in icing wind tunnels are performed as part of the IPS design and certification process [73]. Such experiments are very expensive and time-consuming. Therefore, they might not be affordable in the scope of a UAV development program. A cheaper method to design an IPS is by using numeric simulation tools.

It is important to note that most numerical models have been developed for the high Reynolds numbers of manned aviation ($Re > 2 \times 10^6$) whereas UAVs typically operate in a lower Reynolds regime ($Re < 2 \times 10^6$). This can have a significant impact on the ice accretion process [19], but also on flow characteristics. In particular, laminar boundary layer effects are going to be more dominant at lower Reynolds numbers [153].

In the scope of this study, an electrothermal anti-icing system was considered. This type of system provides heat to specific areas on the wing via electric currents. Electrothermal systems are well-suited for UAVs, as they are light-weight and require only electrical energy, which is often easily available – although limited in amount. Anti-icing systems continuously supply heat in order to avoid ice accretion on critical surfaces [64]. The advantage of such a system is that it does not generate any aerodynamic penalties from ice accretion [86]. This is opposite to de-icing systems, which allow for a certain amount of ice to build up, which is then periodically removed.

Generally, there are two different operation modes for electrothermal anti-icing systems. Systems are called *fully evaporative* if the provided heat is sufficient to evaporate the incoming liquid water within the impingement zone. The advantage of a fully evaporative system is that it has no risk for runback icing and the area to be protected is relatively small. On the draw-back, such systems require high heat fluxes and may result in exceedingly high surface temperatures. An anti-icing system is considered to be *running wet* when it is providing just enough heat to prevent the incoming super-cooled droplets from freezing on the surface. Running wet anti-icing systems typically require a larger area to be heated, but with lower heat fluxes and lower surface temperatures.

The resulting water film from a running wet system may freeze downstream of the heated areas and form runback ice that can have severe effects on the aerodynamics [57, 154].

The objective of this paper was to compare the two icing codes for the purpose of designing a UAV anti-icing system. The comparison focussed on the minimum required heat fluxes for running wet and fully evaporative mode. The comparison aimed to reveal differences in the thermodynamic models of these two codes at low Reynolds numbers. Furthermore, the influence of 3D flow effects on anti-icing was evaluated.

7.2 Numerical Tools

Two numerical tools will be used to assess IPS loads. LEWICE (2D, version 3.2.2) is a widely used first-generation icing tool based on a 2D panel-method [88]. LEWICE has been developed by NASA and has been validated over a wide range of parameters with extensive experimental icing wind tunnel data [89]. LEWICE is formally only validated in a high Reynolds number regime ($Re > 2.3 \times 10^6$) [88]. The 2D panel-method in LEWICE has very low computational requirements which allows LEWICE to obtain a large number of results in a short time. This feature is well suited to study a wide range of icing parameters to gain a better understanding of the dominating variables in a specific icing scenario. Such a feature is particularly relevant for designing an efficient IPS with regards to investigating different cases, configurations, heat requirements, etc. However, because a panel-method captures many of the physical processes by means of (theoretical or experimental) correlation, the simulation of anti-icing loads needs to be validated. In the absence of relevant experimental data for UAVs, LEWICE will be compared to a higher-order code.

ANSYS FENSAP-ICE (version 19.2) is a second-generation, state-of-the-art computational fluid dynamics (CFD) icing code, capable of 2D and 3D icing simulations for a large variety of applications [87]. The code consists of separate modules that aim to directly capture the main physical icing and heat transfer processes [155, 156]: the flow field is simulated with a Reynolds-Averaged Navier-Stokes flow solver; droplet and ice crystal impingement are simulated using a Eulerian approach; ice growth is captured by solving the partial differential equations on the iced geometry.

All CFD flow calculations in FENSAP-ICE were performed by using a steady-state method with streamline upwind artificial viscosity. Turbulence was implemented with a

Spalart-Allmaras (turbulent) or k-ω SST (intermittent transition) model. The discretization for CFD was executed as hybrid O-grids with a structured resolution of the boundary layer and an unstructured far field.

7.3 Method

In this paper, two different approaches were pursued to compare the IPS capabilities of LEWICE and FENSAP-ICE on UAVs. First, the required heat fluxes for a running wet and fully evaporative anti-icing system were compared on a 2D airfoil for three different meteorological cases. Second, the anti-icing loads for a selected icing case were evaluated on a 3D wing. FENSAP-ICE fully simulates the wing whereas LEWICE evaluates four 2D cross-sections of the wing.

The HQ/DS-2.5/13 airfoil with a chord of c=0.4m was chosen as the base 2D geometry. It has been developed for dynamic soaring of gliders at low Reynolds numbers ($Re < 1 \times 10^6$) [157]. This makes the airfoil suitable for many UAV applications and has been considered for several airframe designs. For the 3D wing case, a simple wing using the HQ/DS-2.5/13 airfoil with a span of $b = 1.5\text{m}$, aspect ratio of $\Lambda = 4.7$, and a straight trailing edge was used, see Figure 7.4.

7.4 Results

7.4.1 Case Selection

The task of finding relevant meteorological design cases serves as an example of how LEWICE can be used to quickly investigate a larger number of cases. The entire CFR 14, Part 25, Appendix C icing envelope for continuous maximum icing conditions [73] was used for a parameter study. The minimum and maximum icing conditions are listed in Table 7.1. The running wet heat fluxes for 128 different cases were calculated with LEWICE (Figure 7.1) in about 20 minutes on a standard office laptop. From this, three icing cases that seemed interesting with respect of required heat and impingement limits were chosen to be investigated and are presented in Table 7.1. The Reynolds numbers range from Re=0.6–0.8×10^5. Case A represents the highest required anti-icing loads, Case B exhibits a large impingement zone and the most runback, and Case C is an example of icing during take-off or landing with higher angle of attack.

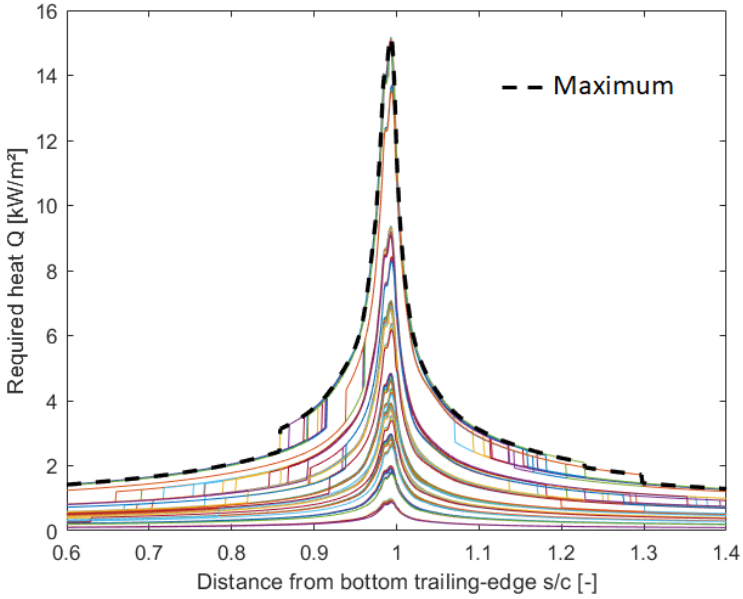

Figure 7.1: Required anti-icing heat fluxes for running wet operation from LEWICE for 128 cases.

7.4.2 2D Running Wet

The required heat fluxes on a running wet IPS for the HQ/DS-2.5/13 airfoil are shown in Figure 7.2 for both numerical codes. The horizontal axis represents the dimensionless wrapping distance from the leading-edge, with negative values indicating the bottom-side of the airfoil. The vertical axis shows the required heat flux to maintain a surface temperature of 0°C and to prevent any ice formation. In order to show the influence of transition, FENSAP-ICE calculations were performed fully-turbulent (*turb*) and using the k-ω SST intermittency transition model (*trans*).

Table 7.1: Anti-icing test cases.

Parameters	min/max	Case A	Case B	Case C
Velocity $\boldsymbol{v_{icing}}$	20 – 25 m/s	25 m/s	25 m/s	20 m/s
Angle of attack $\boldsymbol{\alpha_{icing}}$	0 – 4°	0°	0°	4°
Relative Humidity $\boldsymbol{RH}$	100 %		100 %	
Chord $\boldsymbol{c}$	0.40 m		0.40 m	
Droplet $\boldsymbol{MVD}$	15 – 40 µm	15 µm	40 µm	20 µm
Liquid water content $\boldsymbol{LWC}$	0.04 – 0.76 g/m³	0.20 g/m³	0.13 g/m³	0.43 g/m³
Temperature $\boldsymbol{T_{icing}}$	−2 – −30 °C	−30 °C	−4 °C	−10 °C

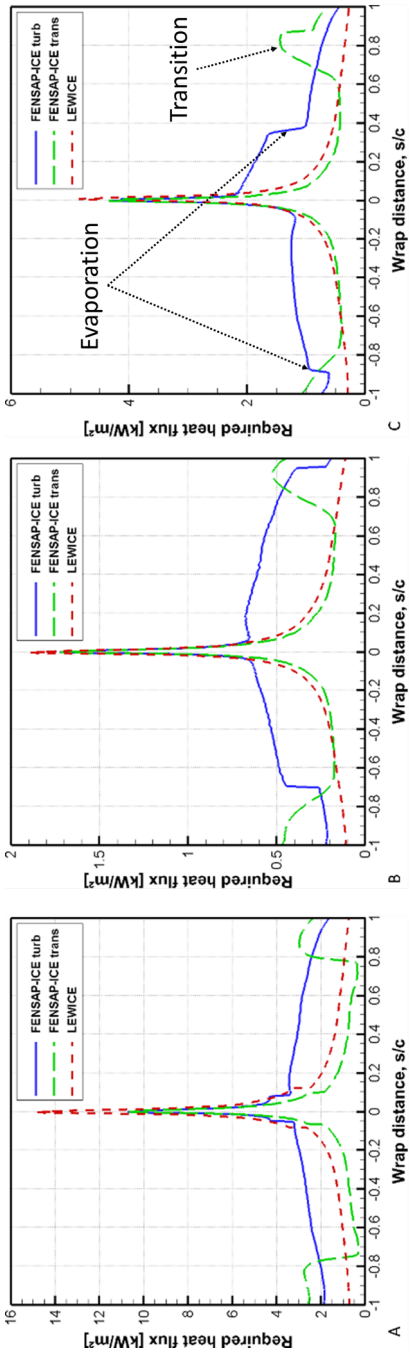

Figure 7.2: Required anti-icing heat fluxes for running wet operation in FENSAP-ICE (turbulent & free transition) and LEWICE for all three icing test cases.

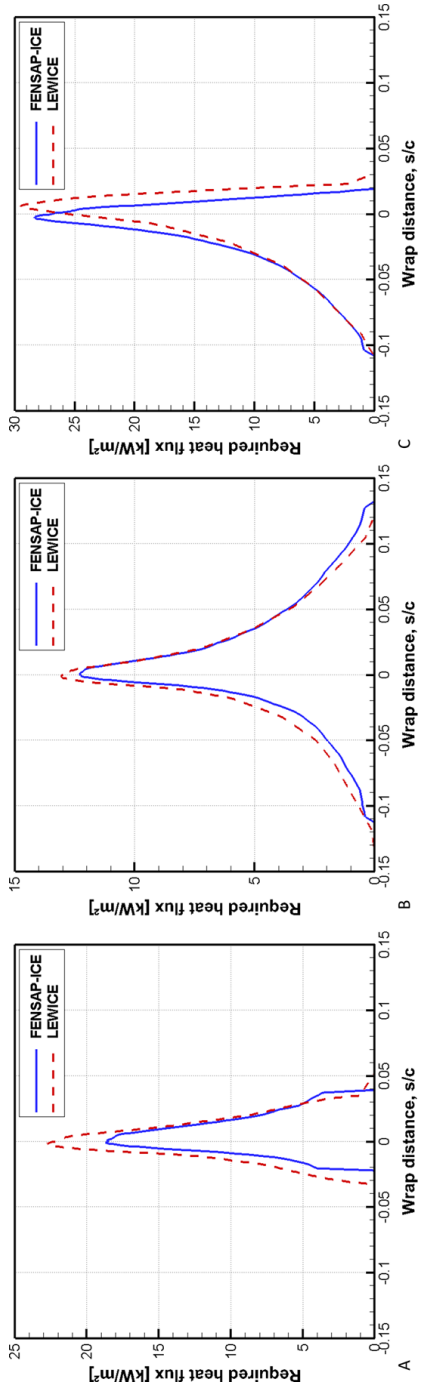

Figure 7.3: Required anti-icing heat fluxes for fully evaporative operation in FENSAP-ICE and LEWICE for all three icing test cases.

Three distinct zones can be identified in each graph. First, the highest heat requirements occur close to the stagnation point at the leading-edge of the airfoil. In this area, the super-cooled cloud droplets collide with the airfoil and require high energy fluxes to prevent instantaneous freezing. The magnitude of this initial heat spike mainly depends on the droplet and ambient temperature and is, therefore, highest for Case A (T_{droplet}=−30°C) and lowest for Case B (T_{droplet}=−4°C). Since flow velocities are low, the role of stagnation point heating is minor.

The second area is defined by heat transfer on a wetted surface. The incoming droplets form a water film on the surface that is transported downstream due to aerodynamic friction. In addition to the convective heat transfer, evaporation cooling needs to be compensated by the anti-icing system. The limits of this wet zone are defined by the location where the liquid water film is completely removed. When the surface becomes dry, a sudden *decrease* of the required heat occurs (e.g. at $s/c = \pm 0.1$ in Figure 7.2a, or at $s/c = -0.7$ in Figure 7.2b for FENSAP-ICE turbulent). This represents the third zone, where the surface is dry, and the required heat flux is driven by compensating the convective heat transfer. Technically this energy is not required for the anti-icing system (waste heat), but it serves as an indicator of the heat transfer model in LEWICE and FENSAP-ICE. A steep *increase* of the required heat flux in the dry or wet zone for the FENSAP-ICE transition results indicates the location of the laminar-turbulent transition point. A turbulent boundary layer increases convective heat transfer due to higher turbulence [158]. An increase in heat flux cannot be detected for LEWICE, indicating that the code does not predict laminar-turbulent transition in any of the three cases. This is an indication that LEWICE is not modeling the low Reynolds aerodynamics correctly.

The green curve in Figure 7.2c serves as an example to apply the three aforementioned thermodynamic regimes. At the leading-edge, the heat transfer is the highest due to incoming droplets. A thin water film will build on the upper side of the airfoil with laminar heat transfer. The laminar-turbulent transition is predicted at $s/c = 0.7$, which is consistent with XFOIL simulations [143]. Downstream of this point, the flow becomes turbulent and increases heat transfer due to increased energy transport in the boundary layer. This accelerates evaporation rates and increases the required heat fluxes. Consequently, at $s/c = -0.85$, the water film disappears, and turbulent convective heat transfer becomes dominant on the dry surface. Without evaporation, the heat requirements are reduced.

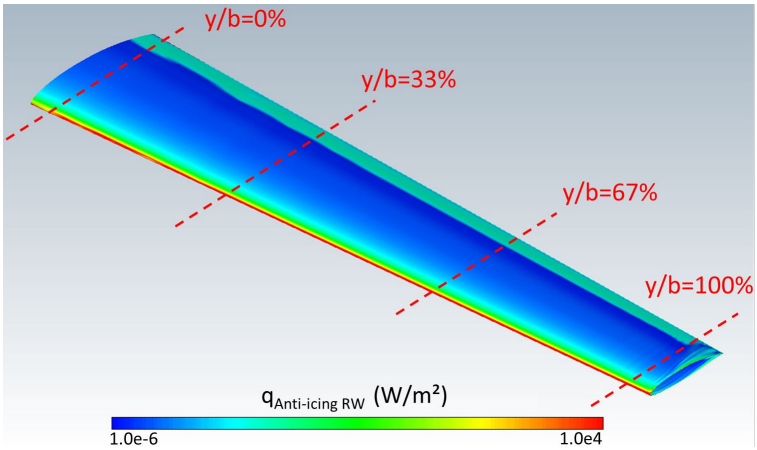

Figure 7.4: FENSAP-ICE running wet solution for the 3D wing with the location of the cross-sections in LEWICE.

For the running wet results, LEWICE predicted larger heat spikes in the impingement area whereas the location and extent were almost identical to FENSAP-ICE. The difference was most pronounced for Case A in Figure 7.2a with a deviation of over 30% whereas in the other cases the deviation was substantially lower. The turbulence model seemed not to have a noticeable effect on the FENSAP-ICE results on the magnitude of the spike. The extent of the wet zone in Case A was quite similar, whereas for Case B and C the differences were significant. In the latter two cases, LEWICE predicted that the surface water film never evaporated from the surface. The turbulent FENSAP-ICE results indicated that evaporation occurred eventually in all cases. With transition, full evaporation occurred only in Case A and partial evaporation in Case C.

7.4.3 2D Fully Evaporative

The results for a fully evaporative anti-icing system are depicted in Figure 7.3. The horizontal axis is cropped since outside of the impingement area the required anti-icing heat fluxes are zero. There were no significant differences between turbulent or transition modeling in FENSAP-ICE, so only one solution is shown. Overall, there was a much stronger overlap for the fully evaporative mode between LEWICE and FENSAP-ICE compared to running wet. Differences in the width and location of the impingement zone can be detected, in particular for Case C in Figure 7.3c with the nonzero angle of attack.

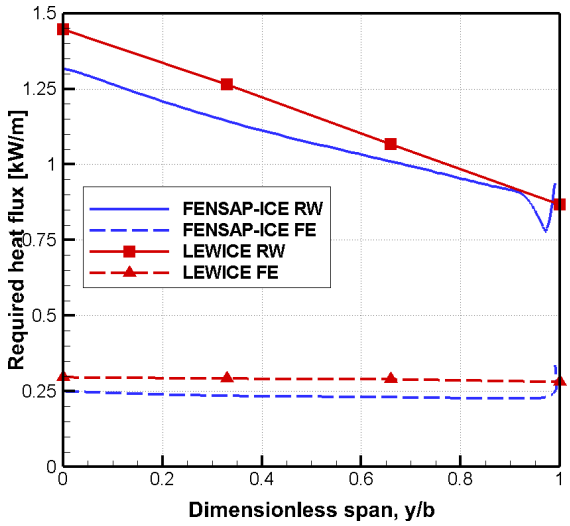

Figure 7.5: Required anti-icing heat fluxes for Case A in FENSAP-ICE and LEWICE for the 3D wing.

This is an indication of differences with the modeling of the droplet trajectories and impingement limits. The maximum surface temperatures required for full evaporation were 12°C, 19°C and 36°C for each of the cases, as indicated by LEWICE. FENSAP-ICE does not readily calculate these numbers and would require substantially more complex conjugate heat transfer simulations.

The total heats required for anti-icing (i.e. the areas under the curves in Figure 7.2 and Figure 7.3) are summarized in Table 7.2. For FENSAP-ICE, only the results with transition are shown. In addition, a value is given for the running wet heat required to keep the first 20% of the airfoil chord ($s/c < 0.2$) free of ice. The reason for this is because anti-icing systems typically only protect the leading-edge of a wing, to prevent the formation of hazardous ice formations. The overview confirmed that both codes were predicting similar trends. Generally, the fully evaporative heat fluxes were closer than the running wet results. This can be explained by the different results for the required heat fluxes and was mostly related to the laminar-turbulent transition modeling – and lack thereof (Figure 7.2). If only the heat fluxes of the leading-edge were considered, the deviations between the two codes were small – since the transition effect was smaller in that region. The only exception is Case A, where significant differences in the required heats at the leading-edge occurred.

7.4.4 3D Wing

Since Case A displayed significant differences in both running wet and fully evaporative mode, it will be used to investigate the heat transfer on a 3D wing. FENSAP-ICE fully resolved the full flow field around the wing in CFD, whereas LEWICE only evaluated four 2D cross-sections. Figure 7.4 displays the running wet heat fluxes on the wing and the location of the 2D LEWICE cuts. The figure shows clearly the high required heat fluxes at the leading edge, and the transition area close to the trailing-edge. In Figure 7.5, the required heat flux for every position along the span is shown for both running wet (*RW*) and fully evaporative (*FE*). For running wet, the required heat decreased along the span for both codes. This was explained by the decrease of the chord and thus the reduction of the heating area. The difference between the two codes seemed to be a constant offset with an identical inclination until $y/b = 0.4$. From there till about $y/b = 0.9$ the FENSAP-ICE solution changed the inclination which seems to be correlated with changes in the transition location. At the very tip, a dip with a consequent increase in the FENSAP-ICE load curve occurred. The dip resulted from a change in the transition point and the consequent increase from intensified heat transfer. Both effects were likely to originate from the wingtip vortex. For fully evaporative, both curves were nearly constant, which indicated that the size of the impingement area did not change significantly along the span. A steep increase of the required heat occurred at the wingtip with FENSAP-ICE, indicated vortex effects.

Table 7.2: Total anti-icing heat fluxes for each 2D case as predicted by the numerical codes.

Required heat q [W/m]	**Case A**		**Case B**		**Case C**	
	LEWICE	FENSAP-ICE	LEWICE	FENSAP-ICE	LEWICE	FENSAP-ICE
Running wet total	1394	1266	205	256	458	607
Running wet 20%	674	439	92	82	205	198
Fully evaporative	299	236	338	311	531	464

7.5 Discussion

The objective of this paper was to investigate the differences between FENSAP-ICE and LEWICE for the simulation of IPS. The results for anti-icing showed that both codes are performing similarly, although differences do occur. The simulations indicated that for the running wet case, the extent of the laminar boundary layer was an important factor. This was not surprising, as convective heat transfer was significantly higher for turbulent boundary layers [158], thus requiring higher heat fluxes to keep the surface at a constant temperature. For the simulation of a UAV IPS, this was relevant because laminar flow characteristics were much more dominant at lower Reynolds numbers compared to manned aviation. The sensitivity of the transition location to the boundary layer thickness and the surface roughness (i.e. from ice accretion or surface water film) should, therefore, be considered when simulating running wet anti-icing systems. From a simulation point of view, this is important, as laminar-turbulent transition modelling with CFD remains a challenging task and may result in low fidelity results.

For running wet and fully evaporative operation modes, LEWICE predicted 10–20% higher maximum required heat fluxes near the leading-edge compared to FENSAP-ICE. For the low-temperature case, a constant offset in the required heat fluxes appeared which is likely to be related to differences in convective heat transfer modelling. This did not occur for wet surfaces. Since only the latter was of interest from a design point of view, these differences may be less significant. All results illustrated that minor differences in the extent and location of the impingement limits between the two codes occur.

With regard to the design of an anti-icing system, several observations could be made. Both, a running wet and a fully evaporative system might be applicable for UAVs. The required heating zone temperatures for full evaporation at the leading-edge were significantly lower than for manned aviation (often 100–200°C) due to the lower wind speeds. For running wet, the required heat fluxes could be reduced if only a part of the leading-edge area was protected. The comparison of required heats in Table 7.2 showed that ambient temperature played a big role in the question which operation mode is the most efficient for UAVs. At moderate temperatures, a running wet system covering a limited area of the leading-edge will require significantly less energy than a fully evaporative system (Case B & C). At very low temperatures (Case A), however, the evaporative system had an advantage. This was because at low temperatures, heating a

very small zone to a high temperature is more efficient than heating a large zone to a moderate temperature. The driving force is the difference between the required surface temperature and ambient conditions.

7.6 Summary

This paper compared two numerical icing codes, LEWICE and FENSAP-ICE, with regards to their capability to predict anti-icing heat requirements for UAV applications. Three cases were chosen from a parameter study based on the CFR 14, Part 25, Appendix C icing envelope for continuous maximum icing conditions. Simulations of a running wet and a fully evaporative system were performed in 2D on the HQ/DS-2.5/13 airfoil. The results show the existence of three distinct thermodynamic regions. Both numerical codes predicted generally similar results, although differences exist. For running wet, it was shown that the choice of the turbulence model (fully turbulent or transition) was significant. LEWICE assumed fully laminar flow over the entire airfoil, whereas FENSAP-ICE predicted transition at approximately $s/c = 0.7$. It was shown that turbulent flow conditions increase evaporation rates and can lead to an earlier disappearance of the water layer compared to laminar conditions. This highlights the importance to understand the interactions between icing and transition for UAV airfoils, as well as the capability to model them accurately. The fully evaporative cases revealed that LEWICE is predicting higher required heat fluxes near the stagnation point and showed differences in the droplet impingement area. The comparison of the total required heat fluxes showed that depending on the ambient temperature, running wet or fully evaporative heating modes offer the lowest power requirements. This indicates that the identification of the critical icing design cases is an important task for the development of a UAV IPS.

Furthermore, the effect of 3D flow on anti-icing loads was investigated on a UAV wing. For this, 3D simulations were carried out with FENSAP-ICE and compared to corresponding 2D cross-sections with LEWICE. The results showed that FENSAP-ICE predicted similar trends as LEWICE for the fully evaporative mode. Differences occurred in the running wet case and were linked to the simulation of the laminar-turbulent transition location. In addition, 3D effects at the wing tip were observed for both modes, likely to be related to the wing-tip vortex. The effects were limited in magnitude and may be neglectable for simple wing geometries.

In summary, the differences between the two codes were moderate, especially for the higher temperatures. The results showed that the boundary-layer conditions and transition location had a major influence on the required heat fluxes for running wet conditions in FENSAP-ICE. This indicated that some focus should be spent on further studies on the effect of initial surface roughness and water film thickness interactions with the boundary layer. 3D effects appeared to be of limited magnitude but may also require closer investigation. Generally, the results suggested that the faster LEWICE tool for the design of UAV IPS may be possible. However, it is important to note that both codes are not validated for predicting IPS loads for the Reynolds number regime of this study. Therefore, the fidelity of the codes cannot be evaluated based on this work alone. Further experimental work for comparison is necessary to build more confidence in these numerical methods.

7.7 Addendum

The basis of this paper was [47], which was published in early 2019. Since then, three icing wind tunnel tests were performed on the D•ICE system, which also contained several anti-icing runs. This addendum takes the anti-icing results from [49] and compares them to FENSAP-ICE and LEWICE. The experiments were conducted on a running-wet IPS with the test cases described in Table 9.1. As discussed later in section 8.3.2, the experimental results are best compared to the peak required anti-icing heat fluxes near the stagnation point from the numerical simulations.

Figure 7.6 shows the experimental and simulation results for three temperatures. All three lines show a clear linear temperature dependency. The lines for LEWICE and FENSAP-ICE have almost identical slopes, whereas data is less clear for the experiments. This may be related to the uncertainty in the experiments at T=−10°C, which will be discussed in section 9.3.1.

There is a clear offset between FENSAP-ICE and LEWICE of 0.3–0.7kW/m². This trend is in line with the findings from above. The experimental data seem to match well with LEWICE for the two lower temperatures but show an offset to the FENSAP-ICE results. This may be related to measurement uncertainties, especially heat conduction into the test wing and electrical losses. Section 9.4 discusses the experimental limitations of the results in more detail.

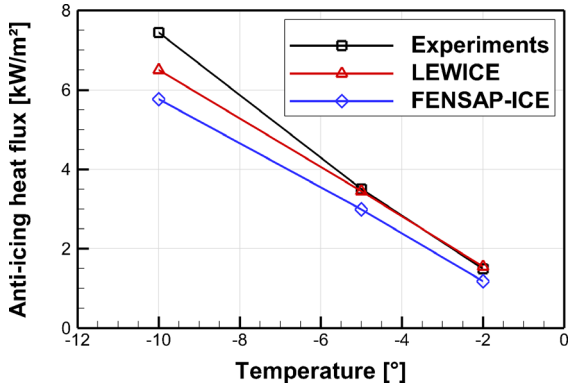

Figure 7.6: Comparison of the minimum required anti-icing heat fluxes from icing wind tunnel experiments and numerical simulations with FENSAP-ICE and LEWICE.

In summary, the comparison between the numerical and experimental anti-icing data adds more confidence to the purely numerical results from above. Due to the quality of the experimental data it is however still not possible to fully validate either of the models. Also, this validation technically applies only for the peak required power near the stagnation point. For practical applications, this is the most important anti-icing parameter to predict – but for validation purposes it would be beneficial to have more datapoints along the surface of an airfoil for comparison.

8 Ice detection, Anti-Icing, and Autonomous Operation of an Electro-Thermal Ice Protection System

8.1 Introduction

Atmospheric in-flight icing is a significant risk of the operations of unmanned aerial vehicles (UAVs) [9]. Icing is a severe risk that can lead to significant aerodynamic performance penalties that can be a great hazard for UAVs [18, 43, 57]. To mitigate these adverse effects, ice protection systems are required. For manned aircraft, ice protection is a well-established field [66], whereas for UAVs very little research exists on IPS today.

In this study, an electrothermal IPS for fixed-wing UAVs with wing-spans of several meters will be investigated. UAVs of this class can be used for a wide range of applications, both military and commercial. Often, it is a key requirement that such UAVs can operate safely and that the operational envelope is not limited by icing risks. For this reason, the availability of reliable IPS is a key requirement for the future development of UAVs.

There is a wide range of IPS concepts that exist, not all of which are suitable for UAVs [31]. UAVs have special requirements for IPS: systems must be lightweight, energy-efficient, and function autonomously [42]. Electrothermal systems are well-suited for UAV applications as they meet these requirements and are a sufficiently mature technology [86].

Figure 8.1: Ice protection system with five heating zones inside the wind tunnel. Four additional thermocouples have been added (blue tape).

Researchers at the Research Centre of Excellence the Autonomous Marine Operations and Systems (AMOS) under the Norwegian University of Science and Technology (NTNU), have developed the IPS technology called D•ICE. D•ICE is a modular, robust, power-efficient, and autonomous ice protection solution that encompasses icing detection and removal capabilities. It enables continuous unmanned aircraft operations globally and in the harshest conditions [29]. This version of D•ICE was based on a nanocarbon-paint electrothermal heating system, while later versions were based on carbon fibre heaters. The technology included a novel estimation, control, and detection algorithms and is being commercialized by UBIQ Aerospace. Since the beginning of that project in 2013, the system has been integrated into several different types and sizes of fixed-wing unmanned aircraft and been tested in icing wind tunnels and in flight. This study describes an experimental test campaign that has been conducted at the Cranfield University icing wind tunnel on that system during autumn 2018. The system has been tested with regard to its capabilities for icing detection, anti-icing, and fully autonomous operation.

Table 8.1: Meteorological and flight conditions for the ice detection, anti-icing and full system runs.

run	Cloud	T [°]	MVD [µm]	LWC [g/m³]	v [m/s]	AOA [°]	RMSE	RMSE (scaled)
#1	Dry	-5	-	-	25	0	0.10	0.07
#2	Wet	-5	20	0.56	25	0	1.21	0.55
#3	Wet	-10	20	0.72	25	0	2.00	0.62
#4	Iced	-10	20	0.72	25	0	1.80	0.31
#5	Dry	-10	-	-	25	4	0.83	0.13
#6	Wet	-10	20	0.72	25	4	1.74	0.71
#7	Wet	+5	20	0.56	25	0	1.43	0.12
#8	Wet	-5	20	0.56	25	0	Anti-Icing	
#9	Wet	-5	20	0.56	25	0	Anti-Icing	
#10	Wet	-10	20	0.72	25	0	Anti-Icing	
#11	Variable	-5	20	0.56	25	0	Full System Test	

8.2 Method

8.2.1 Test Setup

The Cranfield icing wind tunnel is a closed-loop tunnel with a cooling capacity of 450kW and a test section of 760x760mm [95]. The studied airfoil is a RG-15 with a thickness of 8.9% and a chord of 450mm, spanning the entire width of the test section The RG-15 is a low-Reynolds airfoil used for a wide range of UAV and model aircraft applications. The tests were conducted at Reynolds number of ca. Re=9×10^5.

Multiple prototype probes of the airfoil, based on wayfaring principles [159], were made to determine the fastest and most cost-efficient way to produce the model. The final wing-design was constructed from layered, laser-cut ribs of medium-density fiberboard (MDF), which was then covered with 1mm high impact polystyrene (HIPS) sheet. Through testing, the material was determined to be able to withstand the chemicals in the nanocarbon heating paint used for the heating zones. The foil coating allowed for a smooth surface with little need for extensive surface finishing. The HIPS foil along the leading-edge was heat bent to reduce stress and potential fracture, while the trailing edge was constructed of solid layered MDF to enable a large gluing area.

A total of five heating zones were applied to the wing using a carbon nanotube paint that functions as an electrothermal heating source, see Figure 8.1. Each heating zone was

5.4cm wide and covered the entire span of the wing. The paint was using an acrylate bonding system with nanocarbon additives. This builds into conductive paint coatings that generate heat when passed through by electric current. Power was supplied and monitored for each zone individually. In the scope of this study, only the leading-edge zone was used. Power delivery to the heating zones was regulated by using pulse-width modulation (PWM) [160]. Each zone was equipped with a cement on polyimide T-type thermocouple, located underneath the coating, as well as additional external thermocouples (applied with blue tape, see Figure 8.1).

Meteorological conditions were chosen based on typical icing conditions that could be encountered by a fixed-wing UAV for long-endurance missions at cruise speed. Icing processes are typically described by the airspeed v, the temperature T, the liquid water content LWC, the median droplet volume MVD, and the airfoil angle of attack (AOA) α. An overview of the test cases is given in Table 8.1.

8.2.2 Icing Detection

An icing detection concept was tested, that actively uses heat sources to generate a temperature signal. This signal will be characteristic for dry (cloud off, no droplets in the flow), wet (cloud on, droplets in the flow), and iced (ice on airfoil) conditions [29]. The signal was created by heating the leading-edge heating zone for a duration of 10s with a small (~60W) heat spike. Thermocouples were then measuring the resulting temperature changes on the surface for 60s. To distinguish the different environmental conditions, a reference signal was generated for dry conditions. This dry signal was used as a baseline, to which all new signals were compared against. During activation of the icing detection system, temperature signals were generated every 70s and compared to the baseline signal. The root-mean-square error (RMSE) between the observed and reference signal was then calculated. The value of the RMSE serves as an indicator for identifying different environmental conditions. In order to test the functionality of the system, a series of tests at different conditions was conducted. The tests aimed to answer the following questions:

- Can different icing conditions be identified by the detection method?
- Is the system able to detect if ice has already built up on the surface?
- Does the detection algorithm give false alerts if the ambient temperature or the angle of attack changes from the baseline?
- How does the system behave when it encounters a non-freezing cloud?

Answering these questions allows setting an RMSE threshold value that can identify icing conditions. Once hazardous conditions are identified, the heating zones are activated for anti-icing operations. Continuous heating of the leading-edge will prevent ice from accumulating on the surface and therefore mitigates the adverse effects of icing. The system was designed as running-wet, i.e. the incoming droplets are prevented from freezing but not fully evaporated. This introduces the risk of runback icing, which was observed but not studied in detail during this study.

8.2.3 Anti-Icing

A key question for the operation of an anti-icing system is the required surface heat fluxes to prevent ice formation. To achieve this, the surface temperature must be always kept above the freezing temperature. The minimum heat flux requirement of the anti-icing system needs to compensate for all heat losses that occur during icing [161]. This includes convective heat losses, evaporation, impinging heat of the droplets, and radiation.

As part of this study, the minimum required heat fluxes for anti-icing were determined experimentally. This was achieved by operating the anti-icing system with high initial power (6–8kW/m²), which was then step-wise decreased until ice accretion was observed on the leading-edge of the airfoil. Each step the power was decreased by approximately 10% of the initial power. The power was held for 90s during which time the surface was monitored for ice accretion through a 250mm camera lens. If no ice was detected, the power was decreased. This was repeated until ice accretion was observed. The power setting for the last step where no icing occurred, was then defined as the minimum required anti-icing heat flux. This method has been performed twice at T=−2°C to test the repeatability of the results, and once at T=−5°C. These experimental values are then compared to FENSAP-ICE simulation results.

8.2.4 Autonomous IPS

Last but not least, a full system test was conducted, where the anti-icing system was automatically activated once a pre-set RMSE threshold was exceeded. The algorithm for the full system test cycles through the following three modes: step, cool, detect (Figure 8.2). The ‘step’ command lasts 10 seconds and for those 10 seconds, the leading-edge zone is heated with a low PWM value. The ‘cool’ phase lasts 60 seconds – about the amount of time needed until the temperature of the zone has returned to the pre-heat

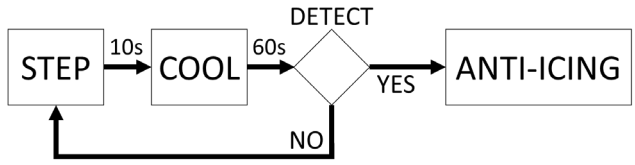

Figure 8.2: Flowchart for autonomous ice detection and anti-icing.

value. The 'detect' command evaluates the temperature signal measured during 'step' and 'cool' to infer whether ice accretion occurs on the airfoil. The detection algorithm uses the captured temperature signal and compares this to a reference signal captured under dry conditions. The RMSE between the two signals is then compared to a threshold value chosen based on previous data. This cycle of three sequential commands continues to run until the system detects ice accretion. When ice is detected, the system switches into an anti-icing mode, where the PWM value of the zone is set to a pre-defined value, that is high enough to prevent ice from building up on the leading-edge.

The experiments were accompanied by numerical simulations. The icing code ANSYS FENSAP-ICE (v19.2) was used to estimate the minimum required heat fluxes for running-wet anti-icing. FENSAP-ICE is a state-of-the-art computational fluid dynamics (CFD) icing code that is able to simulate ice accretion, performance degradation, and anti-icings loads [162]. FENSAP-ICE has been used to estimate anti-icing loads on UAVs before [47], however, due to a lack of experimental data on UAV IPS, the tool is not validated. The FENSAP-ICE simulations were based on monodisperse droplet distributions, calculated on a hybrid 2D mesh with no heat conduction into the airfoil. The predicted heat fluxes were obtained by solving the thermodynamical equations on the surface to maintain a surface temperature of zero degrees [141].

8.3 Results

8.3.1 Icing Detection

The first set of experiments was aimed to calibrate and test the icing detection method during different conditions, which are presented in Table 8.1. following conditions were considered:

- No icing cloud / dry conditions: runs #1, #5;
- Freezing icing cloud / wet conditions: runs #2, #3, #6;
- Non-freezing cloud / wet conditions: run #7;
- Ice present on airfoil but no cloud / iced conditions: run #4.

The reference signal was obtained during a dry run with an ambient temperature of T=−5°C. Figure 8.3 compares the reference signal to a detection signal at identical conditions. This results – as expected – with a very low RMSE and serves as proof that the detection algorithm is able to identify non-icing conditions when the temperature and the flow field are unchanged.

Figure 8.4 shows the "wet, freezing" conditions for a detection signal taken immediately after the droplet cloud was turned on, at the same temperature as the reference signal. It is obvious that the signal during icing conditions is significantly dissimilar to the reference signal, in shape, and maximum temperature change. The RMSE for this initial case was 1.06 which increased to 1.21 during the following detection cycle. This indicates that there is a time dependency on the RMSE signal: the difference between the reference signal and the detection signal under icing conditions will increase with time. This mechanism seems to work fairly quickly and is most likely related to the release of latent heat during freezing in combination with the increased roughness and heat transfer on the surface.

A second test under icing condition was performed, however, at lower temperatures, see Figure 8.5. The difference between the detection signal and the reference signal for this case was even more pronounced and results with an initial RMSE value of 2.00. This test was then continued for a total icing duration of 5min, after which a thin continuous ice layer formed on the leading edge. After this, the droplet cloud was turned off in order to investigate how the detection system would react to the presence of ice on the surface. The resulting detection signal is shown in Figure 8.6. The lack of droplet impingement leads to higher temperatures of the detection signal and leads to an overall reduced RMSE of 1.80. These results show that the sensitivity of the detection system seems to depend on the icing temperature. Larger temperature differences seem to increase the RMSE and increase the detectability of icing conditions. This should be considered in the future for choosing the conditions of the baseline reference signal. Once ice has formed on the surface, it can still be detected, even if there is no droplet impingement (i.e. the icing cloud has been left) present.

To test the robustness of the system towards false icing alerts, a dry test with an increased angle of attack and reduced air temperature was conducted, see Figure 8.7. The detection signal is resulting in a lower temperature increase, which can be attributed to the lower temperatures of the air and airfoil model, as well as to the increased flow velocities near the leading-edge. These differences manifest themselves in an increased RMSE of 0.83 which may be mistakenly interpreted as icing conditions.

In order to adjust for the effect of temperature and angle of attack, a constant scaling factor is introduced. This scaling factor scales the temperature signal (in y-direction) optimally in such a way to minimize the RMSE. The resulting, adjusted detection signal is shown in Figure 8.8 and reduces the RMSE to 0.13. The same approach is then applied to the same case, but with activated droplet cloud. Figure 8.9 depicts the initial, unscaled, wet detection signal. This results in an RMSE of 1.74 which is in line with the previous results. With the constant scaling factor, the wet RMSE is reduced to 0.71, see Figure 8.10. This approach has been applied to all the other tests as well, with the results shown in Table 8.1.

The last test was conducted to see how the system reacts to the occurrence of wet conditions with a temperature above freezing. This case occurs when a UAV is situated within a non-freezing cloud. The signal is shown in Figure 8.11 and displays an RMSE of 1.43 which indicates a substantial difference to the dry reference signal. The scaled RMSE of this case was 0.12.

8.3.2 Required Anti-Icing Heat Loads

Three experiments were performed to determine anti-icing loads with the conditions specified in Table 8.1 (runs #8–10). In addition to the experimental results, FENSAP-ICE simulations were conducted to simulate the minimum required heat fluxes for anti-icing. The results are presented in Figure 8.12 and Figure 8.13. FENSAP- ICE is predicting a distribution of the heat fluxes over the entire width (indicated by the distance s from the leading-edge) of the heating zone, whereas the experiments only yield an averaged value. The simulation results show that the maximum power requirement occurs near the leading-edge at the stagnation point. This is the location with the highest droplet impingement rates and thus the highest required heat fluxes. Power requirements diminish quickly as a function of distance from the stagnation point.

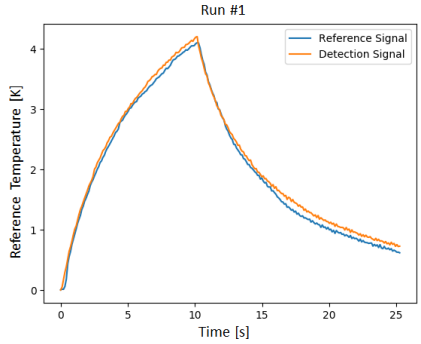

Figure 8.3: Comparison of the baseline signal (orange) with a detection signal (blue) for dry conditions at T=−5°C.

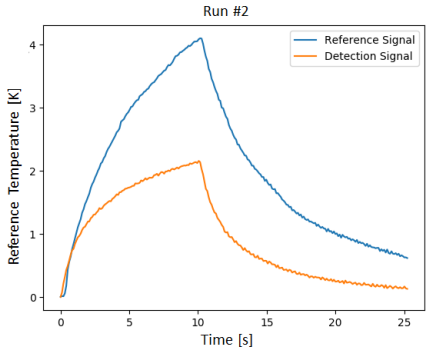

Figure 8.4: Comparison of the baseline signal (orange) with a detection signal (blue) for wet conditions at T=−5°C.

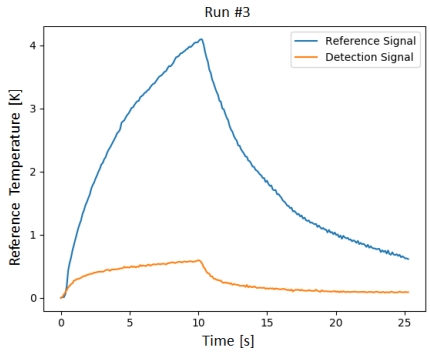

Figure 8.5: Comparison of the baseline signal (orange) with a detection signal (blue) for wet conditions at T=−10°C.

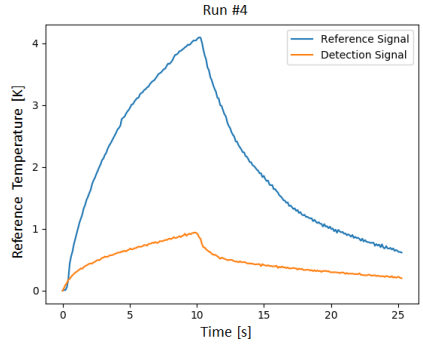

Figure 8.6: Comparison of the baseline signal (orange) with a detection signal (blue) for iced conditions at T=−10°C.

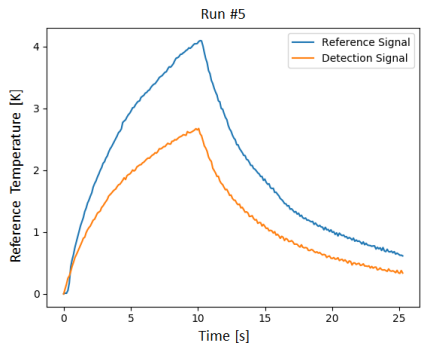

Figure 8.7: Comparison of the baseline signal (orange) with a detection signal (blue) for dry conditions at T=−10°C and AOA=4°.

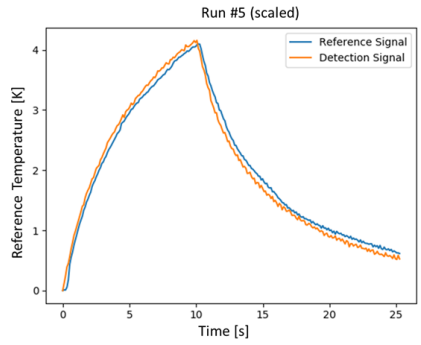

Figure 8.8: Comparison of the baseline signal (orange) with a scaled detection signal (blue) for dry conditions at T=−10°C and AOA=4°.

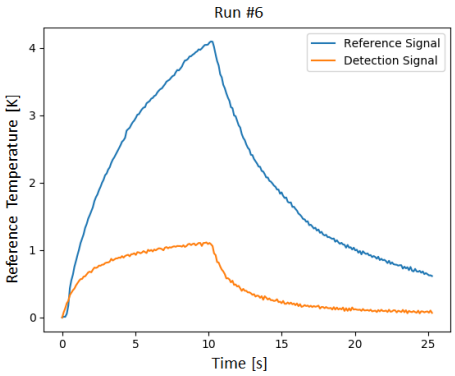

Figure 8.9: Comparison of the baseline signal (orange) with a detection signal (blue) for wet conditions at T=−10°C and AOA=4°.

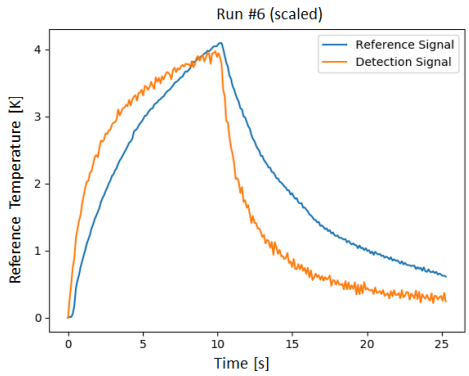

Figure 8.10: Comparison of the baseline signal (orange) with a scaled detection signal (blue) for wet conditions at T=−10°C and AOA=4°.

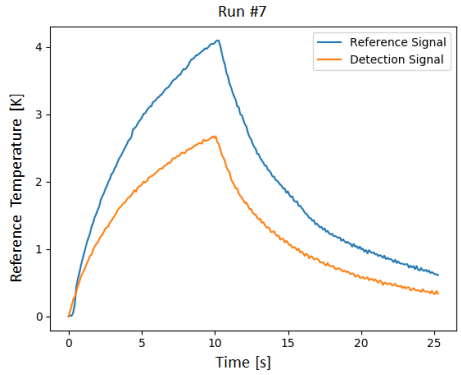

Figure 8.11: Comparison of the baseline signal (orange) with a detection signal (blue) for wet conditions at T=+5°C.

The average heat requirements from FENSAP-ICE have been calculated by integrating the area under the curves.

The experimental results from the two identical runs indicate that the method is repeatable and the results relatively consistent. Compared to the numerical results, the experimental data indicates about 220–270% higher average heat loads. A possible explanation for this is that the experimentally determined minimal heat flux was mainly driven by the peak anti-icing loads. In fact, the heat flux maximums from FENSAP-ICE are in a better match with the experimental data (22–44%). Since the heating zones are located on the outside of the airfoil models, very little heat conduction is occurring inside

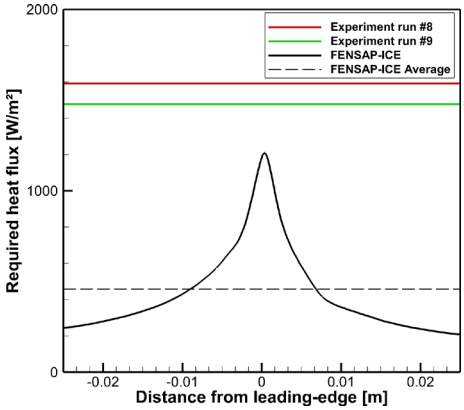

Figure 8.12: Comparison of the required heat fluxes for anti-icing from the experiments and the numerical simulations with FENSAP-ICE for runs #8–9.

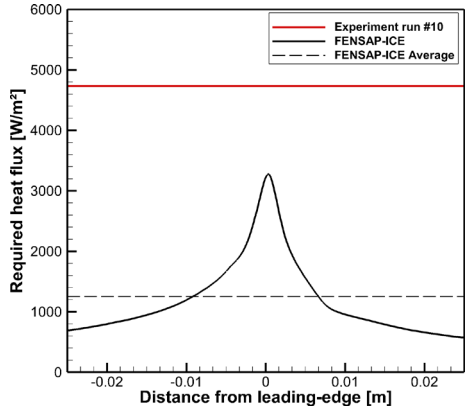

Figure 8.13: Comparison of the required heat fluxes for anti-icing from the experiments and the numerical simulations with FENSAP-ICE for run #10.

the material. This means that the average heat flux values may not be a good indicator for the total required heat loads, but that the peak values near the leading-edge are more important.

8.3.3 Full System Test

A full system test of D•ICE, including automatic icing detection and activation of the anti-icing system, was performed to prove the functionality of the system (run #11). Figure 8.14 shows the details of the case over the runtime. The icing detection algorithm was activated while the cloud was turned off in the wind tunnel. After 180s, the spray bars in the tunnel were turned on (i.e. the cloud). The system was able to identify icing conditions during the second detection cycle, i.e. 140s after the cloud was activated. This autonomously activated the anti-icing system which operated at a constant PWM for a total length of 5min during which no significant ice accretion could be observed on the heated zones, see Figure 8.15. Note that the picture shows some ice accretion near the window and on the external thermocouples. This is related to the inhomogeneity of the heat distribution near the power connectors on the side of the airfoil, and limited heat conduction through the external thermocouples.

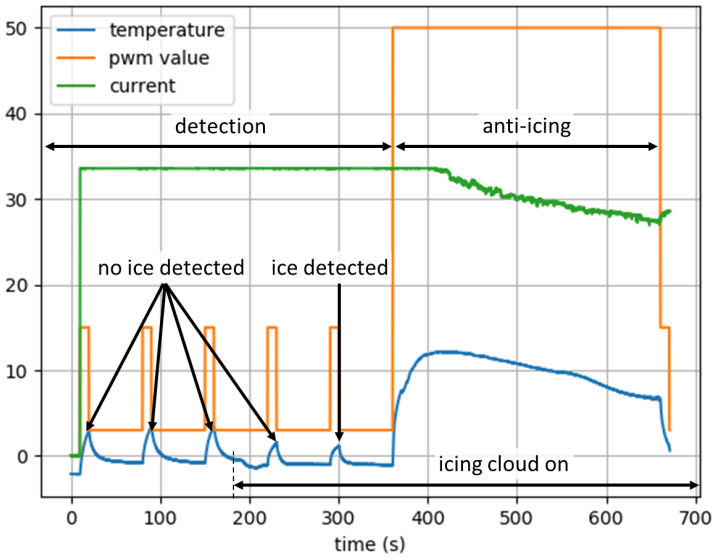

Figure 8.14: Measurements of temperature, power setting (PWM) and current supplied to the leading-edge heat zone for the full system test, run #11.

Figure 8.14 shows that the surface temperature increased rapidly after the anti-icing was turned on and then decreased over the rest of the run duration. This can be most likely explained with the positive temperature dependency on the electrical resistance of the material. The current I is inversely proportional to the resistance R and directly proportional to the heat output ($P=U\cdot I$). The figure shows that the current goes from being saturated to slowly dropping as the resistance in the zones increased. Note that, the reason why the current is saturated during detection is related to the operational mode of the power supply. As long as the PWM is not set to zero, the full current is provided to the transistors.

8.4 Discussion

The presented method for icing detection was tested for different flight conditions and with two evaluation approaches (RMSE & scaled RMSE). The results in Table 8.1 show that the temperature response signal shows significant differences between cases with no icing conditions and iced/wet cases. The arising challenge is to determine a threshold value to distinguish the cases from each other.

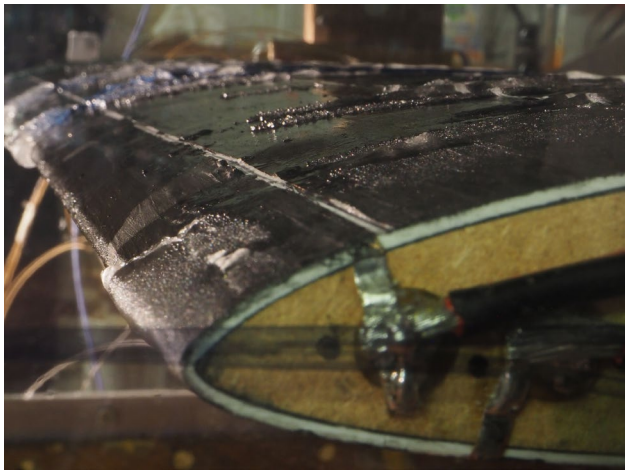

Figure 8.15: Anti-icing test. Partial ice accretion can be seen near the window and on the external thermocouples due to insufficient heating.

Figure 8.16 displays the RMSE and scaled RMSE values for all seven detection cases. Ideally, the threshold value should be selected in a way that it differentiates between the non-icing (runs #1, #5, #7) and the icing cases (runs #2, #3, #4, #6). Using the unscaled RMSE value, this feature cannot be fully achieved, since the RMSE for run #2 (wet, freezing) is lower than for #7 (wet, non-freezing). However, a threshold can be found that is only discriminating between dry and wet conditions, with a value of 1.10. However, by using the scaled RMSE approach, the differences between the cases become much more pronounced and distinguishable. Therefore, a scaled RMSE threshold value of about 0.20 is suitable to differentiate between the non-icing and icing cases.

These results show the capability of the icing detection method to accurately identify conditions that require the activation of an IPS. The scaled RMSE approach seems better suited than using only the absolute RMSE values. The current scaling approach is very simple and leaves room for implementing more sophisticated comparison methods in the future. Further testing is required to build more confidence in the detection system and to identify appropriate scaling methods. Such tests may be conducted using FENSAP-ICE simulations (e.g. to cover a large range of flight and meteorological conditions) additional icing wind tunnel tests, as well as real-world test flights. Detection cases that have not been investigated yet include freezing rain, freezing drizzle, and ice clouds.

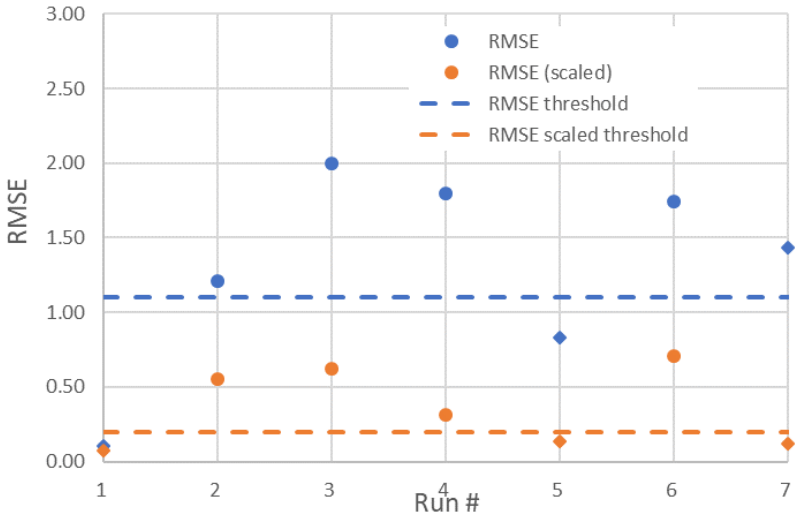

Figure 8.16: Scaled and unscaled RMSE results for all detection runs with threshold levels to distinguish between non-icing and icing conditions. Iced cases are shown with round symbols and non-iced cases with diamonds.

The anti-icing experiments show a reasonably good match with the FENSAP-ICE simulation data if only the maximum heat loads are regarded. Several experimental uncertainties have to be considered for that case. First of all, the heat distribution has not been perfectly homogenous in the leading-edge IPS zone. In particular, the heating has been significantly reduced near the edges of the airfoil, as can be seen in Figure 8.15. This introduces uncertainty on the surface heat fluxes during the anti-icing experiments. At this stage, this error could not be quantified but was estimated at about 10%. A second error is related to the stepwise power decrease, which had a minimum power-step, dictated by the PWM system. Also, it was difficult to observe the exact time point when icing started to occur which may have resulted in overly conservative heat flux estimates in the experiment. For future experiments, it is recommended that more time and smaller power-steps are selected in order to improve the experimental data. Also, narrower heating zones would allow to more accurately capture the exact minimum heating values, especially near the leading-edge.

8.5 Summary

This study investigated three main challenges that are associated with the development of an IPS for UAVs: icing detection, icing mitigation, and autonomous system operation. An icing detection method that utilizes the surface heating coatings to generate thermal signals was tested for different icing and non-icing conditions. The method compares thermal signals to a reference signal and evaluates the difference to the baseline. The experiments have shown that this approach, when combined with a simple scaling method, can accurately distinguish between icing and non-icing cases.

Icing mitigations were performed with an anti-icing system. In the scope of these experiments, the minimum required heat flux to keep the surface free of ice was determined for two meteorological conditions by stepwise reduction of the power supplied to the system. The results were compared to numerical simulations in FENSAP-ICE for validation purposes. The experiments indicated that the peak power requirements near the leading-edge drive the minimum heat fluxes in the experiment. The values compare well with the numerical method. However, the results were not accurate enough to fully validate the numerical methods and more detailed work will be required for higher confidence.

A full system test was conducted, which automatically detected the onset of icing conditions and autonomously initiated mitigation measures in the form of anti-icing. The test proved that the D•ICE technology has the capability to successfully protect a lifting surface from the adverse effects of icing.

9 Experimental Heat Loads for Anti-Icing and De-Icing

9.1 Introduction

In manned aviation, the history of icing research dates back to the 1940s [64]. For unmanned aerial vehicles (UAVs), icing research has a much shorter history and can be considered an emerging research field. Although the first analysis and reports of icing on UAVs date back to the 1990s [9], the research in this area has only recently gained momentum [42]. The reason UAV icing is becoming a trending topic is partly linked to the rise of commercial applications of UAV technologies [2]. In particular, small and medium-sized fixed-wing UAVs with wingspans of a few meters are in the focus of new business opportunities. Examples for the application of such UAVs are package deliveries, search and rescue, environmental monitoring, and agriculture [2]. In addition, UAV technology is adapted by many defense forces around the world [10]. Many UAV missions require operations of unmanned aircraft in adverse weather conditions [11]. One of the main barriers to achieving an all-weather capability of UAVs is to mitigate the risk of atmospheric in-flight icing [42].

Atmospheric icing, or in-cloud icing, occurs when an airframe travels through a cloud containing supercooled liquid droplets that freeze upon impact with the airframe [64]. The resulting ice accretions on the airframe have several hazardous effects: clogging of pitot tubes, adding weight, reducing propeller thrust, and degrading aerodynamic performance [163, 164]. Ice that forms on the leading-edge of lifting surfaces changes the airfoil geometry and leads to a decrease in lift, increase in drag, and a higher stalling risk [57].

There are several key differences between icing on manned and unmanned aircraft. An overview of the special technical and operational challenges of UAVs in icing conditions is given in [42]. Differences are for example related to airframe size, velocity, meteorological environments, mission objectives, propulsion type, and more. One important difference between manned and unmanned icing is the disparity in the

Figure 9.1: Chordwise cut into a 6min of ice accretion shows how the entire leading-edge is covered by ice.

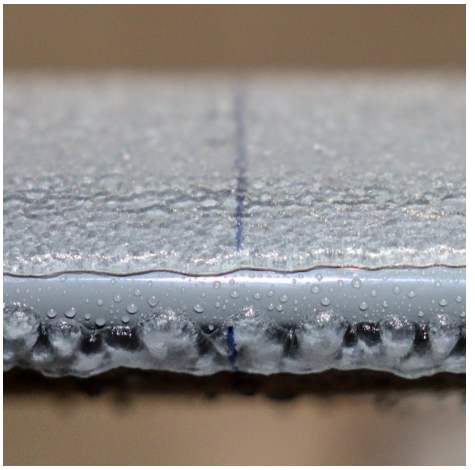

Figure 9.2: Closeup of the leading-edge after 4min of ice accretion with active parting strip heating.

Reynolds number regime. While manned aircraft typically operate at high Reynolds numbers (Re=10^7–10^8), most UAVs fly at significantly lower Reynolds numbers (Re=10^5–10^6). This difference in the Reynolds number regime can have a significant impact on icing processes [19]. It is therefore important that dedicated research for icing matter on UAVs is conducted at low Reynolds numbers.

Electrothermal ice protection systems (IPS) are one type of system that can mitigate the hazards of icing and allow aircraft to operate in all-weather conditions. An IPS can generally be operated in two different modes [165]: anti-icing and de-icing. In anti-icing mode, the surface of the airfoil is heated continuously to avoid any ice accretion at any time. In de-icing mode, the surface is heated periodically, allowing for ice to build up in between the heating cycles. This intercycle ice is removed from the airframe by two processes [86, 166]. First, ice at the interface to the surface is melted, resulting in a liquid water layer. Second, ice is shed from the airframe with the aid of the aerodynamic forces. The ice shedding efficiency is mainly depending on the geometry of the ice shape and the airspeed [77]. The energy amount required for de-icing is typically lower compared to anti-icing, but the intercycle ice generates additional drag [63].

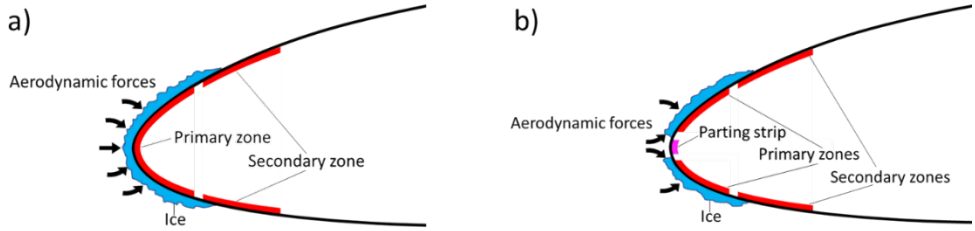

Figure 9.3: Schematic layout of the heating-zones for the conventional de-icing (a) and de-icing with parting strip (b).

A parting strip (PS) is a special heating zone that is continuously heated and can be used to reduce the required energy for de-icing [165]. The parting strip is typically located near the stagnation point and prevents ice from covering the entire leading-edge (Figure 9.1). Instead, the ice will separate into an upper and a lower part (Figure 9.2). This separation increases the aerodynamic forces on the ice (Figure 9.3) and consequently increases ice shedding efficiency.

There are several special design requirements for UAV IPS [42]. Most importantly, the systems need to be lightweight and energy-efficient. Electrothmeral systems are well suited for UAVs since they are mature, lightweight, and can easily be retrofitted to existing airframes (e.g. [31, 48]). Energy-efficiency is, however, a central challenge for electrothermal systems, as they require relatively high amounts of energy, compared to other IPS like chemical or mechanical systems [86]. The energy used for ice protection is energy lost for the propulsion system – using an electrothermal IPS consequently reduces the range and endurance of the UAV.

Electrothermal systems for UAVs must, therefore, be carefully designed to minimize the required heat to operate the system. The goal must be to run an IPS with the minimum required heat loads for each specific icing conditions. To achieve this, a good understanding of the underlying physical processes of anti-icing and de-icing is required. In particular, the influence and interlinkage of icing and IPS parameters on the required heat loads are of significance for the design of energy-efficient systems.

D•ICE is an electrothermal IPS that has been developed at the Centre for Autonomous Marine Operations and Systems at the Norwegian University of Science and Technology (NTNU AMOS) and commercialized by UBIQ Aerospace. The technology is based on

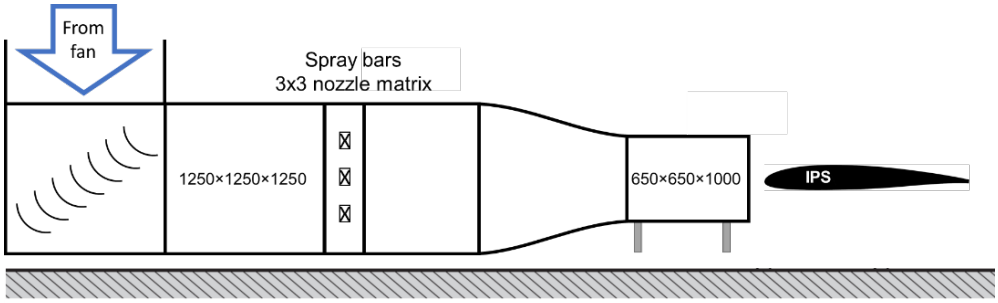

Figure 9.4: Schematics of the icing wind tunnel facility with the ice protection system.

an electrothermal heating system and an icing detection algorithm using thermal signals [48]. The systems use heating zones made of carbon fibre.

In this study, two prototypes of the D•ICE system were tested in the icing wind tunnel facility at the Technical Research Centre of Finland (VTT) during fall 2019. This study aimed to determine the required heat loads for anti-icing and de-icing for a selection of meteorological icing conditions. De-icing loads for two IPS layouts (conventional and parting strip) were compared. A parametric study over the ice shedding time was conducted for both configurations in order to better understand the de-icing physical mechanism. The experiments were conducted at low Reynolds numbers (Re=8–9×10^5) that are typical for small to medium-sized fixed-wing UAVs.

9.2 Methods

9.2.1 Test Setup

The VTT icing wind tunnel is an open-loop wind tunnel (Figure 9.4) situated inside a large climate test chamber [136]. The tunnel has been originally designed for investigations of wind turbine icing at low velocities, up to a maximum airspeed of v=50m/s. The internal test section has a size of 0.65×0.65×1.0m. The icing wind tunnel facility can operate in the temperature range of T=−25…+30°C. A 3×3 spray nozzle grid generates a droplet cloud with a liquid water content range of LWC=0.1…1.0g/m³ and a median (droplet) volume diameter range of MVD=12…30µm.

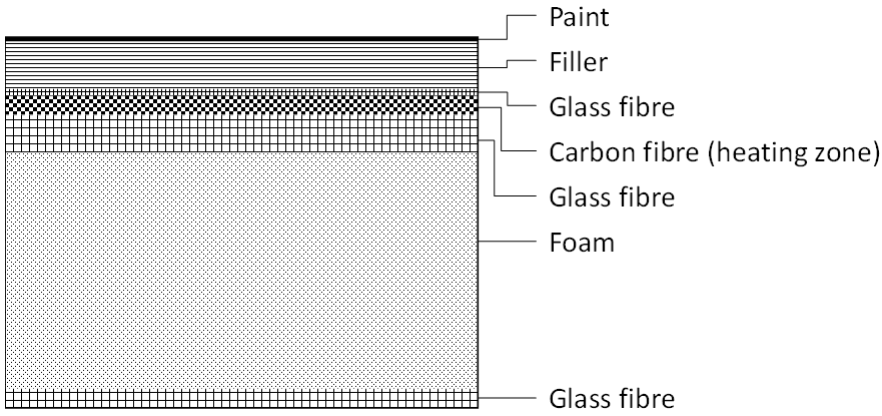

Figure 9.5: Schematic layout of the composite wing structure.

The test wing is a rectangular wing with a chord c=0.45m and a span b=0.65m. The wing is based on the RG-15 airfoil, which is low-Reynolds airfoil specifically designed for UAV and model aircraft. The wing was manufactured from fiber-reinforced epoxy. In this study, we placed the wing at the end of the tunnel for better accessibility to the IPS (Figure 9.4). The electrothermal heating for the IPS was supplied by carbon-fiber heating zones that were integrated into the wing structure (Figure 9.5). Power was supplied and monitored for each zone individually. Power delivery to the heating was regulated via a control board using pulse-width modulation (PWM) [48].

Two D•ICE prototypes were used in this study: a conventional design and a parting strip design. The conventional design (Figure 9.3a) consisted of one primary heating-zone extending over the leading edge, with a total width of 5cm. A secondary heating-zone with a width of 5cm was located on the upper and lower side of the airfoil. The parting strip (Figure 9.3b) design had two primary zones at the leading edge, each with a width of 2.5cm and two secondary zones with a width of 5cm each. A thin heating element acting as parting strip was located between the two primary zones.

9.2.2 Anti-Icing

This study aims to determine the minimum required heat loads for anti-icing and de-icing. For anti-icing (Figure 9.8), the minimum required load was determined by iteratively reducing the power to the heating system until the point when ice accretions

became observable on the heated surfaces. A flowchart of the iterative procedure is shown in Figure 9.6 The process started with a heating load q_{start} that was high enough that in the first step no ice accretion occurred. The value is then halved repeatedly until a heat flux was found where ice occurs. The subsequent heat load was chosen as the mean between the load where ice occurs (q_{low}) and the load where no ice occurred (q_{high}). The procedure continued until the difference between the two loads became smaller than a limit ($q_{limit}\approx 0.3\text{kW/m}^2$). In this study, the limit was determined by the smallest step size of the power control unit. This method was applied for the conditions specified in Table 9.1. Each point has been repeated at least two times to verify repeatability.

9.2.3 De-Icing

For de-icing (Figure 9.7), the situation is more complex, as there are a total of three parameters that can be adjusted: the heat load during the heating cycle $q_{de\text{-}ice}$, the duration of the de-icing cycle $t_{de\text{-}ice}$, and the intercycle time between heating cycles $t_{intercycle}$, time in which ice accretes on the airfoil. To determine the optimal combination of these, a parameter study has been performed for the conditions specified in Table 9.2. In these tests, the de-icing load $q_{de\text{-}ice}$ and the intercycle time $t_{intercycle}$ were set and the resulting de-icing time $t_{de\text{-}ice}$ was then measured manually. The de-icing time was defined as the duration from the moment the heating was turned on until the moment when ice started shedding from the wing. Furthermore, the effect of angle of attack and airspeed on shedding times was investigated.

Table 9.1: Anti-icing test matrix.

Parameter	Range
Velocity v	25 m/s
Temperature T	−2, −5, −10 °C
Reynolds number Re	9×10^5
Liquid water content LWC	0.44 g/m³
Droplet diameter MVD	26 µm
Angle of attack α	0 °

Table 9.2: De-icing test matrix.

Parameter	Range
Velocity v	10, 18, 25 m/s
Temperature T	−2, −5, −10 °C
Reynolds number Re	3×10^5, 6×10^5, 9×10^5
Heat load $q_{de\text{-}ice}$ (approx.)	9, 12, 18 kW/m²
Intercycle time $t_{intercycle}$	120, 240, 360 s
Angle of attack α	0, 4, 8 °
Liquid water content LWC	0.44 g/m³
Droplet diameter MVD	26 µm

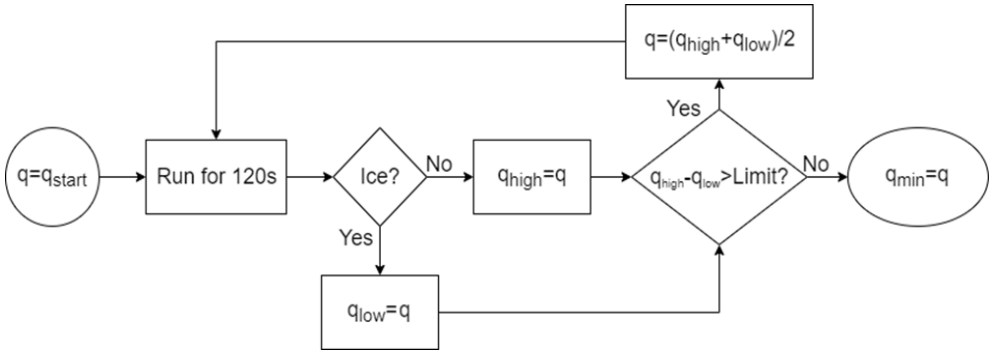

Figure 9.6: Flowchart of the minimum required anti-icing heat load procedure.

9.3 Results

9.3.1 Anti-Icing

The results for the anti-icing loads are shown in Figure 9.9. Two runs were conducted each for T=−2°C and T=−5°C. Four runs were conducted at T=−10°C, since it initially showed a larger variation. This large variation was likely related to the difficulty to identify the exact heat flux when steady-state anti-icing is achieved. The results show a strong linear correlation with the temperature. This behavior was expected and can be explained with the larger temperature difference (between ambient and freezing point) that needs to be overcome by the anti-icing system at lower temperatures.

9.3.2 Ice Thickness

The ice thickness is a key parameter for de-icing and depends on ice accretion time and temperature for v=25m/s (Figure 9.10). The ice thickness showed a good linear fit with the ice accretion time for all temperatures. The highest ice accretion rate occurred at T=−10°C, and was closely followed by T=−5°C. At temperatures close to the freezing point (T=−2°C), the ice accretion efficiency was lower most likely due to the formation of glaze ice. The resulting difference in ice thickness between the temperature was one parameter that affected the shedding times for both IPS systems. A remark is that together with thickness, other ice properties have varied (shape, density, and adhesion strength) for the tested temperature range.

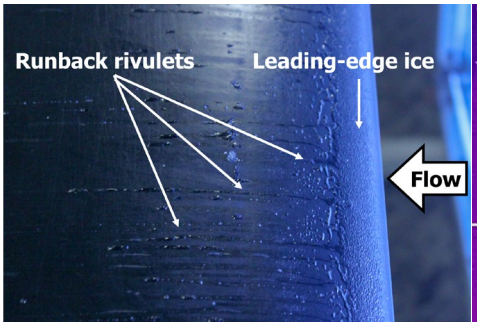

Figure 9.7: De-icing test, moments before the ice shedding. Liquid water is produced from the leading-edge and refreezes downstream.

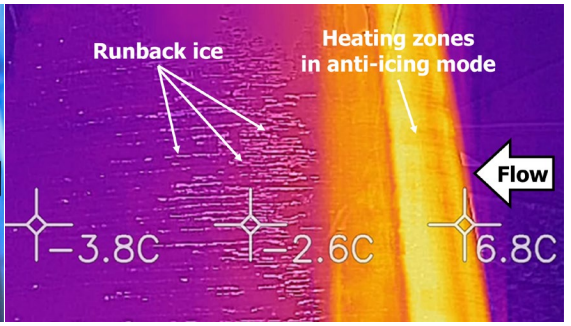

Figure 9.8: Thermal imagine of an anti-icing test. The leading-edge is continuously heated, producing runback water that refreezes downstream.

9.3.3 Conventional De-Icing

Shedding times for the conventional de-icing system were investigated for a range of ice accretion times, temperatures, and power settings (Figure 9.11). The results revealed three mechanisms. First, an increase in de-icing heat flux led to a decrease in shedding times. This was most likely related to a more rapid melting process at the ice/structure interface. Second, an increase in ice accretion time led to an increase in shedding time. A 2min increase in ice accretion time led to an approximate 50% increase in shedding time. This indicated that an increase in ice thickness, and consequently higher aerodynamic shedding forces, did not lead to faster shedding times. Instead, a large ice thickness at the leading-edge might be acting as an ice bridge between the upper and lower ice accretion regions. Moreover, the ice was kept in place by the stagnation pressure, and longer melting times were needed to achieve shedding. Third, the shedding times increase at lower temperatures. This was most likely related to the larger temperature difference that had to be overcome by the IPS. An evaluation of the total energy used ($E=q_{\text{de-icing}} \cdot t_{\text{shedding}}$) revealed a tendency that minimal energy for a given intercycle time is obtained with minimal heat flux. However, the data was not conclusive for all cases, which was mainly attributed to measurement uncertainties.

9.3.4 Parting Strip vs Conventional De-Icing

To showcase the effect of the parting strip on ice shedding, a comparison between the conventional system, the parting strip system with deactivated parting strip, and activated parting strip were conducted (Figure 9.13). The test was run at T=−2°C and $t_{intercycle}$=4min at relatively similar heat fluxes q=[10.5…12.5 kW/m²]. The results showed that there is little difference between the conventional system and the deactivated parting strip. The latter shed ice slightly later compared to the conventional system even though it used almost 20% more power. This was likely related to the unheated gap on the parting strip system (as the parting strip itself was deactivated) which delayed the melting process. The ice/surface interface near the gap needed longer to heat which resulted in the increased shedding time. Also, that area might have been acting as an anchor point of ice, reducing aerodynamic shedding efficiency.

In contrast, shedding times for the system with activated parting strip were substantially lower compared to the conventional system. The parting strip system shed ice more than three times faster than the conventional system. As discussed before, this can be explained by significantly increasing the shedding forces related to the aerodynamic drag of the ice shapes.

9.3.5 Parting Strip De-Icing

Further tests were conducted with variations of intercycle time, heat fluxes, and temperatures (Figure 9.12). Similar to the conventional IPS, decreasing heat fluxes increased shedding time. However, the shedding times for T=−2°C with the lowest heat flux setting decreased uncharacteristically little compared to the higher heat flux cases. Furthermore, while an increase in intercycle time led to increased ice shedding times for T=−5°C (in accordance with the conventional IPS – although with a smaller impact), for T=−2°C it led to decreased shedding times. We were not able to fully explain this behavior without further tests, but these effects may be related to measurement uncertainties (as the values vary in a range of ± 1 s), the difference in ice shapes, or the low adhesion forces of glaze ice cases. Continuous power usage of the parting strip scaled linearly with ambient temperature as $P_{parting\ strip}$=[7.1, 20.2, 45.6 W] for the temperatures T=[−2, −5, −10 °C].

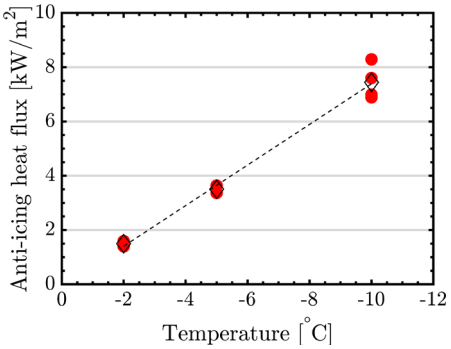

Figure 9.9: Minimum required heat fluxes for anti-icing at different temperatures.

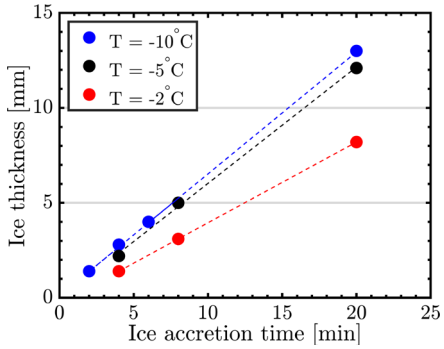

Figure 9.10: Ice thickness over ice accretion time at different temperatures.

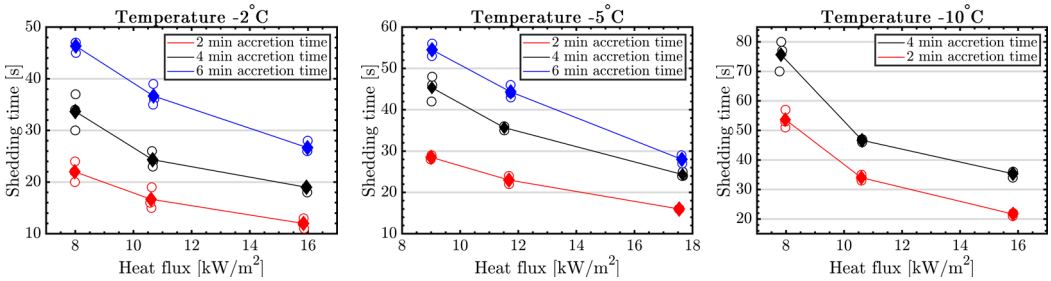

Figure 9.11: Shedding times of the conventional de-icing IPS for three different temperatures: *T*=−2° (left), *T*=−5° (middle), and *T*=−10° (right).

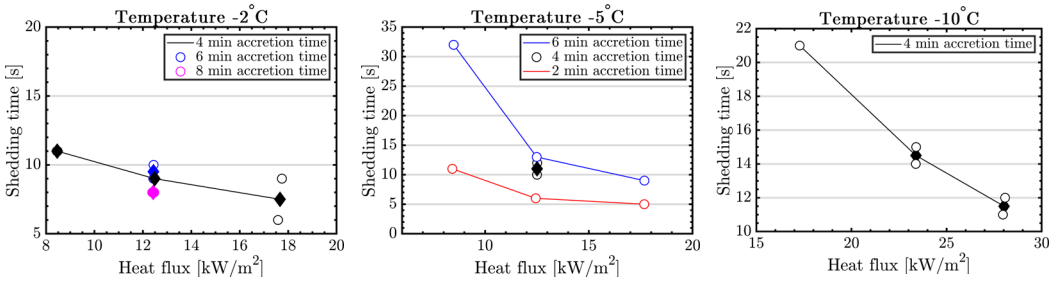

Figure 9.12: Shedding times of the parting strip de-icing IPS for three different temperatures: *T*=−2° (left), *T*=−5° (middle), and *T*=−10° (right).

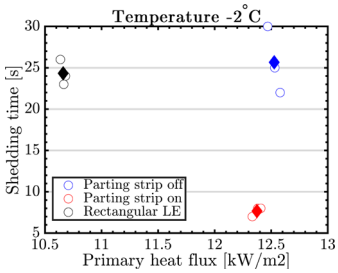

Figure 9.13: Comparison of conventional to parting strip IPS, with activated and deactivated parting strip.

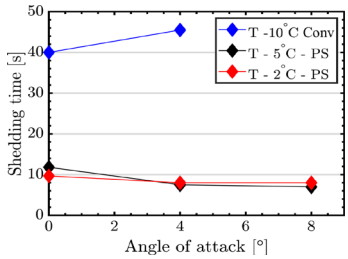

Figure 9.14: Comparison of conventional (Conv) to parting strip (PS) IPS for different angles of attack.

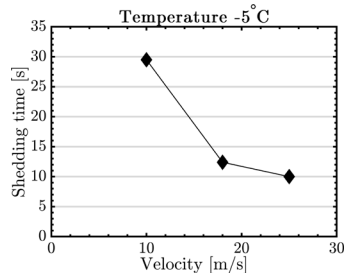

Figure 9.15: Comparison of the parting strip IPS at different velocities.

9.3.6 Angle of Attack

Three test series were conducted to investigate the effect of the angle of attack (AOA) during icing on de-icing efficiency. For the parting strip system, three AOAs $\alpha = [0, 4, 8\,°]$ were tested each at $T = [-2, -5\,°C]$. The conventional de-icing system was tested at two AOAs $\alpha = [0, 4\,°]$ and $T = -10°C$. All three results are shown in Figure 9.14. For the parting strip system, a higher AOA resulted in about 20–30% reduced de-icing times. This might be related to the higher-pressure difference over the airfoil, which resulted from the increase in AOA. This was likely to increase the efficiency of aerodynamic shedding. The temperature seemed to play only a minor role in this mechanism.

For the conventional system, a de-icing time increase of about 10% occurred. This was in line with previous experiences that showed an increase in the de-icing time at higher AOAs. This effect was likely linked to the fact that at higher AOAs a larger area of the airfoil is iced and that the increased aerodynamic forces are less efficient on the fully iced leading-edge.

9.3.7 Airspeed

The influence of the airspeed was tested at $T = -5°C$ on the parting strip system for three airspeeds $v = [10, 18, 25\,\text{m/s}]$. The water flow rate of the droplet spray nozzles was kept constant, meaning that the LWC was coupled to the airspeed. The corresponding values for each airspeed are $LWC = [0.96, 0.69, 0.44\,\text{g/m}^3]$. The results (Figure 9.15) showed a clear trend of a decrease in de-icing time with increasing velocity. This is most likely

related to the substantial decrease in aerodynamic shedding forces, which are kinetic forces and are thus quadratically related to the airspeed [77]. This effect is dominating over secondary effects that would result in a tendency to decrease shedding times for lower airspeeds: First, the increase in LWC leads to larger ice accretions that may lead to a decrease shedding times due to increased drag. Second, the lower airspeeds lead to lower heat convection and thus more efficient heating from the IPS – although this effect might be offset by the higher LWC and larger ice thicknesses. Both these effects were likely subdued by the decrease in aerodynamic forces. In addition, we visually observed that significantly more melting occurred for the lower airspeeds compared to the higher.

9.4 Discussion

The main objective of this study was to compare three different IPS methods: anti-icing, conventional de-icing, and parting strip de-icing. For de-icing, several variations of ice accretion time and heat fluxes were tested. In order to identify the most energy-efficient IPS, a time-averaged energy consumption $\bar{q}$ is calculated for each case:

$$\bar{q} = \frac{q_{\text{de-icing}} \cdot t_{\text{shedding}} + q_{\text{parting strip}} \cdot t_{\text{intercycle}}}{t_{\text{intercycle}} + t_{\text{shedding}}} = \left[\frac{\text{J}}{\text{s}\cdot\text{m}^2}\right] = \left[\frac{\text{W}}{\text{m}^2}\right]$$

This value calculates the total energy that has been spent on IPS in relation to the total cycle time. The unit of $\bar{q}$ is the same unit as for heat fluxes and can thus be directly compared to anti-icing heat loads.

The comparison is performed for each ambient temperature separately (Figure 9.16). Heat flux levels were indicated with “low”, “mid”, and “high” and their numeric value can be identified from Figure 9.11 and Figure 9.12. The first observation was that anti-icing required significantly more energy than all other cases. There was a strong temperature dependency on this effect, which implied that de-icing methods became more efficient compared to anti-icing for lower temperatures. The reason for this was that anti-icing systems need to continuously provide enough heat to compensate for the temperature difference between ambient and freezing point, whereas de-icing systems do this periodically.

The second conclusion was that parting strip de-icing was more energy-efficient than conventional de-icing, for any given intercycle time. The advantage of the parting strip was temperature-dependent, requiring approximately half of the energy than the

conventional IPS for T=−2°C and −5°C. For the lowest temperature T=−10°C, the advantage decreased. The reason for this was not clear. It could be related to the higher ice adhesion forces at a lower temperature or to insufficient heating of the parting strip and a too-small gap in the ice.

Third, a longer ice accretion time led to lower energy requirements for both conventional and parting strip IPS. The system was more efficient since the ratio of ice accretion time to active IPS time was larger, resulting in a larger denominator in $\bar{q}$.

Last, no clear trend could be observed for the influence of the level of the heat flux on the time-averaged energy consumption. It remains unclear if a high heat flux over a shorter time is more energy-efficient compared to a lower heat flux over a longer time. This was explained by the formulation of $\bar{q}$ where the deicing heat flux is linked to the shedding time. Their inverse proportionality made them partly compensate for their behavior.

The outcome of this study strongly indicated that the most energy-efficient method of IPS is a parting strip de-icing system. However, there were several limitations to this study that should be noted. An assessment of IPS efficiency cannot be based solely on its energy consumption. Secondary effects, that add to the overall power consumption of the UAV need to be considered as well. This includes aerodynamic performance degradations by intercycle ice and runback icing. These ice forms introduce aerodynamic penalties by decreasing lift and increasing drag [85, 154]. The UAV needs to compensate these, by increasing thrust and AOA. This will require additional power consumption that needs to be considered for the overall assessment of IPS efficiency. With regard to the size and layout of the heating panels, we found that the most important parameters are to keep the gap between zones minimal. Also, that the entire area that is covered by ice is heated.

Runback icing occurred during both, anti-icing and de-icing, and can be observed in Figure 9.7 and Figure 9.8. In addition to the aerodynamic penalties, runback icing introduces the risk of freezing on downstream control surfaces. This can block their movement and is a severe risk for the UAV [65]. Control of runback icing with an IPS can be achieved for example by multiple heating zones that are operated sequentially.

De-icing also introduces the risk of shed ice hitting critical components downstream. This is a risk for equipment like antennas, sensors, propellers, or engine inlets that are

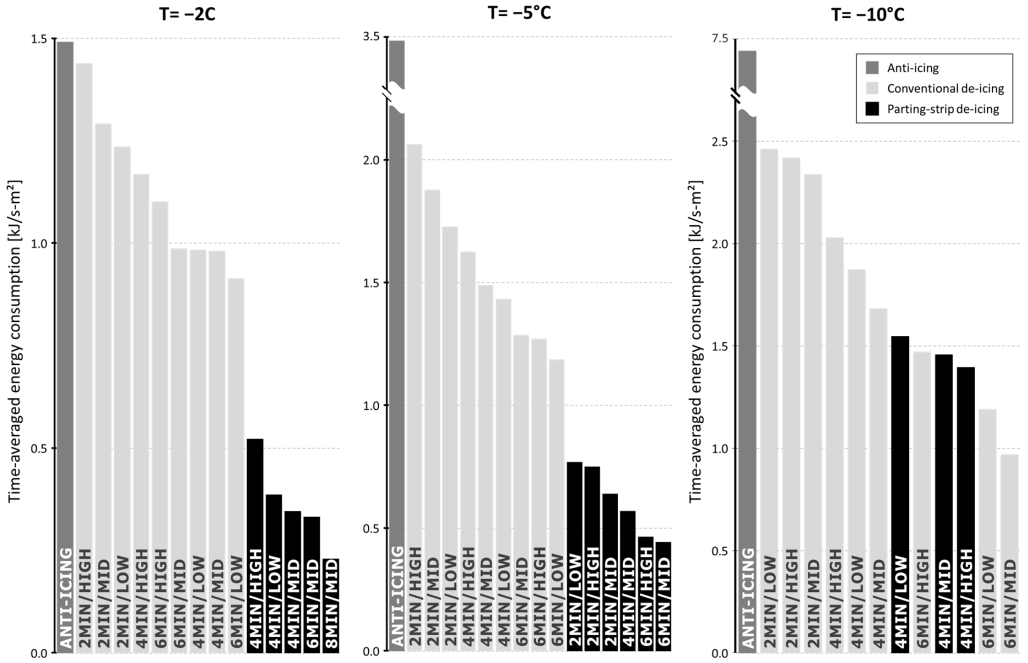

Figure 9.16: Overview of the time-averaged total energy consumption for all IPS runs.

located downstream of protected surfaces [86]. This risk is non-existent for anti-icing IPS and needs therefore careful evaluation for de-icing IPS.

There are several limitations to the experimental methods that add uncertainty to this study. First, the calculation of the heat fluxes was based on the electric power provided to the heating zones. In reality, only a part of this power is effectively used by the IPS. The largest loss occurs due to heat conduction into the wing. Furthermore, losses due to the electric system were not accounted for. We recommend that for future tests the actual heat flux generated by the heating panels should be measured. Second, the ice shedding times were observed manually. This added subjectivity to the test (based on the experimenter's reaction time) and limited the accuracy of the time measurement.

Video data were collected during these tests, but to process this data takes substantial work. High-speed flow visualizations of the de-icing experiments were recorded at 60 and 120 frames per second from 3 viewpoints. The video-data results could highly increase the shedding time measurement accuracy and give more information about the ice shedding mechanism. Filmed in high-resolution, these visual observations show the

liquid layer formation under the ice. This could give more information about the detachment mechanism and could be used for a qualitative runback ice investigation.

9.5 Conclusion

Atmospheric icing imposes limitations on UAVs that can be overcome with IPS. An electrothermal IPS was tested at the icing wind tunnel facilities of VTT. The main objective of this study was to identify which IPS method was the most energy-efficient and to investigate the effect of angle of attack and airspeed on de-icing. The results suggest that anti-icing was the least energy-efficient method of IPS. De-icing has proven to require substantially lower heat loads at all temperatures. A conventional IPS, with a periodically heated leading-edge, and a parting strip IPS, with a continuously heated small area, were tested for de-icing. De-icing with the parting strip has shown to require up to 50% less energy compared to a conventional de-icing system.

This study showed that the energy-efficiency of an IPS is determined by the IPS method chosen. An efficient IPS needs, therefore, to be carefully engineered and controlled. There is a large number of parameters that influence IPS efficiency, which need to be balanced and adjusted depending on the icing conditions. This experimental work offered additional insights into the interrelation of these parameters and can be used for comparison with numerical methods.

Under the assumption that the ice shedding mechanism for a de-icing case results from a force imbalance between the aerodynamical and viscous forces at the substrate surface – future work will be to couple these experiments with phase change and aerodynamical simulations, the latter validated against simplified force measurements. This would increase the understanding of the de-icing mechanisms and help to further improve the electrothermal IPS efficiency.

.

Part V

Epilogue

10 Concluding Remarks and Future Work

The goal of this thesis was to investigate the challenge of atmospheric in-flight icing on UAVs. Since little research was available for this field, the thesis aimed to answer a wide range of basic questions. Why is icing on UAVs a problem? What are the specific issues of icing on UAVs? How can we predict ice accretions on UAVs? What impacts does icing have on UAVs? How can we protect UAVs from icing? And, how much energy is required for an active UAV IPS?

The answers provided by this thesis can be summarized in short as follows: Atmospheric icing is a severe hazard for UAVs and restricts their operational envelope. Icing limits UAV usefulness and can be a significant obstacle for emerging applications, e.g. package deliveries or UAV operation in cold climates or environments. This is the motivation for increasing our understanding of icing effects on UAVs and ways of mitigating them.

Icing on UAVs differs from icing on manned aircraft in several key aspects. First, due to their smaller size and lower velocities, UAVs are more sensitive to icing. Second, due to the difference in their mission profile, UAVs may be exposed for longer durations to icing conditions. Third, icing nowcasting and forecasting tools are not accurate enough to be used for mission planning of UAVs that operate close to the ground. Last but not least, while a large amount of research and tools exist for manned aircraft, it is unclear to which degree they can be applied for UAVs. One of the main differences is related to the difference in the Reynolds number regime, with UAVs operating at substantially lower Reynolds numbers compared to manned aircraft.

Ice accretions can be predicted on UAVs with experimental methods in icing wind tunnel tests and numerical simulations with tools like LEWICE or FENSAP-ICE. Renting experimental facilities is expensive and time-consuming, so simulations are beneficial. Comparisons between the experiments and simulations have shown that the numerical methods manage to capture the general ice shapes reasonably well. However, there are still significant limitations, especially when it comes to the complexity of the ice shapes

and icing limits. The data generated in this thesis is suited for better validation of numerical tools in the future, but no in-depth analysis has been performed yet.

Ice on UAVs causes flow disruptions in form or separation bubbles and increased turbulence, which consequently leads to a decrease in aerodynamic performance. This thesis has shown through wind tunnel experiments and numerical simulations that ice can lead to a substantial reduction in lift, increase in drag, and deterioration of the stall behaviour. Numerical simulations are an easy tool to investigate the influence of different icing parameters on these performance penalties. Comparison with experiments has shown that the simulations perform well for simpler icing cases but have limitations when ice shapes become more complex. This thesis also demonstrated that the most hazardous meteorological icing conditions occur close to the freezing point with small droplet sizes. Furthermore, it was shown, that smaller aircraft sizes are more sensitive to icing compared to larger aircraft.

IPS are used to prevent the adverse effects of icing. This study briefly discusses the main IPS technologies and the key requirements for a UAV-specific system (mainly: weight and energy-efficiency). One example of such a system is the electrothermal D•ICE system based on carbon fibre heating. This thesis explored different operational modes and designs of this IPS with the aim to find the most energy-efficient mode. In terms of pure energy requirements for removing ice from a fixed-wing surface, a de-icing system with a parting strip was the best solution.

In the following, the overall conclusions from this thesis are drawn for each part in more detail. Also, the potential of future work is discussed for each section individually.

Part I focussed on the general challenges of atmospheric in-flight icing on UAVs and discussed differences to icing on manned aircraft. Several key differences were identified, some of which were addressed throughout this thesis and which will be addressed later. Topics that are highly relevant for UAV icing but have not been covered further in this thesis should be investigated in the future. In particular, ice detection is a key requirement for the safe operation of UAVs with and without IPS for BVLOS operations. More research is required in identifying and designing ice sensors and methods that are suited for UAVs. Another open issue is the characterisation of icing environments for UAVs. This includes better nowcasting and forecasting models for icing that can be used for mission and path-planning of UAVs that operate in areas with icing risks.

Part II consisted of experimental and numerical work on the ice accretions on UAV airfoils at low Reynolds numbers. The experimental ice shape data that was collected during the icing wind tunnel campaigns was compared to the simulation tools FENSAP-ICE and LEWICE. The comparison showed that FENSAP-ICE was able to get a higher fidelity than LEWICE when it came to ice thicknesses and shape. However, neither of the codes was able to capture icing limits and the total ice area correctly.

Further work is planned with the existing datasets. A more in-depth comparison with numerical models will be conducted, aimed to validate numerical models for low-Reynolds applications. The full ice shape dataset will be made available to the scientific community. In addition, more work is planned for ice shape digitalization techniques that will allow more accurate capturing of the experimental ice shapes.

Part III investigated several effects of icing on aerodynamic performance. First, a comparison between experimental tests in a conventional wind tunnel and a numerical method was conducted. The results showed that the simulations were able to capture the general lift, drag, and stall behaviour for simpler icing cases. The numerical method showed limitations in accuracy when it came to complex ice shapes, in particular ice shapes that generated large separation zones. It was not entirely clear to which degree these deviations are related to the low Reynolds number regime or to the general limitation of the numerical method. Further work on this topic should use higher-order numerical schemes with more advanced turbulence models. Also, additional wind tunnel tests are planned on a UAV-specific airfoil. In addition to the measurement of lift and drag, and moments should be measured. Flow visualization techniques, e.g. particle image velocimetry, could offer additional insights into the effects of ice accretion on the flow at low Reynolds numbers. Furthermore, there is a need for validation of the entire process chain, to compare the simulated performance losses on a simulated ice shapes to experimental performance losses on an experimental ice shape at identical icing conditions.

Another objective in this part was to investigate the influence of meteorological icing parameters on ice accretion and icing performance penalties with numerical tools. The results showed that the largest performance degradations occur at temperatures close to the freezing point. This is important information for the design of IPS and mission planning in icing environments. Further work is planned to extend the investigated icing envelope to intermittent maximum icing (cumulus clouds) and SLD conditions.

Furthermore, the effect of airspeed and chord size on icing penalties was investigated numerically. A parameter study was conducted ranging from low to high Reynolds numbers. The results indicated that the airfoil size had a large influence on the level of performance penalties. Smaller chord lengths led to less total ice mass but higher relative ice thicknesses, larger specific ice areas, and extended icing limits. This led to significantly higher penalties in drag and lift. The effect of airspeed was mostly related to the additional aerodynamic heating which affected the icing regime. An increase in airspeed could change rime-like ice shapes to glaze. In the transition area, ice shapes with large horns and large performance penalties occurred. These results showed that UAVs are more sensitive to icing due to their typically smaller size and lower velocities compared to manned aircraft. Further work on this topic should aim to gain a wider understanding of combinations of meteorological and flight conditions that lead to worst-case icing scenarios.

Part IV described and investigated an electrothermal IPS that was designed specifically for UAVs. Numerical simulations indicated that the calculation of the required heat loads is mostly independent of 3D effects. Furthermore, the simulations showed that a running-wet anti-icing system is in almost all cases more energy-efficient than a fully evaporative system. To build more confidence in the numerical methods, more validation work should be conducted.

The electrothermal IPS was tested in an icing wind tunnel during several campaigns. The tests showed the capability of the system to autonomously detect icing and initiate icing mitigation actions. More work is required on showing the robustness of the ice detection algorithm, especially in natural icing conditions. Flight tests with the IPS are planned for the near future.

Finally, experimental tests were conducted to explore the most energy-efficient operation mode of the IPS. Anti-icing, conventional de-icing, and parting strip de-icing were compared to each other. The results showed that de-icing with a parting strip was the most energy-efficient method of ice mitigation. Further work on this topic should aim to improve the understanding of the underlying physics of ice shedding, possibly with the help of simulations. Also, more research is needed in order to assess the total power usage of the IPS, including the added drag from intercycle ice accretion during de-icing. Furthermore, the effects of runback icing on performance degradations and

ways to minimize runback icing need to be explored, too. The risk of detached ice fragments hitting downstream aircraft components should also be investigated further.

The results of this thesis are relevant to several potential stakeholders. First and foremost, this work highlights the hazards of icing to all UAV operators. UAV designers or manufacturers might find this information useful in deciding if a certain UAV type may or may not need an IPS. For IPS manufacturers this work offers relevant information about the specific requirements of UAV IPS and the differences to manned aircraft. Developers of numerical icing simulations tools can use the experimental data provided in this thesis for validation and improvement of their codes. Regulatory bodies can use the validation work in this thesis to evaluate the fitness of numerical icing simulations to be used for the certification of UAVs. This thesis also provides input for developers of autopilots and path planning algorithms to account for icing performance penalties or IPS energy requirements.

On a more generalized level, there are still several aspects of icing on UAVs that need further research. Based on this thesis the following additional fields have been identified:

- **Validation of numerical methods**. Further work to validate the existing numerical simulation tools for low Reynolds number applications.
- **Icing on rotors:** Numerical simulations of ice accretion, icing penalties, and ice shedding on rotors and propellers.
- **Icing on pitot tubes:** Investigation of icing rates on UAV pitot tubes with experiments and numerical simulations. Development of energy-efficient heated pitot tubes for UAVs.
- **Runback ice and intercycle ice:** Numerical and experimental studies on the effect of runback ice and intercycle ice on the aerodynamic performance at low Reynolds numbers.
- **Icing nowcasting and forecasting:** Development of icing products suitable for UAVs that operate at low altitudes. This also includes a better understanding of icing at lower altitudes.
- **Icing detection:** Development of ice sensors for UAVs which are low-cost, lightweight, small, energy-efficient but also sensitive to small amounts of icing.

- **IPS technologies:** Development of novel IPS technologies or transfer mature solutions to UAVs. This includes also passive (icephobicity) or hybrid IPS.
- **Regulations:** Development of international certification rules for the operation o UAVs in icing conditions. Also, the generating icing envelopes for specific UAV applications.
- **Ice-robust autopilots:** Development of autopilots methods that can detect icing based on performance changes and tolerate limited amounts of ice. This also includes path-planning methods that consider icing conditions.

11 Bibliography

[1] Federal Aviation Administration, *FAA National Forecast 2019-2039*, Report, 2019.

[2] Shakhatreh, H., Sawalmeh, A. H., Al-Fuqaha, A., Dou, Z., Almaita, E., Khalil, I., Othman, N. S., Khreishah, A., and Guizani, M., "Unmanned Aerial Vehicles (UAVs): A Survey on Civil Applications and Key Research Challenges," *IEEE Access*, vol. 7, 2019, pp. 48572–48634.

[3] ICAO, *Unmanned Aircraft Systems (UAS)*, ICAO Technical Report CIR328, 2011.

[4] Campbell, S. E., Clark, D. A., and Evans, J. E., "Preliminary UAS Weather Information Gap Analysis for UAV Operations," 2017.

[5] Cao, Y., Tan, W., and Wu, Z., "Aircraft icing: An ongoing threat to aviation safety," *Aerospace Science and Technology*, vol. 75, 2018, pp. 353–385.

[6] Leary, W. M., *We Freeze to Please: A History of NASA's Icing Research Tunnel and the Quest for Flight Safety*, National Aeronautics and Space Administration, 2002.

[7] Bernstein, B. C., Wolff, C. A., and McDonough, F., "An Inferred Climatology of Icing Conditions Aloft, Including Supercooled Large Drops. Part I," *Journal of Applied Meteorology and Climatology*, vol. 46, Jan. 2007, pp. 1857–1878.

[8] Bernstein, B. C., and Le Bot, C., "An inferred climatology of icing conditions aloft, including supercooled large drops. Part II: Europe, Asia, and the Globe," *Journal of Applied Meteorology and Climatology*, vol. 48, 2009, pp. 1503–1526.

[9] Siquig, A., *Impact of Icing on Unmanned Aerial Vehicle (UAV) Operations*, Naval Environmental Prediction Research Facility Report, 1990.

[10] Peck, L., Ryerson, C. C., and Martel, C. J., *Army Aircraft Icing*, Cold Regions Research and Engineering Laboratory Report, 2002.

[11] Haulman, D. L., *U.S. Unmanned Aerical Vehicles in Combat 1991-2003*, Air Force Historical Research Agency Report, 2003.

[12] United Kingdom Defence Safety Authority, *Loss of Watchkeeper (WK042) Unmanned Air Vehicle over Cardigan Bay in West Wales*, Service Inquiry, 2017.

[13] Koenig, G. G., Ryerson, C. C., and Kmiec, R., "UAV Icing Flight Simulation," *40th Aerospace Sciences Meeting & Exhibit*, Reno: AIAA-2002-0812, 2002.

[14] Bottyán, Z., "In-flight icing characteristics of unmanned aerial vehicles during special atmospheric condition over the Carpathian-basin," *Landscape & Environment*, vol. 7, 2013, pp. 74–80.

[15] Williams, N., Benmeddour, A., Brian, G., and Ol, M., "The effect of icing on small unmanned aircraft low Reynolds number airfoils," *17th Australian International Aerospace Congress (AIAC)*, Melbourne: 2017.

[16] Oo, N. L., Kay, N. J., Brenkley, A. J., and Sharma, R. N., "Investigation into the behaviour of an iced low Reynolds number aerofoil," *10th International Micro-Air Vehicles Conference*, 2018.

[17] Oo, N. L., Richards, P. J., and Sharma, R. N., "Numerical investigation of clean and ice-accreted aerofoils at low Reynolds number and low angle of attack," *21st Australasian Fluid Mechanics Conference*, 2018.

[18] Szilder, K., and Yuan, W., "In-flight icing on unmanned aerial vehicle and its aerodynamic penalties," *Progress in Flight Physics*, vol. 9, 2017, pp. 173–188.

[19] Szilder, K., and McIlwain, S., *In-Flight Icing of UAVs - The Influence of Reynolds Number on the Ice Accretion Process*, SAE Technical Paper 2011-01-2572, 2011.

[20] Avery, A. S., *Ice Accretion on Small Unmanned Aircraft*, Oklahoma State University PhD Thesis, 2019.

[21] Tran, P., Barruzi, G., Tremblay, F., Habashi, W., Petersen, P., Ligget, M., Vos, J., Benquet, P., and Fiorucci, S., "FENSAP-ICE Applications to Unmanned Aerial Vehicles (UAV)," *42nd AIAA Aerospace Sciences Meeting and Exhibit*, Reno: American Institute of Aeronautics and Astronautics, 2004.

[22] Li, L., Liu, Y., Zhang, Z., and Hu, H., "Effects of thermal conductivity of airframe substrate on the dynamic ice accretion process pertinent to UAS inflight icing phenomena," *International Journal of Heat and Mass Transfer*, vol. 131, 2019, pp. 1184–1195.

[23] Liu, Y., Li, L., Ning, Z., Tian, W., and Hu, H., "Experimental Investigation on the Dynamic Icing Process over a Rotating Propeller Model," *Journal of Propulsion and Power*, vol. 34, 2018, pp. 933–946.

[24] Liu, Y., Li, L., Chen, W., Tian, W., and Hu, H., "An experimental study on the aerodynamic performance degradation of a UAS propeller model induced by ice accretion process," *Experimental Thermal and Fluid Science*, vol. 102, 2019, pp. 101–112.

[25] Liu, Y., Li, L., Li, H., and Hu, H., "An experimental study of surface wettability effects on dynamic ice accretion process over an UAS propeller model," *Aerospace Science and Technology*, vol. 73, 2018, pp. 164–172.

[26] Yan, S., Opazo, T. I., Langelaan, J. W., and Palacios, J. L., "Experimental Evaluation and Flight Simulation of Coaxial-rotor Vehicles in Icing Clouds," *Journal of the American Helicopter Society*.

[27] Yan, S., Opazo, T., Palacios, J., Langelaan, J. W., and Germain, L.-D., "Experimental evaluation of multi-rotor UAV operation under icing conditions," *Annual Forum Proceedings - AHS International*, 2018.

[28] Fengler, M., *Study of Propeller Icing Hazard in Mini-UAV Aviation*, Meteomatics GmbH Technical Report, 2017.

[29] Sørensen, K. L., *Autonomous Icing Protection Solution for Small Unmanned Aircraft*, NTNU PhD Thesis, 2016.

[30] Buschhorn, S. T., Kessler, S. S., Lachmann, N., Gavin, J., Thomas, G., and Wardle, B. L., "Electrothermal Icing protection of Aerosurfaces Using Conductive Polymer Nanocomposites," *54th AIAA/ASME/ASCE/AHS/ASC Structures, Structural Dynamics, and Materials Conference*, Boston: AIAA 2013-1729, 213AD.

[31] Lawson, C. P., "Electrically powered ice protection systems for MALE UAVs - Requirements and integration challenges," *ICAS-Secretariat - 25th Congress of the International Council of the Aeronautical Sciences*, Hamburg: 2006.

[32] Rashid, T., Mughal, U. N., and Virk, M. S., "Atmospheric icing sensors for UAV's," *4th IEEE International Conference on Cognitive Infocommunications, CogInfoCom*, Budapest: 2013.

[33] Sorensen, K. L., Blanke, M., and Johansen, T. A., "Diagnosis of Wing Icing Through Lift and Drag Coefficient Change Detection for Small Unmanned Aircraft," *IFAC-PapersOnLine*, vol. 48, 2015, pp. 541–546.

[34] Botura, G., and Fahrner, A., "Icing Detection System - Conception, Development, Testing and Applicability to UAVs," *2nd AIAA "Unmanned Unlimited" Conf. and Workshop & Exhibit*, San Diego: AIAA 2003-6637, 2003.

[35] Tousi, M. M., and Khorasani, K., "Fault diagnosis and recovery from structural failures (icing) in unmanned aerial vehicles," *3rd Annual IEEE Systems Conference*, Vancouver: 2009.

[36] Rotondo, D., Cristofaro, A., Johansen, T. A., Nejjari, F., and Puig, V., "Robust fault and icing diagnosis in unmanned aerial vehicles using LPV interval observers," *International Journal of Robust and Nonlinear Control*, vol. 29, 2019, pp. 5456–5480.

[37] Cristofaro, A., Johansen, T. A., and Aguiar, A. P., "Icing Detection and Identification for Unmanned Aerial Vehicles Using Adaptive Nested Multiple Models," *Int. J. Adapt. Control Signal Process.*, vol. 31, Nov. 2017, pp. 1584–1607.

[38] Armanini, S. F., Polak, M., Gautrey, J. E., Lucas, A., and Whidborne, J. F., "Decision-making for unmanned aerial vehicle operation in icing conditions," *CEAS Aeronautical Journal*, vol. 7, 2016, pp. 663–675.

[39] Caliskan, F., and Hajiyev, C., "A review of in-flight detection and identification of aircraft icing and reconfigurable control," *Progress in Aerospace Sciences*, vol. 60, 2013, pp. 12–34.

[40] Hovenburg, A. R., Andrade, F. A. A., Hann, R., Rodin, C. D., Johansen, T. A., and Storvold, R., "Long range path planning using an aircraft performance model for battery powered sUAS equipped with icing protection system," 2020.

[41] Narum, E. F. L., Hann, R., and Johansen, T. A., "Optimal Mission Planning for Fixed-Wing UAVs with Electro-Thermal Icing Protection and Hybrid-Electric Power Systems," *International Conference on Unmanned Aircraft Systems (ICUAS)*, 2020.

[42] Hann, R., and Johansen, T., *Unsettled Topics in UAV Icing*, SAE Edge Research Report, 2020.

[43] Hann, R., Hearst, R. J., Sætran, L., and Bracchi, T., "Experimental and Numerical Icing Penalties of an S826 Airfoil at Low Reynolds Numbers," *Aerospace*, vol. 7, 2020.

[44] Hann, R., and Johansen, T. A., "UAV Icing: The Influence of Airspeed and Chord Length on Performance Degradation," *Aircraft Engineering and Aerospace Technology,* submitted 2020.

[45] Hann, R., "UAV Icing: Ice Accretion Experiments and Validation," *SAE Technical Papers*, SAE Technical Paper 2019-01-2037, 2019.

[46] Fajt, N., Hann, R., and Lutz, T., "The Influence of Meteorological Conditions on the Icing Performance Penalties on a UAV Airfoil," *8th European Conference for Aeronautics and Space Sciences (EUCASS)*, Madrid: 2019.

[47] Hann, R., "UAV Icing: Comparison of LEWICE and FENSAP-ICE for Anti-Icing Loads," *AIAA Scitech Forum*, San Diego: AIAA 2019-1286, 2019.

[48] Hann, R., Borup, K., Zolich, A., Sorensen, K., Vestad, H., Steinert, M., and Johansen, T., "Experimental Investigations of an Icing Protection System for UAVs," *SAE Technical Papers*, SAE Technical Paper 2019-01-2038, 2019.

[49] Hann, R., Enache, A., Nielsen, M. C., Stovner, B. N., van Beeck, J., and Johansen, T. A., "UAV Icing: Experimental Heat Loads for Electro Anti-Icing and De-Icing," *Atmospheric and Space Environments Conference*, Reno: 2020.

[50] Hann, R., Wenz, A., Gryte, K., and Johansen, T. A., "Impact of atmospheric icing on UAV aerodynamic performance," *Workshop on Research, Education and Development of Unmanned Aerial Systems, (RED-UAS)*, Linköping: 2017.

[51] Winter, A., Hann, R., Wenz, A., and Johansen, T. A., "Stability of a Flying Wing UAV in Icing Conditions," *8th European Conference for Aeronautics and Space Sciences (EUCASS)*, Madrid: 2019.

[52] Brandrud, L., Kroegenes, J., Hann, R., Bartl, J., Bracchi, T., and Saetran, L., "Aerodynamic Performance of the NREL S826 Airfoil in Icing Conditions," *Wind Energ. Sci. Discuss.*, vol. in review, 2017, pp. 1–17.

[53] Hann, R., "UAV Icing: Comparison of LEWICE and FENSAP-ICE for Ice Accretion and Performance Degradation," *Atmospheric and Space Environments Conference*, Atlanta: AIAA 2018-2861, 2018.

[54] Gryte, K., Hann, R., Alam, M., Roháč, J., Johansen, T. A., and Fossen, T. I., "Aerodynamic modeling of the Skywalker X8 Fixed-Wing Unmanned Aerial Vehicle," *2018 International Conference on Unmanned Aircraft Systems (ICUAS)*, 2018, pp. 826–835.

[55] IPCC, *IPCC Special Report on the Ocean and Cryosphere in a Changing Climate*, 2019.

[56] Storvold, R., Sweatte, C., Ruel, P., Wuennenberg, M., Tarr, K., Raustein, M., Hillesøy, T., Lundgren, T., and Sumich, M., *Arctic Science RPAS Operator's Handbook*, Arctic Monitoring and Assessment Programme (AMAP), 2015.

[57] Bragg, M. B., Broeren, A. P., and Blumenthal, L. A., "Iced-airfoil aerodynamics," *Progress in Aerospace Sciences*, vol. 41, 2005, pp. 323–362.

[58] Janjua, Z. A., Turnbull, B., Hibberd, S., and Choi, K. S., "Mixed ice accretion on aircraft wings," *Physics of Fluids*, vol. 30, 2018.

[59] Bernstein, B. C., Ratvasky, T. P., Miller, D. R., and McDonough, F., *Freezing Rain as an In-Flight Icing Hazard*, NASA Technical Memorandum NASA/TM-2000-210058, 2000.

[60] Farzaneh, M., *Atmospheric icing of power networks*, Springer, 2008.

[61] Mason, J. G., Strapp, J. W., and Chow, P., "The ice particle threat to engines in flight," *44th AIAA Aerospace Sciences Meeting*, Reno: AIAA 2006-206, 2006.

[62] Makkonen, L., "Modeling of Ice Accretion on Wires," *Journal of Climate and Applied Meteorology*, vol. 23, 1984, pp. 929–939.

[63] Kind, R. J., Potapczuk, M. G., Feo, A., Golia, C., and Shah, A. D., "Experimental and computational simulation of in-flight icing phenomena," *Progress in Aerospace Sciences*, vol. 34, 1998, pp. 257–345.

[64] Gent, R. W., Dart, N. P., and Cansdale, J. T., "Aircraft icing," *Philosophical Transactions of the Royal Society of London. Series A: Mathematical, Physical and Engineering Sciences*, vol. 358, Nov. 2000, pp. 2873–2911.

[65] Lynch, F. T., and Khodadoust, A., "Effects of ice accretions on aircraft aerodynamics," *Progress in Aerospace Sciences*, vol. 37, 2001, pp. 669–767.

[66] FAA, *Aircraft Ice Protection*, Federal Aviation Administration Advisory Circular AC 20-73A, 2006.

[67] Neel, C. J., and Bright, L., *The Effect of Ice Formation on Propeller Performance*, NACA Technical Note NACA/TN/2212, 1950.

[68] Flemming, R. J., "The past twenty years of icing research and development at Sikorsky Aircraft," *40th AIAA Aerospace Sciences Meeting and Exhibit*, 2002.

[69] Cao, Y., and Chen, K., "Helicopter icing," *Aeronautical Journal*, vol. 114, 2010, pp. 83–90.

[70] De Souza, J. R. B., Lisboa, K. M., Cerqueira, I. G., Zotin, J. L. Z., Naveira-Cotta, C. P., and Cotta, R. M., "Conjugated heat transfer analysis of heated aeronautical pitot probes with flight tests experimental validation," *Heat Transfer Engineering*, vol. 36, 2015, pp. 991–1000.

[71] Gardner, L., Moon, G., and Whyte, R. B., *Aircraft carburetor icing studies*, SAE Technical Paper 710371, 1971.

[72] Pfeifer, G., *Aircraft engine icing, technical summary*, AGARD AGARD Icing Testing for Aircraft Engines, AGARD CP 236, 1978.

[73] Federal Aviation Administration, *14 CFR Parts 25 and 29, Appendix C, Icing Design Envelopes*, DOT/FAA/AR-00/30, 2002.

[74] New Zealand Civil Aviation Authority, *Aircraft Icing Handbook*, 2000.

[75] Green, S. D., "A study of U. S. inflight icing accidents and incidents, 1978 to 2002," *44th AIAA Aerospace Sciences Meeting*, Reno: AIAA 2006-82, 2006.

[76] Jeck, R., *The Upper and Lower Temperature Limits for Aircraft Icing*, Federal Aviation Administration Icing Information Note, 2004.

[77] Scavuzzo, R. J., Chu, M. L., and Ananthaswamy, V., "Influence of aerodynamic forces in ice shedding," *Journal of Aircraft*, vol. 31, 1994, pp. 526–530.

[78] Chao, H., Cao, Y., and Chen, Y., "Autopilots for small unmanned aerial vehicles: A survey," *International Journal of Control, Automation and Systems*, vol. 8, 2010, pp. 36–44.

[79] Masters, C. O., *A New Characterization of Supercooled Clouds below 10,000 Feet AGL*, FAA Technical Report DOT/FAA/CT-83/22, 1985.

[80] Jeck, R. K., *A New Data Base of Supercooled Cloud Variables for Altitudes up to 10,000 Feet AGL and the Implications for Low Altitude Aircraft Icing*, FAA Technical Report DOT/FAA/CT-83/21, 1983.

[81] Battisti, L., *Wind Turbines in Cold Climates*, Springer, 2015.

[82] Bernstein, B. C., McDonough, F., Politovich, M. K., Brown, B. G., Ratvasky, T. P., Miller, D. R., Wolff, C. A., and Cunning, G., "Current Icing Potential: Algorithm Description and Comparison with Aircraft Observations," *Journal of Applied Meteorology*, vol. 44, 2005, pp. 969–989.

[83] Jeck, R. K., *A History and Interpretation of Aircraft Icing Intensity Definitions and FAA Rules for Operating in Icing Conditions*, Federal Aviation Administration Technical Report DOT/FAA/AR-01/91, 2001.

[84] Homola, M. C., Nicklasson, P. J., and Sundsbø, P. A., "Ice sensors for wind turbines," *Cold Regions Science and Technology*, vol. 46, 2006, pp. 125–131.

[85] Broeren, A. P., Bragg, M. B., and Addy, H. E., "Effect of intercycle ice accretions on airfoil performance," *Journal of Aircraft*, vol. 41, 2004, pp. 165–174.

[86] Thomas, S. K., Cassoni, R. P., and MacArthur, C. D., "Aircraft anti-icing and de-icing techniques and modeling," *Journal of Aircraft*, vol. 33, 1996, pp. 841–854.

[87] Habashi, W. G., Aubé, M., Baruzzi, G., Morency, F., Tran, P., and Narramore, J. C., "FENSAP-ICE : A Fully-3D in-Flight Icing Simulation System for Aircraft, Rotorcraft and UAVs," *24th International Congress of the Aeronautical Sciences*, ICAS, 2004.

[88] Wright, W., *User's Manual for LEWICE Version 3.2*, NASA/CR—2008-214255, 2008.

[89] Wright, W., and Rutkowski, A., *Validation Results for LEWICE 2.0*, NASA Technical Report NASA/CR—1999-208690, 1999.

[90] Anderson, D. N., *Manual of Scaling Methods*, NASA Technical Report NASA/CR—2004-212875, 2004.

[91] IEA Wind Task 19, *Available Technologies for Wind Energy in Cold Climates*, Technical Report, 2018.

[92] Hann, R., "Opportunities and Challenges for Unmanned Aerial Vehicles (UAVs) in the Arctic," *13th ArcticNet Annual Scientific Meeting*, 2017.

[93] Liu, Y., Li, L., and Hu, H., "Effects of Ice Accretion on the Aerodynamic Performance and Wake Characteristics of an UAS Propeller Model," *tmospheric and Space Environments Conference*, Atlanta: AIAA 2018-3496, 2018.

[94] SAE International, *Icing Wind Tunnel Interfacility Comparison Tests*, Aerospace Information Report AIR5666, 2012.

[95] Hammond, D. W., and Luxford, G., "The Cranfield University Icing Tunnel," *41st Aerospace Sciences Meeting and Exhibit*, 2003.

[96] Rohatgi, A., "WebPlotDigitizer", Software, Retrieved 06/2018: www.automeris.io/WebPlotDigitizer.

[97] SAE International, *Calibration and Acceptance of Icing Wind Tunnels*, Aerospace Recommended Practice ARP5905, 2015.

[98] Macklin, W. C., "The density and structure of ice formed by accretion," *Quarterly Journal of the Royal Meteorological Society*, vol. 88, 1962, pp. 30–50.

[99] Jones, K. F., "The density of natural ice accretions related to nondimensional icing parameters," *Quarterly Journal of the Royal Meteorological Society*, vol. 116, 1990, pp. 477–496.

[100] Vargas, M., Broughton, H., Levy, P., Sims, J. J., Bleeze, B., and Gaines, V., *Local and Total Density Measurements in Ice Shapes*, NASA/TM—2005-213440, 2007.

[101] NATO RTO Technical Report 38, *Ice Accretion Simulation Evaluation Test*, RTO-TR-038 AC/323(AVT-006)TP/26, 2001.

[102] Occipital Inc, "Structure sensor" - Retrieved www.structure.io/structure-sensor.

[103] Koenderink, J. J., and van Doorn, A. J., "Affine structure from motion.," *Journal of the Optical Society of America. A, Optics and image science*, vol. 8, Feb. 1991, pp. 377–385.

[104] AgiSoft, "PhotoScan Professional", Software, Retrieved 06/2018: www.agisoft.com/downloads/installer.

[105] Addy, H. E., *Ice Accretions and Icing Effects for Modern Airfoils*, Technical Publication NASA/TP--2000-210031, 2000.

[106] Wallenius, T., and Lehtomäki, V., "Overview of cold climate wind energy: challenges, solutions, and future needs," *WIREs Energy and Environment*, vol. 5, 2016, pp. 128–135.

[107] McTavish, S., Feszty, D., and Nitzsche, F., "Evaluating Reynolds number effects in small-scale wind turbine experiments," *Journal of Wind Engineering and Industrial Aerodynamics*, vol. 120, 2013, pp. 81–90.

[108] Wood, D., *Small Wind Turbines*, Springer, 2011.

[109] Leary, J., Schaube, P., and Clementi, L., "Rural electrification with household wind systems in remote high wind regions," *Energy for Sustainable Development*, vol. 52, 2019, pp. 154–175.

[110] Probst, O., Martínez, J., Elizondo, J., and Monroy, O., "Small Wind Turbine Technology," *Wind Turbines*, I. Al-Bahadly, ed., IntechOpen, 2011.

[111] Carbon Trust, *Small-scale wind energy Policy insights and practical guidance*, Report, 2008.

[112] Shu, L., Liang, J., Hu, Q., Jiang, X., Ren, X., and Qiu, G., "Study on small wind turbine icing and its performance," *Cold Regions Science and Technology*, vol. 134, 2017.

[113] Feng, F., Li, S., Li, Y., and Tian, W., "Numerical simulation on the aerodynamic effects of blade icing on small scale Straight-bladed VAWT," *Physics Procedia*, vol. 24, 2012, pp. 774–780.

[114] O'Meara, M. M., and Mueller, T. J., "Laminar Separation Bubble Characteristics on an Airfoil at Low Reynolds Numbers," *AIAA Journal*, vol. 25, 1987, pp. 1033–1041.

[115] Seifert, H., and Richert, F., "Aerodynamics of Iced Airfoils and Their Influence on Loads and Power Production," *European Wind Energy Conference*, Dublin: 1997.

[116] Jasinski, W. J., Selig, M. S., Bragg, M. B., and Shawn C, N., "Wind Turbine Performance Under Icing Conditions," *Journal of Solar Energy Engineering*, vol. 120, 1998, pp. 60–65.

[117] Etemaddar, M., Hansen, M. O. L., and Moan, T., "Wind turbine aerodynamic response under atmospheric icing conditions," *Wind Energy*, vol. 17, 2014, pp. 241–265.

[118] Han, Y., Palacios, J., and Schmitz, S., "Scaled ice accretion experiments on a rotating wind turbine blade," *Journal of Wind Engineering and Industrial Aerodynamics*, vol. 109, 2012, pp. 55–67.

[119] Gao, L., Liu, Y., and Hu, H., "An experimental investigation on the dynamic ice accretion process over the surface of a wind turbine blade model," *9th AIAA Atmospheric and Space Environments Conference, 2017*, 2017, pp. 1–18.

[120] Hochart, C., Fortin, G., Perron, J., and Ilinca, A., "Wind turbine performance under icing conditions," *Wind Energy*, vol. 11, 2008, pp. 319–333.

[121] Hudecz, A., Koss, H., and Hansen, M. O. L., "Ice Accretion on Wind Turbine Blades," *15th International Workshop on Atmospheric Icing of Structures (IWAIS XV)*, St John's: 2013.

[122] Knobbe-Eschen, H., Stemberg, J., Abdellaoui, K., Altmikus, A., Knop, I., Bansmer, S., Balaresque, N., and Suhr, J., "Numerical and experimental investigations of wind-turbine blade aerodynamics in the presence of ice accretion," *AIAA Scitech Forum*, San Diego: AIAA 2019-0805, 2019.

[123] Jin, J. Y., and Virk, M. S., "Study of ice accretion and icing effects on aerodynamic characteristics of DU96 wind turbine blade profile," *Cold Regions Science and Technology*, vol. 160, 2019.

[124] Jin, J. Y., and Virk, M. S., "Experimental study of ice accretion on S826 & S832 wind turbine blade profiles," *Cold Regions Science and Technology*, vol. 169, 2020.

[125] Bartl, J., Sagmo, K. F., Bracchi, T., and Sætran, L., "Performance of the NREL S826 airfoil at low to moderate Reynolds numbers — A reference experiment for CFD models," *European Journal of Mechanics / B Fluids*, vol. 75, 2019, pp. 180--192.

[126] Barlow J, Rae W, P. A., *Low-Speed Wind Tunnel Testing*, Wiley, 1999.

[127] Habashi, W. G., Morency, F., and Beaugendre, H., "A Second Generation 3D CFD- based In-Flight Icing Simulation System," 2003.

[128] Reid, T., Baruzzi, G., Ozcer, I., Switchenko, D., and Habashi, W. G., "FENSAP-ICE Simulation of icing on wind turbine blades, part 1: Performance degradation," *51st AIAA Aerospace Sciences Meeting including the New Horizons Forum and Aerospace Exposition*, Grapevine: AIAA 2013-0750, 2013.

[129] Steinbrenner, J. P., "Construction of prism and hex layers from anisotropic tetrahedra," *22nd AIAA Computational Fluid Dynamics Conference*, 2015.

[130] ANSYS, "ANSYS FENSAP-ICE User Manual 18.2," 2017.

[131] Blazek, J., *Computational Fluid Dynamics: Principles and Applications*, Butterworth-Heinemann, 2015.

[132] Roache, P. J., "Quantification of Uncertainty in Computational Fluid Dynamics," *Annual Review of Fluid Mechanics*, vol. 29, 1997, pp. 123–160.

[133] Sagmo, K., Bartl, J., and Sætran, L., "Numerical simulations of the NREL S826 airfoil," *Journal of Physics: Conference Series*, vol. 753, Sep. 2016.

[134] Hansman, R. J., Breuer, K. S., Reehorst, A., and Vargas, M., "Close-up Analysis of Aircraft Ice Accretion," *31st Aerospace Sciences Meeting and Exhibit*, Reno: AIAA-93-0029, 1993.

[135] Somers, D. M., *The S825 and S826 Airfoils*, Technical Report NREL/SR-500-36344, 2005.

[136] Tiihonen, M., Jokela, T., Makkonen, L., and Bluemink, G., "VTT Icing Wind Tunnel 2.0," *Winterwind Conference*, 2016.

[137] Shin, J., and Bond, T. H., "Experimental and computational ice shapes and resulting drag increase for a NACA 0012 airfoil," *5th Symposium on Numerical and Physical Aspects of Aerodynamic Flows*, 1992.

[138] Krøgenes, J., and Brandrud, L., *Aerodynamic Performance of the NREL S826 Airfoil in Icing Conditions*, NTNU MSc Thesis, 2017.

[139] Ericsson, L. E., and Reding, J. P., *Unsteady Airfoil Stall*, NASA Report CR-66787, 1969.

[140] Lissaman, P. B. S., "Low-Reynolds-number airfoils," *Annual Review of Fluid Mechanics*, vol. 15, 1983, pp. 223–239.

[141] Héloïse, B., François, M., and Wagdi G., H., "FENSAP-ICE's three-dimensional in-flight ice accretion module: ICE3D," *Journal of Aircraft*, vol. 40, 2003.

[142] Bourgault, Y., Boutanios, Z., and Habashi, W. G., "Three-Dimensional Eulerian Approach to Droplet Impingement Simulation Using FENSAP-ICE, Part 1: Model, Algorithm, and Validation," *Journal of Aircraft*, vol. 37, 2000, pp. 95–103.

[143] Drela, M., *XFOIL: An Analysis and Design System for Low Reynolds Number Airfoils*, Berlin, Heidelberg: Springer Berlin Heidelberg, 1989.

[144] Fajt, N., *The Influence of Meteorological Conditions on the Icing Performance Penalties on a UAV Airfoil*, University of Stuttgart MSc Thesis, 2019.

[145] Sartorius, D., *Hitzdrahtmessungen zur Grenzschicht- und Nachlaufentwicklung bei Ablöseblasen in der Nähe der Profilhinterkante*, Diploma thesis, University of Stuttgart, 2001.

[146] Selig, M. S., Lyon, C. A., Giguere, P., Ninham, C. P., and Guglielmo, J. J., *Summary of Low-Speed Airfoil Data Vol. 2*, SoarTech Publications, 1996.

[147] SAE International, *Icing Wind Tunnel Interfacility Comparison Tests*, Aerospace Information Report AIR6189, 2017.

[148] Spalart, P., and Allmaras, S., "A one-equation turbulence model for aerodynamic flows," *30th Aerospace Sciences Meeting and Exhibit*, 1992.

[149] Chung, J. J., and Addy, H. E. J., *A Numerical Evaluation of Icing Effects on a Natural Laminar Flow Airfoil*, NASA Technical Report NASA/TM-2000-209775, 2000.

[150] Ozcer, I., Switchenko, D., Baruzzi, G. S., and Chen, J., "Multi-Shot Icing Simulations with Automatic Re-Meshing," *International Conference on Icing of Aircraft, Engines, and Structures*, SAE Technical Paper 2019-01-1956, 2019.

[151] Wang, C., Chang, S., and Su, X., "Simulation of Ice Accretion on Three Dimensional Wing," SAE Technical Paper 2011-38-0043, 2011.

[152] Goraj, Z., "An Overview of the De-icing and Anti-icing Technologies with Prospects for the Future.," *24Th International Congress of the Aeronautical Sciences*, 2004.

[153] Schlichting, H., "Boundary-Layer Theory," 1968.

[154] Whalen, EA; Broeren, AP; Bragg, M., "Characteristics of Runback Ice Accretions and Their Aerodynamic Effects," 2007.

[155] Morency, F., Beaugendre, H., Baruzzi, G., and Habashi, W., "FENSAP-ICE - A comprehensive 3D simulation system for in-flight icing," *15th AIAA Computational Fluid Dynamics Conference*, 2001.

[156] Reid, T., Baruzzi, G. S., Ozcer, I. A., and Habashi, W. G., "FENSAP-ICE: 3D Simulation, and Validation, of De-icing with Inter-cycle Ice Accretion," SAE Technical Paper 2011-38-0102, 2011.

[157] Quabeck, H., *HQ-Profile für den Modellflug*, HQ-Modellflugliteratur, 2014.

[158] Kays, W. M., Crawford, M. E., and Weigand, B., *Convective heat and mass transfer*, McGraw-Hill, 2005.

[159] Steinert, M., and Leifer, L. J., "Finding One's Way: Re-Discovering a Hunter-Gatherer Model based on Wayfaring," *International Journal of Engineering Education*, vol. 28, 2012.

[160] Holmes, D. G., and Lipo, T. A., *Pulse width modulation for power converters: principles and practice*, John Wiley & Sons, 2003.

[161] Dillingh, J. E., and Hoeijmakers, H. W., "Numerical simulation of airfoil ice accretion and thermal anti-icing systems," *ICAS Congress Proceedings*, 2004.

[162] Habashi, W. G., "Recent Progress In Unifying CFD and In-Flight Icing Simulation," *Tenth International Congress of Fluid Dynamics*, Ain Soukhna: 2010.

[163] Vukits, T. J., "Overview and risk assessment of icing for transport category aircraft and components," *40th AIAA Aerospace Sciences Meeting and Exhibit*, 2002.

[164] FAA, *Pilot Guide: Flight in Icing Conditions*, Federal Aviation Administration Advisory Circular AC 91-74B, 2015.

[165] SAE International, *Ice, Rain, Fog, and Frost Protection*, Aerospace Information Report AIR1168/4, 2016.

[166] Enache, A., Bernay, B., Glabeke, G., Planquart, P., and van Beeck, J., "Ice shedding phenomenon: an experimental and numerical investigation," *Atmospheric and Space Environments Conference*, AIAA, 2020.

[167] Sørensen, K. L., Helland, A. S., and Johansen, T. A., "Carbon nanomaterial-based wing temperature control system for in-flight anti-icing and de-icing of unmanned aerial vehicles," *IEEE Aerospace Conference Proceedings*, 2015.

[168] Wenz, A., and Johansen, T. A., "Icing detection for small fixed wing UAVs using inflight aerodynamic coefficient estimation," *IEEE Conference on Control Applications (CCA)*, 2016.

[169] Anderson, J. D., *Fundamentals of aerodynamics*, McGraw-Hill, 2010.

[170] Beard, R. W., and McLain, T. W., *Small unmanned aircraft: Theory and practice*, Princeton university press, 2012.

Appendix

A1 Flight Simulation of a UAV in Icing Conditions

A1.1 Introduction

In recent years, there has been a strong development and an increased utilization of unmanned aerial vehicles (UAVs). These automated drones are suitable for a wide range of applications and are used in many different industry or science areas today. Fixed-wing UAVs are well suited for remote sensing operations in isolated and harsh areas, such as the Arctic. However, cold climate conditions impose very special challenges for UAV operations. This is a topic that has only recently shifted into the focus of research.

The main problem for fixed-wing UAVs in cold climate conditions is atmospheric icing [9]. This type of icing occurs when super-cooled droplets in clouds collide with the leading-edge of the vehicle and form ice. This ice is considered to cause significant reduction in the aerodynamic performance. Icing has been attributed as the main reason for UAV losses in cold climate regions.

Atmospheric icing is not an issue only affecting UAVs. It is also relevant for manned aviation, wind turbines and building structures (e.g. power lines or masts). As such, there has been significant research performed on the topic, with the main focus being on aircraft icing. Transferring results from (commercial or military) aircrafts to UAVs is not a trivial task for a number of reasons. The main one being the difference in the Reynolds (Re) number regime between the two applications. Aircrafts are typically operating at relatively high Reynolds numbers $Re = [1...10 \times 10^6]$. Due to their smaller size and generally lower velocities, UAVs operate in the low-Reynolds number regime $Re = [1...10 \times 10^5]$.

The difference of approximately one order of magnitude in the Reynolds number has a significant impact on the flow characteristics. At low Reynolds numbers, the viscous forces are dominating over the inertial forces, which means that viscous boundary layer effects are more significant. For example, the transition point between laminar and turbulent flow occurs later (i.e. more downstream) for low Reynolds numbers. In

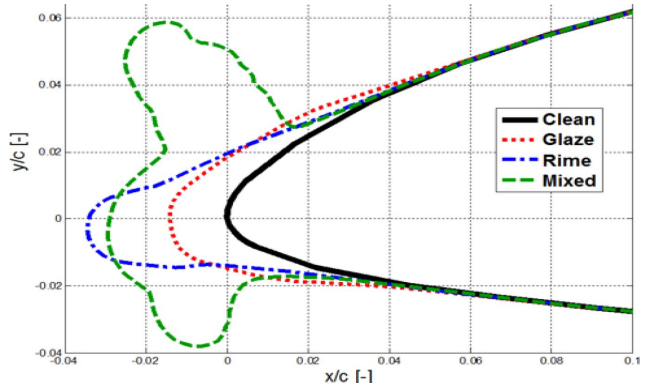

Figure A1.1: Icing test cases geometry.

addition, laminar separation almost exclusively occurs in the low Reynolds number regime. For this reason, it necessary to study the impact of atmospheric icing on UAVs specifically.

Recently there have been research efforts to detect icing in flight [33, 37, 167, 168]. Test flights with real UAVs in icing conditions are risky and it is challenging to acquire reliable baseline data of the aerodynamic coefficients in icing. Therefore, there is a need to generate datasets using flight simulators that can simulate the behaviour of a UAV in icing conditions to be able to test and develop new icing detection algorithms.

This paper makes an assessment of the impact of icing on the aerodynamic performance by using simulation tools and generic meteorological icing cases. The resulting lift, drag and momentum coefficients are then implemented in an existing UAV simulator and implications of icing on the autopilot reaction are studied.

A1.2 Methods

For low Reynolds numbers with free transition, the accurate prediction of lift and drag with CFD is challenging. This is due to the occurrence of laminar separation effects (e.g. laminar bubbles) which cannot be captured fully with common RANS-CFD methods [131]. In order to mitigate this problem, the calculations were performed fully-turbulent. This assumption is considered to be acceptable since the occurrence of ice

results in surface roughness heights that are likely to be large enough to trigger laminar-turbulent transition at the leading-edge.

A1.2.1 Numerical Tools

Several simulation tools have been utilized for this study. For the generation of 2D ice shapes, the LEWICE code (version 3.2.2) has been applied [88]. LEWICE is a widely used 2D ice accretion tool that has been developed for aerospace applications and which has been validated over a large range of parameters [89]. However, LEWICE is limited to Reynolds-numbers $Re>2.3\times10^6$ which falls out of the range for typical UAV applications. However, there are indications that the simulation methods used are also applicable for lower Reynolds-numbers, as long as there are no major low Reynolds effects present [65]. A strict proof of this is however still missing and should be investigated in the future.

The flow field around the iced geometries was solved with FENSAP, a state-of-the-art Reynolds-Averaged Navier-Stokes CFD solver [87]. The solver is part of the software package FENSAP-ICE which is a 3D icing simulation tool. In this study however, for the sake of simplicity, LEWICE was used for the ice generation and FENSAP only as a steady-state flow field solver. The turbulence model has been chosen as Spalart-Allmaras since it performs well for turbulent flows with negative pressure gradients [148]. Furthermore, a streamline upwind artificial viscosity is used.

A1.2.2 Geometry and Test Case

In order to assess the impact of icing on the aerodynamic performance of UAVs, icing was simulated on a 2D airfoil. The NREL S826 airfoil was selected due to the availability of experimental data to validate the simulation results [43]. The S826 airfoil was developed for 20–40m diameter horizontal-axis wind turbines with variable-pitch control. The main characteristics of the airfoil are a lift-to-drag ration, docile stall characteristics and insensitivity to transition [135]. This makes them relevant for UAV purposes (e.g. for long- endurance flights), although the design Reynolds number of $Re=1.5\times10^6$ is slightly higher than most UAV applications. Icing cases are generally defined by the following parameters: free stream icing velocity v_{icing}, duration of icing t_{icing}, airfoil chord length c, angle of attack (AOA) α_{icing}, liquid water content LWC, median volume diameter MVD and ambient temperature T_∞ [88]. For this study, a large number of combinations of these parameters have been simulated with LEWICE in order

Table A1.1: Icing test case parameters.

Parameter	Icing Type		
	Glaze	***Mixed***	***Rime***
v_{icing}	$25m/s$	$40m/s$	$25m/s$
t_{icing}	40 min	40 min	40 min
c	$0.3m$	$0.3m$	$0.3m$
α_{icing}	$0°$	$0°$	$0°$
MVD	$30\mu m$	$20\mu m$	$20\mu m$
LWC	$0.34g/m^3$	$0.55g/m^3$	$0.44g/m^3$
T_∞	$-2°C$	$-4°C$	$-10°C$
k_s	$0.6mm$	$1mm$	$1mm$

to find representative ice shapes for different icing cases. Based on the geometrical characteristics of the ice accretion such as location, extent, size, curvature, three ice shapes have been selected, Figure A1.1. In accordance with certification regulations of aircraft icing, an empirical correlation for droplet size and water content applicable for stratus clouds has been used [73]. The icing cases are mainly distinguished by the temperature at which they form and are summarized in Table A1.1. Reynolds numbers range from Re=0.9–1.4×10^6, depending on the airspeed.

Glaze ice is an ice type that forms at temperatures very close to freezing conditions. It is dominated by a low mass fraction of particles that freeze on impact. The majority of droplets form a liquid water film on the surface of the airfoil which will either freeze or evaporate. Due to aerodynamic friction, the liquid film will be flowing downstream as so- called runback. Glaze typically appears as transparent ice with a smooth surface.

At very low temperatures, all droplets freeze on impact and form rime ice. Due to entrapped air between the frozen droplets, rime appears as white and displays rugged, rough surface. Rime is one of the most commonly encountered ice forms in aviation. Mixed icing is an ice type that is formed in the temperature regime between rime and glaze. Therefore, it is characterized by a balanced ratio between instantaneous freezing and surface freezing. Due to this characteristic, the mixed ice builds up ice horns at an approximately 45° angle. The surface roughness k_s for each icing case was approximated using empirical correlations [137]. Generally, surface roughness is mainly driven by temperature and velocity, but also by droplet size. In cases with significant amount of instantaneous freezing (rime and mixed), the roughness will be larger than for cases with

surface freezing (glaze). It should be noted that the selected ice shapes may not be entirely representative for each icing type as ice shapes vary extensively over the parameters stated above. However, as they serve well to give an overview of the main mechanisms and impacts.

In this work, the complexity of the problem was reduced by only performing 2D simulations. Quantitative transferal of 2D simulations to 3D and to real-life flight characteristics is limited. However, it is considered that that the results allow for a qualitative assessment of the icing impact.

A1.3 Simulation Results

To evaluate the aerodynamic performance impact of icing, three key dimensionless characteristics are considered. The lift coefficient C_L represents the uplift force generated by the airfoil, the drag coefficient C_D relates to the resisting force of the airfoil and the moment coefficient C_M to the resulting airfoil moment [169]. All coefficients are related quadratic to the velocity and linearly to air density and chord length. Experimental validation results to verify the FENSAP simulations have been generated in a wind tunnel study using 3D printed artificial ice shapes on the NREL S826 airfoil [43]. An example for this is depicted in Figure A1.2 for the clean case. In general, the experimental data shows good fit with both simulation results in the linear section of the lift curve. The FENSAP results show a slight deviation of the gradient, which can be attributed to the simulations being run fully-turbulent and thus not resolving any laminar effects.

For the same reasons FENSAP is slightly over-predicting the maximum lift angle and maximum lift value. In the stall region, XFOIL shows an early onset of the trailing edge stall and a low maximum lift. This is likely to be related to the inaccurate formulation of the turbulent flow behavior inherent to any 2D panel code. The validation results for the drag coefficient as well as icing cases are not shown here, but exhibit the same good fit with similar behavior stall behavior as for the lift coefficient [43][52][52][52][51][50].

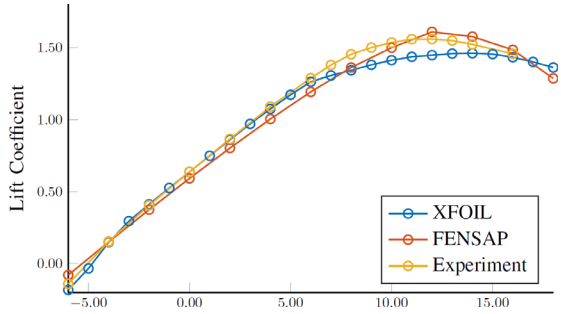

Figure A1.2: Experimental and simulation lift curves for the clean S826 airfoil at $Re = 2\times10^5$.

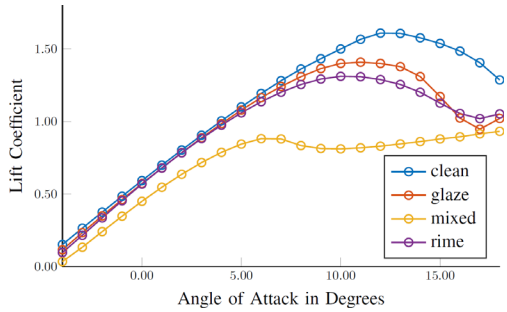

Figure A1.3: FENSAP simulation results of the lift curves for the clean and iced S826 airfoil at $Re = 2\times10^5$.

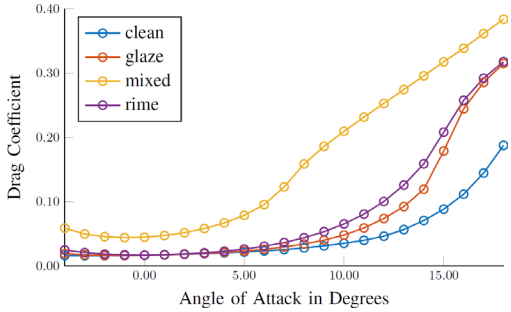

Figure A1.4: FENSAP simulation results of the drag curves for the clean and iced S826 airfoil at $Re = 2\times10^5$.

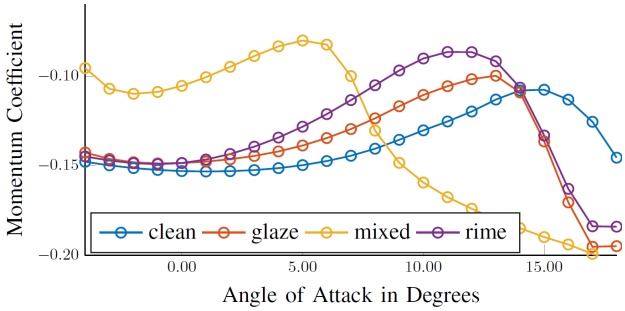

Figure A1.5: FENSAP simulation results of the moment curves for the clean and iced S826 airfoil at $Re = 2\times10^5$.

All icing cases show a clear negative impact on the aerodynamic performance. The lift curves in Figure A1.3 are affected in two ways. Firstly, the maximum lift angle is clearly reduced in all cases. A reduction of the maximum lift angle will negatively influence the stall behavior of a UAV. This is particularly relevant when operating at low velocities as that has to be compensated by a higher angle of attack. The reduction of maximum lift and lift angle may also be a critical issue for UAVs that facilitate for deep-stall landing maneuvers. The second effect is that for the mixed icing case the lift curves are shifted to lower values. This means that to maintain a specific point in the flight envelope, either the AOA or the velocity of the UAV has to be increased. As stated earlier, increasing the AOA is linked to an elevated risk for stall. The gradient of the lift curves seems not to be affected in a significant way for either case. The drag curves in Figure A1.4 show that all icing cases increase the aerodynamic resistance compared to the clean case. The increase in drag is larger for high AOAs. This is due to an earlier onset of trailing-edge separation. Again, the drag increase is most severe for the mixed icing case. Therefore, the thrust will have to be increased in order to overcome the additional drag force. As thrust generation is linked to fuel consumption, the effective range is decreased by icing. If a UAV does not have sufficient thrust reserves (i.e. the thrust cannot be increased further), it will have to decrease velocity and increase the AOA, which again is linked to an increased risk of stall.

In general, it can be observed that the type of icing has a significant impact on the severity of the degradation of the aerodynamic performance. Rime and glaze ice have apparently weaker effects on lift and drag than mixed. In the region of the lift and drag

curve with no flow separation (α = [4...8°]) rime and glaze show very little deviation from the clean case. Only at the more extreme AOAs the decrease of lift and increase in drag becomes substantial. This can be attributed to the relative smooth geometry which only affects the onset of trailing-edge flow separation at very high/low AOAs.

Rime ice shows a slightly stronger performance degradation than glaze. This can be attributed to the larger ice accretion and larger surfaces roughness of rime compared to the glaze case. Hence for the rime case the friction in the boundary layer will be increased which leads to higher drag and earlier onset of trailing-edge stall. Mixed ice is showing the strongest impact on lift, maximum lift angle and drag. The mixed ice geometry is the most complex geometry of all cases, with large convex and concave curvatures. In particular, the ice horns will generate turbulent flow separation on the top and the bottom of the leading edge. Separation bubbles cause increased drag and reduced lift [169]. In addition, the turbulence intensity in the boundary layer will be increased by the leading-edge separation, which will lead to an onset of trailing edge separation at lower AOAs compared to clean, rime and glaze.

Icing is affecting the pressure distribution over the surface and hence also affecting the moment. Similar to the lift and drag, the biggest impact on the moment curves in Figure A1.5 can be seen for the mixed icing case and in the stall region. The relatively smooth geometries of glaze and rime follow the trends of the clean curve with some offset at higher angles of attack. For mixed icing the curves shows a significantly abnormal behavior which is again related to the occurrence of the leading edge separation bubbles at the ice horn. The mixed icing case is therefore likely to impose significant challenges for the stability of the aircraft.

A1.4 Flight Simulation

The lift, drag and moment from the numerical icing simulation discussed in the previous sections, were used to expand an existing UAV simulator with the capability to simulate flights in icing conditions. The design of the flight simulator mainly follows Beard et al. [170] and uses a dynamic and a kinematic model of the aircraft to simulate its behavior. An autopilot was added to control the simulated aircraft's altitude, course and airspeed using successive loop closure with PID controllers and a state machine as described in [170]. For a more detailed discussion of the UAV modeling, control and simulation we refer to [170].

Table A1.2: Coefficients for flight simulations.

Parameter	Value	Parameter	Value
V_a	$20m/s$	$C_{L_{\delta_e}}$	0.587
ρ	$1.2250kg/m^3$	$C_{m_{\delta_e}}$	-0.971
S	$0.25m^2$	$C_{D_{\delta_e}}$	0.846
c	0.36	$C_{L_{\alpha},s}$	-0.3
C_{L_q}	3.89	$C_{D_{\alpha},s}$	0.01
C_{D_q}	0	$C_{m_{\alpha},s}$	0.14
M	$4kg$	P_{motor}	$600W$

In this paper we have focused on the influences of icing on the longitudinal aerodynamic forces. The lift and drag forces are given by

$$\begin{bmatrix} f_L \\ f_D \end{bmatrix} = \frac{1}{2}\rho S V_a^2 \begin{bmatrix} C_{L_\alpha}(\alpha) + C_{L_q}(\alpha)\frac{c}{2V_a} + C_{L_{\delta_e}}\delta_e \\ C_{D_\alpha}(\alpha) + C_{D_q}(\alpha)\frac{c}{2V_a} + C_{D_{\delta_e}}\delta_e \end{bmatrix}$$

where V_a is the airspeed, ρ is the air density, S is the wing area, c is the chord length, δ_e is the elevator deflection angle, C_L is the aerodynamic lift coefficient, C_D is the aerodynamic drag coefficient, C_{Lq} is the pitch rotation lift coefficient, C_{Dq} is the pitch rotation drag coefficient, C_{L_e} is the elevator lift coefficient and C_{D_e} is the elevator drag coefficient. The lift and drag forces can be converted to body forces using

$$\begin{bmatrix} f_x \\ f_z \end{bmatrix} = \begin{bmatrix} \cos(\alpha) & -\sin(\alpha) \\ \sin(\alpha) & \cos(\alpha) \end{bmatrix} \begin{bmatrix} f_L \\ f_D \end{bmatrix}$$

The pitch moment is given by

$$m = \frac{1}{2}\rho S V_a^2 c \left(C_{m_\alpha}(\alpha) + C_{m_q}(\alpha)\frac{c}{2V_a} + C_{m_{\delta_e}}\delta_e \right)$$

where C_m is the aerodynamic torque coefficient, C_{mq} is the pitch dampening coefficient and C_{m_e} is the elevator torque coefficient. We will assume that additional to the NREL S826 airfoil the aircraft is also equipped with a horizontal stabilizer which counteracts the moment created by the airfoil so that the aircraft fulfills trim conditions in clean conditions and normal cruise. Therefore, the C_L, C_D and C_m are modeled as follows

$$\begin{aligned} C_{L_\alpha} &= C_{L_\alpha,s} + C_{L_\alpha,airfoil} \\ C_{D_\alpha} &= C_{D_\alpha,s} + C_{D_\alpha,airfoil} \\ C_{m_\alpha} &= C_{m_\alpha,s} + C_{m_\alpha,airfoil} \end{aligned}$$

where the airfoil parameters are given by the respective curves for each icing scenario shown in Figure A1.3, Figure A1.4, and Figure A1.5. Since the numerical simulations only output discrete values, spline interpolation was used to generate continuous curves. The stabilizer coefficients $C_{L\alpha,s}$ and $C_{m\alpha,s}$ are chosen to compensate for the lift and torque created by the airfoil at $\alpha = 0°$ and $V_a = 20$m/s. Values for the different coefficients can be found in Table A1.2. Where M is the mass of the UAV and P_{motor} is the maximum power of the propulsion system. The coefficients in Table A1.2 are assumed to be not affected by icing.

A1.5 Flight Simulation Results

In this section results from the flight simulator in different icing conditions are shown. The implementation was done in Matalab / Simulink.

A1.5.1 Flight Scenario

The aircraft is flying in a constant horizontal wind of 8m/s added by Dryden wind gusts assuming a wind speed of 6m/s at 10m above ground. The aircraft's autopilot is set to fly at a constant course and a constant airspeed while performing the altitude changes shown in Figure A1.6. This scenario is simulated for the three different icing scenarios from Table A1.1 and the clean case.

A1.5.2 Angle of Attack

Figure A1.7 shows the AOA for the entire flight. Notable the AOA does not show a significant difference in the cruise phases between the clean, rime and glaze cases. However due to the flatter lift gradient in mixed icing conditions (3) the autopilot adjusts to a higher AOA during cruise, causing the aircraft to stall permanently and thus no stable flight is possible. To circumvent this the airspeed has to be adjusted to a higher value of $V_a = 22$m/s. Figure A1.8 shows the angle of attack during a climb. The figure clearly

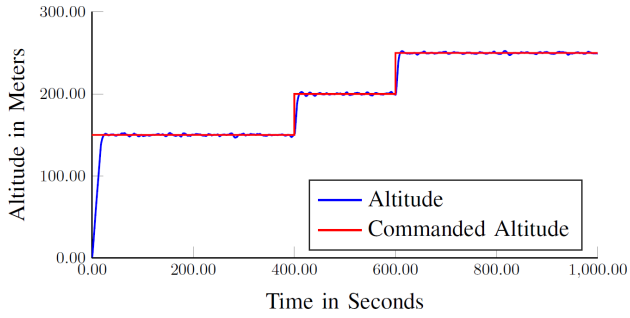

Figure A1.6: Commanded and resulting altitude of the UAV.

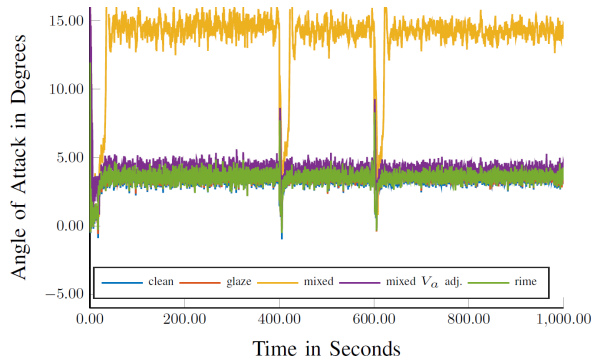

Figure A1.7: Angle of Attack for different icing conditions.

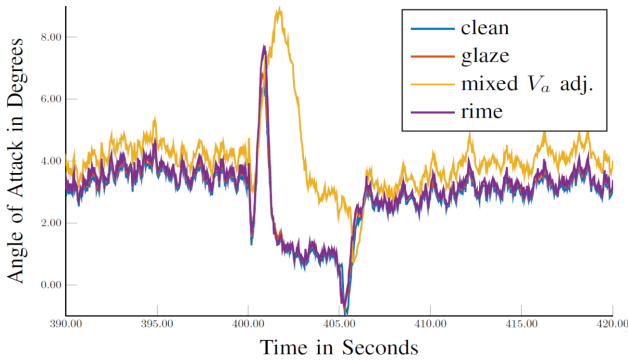

Figure A1.8: Angle of Attack during climb for different icing conditions.

shows a significantly increased AOA in the mixed icing cases during climbing compared to the clean case, even with increased airspeed. The difference in AOA is most significant around $t = 400$s where the pitch angle is increased and the AOA in the mixed ice case rises above the stall angle (see Figure A1.3). For the other icing cases AOA is only slightly increased but remains below stall angle. The negative AOA around $t = 405$s is a result of a negative pitch rotation and compensates for the higher airspeed.

A1.5.3 Elevator Deflection

Figure A1.9 shows the elevator deflection for the entire flight for the different icing scenarios. We see that due to the change in the moment coefficient in the mixed ice case (see Figure A1.5) the autopilot has to apply a constant elevator deflection in order to keep the aircraft level. Note that in the clean case a small negative deflection is necessary to achieve trim conditions. For the glaze and rime icing scenarios this moment is compensated for by the change in moment coefficient, decreasing the need for elevator deflections.

A1.5.4 Airspeed

During climbs the autopilot does not hold the airspeed but applies full thrust in order to facilitate the altitude changes more quickly. This leads to deviations from the desired airspeed. Figure A1.10 shows an example of the airspeed change during an altitude change for the different icing scenarios. The lower airspeed during climb in the mixed icing case is caused by the increased drag coefficient and angle of attack. This results in a decreased climbing performance in these conditions.

A1.5.5 Energy Consumption

Table A1.3 shows the cumulative energy consumption during flight for the four different scenarios. We see again that the mixed ice case deviates significantly from the other scenarios, both with and without adjusted airspeed. The increased energy consumption is a result of the increased angle of attack and the increased airspeed, which is needed to achieve the required lift force. This means that the drag and thus the energy consumption is not solely heightened by the increased parasite drag but also by the suboptimal operation point, leading to a significantly diminished range.

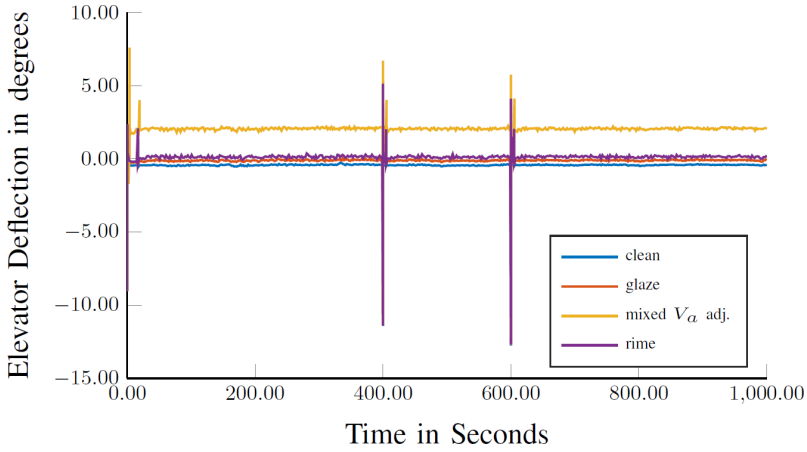

Figure A1.9: Elevator deflections.

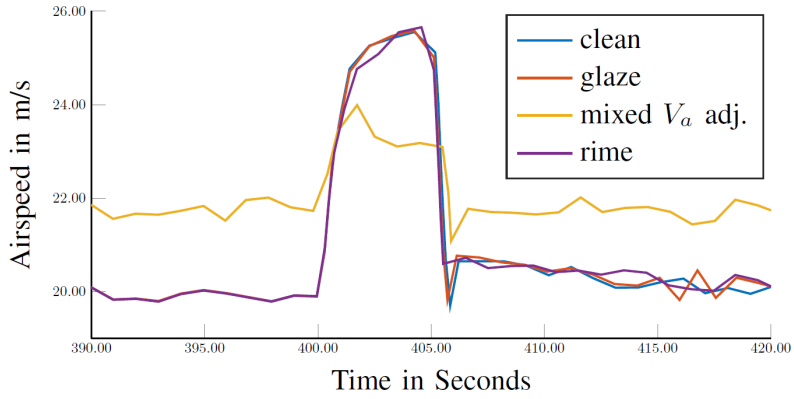

Figure A1.10: Airspeed during climb for different icing conditions.

Table A1.3: Energy consumption.

Clean	**Glaze**	**Mixed**	**Mixed adj.** V_a	**Rime**
$116Wh$	$115Wh$	$153Wh$	$138Wh$	$116Wh$

A1.6 Conclusion

In summary, the simulation results have shown a very clear and distinct impact of icing on the aerodynamic performance of a 2D airfoil. Generally, it can be observed that lift and the maximum lift angle are decreased and drag is increased substantially. The geometry of the ice shape has a significant effect on the degree of performance degradation. When separation is present at the leading-edge, the negative impact will be amplified. Hence it can be concluded that icing conditions that lead to the accretion of pronounced ice horns are most intrusive on the airfoil performance. The results showed that the level of performance degradation was strongly linked to the ice geometry. This means that a good understanding of which meteorological icing conditions lead to the most dangerous ice shapes is key for the understanding of icing effects on UAVs.

Further work should focus on investigating the impact of icing on different kinds of airfoils and over a larger range of atmospheric and operational parameters. In addition, more validation work needs to be performed to build trust towards the simulation results. There are currently ongoing wind tunnel experiments with artificial ice shapes that will provide validation data in the future.

Furthermore, we have shown how to implement these results into an existing flight simulator. The simulation results show the reaction of a standard autopilot to the performance and stability degradation in icing conditions and the impact on the energy consumption. These results will be used in the future in order to design novel ice detection methods for UAVs prior to test flights.

A2 Stability of a UAV in Icing Conditions

Note that this appendix uses its own reference system, independent from the rest of the thesis. This concerns the numbering of figures, tables, and bibliography.

Nomenclature

Whenever possible, the symbols here are chosen in accordance with ISO1151 [1].

$(\cdot)_0$	Mean value
$(\cdot)_A$	Amplitude
α	Angle of attack (AOA)
β	Angle of sideslip (AOS)
ω	Oscillation frequency
θ	Pitch angle
ϱ	Air density
b	Wing span
c	Chord
c_M	Mean Aerodynamic Chord (MAC)
k_s	Surface roughness
L, D, Y	Lift, drag and side force in air-path axes
l, m, n	Roll, pitch, yaw moment
p, q, r	Roll, pitch and yaw rate
S	(Wing) reference area
T_∞	Outside air temperature
u_b, v_b, w_b	Velocities in body-fixed x, y, z direction
V_a	Free stream velocity
ALE	Arbitrary Lagrangian-Eulerian
CFD	Computational Fluid Dynamics
LWC	Liquid water content
MVD	Median volume diameter
UAV	Unmanned aerial vehicle

1. Introduction

During the last eighty years, there has been substantial research on icing of large aircraft [2–4]. Flying wings are also well understood [5] and have been used for decades in niche applications ranging from model airplanes to the strategic bomber *Northrop B-2 Spirit*. However, there is very little published research in icing of flying wings, especially at low Reynolds numbers. Before the advent of autonomous or at least radio controlled commercial flight of small aircraft, there has been little interest in investigating these icing effects on low-Reynolds aircraft: Commercial aviation has used manned aircraft with ice-protection systems, and hobbyists have little reason to fly in icing conditions, which

are most commonly encountered in clouds. This study aims to close this gap by first describing a generic method to determine relevant aerodynamic properties with numeric simulations and then apply these methods to a medium-sized flying wing.

The issue of icing of unmanned aerical vehicles (UAV) has been known to researches since at least the early 1990s [6], but has only recently been addressed. Given the ever-growing list of applications of UAVs, ranging from scientific and commercial applications such as aerial photography to governmental and military tasks such as border control, it is apparent that all-weather capabilities, including flight into suspected icing conditions, are of major concern. This especially applies to flight in cold climates such as the Arctic, but can also be a concern in moderate climates [7]. In consequence, if operation capabilites should not be limited, there are only two possibilities: either the small UAV needs to have a classical ice protection that is able to remove ice accrecion [8] – or flight with iced wings has to be safely possible despite the severely degraded key flight characteristics such as maximum lift, drag, stall angle of attack (AOA) and stability [9, 10]. Since ice protection equipment may require structural changes and additional weight due to additional equipment and often consumes large amounts of energy, it may be advantageous to accept aerodynamic penalties in these situations and let the flight controllers handle the icing conditions to the degree possible, especially if icing only occurs occasionally. This knowledge could also enable a short-term icing severity forcast that could help in the decision to continue or abort a flight.

Recent accidents have shown that even in the 21st century, and with aircraft equipped with ice protection systems, icing remains a major concern. For example, there have been four losses of the ATR-72 alone between 1994 and 2012 that have icing as suspected cause or contributing factor [7, 11–13]. The US military has lost several aircraft in Afghanistan and had to withdraw UAVs from Hungary due to their inability to fly safely in these conditions [14, 15].

To develop autopilots or fly-by-wire-systems that are capable of flying with iced wings, it is necessary to know the static and dynamic behaviour of the entire aircraft with iced airfoils. However, the analytical or empirical methods of estimating the relevant factors all have limitations that make them inadequate for the problem:

Determining the static behaviour such as the pitch stability, i. e. the aircrafts tendency to return to equilibrium after a pitch perturbation, using CFD methods for an arbitrary geometry can be done with static simulations that are computationally cheap compared to time-dependent simulations. For this, simulating the airflow at a few (≈ 15) distinct values for the AOA (α) and angle of sideslip (AOS, β) is sufficient. The main challenge here is not to determine the changes in forces and moments to the iced airfoil, but to determine appropriate ice shapes using experiments in icing wind tunnels [10] or numerical tool such as FENSAP-ICE, LEWICE or others [16, 17].

Determining the dynamic behaviour such as damping, however, is not as simple: Etkin [18] lists several analytical methods to determine the quasi-static stability derivatives (i. e. those that depend on the roll-, pitch-, and yaw rates p, q, r), but these methods are only applicable for a very narrow set of conditions, such as attached airflow at zero AOA. This proves to be even more challenging for the dynamic derivatives (i. e. those that depend on $\dot{\alpha}$ and $\dot{\beta}$), where he only offers a method for estimating the $\dot{\alpha}$ derivatives for a thin sheet. Additionally, many analytical methods assume a tailed aircraft where the tail dominates the pitch and yaw behaviour.

XFLR5 is a software, originally developed for model airplanes, that is capable of estimating many aspects of small aircraft aerodynamics with decent accuracy [19, 20], but has severe limitations that make it unsuitable for iced caluclations. See Sec. 3.1 for a discussion of XFLR in context of iced simulations.

For this reason, time-dependent numerical simulations have to be used for all quasi-static and dynamic derivatives. Building on the previous work from Murman [21] and its more practical, application-oriented realization by Schmidt and Newman [22], the decision has been made to use Computational Fluid Dynamics with Arbitrary Lagrangian-Eulerian methods (CFD-ALE) to simulate the dynamic behaviour and determine the derivatives using a simple curve fitting process implemented in MATLAB.

Dynamic experiments in wind tunnels are possible, but uncommon, difficult and expensive. This data was not available for the airframe that was used for the simulations here. Flight tests, an important part of every flight test programme for manned flight, are also possible. They always carry the risk of damaging the vehicle and therefore have to be done safely and carefully. They are more useful at the end of the development cycle to verify and certify the previous development. Flight test data with artificial ice shapes have been performed with the UAV used for the numerical simulations, but have not yet been evaluated in detail. For this reason, 2D results found in the literature [23] are used to verify the model proposed here.

Hann et al. have investigated three icing scenarios and the influence on UAV operations in a previous work [9]. Their study however used a 2D airfoil in a classic wing-and-tail configuration to extrapolate results that should be qualitatively, but not necessarily quantitatively correct. 2D simulations can not yield results for the lateral case. Additionally, only static investigations were performed and thus no dynamic derivatives included. The three ice formes used in that study were based on 14 CFR Part 25, App. C for maximum continuous icing [24]. Of these cases, the worst case – mixed ice – has been chosen in this study.

2. Methodology

2.1 Ice model and tools

There are three major classes of ice that form in icing conditions: glaze ice, rime ice and mixed ice [25]. Glaze ice forms at relatively high temperatures just below the freezing point and is characterized by a smooth, translucent ice cover that has relatively little influence on the airflow, but is dangerous due to the potentially very high growth rates and the potential of runback behind the leading edge, that can lead to blocked control surfaces in extreme cases. At the other end of the spectum, i. e. at low temperatures below approximately minus five degrees Celsius, rime ice forms, which is characterized by a very rough, opaque surface, which has a stronger influence on airflow than glaze ice, but due to the low liquid water content of air at these temperatures, the growth rates of rime ice are typically low. For this reason, it is arguably the least dangerous icing condition.

The icing conditions with the largest impact on flight characteristics [9], that is the largest penalties on maximum lift, drag, pitch stability and stall angle, is mixed ice. This type forms at temperatures between glaze and rime, and is characterised by horn-like structures roughtly 45° to the airflow that cause detachment bubbles and fully turbulent airflow. A cross section of the iced airfoil with clearly visible horns can be found in Fig. 2. This is a plot of the ice shape that was used in this work, as it is deemed the worst case. The environmental conditions that lead to this mixed ice condition were identical to the previous work by Hann et al. [9], and are repeated in Tab. 1. Note that the icing velocity $V_{a,\text{icing}}$ of 40 m/s is almost twice the typical cruise speed of the UAV. This speed was selected to obtain the distinct horn formation [16].

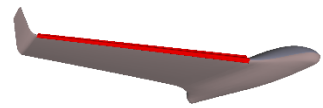

Figure 1: Ice accretion on X8 model

Within this work, it is assumed that ice only forms on the wings, so the body, propeller, and winglets are not affected by icing. This is clearly visible in Fig. 1, which shows the model of Skywalker X8 used for the simulations, as the red-shaded area.

Table 1: Values used for icing simulation

Property	Symbol	Value
Icing velocity	V_{icing}	40 m/s
Icing time	t_{icing}	40 min
Chord	c	0.3 m
Icing AOA	α_{icing}	0°
Median volume diameter	MVD	20 µm
Liquid water content	LWC	0.55 g/m^3
Outside air temperature	T_∞	-4°C
Surface roughness	k_s	1 mm

Table 2: Physical properties of X8

Property	Value
Takeoff mass	4 kg
Wing span	2.1 m
Mean aerodynamic chord	0.35 m
Airfoil	unspecified [26]
Cruise speed	≈ 20 m/s
Sweep at leading edge	≈ 30°
Wing area (without body)	≈ 0.4 m^2
Wing reference area (defined)	0.75 m^2

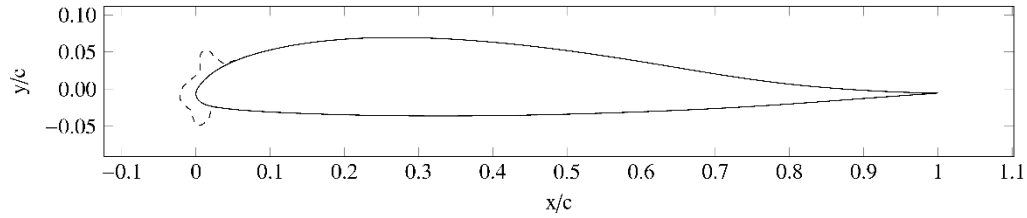

Figure 2: X8 cross section of the wing for the iced and clean configuration

This model is then discretized into a mesh using Pointwise, which is then used with the ALE method of FENSAP to generate time-dependent forces and moments. FENSAP is the flow solver [27] of the FENSAP-ICE toolbox that is developed by ANSYS Inc. To obtain the airflow solution, FENSAP solves the unsteady compressible Reynolds-

averaged Navier Stokes (RANS) equations [28]. Turbulence is simulated by the either the Spalart-Allmeras or the $k-\omega-SST$ model.

FENSAP-ICE is a state-of-the-art toolbox that coveres several aspects of icing in context of fluid dynamics: Amongst other things, FENSAP-ICE is able to simulate ice accretion, aerodynamic forces and moments, instationary effects and mesh deformation. In this study, only the flow solver FENSAP has been used. With the ALE toolbox, sinusoid oscillations around all three body-fixed axes (three rotations, three translations) can be simulated. This is done by moving the mesh relative to the flow [29].

After parsing the output files, the data is processed using MATLAB's curve fitting toolbox.

2.2 Flight mechanics model and curve fitting

The common [18, 26, 30, 31] flight mechanics model for rigid aircraft has been used in this work: This model assumes that the longitudinal parameters angle of attack α, pitch rate q and change of angle of attack $\dot{\alpha}$ have no influence on the side force Y, the roll moment l and the yaw moment n – and the lateral parameter angle of sideslip β, roll rate p, yaw rate r and change of angle of sideslip $\dot{\beta}$ have no influence on lift L, drag D and pitching moment m. All forces are given in the air-path fixed coordinate system, the moments in body-fixed axes.

$$L \approx \frac{1}{2}\varrho V_a^2 S \quad \cdot (C_L(\alpha) + C_{L_q}\frac{c_M}{2V_a}q + C_{L_{\dot{\alpha}}}\frac{c_M}{2V_a}\dot{\alpha}) \tag{1}$$

$$D \approx \frac{1}{2}\varrho V_a^2 S \quad \cdot C_D(\alpha) \tag{2}$$

$$m \approx \frac{1}{2}\varrho V_a^2 S\, c_M \cdot (C_m(\alpha) + C_{m_q}\frac{c_M}{2V_a}q + C_{m_{\dot{\alpha}}}\frac{c_M}{2V_a}\dot{\alpha}) \tag{3}$$

$$Y \approx \frac{1}{2}\varrho V_a^2 S \quad \cdot (C_Y(\beta) + C_{Y_p}\frac{b}{2V_a}p + C_{Y_r}\frac{b}{2V_a}r + C_{Y_{\dot{\beta}}}\frac{b}{2V_a}\dot{\beta}) \tag{4}$$

$$l \approx \frac{1}{2}\varrho V_a^2 S\, b \cdot (C_l(\beta) + C_{l_p}\frac{b}{2V_a}p + C_{l_r}\frac{b}{2V_a}r + C_{l_{\dot{\beta}}}\frac{b}{2V_a}\dot{\beta}) \tag{5}$$

$$n \approx \frac{1}{2}\varrho V_a^2 S\, b \cdot (C_n(\beta) + C_{n_p}\frac{b}{2V_a}p + C_{n_r}\frac{b}{2V_a}r + C_{n_{\dot{\beta}}}\frac{b}{2V_a}\dot{\beta}) \tag{6}$$

In this set of equations, the model is linearized in all parameters except α and β, and the constant influence of B on A is given as *stability derivative* C_{A_B}. The p, q, r-derivatives are called the *quasi-static* derivatives, and the $\dot{\alpha}, \dot{\beta}$-derivative *dynamic* derivatives. The quasi-static and dynamic derivatives are summarized to "instationary derivatives" within this paper. Note that the derivatives are assumed to be constant, i. e. $C_{L_q} \neq f(\alpha, \dot{\alpha}, q, \dots)$, which is *not* the case for the dynamic derivatives that are inherently dependent on the motion itself. However, for a given reduced frequency, these derivatives are useful nonetheless, e. g. for verification – see Sec. 3.2.

The model for drag is different than the model for all other forces and moments. It does not allow for determining the instationary derivatives. For a disussion of the reasons for this decision, see Sec. 5.3

There are slightly different ways to non-dimensionalize the coefficients, which usually differ by the used reference length and factors of two. The above notation was chosen because it is in line with the previous work of Gryte et al. [26]. Additionally, the wingspan b, the MAC c_M and the wing reference area S are the same, so the numerical results can be compared directly.

After linearization in α and β, these six equations are directly used for the curve fitting process, contrary to the approach Schmidt and Newman have used [22]. This removes the restrictions that the model can only be used for the longitudinal motion.

2.3 Determining the static behaviour

By running static CFD simulations, where the AOA and AOS are varied in steps of one to two degrees from low to high values and the resulting forces and moments are calculated, the static behaviour can be determined. This is often called a "AOA sweep" and "AOS sweep", respectively. In case of the AOA this is done until stall, while for the AOS, 10° is seen as the maximum realistic value. The forces and moments determined at these static, discrete points, can then be used for the simulator using a simple interpolation. Additionally, the linearized model (e. g. $C_L(\alpha) \approx C_{L_\alpha}\alpha + C_{L_0}$) can be determined by a linear regression after the values that are clearly beyond the linear range (onset of stall) are removed.

2.4 Reduced frequency approach with a single oscillation (determining instationary derivatives)

Previous work by Murman [21] has shown that determining the system response to a single reduced frequency is often precise enough and much less computationally expensive than a full time-dependent simulation which attempts to resolve all frequency modes. *Reduced frequency* referes to a non-dimensionalized frequency

$$k = \frac{\omega c}{2V_a} \tag{7}$$

with the oscillation frequency ω, the chord c (in two-dimensional cases c, in three-dimensional cases the mean aerodynamic chord (MAC) c_M is used instead) and the free stream velocity V_a. This number serves as a measurement of the "unsteadiness" of the problem. The model from Eq. (1) to Eq. (6) is only valid for $0 < k \ll 1$ [18].

The aircraft's flight on the desired trajecotry is simulated, and the aircraft's response is calculated. This is similar to wind tunnel tests, where the aircraft is fixed "on rails", and the outside forces and moments that are applied to the structure are measured. Note that the control surfaces are in neutral position all the time and not used to generate the necessary flight paths, and therefore the control derivatives are not determined.

The linearized flight model from Sec. 2.2 has three ($\alpha, \dot{\alpha}, q$-derivatives) or four ($\beta, \dot{\beta}, p, r$-derivatives) degrees of freedom, respecitvely, but the forced oscillation only two (the motion itself and its derivative). For this reason, there is a linear dependency between the parameters determined by the curve fitting. By chosing the flight path as described in Sec. 2.4.1 and 2.4.2, this linear dependency can be resolved and all 15 instationary derivatives can be determined. The curve fitting also determines the linearized static behavoiur (e. g. $C_L(\alpha) \approx C_{L_0} + C_{L_\alpha}\alpha$), but this can be more easily and more precisely determined by the α and β sweep as described in Sec. 2.3.

When forced into an oscillation, the resulting forces and moments will have a phase lag δ compared to the exciting function, as can be seen in Fig. 3. This phase lag of a few degrees is determined in the curve fitting process and contains the information about the instationary stability derivative. For this to work, the resulting force must be lineary dependent on the exciting function: $C_L = m \cdot \alpha(t) + n \cdot \dot{\alpha}(t)$. This is the reason why local linearity is a necessary precondition for this model to work. Local linearity means that the deviation between the linear model and the numerical results in the oscillation interval (for example $\alpha_0 \pm \alpha_A$) must be low. In other words the curvature of the corresponding function (for example at $C_L(\alpha_0)$) must be low.

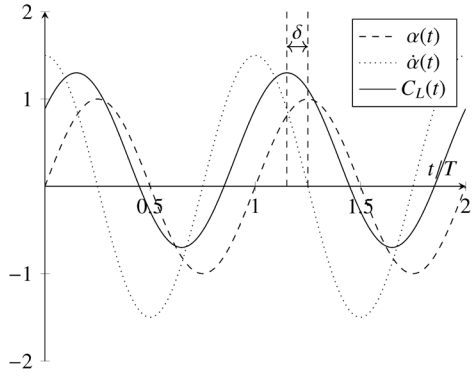

Figure 3: Exaggerated illustration of the Schmidt and Newman-approach

In the following descriptions a pure sine exciting function is assumed. All oscillations have a mean value (e. g. α_0), an amplitude (e. g. α_A), and a frequency ω, so for the AOA the exciting function would be $\alpha(t) = \alpha_0 + \alpha_A \sin(\omega t)$.

2.4.1 Test cases – longitudinal

The three parameters in the longitudinal motion are $\alpha, \dot{\alpha}, q$, which can be changed by either a pitching motion (i. e. changing the pitch angle θ), or a translational plunging motion around the aircraft's body-fixed z-axis.

To increase readability, the following section only lists the equations for lift. The equations are analogous for the pitching moment.

These three cases are illustrated in Fig. 4. Note that in the first and third case, a mean AOA of zero degrees is illustrated – this is a special case: both cases can have a nonzero mean AOA. The blue arrows indicate the air stream

velocity, the red arrows the body-fixed x-axis and the grey dotted line the flight path. The angle between the red and blue arrows is the AOA.

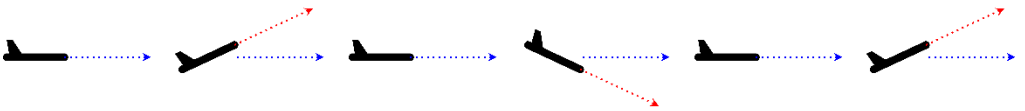

(a) Pure pitching with $q = \dot{\alpha} \neq 0$

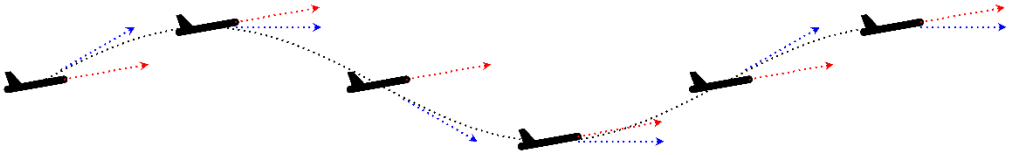

(b) Pure plunging with $q = 0, \dot{\alpha} \neq 0$

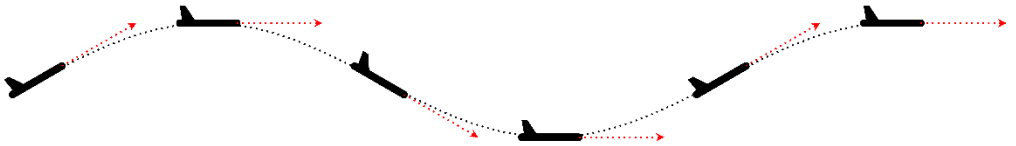

(c) Pitch-plunging with $q \neq 0, \dot{\alpha} = 0, \alpha = 0$

Figure 4: Illustration of the three longitudinal flight paths

Case a: Pure pitching motion In this case, the aircraft pitches on a horizontal flight path without changes in flight altitude/vertical velocity.

$$\theta(t) = \alpha(t) = \alpha_0 + \alpha_A \cdot \sin(\omega t) \tag{8}$$

$$\Rightarrow \quad q = \dot{\theta} = \alpha_A \cdot \omega \cdot \cos(\omega t) \tag{9}$$

$$\Rightarrow \quad \dot{\alpha} = \alpha_A \cdot \omega \cdot \cos(\omega t) \tag{10}$$

From comparing Eq. (9) and (10), it is obvious that $\dot{\alpha} = q$. Therefore only a combined damping derivative $C_{L_{\text{damp}}}$ can be determined:

$$C_L(t) \approx C_{L_0} + C_{L_\alpha}\alpha(t) + C_{L_q}\frac{c}{2V_a}q(t) + C_{L_{\dot{\alpha}}}\frac{c}{2V_a}\dot{\alpha}(t) \tag{11}$$

$$C_L(t) \approx C_{L_0} + C_{L_\alpha} \cdot \alpha(t) + \underbrace{(C_{L_q} + C_{L_{\dot{\alpha}}})}_{C_{L_{\text{damp}}}}\frac{c}{2V_a}\dot{\alpha}(t) \tag{12}$$

$$C_L(t) \approx C_{L_0} + C_{L_\alpha} \cdot (\alpha_0 + \alpha_A \sin(\omega t)) + C_{L_{\text{damp}}}\underbrace{\frac{c}{2V_a}}_{k}\omega\,\alpha_A \cos(\omega t) \tag{13}$$

Since $C_{L_{\text{damp}}}$ is assumed to be constant, the phase difference δ between the exiting function and the system response is directly dependent on k. Choosing a too low value of k for the simulations therefore results in a very small phase lag that is difficult to resolve in the fit. Chosing a too high value of k violates the assumption of the model ($k \ll 1$) and leads to wrong results.

Case b: Pure plunging motion In this case, the pitch angle θ is kept constant, and the AOA $\alpha = \arcsin(w_b/V_a) \approx w_b/V_a$ is varied by changing the vertical velocity.

$$\theta(t) = \theta_0 \tag{14}$$

$$\alpha(t) = \frac{w_A}{V_a} \cdot \sin(\omega t) = \alpha_{A,\text{equiv.}} \cdot \sin(\omega t) \tag{15}$$

$$\Rightarrow \quad q = 0 \tag{16}$$

$$\Rightarrow \quad \dot{\alpha} = \alpha_{A,\text{equiv.}} \cdot \omega \cdot \cos(\omega t) \tag{17}$$

Therefore, the q-derivative is undefined and only the $\dot{\alpha}$-derivative is determined:

$$C_L(t) \approx C_{L_0} + C_{L_\alpha} \cdot \alpha(t) + C_{L_{\dot{\alpha}}} \frac{c}{2V_a} \dot{\alpha}(t) \tag{18}$$

Case c: Combined pitching and plunging motion In this case, the AOA is kept constant by plunging down when the UAV is pitched down. The plunging velocity is chosen such as that the increase in AOA from the down-motion is equal to the decrease of AOA from the pitch down-motion – and vice versa.

$$\theta(t) = \theta_0 + \theta_A \sin(\omega t) \tag{19}$$

$$w(t) = w_A \sin(\omega t) \Rightarrow \alpha_{\text{equiv}}(t) = \alpha_{A,\text{equiv.}} \cdot \sin(\omega t) \tag{20}$$

$$\Rightarrow \quad \alpha(t) = \alpha_0 + \underbrace{(\theta_A + \alpha_{A,\text{equiv.}})}_{=0} \sin(\omega t) \tag{21}$$

$$\Rightarrow \quad q = \theta_A \omega \cos(\omega t) \tag{22}$$

In this case, the AOA is kept constant, which means that the terms C_{L_0} and $C_{L_\alpha}\alpha$ are linearly dependent and cannot be determined by the curve fitting process. Only the q-derivative can be determined.

$$C_L(t) = \underbrace{C_{L_0} + C_{L_\alpha}\alpha}_{\text{const.}} + C_{L_q} \frac{c}{2V_a} q(t) \tag{23}$$

2.4.2 Test cases – lateral

The lateral test cases are very similar to the longitudinal cases, except in all cases the mean AOS is zero ($\beta = 0$), and that there are four properties/derivatives for each of the three forces and moments. Only the exciting functons are given here, and the side force Y is used as place holder for the roll moment l and yaw moment n. A sidewards motion (equivalent to the plunging described above) is called "traversal" in this paper. For symmetry reasons, the constant factors $C_{Y_0}, C_{l_0}, C_{n_0}$ should all be zero. To improve the curve fitting process, these factors are included in the model, but the numerical values determined by the fit are always very small.

Case d: Pure Yawing In this case, the AOS is time-dependent and the yaw rate is equal to the change in AOS $\dot{\beta}$. Similar to case a, only a combined derivative $C_{Y_{\text{damp}}} = C_{Y_{\dot{\beta}}} + C_{Y_r}$ can be determined.

$$\beta(t) = \beta_A \sin(\omega t) \tag{24}$$

$$\dot{\beta}(t) = \beta_A \omega \cos(\omega t) \tag{25}$$

$$r = \dot{\beta}(t) \tag{26}$$

$$C_Y(t) = C_{Y_0} + C_{Y_\beta}\beta(t) + C_{Y_{\text{damp}}} \frac{b}{2V_a} \dot{\beta}(t) \tag{27}$$

Case e: Pure Traversal In this case, the AOS is time dependent, and the yaw rate is zero. With the side-velocity amplitude v_A, the equvivalent AOS is $\beta_{A,\text{equiv.}} \approx v_A / V_a$

$$\beta(t) = \beta_{A,\text{equiv.}} \sin(\omega t) \tag{28}$$

$$\dot{\beta}(t) = \beta_{A,\text{equiv.}} \omega \cos(\omega t) \tag{29}$$

$$r = 0 \tag{30}$$

$$C_Y(t) = C_{Y_0} + C_{Y_\beta}\beta(t) + C_{Y_{\dot{\beta}}} \frac{b}{2V_a} \dot{\beta}(t) \tag{31}$$

Case f: Yawing and traversal In this case, the AOS is zero, and the yaw rate is nonzero

$$\beta(t) = \dot{\beta} = 0 \tag{32}$$
$$r(t) = \beta_A \omega \cos(\omega t) \tag{33}$$
$$C_Y(t) = C_{Y_0} + C_{Y_r} \frac{b}{2V_a} r \tag{34}$$

Case g: Pure rolling In this case, the AOS is zero, and the roll-rate is time-dependent.

$$\beta(t) = \dot{\beta} = 0 \tag{35}$$
$$p(t) = p_A \omega \cos(\omega t) \tag{36}$$
$$C_Y(t) = C_{Y_0} + C_{Y_p} \frac{b}{2V_a} p \tag{37}$$

3. Validation of the instationary results

There is no suitable experimental data from the Skywalker X8 available to direcly compare the results from the simulations to. Therefore, to validate the methodology, three different indirect approaches were employed:

- Comparison with XFLR5 and wind tunnel, where available
- Check of internal consistency
- Comparison with 2D test cases from the literature

None of these approaches yield a definite proof that the proposed method and results are adequate, but taken together they may offer a strong indication that the results are accurate.

Lacking the required experimental data, the lateral results can only checked for internal consistency and compared with the XFLR5 results. However, Murman has already shown in [21], that the method works for the lateral derivatives. It is therefore assumed that if the longitudinal verification is successful, the method also works in the lateral case.

3.1 Comparison with XFLR5 results

Gryte et al. [26] have already compared the XFLR5 results to the wind tunnel data, where it was shown that the static XFLR5 results are reasonable, but an assessment of the instationary XFLR5 results was not possible with the available data. The XFLR5 calculations are listed together with the results of this work in the tables in the next section. No attempt of a quantitative comparison with XFLR5 is made, because the XFLR5 results themselfs have severe limitations. The methods used by XFLR5 work reasonably well for the clean case and simple geometries [19, 20], but fail to deliver accurate results in more complex cases [32]. The XFLR5 documentation does not go into detail how the quasi-stationary stability derivatives are determined, but explicitly states that "the potential flow model is only valid in conditions of limited flow separation" [33], an condition that is violated in the iced case. XFLR5 also generally is limited to simple geometries and for example is unable to accurately predict a wing-body intersection or large control surface deflections. Last, XFLR5 tends to under-estimate drag even in ideal conditions. In summary, trying to simulate icing would violate almost all recommendations mentioned in the XFLR5 manual [33].

3.2 Check of internal consistency

Two main checks were done: verification of the sample rate (i. e. unsteady CFD time step) and verification of the damping sums. The sample rate was increased from about 20 samples per period to 1000 samples per period. The results from 20 samples per period differed from the other results by less than 5%, and more than 100 samples per period did not significantly alter the results, see Tab. 3. For this reason, 100 samples per period was chosen as a compromise between computational complexity and precision. The test case is equivalent to the low AOA clean test case from the previous section.

For the test cases a-f, the internal consistency can also be checked. This means, that the results from the pure pitching/yawing cases should be the sum of the other instationary derivatives. Table 4 and 5 list the results of the longitudinal comparison. The agreement is good, except for the high AOA clean cases, which might be caused by large non-linearities due to the onset of flow separation at 8° AOA.

Table 3: Comparison between the dynamic derivatives for different sample rates

Case	Samples (1/T)	$C_{L_{\text{damp}}}$	Δ	$C_{m_{\text{damp}}}$	Δ
Sample rate 1	50	2.52	-5.62%	-1.38	-3.50%
Sample rate 2	100	2.63	-1.50%	-1.42	-0.70%
Sample rate 3	200	2.66	-0.37%	-1.43	0.00%
Sample rate 4	500	2.67	–	-1.43	–

Table 4: Comparison of directly determined (“damp”) and summed (“sum”) lift derivatives

Case	C_{L_q}	$C_{L_{\dot{\alpha}}}$	$C_{L_{\text{damp}}}$	$C_{L_{\text{sum}}}$	ΔC_L
X8 Clean Low AOA	4.64	-1.89	2.63	2.75	-0.12
X8 Clean High AOA	4.60	-0.25	2.89	4.35	-1.46
X8 Iced Low AOA	-3.31	3.27	0.21	-0.04	0.25
X8 Iced High AOA	-3.51	5.43	2.24	1.92	0.32

Table 5: Comparison of directly determined (“damp”) and summed (“sum”) pitching moment derivatives

Case	C_{m_q}	$C_{m_{\dot{\alpha}}}$	$C_{m_{\text{damp}}}$	$C_{m_{\text{sum}}}$	ΔC_m
X8 Clean Low AOA	-1.99	0.63	-1.31	-1.36	0.06
X8 Clean High AOA	-0.28	-1.35	-1.50	-1.63	0.13
X8 Iced Low AOA	-2.00	-0.64	-2.65	-2.64	-0.01
X8 Iced High AOA	-2.12	1.13	-0.99	-0.98	0.01

3.3 Two dimensional verification simulations

In the 1970s and 80s, investigations in the dynamic behaviour of helicopter blades has been made and summarized in the AGARD-R-702 report [23]. For the verification here, two-dimensional results with the symmetric laminar flow airfoil NACA 64_A010 were chosen. These cases have the AGARD-IDs “DI7” and “DI29”. Of all two dimensional airfoil experiments, these two cases were the closest to the problem at hand in Mach number. The two 2D cases were simulated with the unsteady ALE approach in FENSAP for for longitudinal movements as decribed above (Case a). The test parameters are listed in Tab. 6, and the results in Tab. 7.

The results show good agreement for the dynamic derivatives ($C_{L_{\text{dyn,AGD}}} \approx C_{L_{\text{dyn,CFD}}}$ and $C_{m_{\text{dyn,AGD}}} \approx C_{m_{\text{dyn,CFD}}}$), but poor agreement for the static pitch derivative C_{m_α}. This value should theoretically be close to zero in both cases: In subsonic flow the neutral point is approximately at 25% c, and characterized by a pitching moment that is almost independent of the AOA. The reason for the differences could not be determined. Possible explainations include simulation errors, for example caused by transition issues, and measurement errors in the report. During the AGARD experiments, the forces and moments were derived from the pressure distribution instead of being measured directly.

The method is only used to determine instationary results, where the agreement is good. Nonetheless, further verification simulations that aim to resolve the disagreement, should be considered.

Table 6: Properties used in verification simulations

Property	CT 1 (DI 7)	CT 2 (DI 29)
Profile	NACA 64_A010	NACA 64_A010
Chord	0.5 m	0.5 m
Frequency	10.4 Hz	10.8 Hz
Mach-number	0.490	0.502
α_0	-0.01°	-0.22°
α_A	0.96°	1.02°
Rotation axis	0.233 x/c	0.269 x/c
Moment ref. axis	0.25 x/c	0.25 x/c
Reynolds-number	$2.52 \cdot 10^6$	$9.98 \cdot 10^6$
Transition	Free	Free

Table 7: Comparison between AGARD results and CFD-ALE simulations)

Test Case	k	$C_{L_\alpha,\text{AGD}}$	$C_{L_\alpha,\text{CFD}}$	$C_{L_{\text{dyn}},\text{AGD}}$	$C_{L_{\text{dyn}},\text{CFD}}$	$C_{m_\alpha,\text{AGD}}$	$C_{m_\alpha,\text{CFD}}$	$C_{m_{\text{dyn}},\text{AGD}}$	$C_{m_{\text{dyn}},\text{CFD}}$
CT 1 (DI7)	0.1	6.139	5.75	-11.49	-9.45	0.165	-0.10	-1.36	-1.45
CT 2 (DI29)	0.1	6.163	5.68	-10.36	-9.42	0.167	-0.10	-2.01	-1.17

4. Results

Simulations were conducted using the existing UAV platform at the NTNU UAVlab, which is a *Skywalker X8* medium-sized flying wing with swept wings and relatively large winglets that also serve as a vertical stabilizer. Some physical properties are listed in Tab. 2. The aircraft has no rudder, which means that the yaw stability is of very high concern, as electronic yaw compensation is not possible.

4.1 Static Behaviour

Results from the AOA and AOS sweeps as desribed in Sec. 2.3 can be found in Fig. 5. Only the sweeps for the decoupled model, i. e. without the influence of β on L, D, m, are plotted. Tab. 8 lists the linearized parameters (except for drag) for small α and β, where for example $C_L(\alpha) \approx C_{L_\alpha}\alpha + C_{L_0}$ with α in radians.

4.2 Instationary behaviour

All simulations have been conducted with an amplitude of 2° and a frequency of 2 Hz, which is equivalent to $k = 0.13$ at a free stream velocity of 17 m/s for the given geometry with $c_M = 0.35$ m. All simulations have been performed at a low AOA of 2°, and a high AOA of 8°, which is close to the stall angle for the iced case. The curve fitting also determines static derivatives, but these are not listed because the sweeps from the previous section is are more precise. The XFLR5 data is, where available, listed and taken from Gryte et al. [26].

Table 8: Parameters for linearizations of AOA and AOS dependencies

Function	Linear factor clean	Constant factor clean	Linear factor iced	Constant factor iced
$C_L(\alpha)$	4.06	0.03	3.26	0.01
$C_m(\alpha)$	-1.00	0.00	-0.83	0.00
$C_Y(\beta)$	0.16	0.00	0.17	0.00
$C_l(\beta)$	-7.6×10^{-2}	0.00	-6.5×10^{-2}	0.00
$C_n(\beta)$	2.2×10^{-2}	0.00	2.6×10^{-2}	0.00

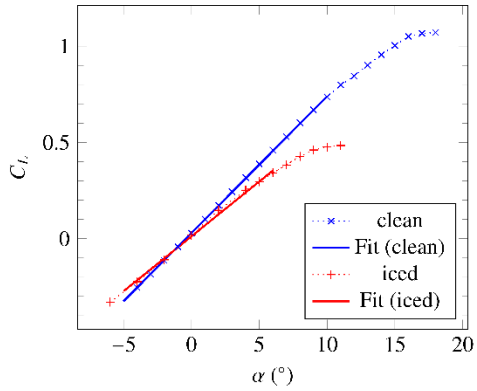

(a) Lift over AOA

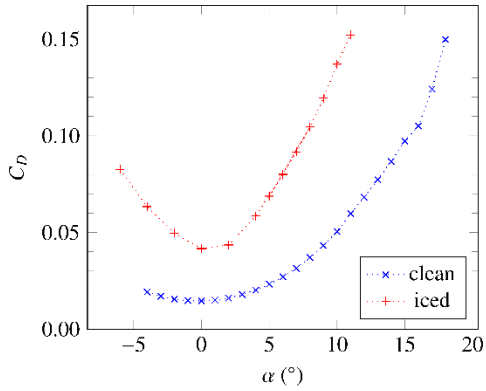

(b) Drag over AOA

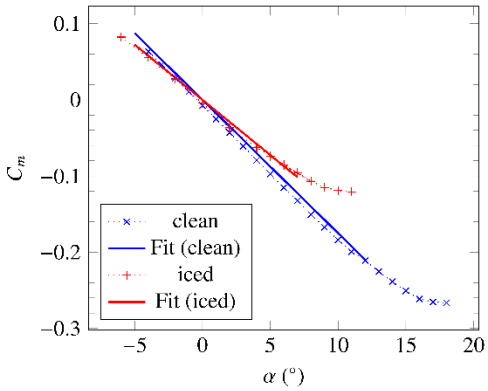

(c) Pitching moment over AOA

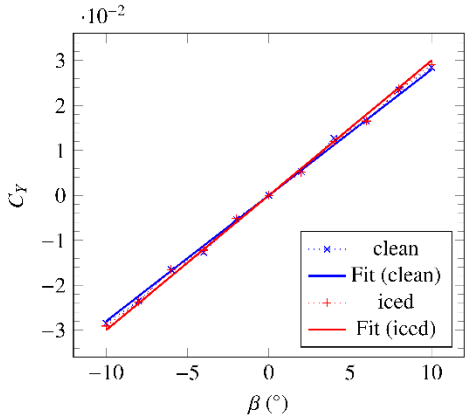

(d) Side foce over AOS

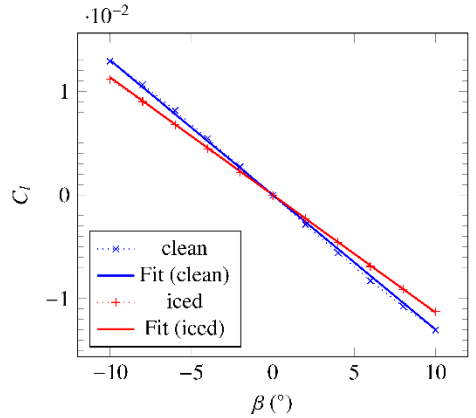

(e) Roll moment over AOS

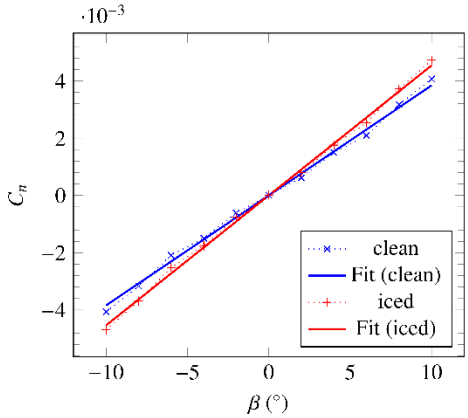

(f) Yaw moment over AOS

Figure 5: Static longitudinal and lateral behaviour, clean and iced. Parameters of fitted curves in Tab. 8

Table 9: Comparison of the longitudinal derivatives at all four points

Derivative	Clean Low AOA	Iced Low AOA	Clean High AOA	Iced High AOA	XFLR5
C_{L_q}	4.64	-3.31	(4.60)	-3.51	3.87
$C_{L_{\dot{\alpha}}}$	-1.89	3.27	(-0.25)	5.43	
$C_{L_{\text{dyn}}}$	2.65	0.20	2.89	2.24	
C_{m_q}	-2.00	-2.00	(-0.29)	-2.12	-1.3
$C_{m_{\dot{\alpha}}}$	0.63	-0.63	(-1.35)	1.13	
$C_{m_{\text{dyn}}}$	-1.32	-2.65	-1.50	-0.99	

Table 10: Comparison of all instationary lateral derivatives

Derivative	Clean	Iced	XFLR5
$C_{Y_{\dot{\beta}}}$	-0.023	-0.034	
C_{Y_p}	-0.185	-0.133	-0.137
C_{Y_r}	0.005	0.002	0.084
$C_{Y_{\text{dyn}}}$	-0.042	-0.038	
$C_{l_{\dot{\beta}}}$	0.028	0.123	
C_{l_p}	-0.409	-0.407	-0.404
C_{l_r}	0.039	0.158	0.056
$C_{l_{\text{dyn}}}$	-0.010	-0.026	
$C_{n_{\dot{\beta}}}$	-0.011	-0.029	
C_{n_p}	0.027	0.017	0.004
C_{n_r}	-0.022	-0.049	-0.012
$C_{n_{\text{dyn}}}$	0.011	0.018	

5. Discussion

5.1 Static behaviour

The illustrations in Fig. 5 clearly show a severe degradation especially in lift and drag, where drag roughly triples at most AOAs, and the maximum lift coefficient is reduced by about 50% from 1.1 at 18° to 0.48 at 11°. At a moderate AOA of 4°, the drag coefficient increases from 0.02 to 0.05, at a high AOA of 10° C_D increases from 0.05 to 0.14. This result is very similar to the 2D-simulations from Hann et al. [9].

The side force is virtually unaffected by icing, which can be explained by the winglets not having ice accretion in the model. The different slopes in Fig. 5 (d) are within rounding error range. The roll stability $C_l(\beta)$ is slightly reduced, but the yaw/weathercock stabilily $C_n(\beta)$ is actually *increased*. The reason for this could be that due to the wing's sweep, the forward facing wing has a larger drag than the rearward wing – and with iced wings, this difference between the leading and trailing wing is amplified, leading to a higher yaw stiffness. X8 has no rudder, so a high yaw stiffness is very positive, because the inevitable side slip after an aileron input is then reduced sooner.

5.2 Instationary behaviour

The longitudinal results as presented in Tab. 9 are inconclusive. They show no clear correlation between clean and iced, nor between low and high AOAs. For the important pitch damping derivative C_{m_q}, we see that the iced cases and the low AOA clean case are very similar. The high AOA case shows nonlinear behaviour and thus a poor curve fit, so this data is unreliable. The values determined by a fit with a low R^2-value are written in parentheses.

The large changes in the quasi-static lift derivative C_{L_q} from the clean to the iced case may be explained by the fact that the additional lift that would ordinarily be generated by the warped airflow with a pitch rate can not be delivered anymore. A partial stall with the corresponding decrease in lift could be a consequence and would explain the negative lift derivative.

The lateral results, all determined at a low AOA, partially can be well explained, and partially are more surprising. For example, the increase in C_{n_r} can probably be easily explained: During a yawing motion, the slower, inner wing

has less drag due to the lower dynamic pressure. Since the difference in drag is higher for the iced wing, this results in a yawing moment that reduces the yaw rate and tries to return the two wings to equilibrium. In contrast, the increase in yaw-rate induced roll C_{l_r} is more surprising. The slower, inner wing produces less lift due to the lower dynamic pressure and a roll moment is the result. According to Etkin [18], this roll moment is proportional to C_L in undisturbed flight, a factor that is slightly decreased for the wing at $\alpha = 2°$.

A higher (absolute) value of the derivatives is not necessarily better, for example an excessive damping could also lead to sluggish flight behaviour. For this reason, no attempt of a qualitative assessment of the instationary derivatives is made here, and the consequences of changes to the instationary derivatives should be investigated using flight simulations with and without changes to the controllers. The importance of these derivatives also depends on the flight platform. For example, a high yaw rate induced roll moment (C_{l_r}) may be desired in a plane without ailerons where the bank angle only is a result of rudder input – whereas in typical tailed aircraft with ailerons and rudder such behaviour might be not desired because compensation with ailerons is required in stationary curved flight.

5.3 Instationary drag

As already mentioned, the model fails when trying to determine the dynamic drag influences. The reason for this is that, even at small AOAs, drag is very non-linear so that the linearized model as shown above does not apply. Several attempts to model the drag using the induced-drag formula, two of which are shown below, were made. This formula assumes a non-lift dependent drag (parasitic drag, C_{D_P}, signified with a capital P and not to be confused with the drag caused by roll rate C_{D_p}) and a lift-dependent drag (induced drag, C_{D_i}).

$$C_D(\alpha) \approx C_{D_P} + C_{D_i} = C_{D_P} + \frac{C_L^2(\alpha)}{\pi e_0 \Lambda} \tag{38}$$

$$\approx C_{D_P} + \frac{(C_{L_\alpha}\alpha + C_{L_0})^2}{\pi e_0 \Lambda} \tag{39}$$

$$\approx C_{D_P} + \frac{(C_{L_\alpha}\alpha + C_{L_0} + C_{L_q}\frac{c}{2V_a}q + C_{L_{\dot\alpha}}\frac{c}{2V_a}\dot\alpha)^2}{\pi e_0 \Lambda} \tag{40}$$

The model equations (Eq. (39) and (40)) were then introduced instead of $C_D(\alpha)$ into Eq. (2). None of the variations yielded usable fits for the dynamic drag. In every case, either the fit was poor or the determined values deemed as highly unlikely. Additionally, there is no established model for dynamic drag, and the dynamic drag is usually neglected [18, 31] because its influcence is assumed to be minor. The changes in drag caused by the dynamic effects, even if they had non-negligible values, also have little impact on flight characteristics as long as enough engine thrust is available. For this reason, the decision has been made not to attempt to determine values for C_{D_q} and $C_{D_{\dot\alpha}}$.

6. Further work

Most discrepancies can likely be explained by non-linearities in the simulations. For this reason, investigating the effects with other parameters that reduce the non-linearities, may be advised. For example, lower oscillation amplitudes, or different mean AOAs could lead to clearer results. Using a finer discretization in the parameters $\omega, \alpha_0, \alpha_A, k, \ldots$ could yield hints to model restrictions and correlations between the parameters. This can easily be done with this model since only a few restrictions in these parameters are required to guarantee the model assumptions.

Alternatively, the demands for linear behaviour in α and β can possibly be relaxed by changing the fitted model function from the linearized function (11) to the semi-linearized model (1) with the results from the static sweeps. This may increase the quality of the results, especially for high-AOA-cases and for drag at all AOAs.

Further work that investigates the impact on the flight behaviour caused by the changes to the derivatives is already planned. For this, an existing flight simulator is modified to incorporate the results from this work. Afterwards, flight tests with 3D-printed artificial ice shapes are desirable to verify the results in real flight conditions.

To improve the flight simulations, the control derivatives, i. e. the system response to control surface input, should also be investigated. It may be interesting to investigate the influence of other ice shapes and on different aircraft configurations (particularly conventional tailed aircraft). For the flight simulators, it would be advantageous to have some continuous icing model that uses an appropriate interpolation between the investigated points. This could then be included in other applications such as the observer based icing detection system by Seron et al. [34]. For this, it is likely necessary to investigate influences of the parameters on the results further.

7. Conclusion

In this work, a previously established and validated method to determine quasi-static and dynamic stability derivatives using time-dependent CFD-ALE simulations was used to determine the instationary behaviour of a severely iced flying wing at low Reynolds numbers. Together with new stationary 3D simulations, this allows a quantitative assessment of changes to flight characteristics compared to the clean case. The method is generic and can be applied to all aircraft and icing conditions at almost all points in the flight envelope.

The model was validated once more against 2D test cases found in the literature. It has a high internal consistency if the model limitations are met. Therefore, even without experimental comparisons, there are strong indications that the model is adequate.

The results show a clear deterioration of static longitudinal flight performance, smaller but noticeable changes in the static lateral characteristics, and significant changes in some instationary properties. This data forms a basis to investigate changes to the flight properties of the full aircraft in severe icing conditions using a flight simulator and could be used in future for applications such as icing-tolerant autopilots or electronic in-flight icing detection.

8. Acknowledgments

The first author would like to thank the European Union for supporting this work that was done as part of a master's thesis via the Erasmus+ programme.

The author would also like to thank Dr. Werner Grimm from the Institute of Flight Mechanics and Control (iFR) at the University of Stuttgart, who has agreed to supervise him during his master's thesis.

The research was funded by the Norwegian Research Council (project no. 223254) through the NTNU Centre of Autonomous Marine Operations and Systems (NTNU AMOS) at the Norwegian University of Science and Technology, and partially by CIRFA grant number 237906.

References

[1] ISO. ISO 1151-1:1988 – Flight dynamics – Concepts, quantities and symbols – Part 1: Aircraft motion relative to the air. Technical report, 1988.

[2] Thomas P. Ratvasky, Judith Foss Van Zante, and J. T. Riley. NASA/FAA Tailplane Icing Program Overview (AIAA-99-0370). Technical report, 1999.

[3] Frank T Lynch and Abdollah Khodadoust. Effects of ice accretions on aircraft aerodynamics. *Progress in Aerospace Sciences*, 37(8):669–767, 2001.

[4] C. Deiler and T. Kilian. Dynamic aircraft simulation model covering local icing effects. *CEAS Aeronautical Journal*, 9(3):429–444, 2018.

[5] Karl Nickel and Michael Wohlfahrt. *Tailless Aircraft in theory & practice*. Butterworth Heinemann, 1992.

[6] R. A. Siquig. Impact of Icing on Unmanned Aerial Vehicle (UAV) Operations. Technical report, Naval Environmental Prediction Research Facility, 1990.

[7] Aviation Safety Network (ASN). ASN Aircraft Accident ATR 72-212 CU-T1549. https://aviation-safety.net/database/record.php?id=20101104-0 (accessed 2019-06-18).

[8] Richard Hann, Kasper Borup, Artur Zolich, Kim Sorensen, Håvard Vestad, Martin Steinert, and Tor Johansen. Experimental Investigations of an Icing Protection System for UAVs. In *SAE Technical Paper*. SAE International, 2019.

[9] Richard Hann, Andreas Wenz, Kristoffer Gryte, and Tor Arne Johansen. Impact of Atmospheric Icing on UAV Aerodynamic Performance. In *Workshop on Research, Education and Development of Unmanned Aerial Systems (RED-UAS)*, Linköping, 2017.

[10] Richard Hann. UAV Icing: Ice Accretion Experiments and Validation. In *SAE Technical Paper*. SAE International, 2019.

[11] Aviation Safety Council. Transasia GE 791 Occurrence Investigation Report. Technical report, 2002.

[12] National Transportation Safety Board (NTSB). Aircraft Accident Report: American Eagle Flight 4184. Technical report, 1996.

[13] Interstate Aviation Committee. Final report on results of investigation of accident (VP-BYZ). Technical report, 2013.

[14] Dr. Daniel L. Haulman. U.S. Unmanned Aerical Vehicles in Combat, 1991-2003, 2003.

[15] Lindamae Peck, Charles C. Ryerson, and C. James Martel. Army Aircraft Icing (ERDC/CRREL TR-02-13). Technical report, US Army Corps of Engineers – Cold Regions Research and Engineering Laboratory, 2002.

[16] Richard Hann. UAV Icing: Comparison of LEWICE and FENSAP-ICE for Ice Accretion and Performance Degradation. *2018 Atmospheric and Space Environments Conference*, pages 1–8, 2018.

[17] K Szilder and W Yuan. In-flight icing on unmanned aerial vehicle and its aerodynamic penalties. *Progress in Flight Physics*, 9:173–188, 2017.

[18] Bernard Etkin and Lloyd Duff Reid. *Dynamics of Flight*. John Wiley & Sons, Inc., 1996.

[19] Kristofer Gryte, Richard Hann, Mushfiqul Alam, Jan Rohac, Tor Arne Johansen, and Thor I. Fossen. Aerodynamic modeling of the Skywalker X8 Fixed-Wing Unmanned Aerial Vehicle. *2018 International Conference on Unmanned Aircraft Systems, ICUAS 2018*, pages 826–835, 2018.

[20] A Deperrois. Modal analysis and experimental validation. Technical report, 2011.

[21] Scott M. Murman. Reduced-Frequency Approach for Calculating Dynamic Derivatives. *AIAA Journal*, 45(6):1161–1168, 2007.

[22] Stefan Schmidt and Daniel M Newman. Estimation of Dynamic Stability Derivatives of a Generic Aircraft. *17th Australasian Fluid Mechanics Conference (AFMC)*, 2010.

[23] NATO Advisory Group for Aerospace Research and Development (AGARD). AGARD-R-702 - Compendium of Unsteady Aerodynamic Measurments. Technical report, NATO, 1982.

[24] Federal Aviation Administration. Part I – Athmospheric Icing Conditions. 14 CFR 25 Appendix C, 2011.

[25] R. W. Gent, N. P. Dart, and J. T. Cansdale. Aircraft icing. *Philosophical Transactions of the Royal Society A: Mathematical, Physical and Engineering Sciences*, 358(1776):2873–2911, 2000.

[26] Kristoffer Gryte, Richard Hann, Mushfiqul Alam, Jan Rohac, Tor Arne Johansen, and Thor I. Fossen. Aerodynamic modeling of the Skywalker X8 Fixed-Wing Unmanned Aerial Vehicle. *2018 International Conference on Unmanned Aircraft Systems, ICUAS 2018*, pages 826–835, 2018.

[27] ANSYS Inc. ANSYS FENSAP-ICE User Manual. Technical report, 2017.

[28] Pascal Tran, Guido Barruzi, Frederic Tremblay, Wagdi Habashi, Perry Petersen, Mark Ligget, Jan Vos, Pascal Benquet, and Stefano Fiorucci. FENSAP-ICE Applications to Unmanned Aerial Vehicles (UAV). (January), 2013.

[29] C. W. Hirt, A. A. Amsden, and J. L. Cook. An arbitrary Lagrangian-Eulerian computing method for all flow speeds. *Journal of Computational Physics*, 14(3):227–253, 1974.

[30] Randal W Beard and Timothy W McLain. Small Unmanned Aircraft – Chapter 4: Forces and Moments. In *Small Unmanned Aircraft – Theory and Practice*. Princeton University Press, 2012.

[31] Jan Roskam. *Airplane Flight Dynamics and Automatic Flight Controls - Part I*. DARcorporation, Lawrence, KS, 3rd editio edition, 2001.

[32] A Deperrois. About XFLR5 calculations and experimental measurements. Technical Report October, 2009.

[33] A Deperrois. Theoretical limitations and shortcomings of XLFR5. Technical Report June, 2019.

[34] Maria M Seron, Tor Arne Johansen, José A De Doná, and Andrea Cristofaro. Detection and Estimation of Icing in Unmanned Aerial Vehicles using a Bank of Unknown Input Observers. pages 1–28, 2015.

ISBN 978-82-326-4748-4 (printed version)
ISBN 978-82-326-4749-1 (electronic version)
ISSN 1503-8181

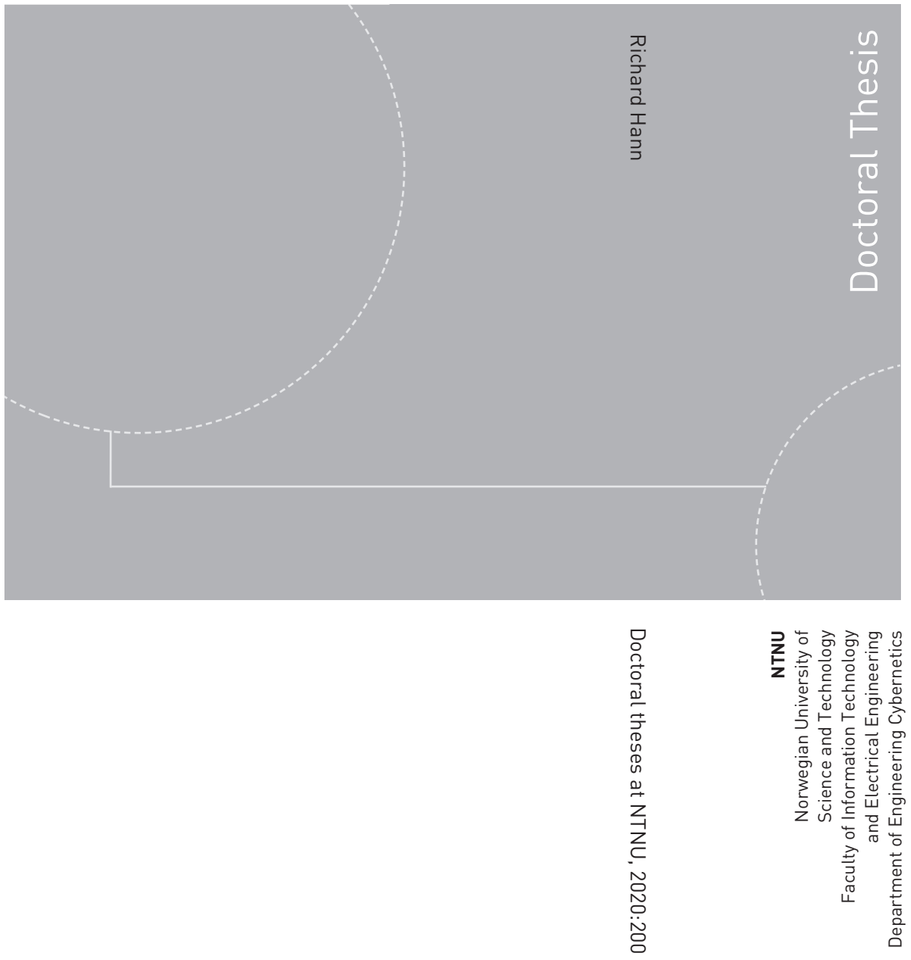

Doctoral theses at NTNU, 2020:200

Richard Hann

Atmospheric Ice Accretions, Aerodynamic Icing Penalties, and Ice Protection Systems on Unmanned Aerial Vehicles

NTNU
Norwegian University of
Science and Technology
Faculty of Information Technology
and Electrical Engineering
Department of Engineering Cybernetics

NTNU
Norwegian University of
Science and Technology

Doctoral theses at NTNU, 2020:200

NTNU

NTNU
Norwegian University of
Science and Technology